NATURAL
PARAMETERIZATION

AARHUS
UNIVERSITY
DEPARTMENT OF ENGINEERING

DATA SHEET

Author: Torben BRØCHNER
Department of Engineering – Mechanical Engineering,
Aarhus University

Abstract: The objective of this project has been to develop an
approach for imitating physical objects with an underlying
stochastic variation. The key assumption is that a set of
"natural parameters" can be extracted by a new subdivision
algorithm so they reflect what is called the object's "geometric
DNA". A case study on one hundred wheat grain cross-
sections (*Triticum aestivum*) showed that it was possible to
extract thirty-six such parameters and to reuse them for Monte
Carlo simulation of "new" stochastic phantoms which possess
the same stochastic behavior as the "original" cross-sections.

NATURAL PARAMETERIZATION

Torben Brøchner

Aarhus University, Department of Engineering

Abstract

The objective of this project has been to develop an approach for imitating physical objects with an underlying stochastic variation. The key assumption is that a set of "natural parameters" can be extracted by a new subdivision algorithm so they reflect what is called the object's "geometric DNA". A case study on one hundred wheat grain cross-sections (*Triticum aestivum*) showed that it was possible to extract thirty-six such parameters and to reuse them for Monte Carlo simulation of "new" stochastic phantoms which possess the same stochastic behavior as the "original" cross-sections.

A B S T R A C T

Today, high resolution scanners are able to capture the geometrical details of natural objects like never before. As a result, highly irregular look-a-like phantoms, based on scanned observations, are receiving increasing attention in the field of multi-physics modeling. A few models within Biosystems applications such as grain, soil and natural fluid transport, are already being investigated by the latest multi-physics software. However, with regard to multiresolution modeling of natural objects, there is an identified need for new parametric simulation approaches that can handle roughness and other complex geometries that vary from scan to scan and over time. One of the first approaches to stochastic phantom generation was published by Baek, SY. & Lee, K., Seoul National University, January 2012. This approach focused on the generation of smooth, human body surfaces, from a 3D template based on whole body scans. However, the geometry of objects investigated in Biosystems engineering is not smooth. On the contrary, most natural objects are characterized by irregular shapes, rough textures, hair, and other geometric complexities that make template based modeling unreachable. Therefore, an alternative parameterization approach is required for rough objects. Specifically, there is a need for a novel generic parameterization approach, based on scanned objects, that is able to model irregular space-time variations in naturally rough objects as easily as today's free-form modeling is able to model smooth objects.

The objective of this project has been to imitate geometries of objects with an underlying stochastic variation. In order to do so a two-step approach was introduced. The first step is dedicated to the extraction of intrinsic parameters from samples of specific objects. In the second step, these parameters, popularly referred to as the "geometric DNA," are used for re-parameterization into imitation meshes, which are then displayed as phantoms. A central assumption of this approach is that it is possible to extract, at minimum, one unique constellation of parameters for any natural object in such a way that they behave like generalized coordinates. In other words, the extracted parameters are perceived as independent degrees of freedom variables which are able to model the entire geometry. This assumption also forms the basis for subsequent generation of stochastic phantoms through Monte Carlo simulations of new independent parameters. The final outcome is a series of new phantoms, which appear in such shape and detail that experts are likely to recognize them as "feasible imitations" of the underlying objects. In other words, the goal is to create "look alike" phantoms that appear with the same stochastic characteristics as observed in the original object.

In a case study of one hundred wheat grain cross-sections, parameter extraction was initiated using expert knowledge of the "bow-line," a characteristic landmark for wheat grains. This unique landmark of all wheat grains was identified in every single object in the sample. Computationally, the "bow-line" was localized by a dedicated identification algorithm based on the convex hull of the cross-section and a special anti podal pair's constellation. It was demonstrated that the "bow-line" landmark, and another seventeen unique master parameters for each cross-section, could be extracted. This means that it was possible to extract a total set of eighteen parameters, which were then used to form the set of so-called "master parameters". Thereafter, an automated segmentation routine was used to divide the cross-section outline into six tortuous segments. From each such segment, another three iterated parameters were extracted using an iterative replication approach. Since three iterated parameters were extracted for each of the six segments, an additional set of eighteen new "iterated parameters" was formed. During the iterative replication of the iterated parameters, the maximum relative error for replication of the one hundred cross-sections areas was found to be less than one percent. The eighteen master parameters, along with the set of eighteen iterated parameters, gave a total of thirty six

"natural parameters" for each cross-section. A set of natural parameters and the constellation they form is called a "master mesh". This master mesh is a parameteric representation of the objects "geometric DNA". Mathematically, the extraction of the eighteen iterated parameters was accomplished using a novel multiresolution parametric subdivision approach called Frenet subdivision. This approach is a variant of the well-known Catmull-Clark approach, however, it includes Frenet vectors and natural equations explicitly. In this case study, a novel concept called "goodness of replication" was introduced to control the "fitting" of the generated geometry to the observed geometry with a high "efficiency of replication". An iterated solution for such a "replication problem" is an extremal, represented by a set of iterated parameters. Finally, all the extracted parameters were stored in a parametric bank and treated by chemometrics. In the final step, the treated parameters were reparameterized into stochastic phantoms.

In stochastic phantom simulation, new "imitations" are created from input parameters, i.e. mean value and standard deviation, which are taken from the parametric bank. In the case study on wheat grains, one hundred such phantoms were generated as imitations of the original wheat grains. Mathematically, "reparameterization" is based on Frenet subdivision for the mesh generation. To control the imitation meshes a novel concept called "goodness of imitation" was introduced. This novel concept ensures that the stochastic distribution of a set of indicators for the imitation meshes does not differ significantly from the distribution of the same indicators of the "real" objects. Results obtained from the case study on wheat grains verify that extracted natural parameters can be modelled as independent random variables in such a way that realization can be obtained from simple Monte Carlo simulations. Furthermore, from the master mesh it was possible to generate realizations from Monte Carlo simulations with distributions for area variations, which at a five percent significance level for two-sample Kolmogorov-Smirnov tests, do not differ significantly from what was found in the original sample objects. This indicates that the "new" phantoms were able to imitate the "real" objects with a high efficiency of imitation.

Weaknesses in natural parameterization are likely to be revealed when further case studies are performed. However, the aim of this first approach is for parts of the method to be applied to a wide range of application objects and phenomena. The theoretical basis of natural parameterization is founded on fundamentals from calculus of variation, vector calculus, differential geometry, biometrics, finite elements, multi-variate optimization, and chemometrics. As such, adoption and modification of the approach for use within each different discipline is hopefully straightforward. The new approach for human body surfaces, natural parameterization, and other stochastic modeling approaches might initiate experimentation on pseudo-natural objects. This means that real human beings, animals, biomasses, vegetation, soil, fracture, flows, or other objects or phenomena with an underlying stochastic behaviour may have the potential to be substituted with stochastic phantoms during experimentation. Future experimentation and FE-based multi-physics analysis on new stochastic phantoms has the potential to identify opportunities for simulation and reduce laboratory expenses in empirically based studies.

Keywords

natural parameterization, geometric DNA, parametric meshing, parameter extraction, reparameterization, tortuous mesh, observation mesh, master mesh, goodness of replication, tortuosity pole, natural parameters, master parameters, iterated parameters, Dido's problem, Frenet subdivision, alpha-beta decomposition, parametric bank, goodness of imitation, stochastic phantoms

Assume that a sample of "real" walnuts are scanned and individually modeled by 3D meshes. Then imagine that their "geometric DNA" can be extracted by an automated procedure and later reused to generate a set of "new walnuts". Each of these "new" walnuts differs from all the "real wallnuts" and also amongst each other, i.e. all the "new wallnuts" are unique. Now, if observations are performed on the "new walnuts" it will be found that their stochastic variation does not differ from the "real" walnuts, i.e. the "new" wallnuts are good imitations of the "real" ones. In conclusion, the "new" and the "real" wallnuts seem to be alike!

- This is what natural parameterization is about!

SUMMARY

Advances in scanning technology enable mesh-representation of 3D objects in increasing detail. Today, a few such natural meshes are used for multi-physics modeling of human body parts and grains. Models of other biomasses and objects such as vegetation, soil, and phenomena such as natural fluid flow and crack growth in various materials, are expected to be new targets for similar multi-physics modeling in the near future. Traditionally, natural objects and phenomena are investigated through costly field or laboratory experiments in Biosystems engineering, medicine, and other sciences. With the use of emerging multi-physics software, new opportunities to supplement today's experiments with tomorrow's sophisticated computer simulation lie within our reach. However, if they are to obtain reliable results, new multi-physics models require geometric meshes that provide a much higher level of detail than is currently available. The absence of irregular and very complex meshes is a key barrier for complex modeling since even with todays most advanced NURBS based meshing software the geometry modeling costs are very high. An even bigger problem arises when stochastic variations are to be included in such modeling. The goal of this study is to take the first step in the development of a generic approach for the generation of rough geometries with natural and abnormal variations with a high level of detail. The aim is to let this detailed modeling be a natural extension of today's free-form approaches for smooth geometries. The intention is that the new meshing techniques will be customizable through perturbation modeling based on parametric subdivision. Finally, the new approach is intended to be fully parametric, i.e. all geometric quantities are modeled by parameters, which again are modeled as random variables. This means that the resulting model becomes a stochastic representation of the underlying object and is said to reflect the objects' "geometric DNA". In the following discussion, the working title for a first version of such an approach is: *"natural parameterization."*

Specifically, natural parameterization is intended to be a systematic approach that contributes to *parametric meshing of natural geometries*. The outcome is *imitation meshes* (represented as *stochastic phantoms*), which are supposed to "look natural." In other words, they appear with the same underlying stochastic variations, *natural* or *abnormal,* as the observed natural geometries. The approach is founded on a *generic discretization model* for natural geometries in 3D and is operationalized as a *two-step process*.

The first step, called *parameter extraction,* operates on *observation meshes* which are preprocessed meshes originating from *sample observations*. From these meshes, *characteristic quantities* are *extracted*, *normalized,* and finally *stored* in a *parametric bank* as *natural parameters*. Most of the parameters included are intuitively controlled by the modeler. Many are even measurable from the natural object directly. In general, the parameterization focusses on location and orientation quantities and their perturbations. Technically, an observation mesh is segregated into a new parametric master mesh called the *master mesh*. Thereafter, this master mesh is subdivided parametrically into finer meshes called *iterated meshes.* After some *recurrences* these *iterated meshes* form a *limit mesh*. Because the parameterization follows this strategy, the parameters used are classified as *master parameters* or *iterated parameters* respectively. The master parameters carry information related to *size and landmarks,* whereas iterated parameters reflect *location* and *orientation* of the shape. The parameter extraction of master parameters is governed by expert knowledge, whereas the extraction of iterated parameters follows a decision rule called the goodness of replication. This rule ensures that an extracted replication mesh is considered the extremal mesh, amongst a set of feasible meshes, if it contains the smallest tortuosity with a replication error lower than a prescribed limit value. A tortuous version of the Catmull-Clark subdivision is used to form a novel parametric mesh engine suitable for rough geometries. Algorithmically, this engine enables the creation of 3D *curves, surfaces,* and *volumes* with *smooth*, *rough,* and *fractal* characteristics. The mesh engine is called *Frenet subdivision* since it explicitly includes Frenet vectors and natural equation values for embedded tortuous curves. The resulting meshes are mesh-fields rather than conventional meshes of interconnected vertices. This is because the new meshes also include information on *Frenet vectors*, *curvatures* and *parameter settings*. One complication is finding a combination of parameters that can be extracted in such a way that they form the same identical set of parameters, just with different values for each of the objects in the sample. This set of *feasible parameters* must exist, and it must be verified that these parameters are weakly correlated so that they can be modeled as independent random variables. Theoretically, this makes it plausible that mapping from an *observation space* to a *parametric space* is possible. However, due to the built-in non-linearity of rough geometries, a novel stochastic decomposition founded on Reynolds averaging is introduced. Its purpose is to decompose each random parameter into two components. One component, called the *alpha-component,* is used to model the main fluctuations (i.e. the dominant part of the natural variations), whereas the *beta-component* is used to model the semi-stationary variations (i.e. small induced numerical errors and/or small mean value variations). This *alpha-beta decomposition* delivers stochastic information on the parameters, which are then formally stored in a *parametric bank* along with other relevant information. Over time, if the bank is continuously extended and updated with new information, the natural object becomes *better explained,* and better understood*. The parametric bank then becomes a parametric *knowledge base* for that object.

The second step, called *reparameterization* is designed for *regeneration* of new *imitation meshes* from the alpha-beta decomposed parameters drawn from the parametric bank. However, before the regeneration into imitation meshes takes place, the modeler might *pre-manipulate* the parameters. Because the approach is made fully customizable, the model can be adjusted to meet experimental requirements in terms of volume, area, arc length, straightness, roundness and roughness. Theoretically, the stochastic simulation of new meshes follows a novel decision rule called *goodness of imitation*. It ensures that the stochastic simulation first produces a proper mean value imitation before the dominant variation simulation is applied. Ultimately, goodness of imitation ensures that meshes simulated by random number generators match the underlying stochastic behavior of the natural object with a high efficiency of imitation.

In general, the problems to be solved numerically are highly nonlinear making the new meshing algorithms very CPU demanding. For increased speed of convergence and stability, the highly non-linear multivariate optimization algorithm, which is a key part of the extraction of parameters, must be enhanced in the future. Also, it must be noted that the new algorithmic design and its implementation as a unified approach is just in its infancy. However, in this piloting case study, a set of imitation meshes called *wheat cross-section phantoms* are generated. Despite the complexity, the aim is to make stochastic imitation modeling a *customizable* tool for *free form simulation modeling* - an ambition that could realistically be fullfilled in a few years from now. Technically, these new phantoms are formed as conventional *tri or quad meshes* and are intended for *patch graphics* visualizations for further *post processing* by FEA based *multi-physics software* or for *materialization* into *physical models*. The alpha-beta mesh generator is also useful for more simple deterministic or pseudo-stochastic phantom generations. The simplest phantoms are called deterministic *replica phantoms.* They replicate the observation mesh as a one to one fit. *Mean value meshes,* which produce a single mesh from the mean values of the extracted parameters, are not fully stochastic but rather pseudo-stochastic. Furthermore, it is possible to generate *synthetic phantoms* based on purely synthetic parameters. In these cases, the new mesh engines act like conventional deterministic mesh generators.

An indirect capability validation of the developed algorithms was performed as a case study on a sample of one hundred wheat grain cross-sections (*Triticum aestivum*). The observation mesh for each cross-section was represented by pseudo-3D polyhedral with an artificial unit thickness. For the one hundred objects, the maximum relative error of replication was less than one percent. The reparameterization was performed in accordance with the new concept on goodness of imitation and it is verified that the master mesh was able to generate realizations from Monte Carlo simulations. A comparison between the distribution of the segment and cross-section areas from the simulated and real meshes was performed using the corresponding two data vectors. The test was performed as a two-sample Kolmogorov-Smirnov test. The null-hypothesis, that the cross-section and segment areas from the two data vectors were distributed equally, was not rejected at five percent significance level. In other words, the "new" simulated wheat cross-section phantoms were found to imitate the "real" wheat grain cross-sections with a high efficiency of imitation.

Table of Contents

Acknowledgement

I would like to thank a number of people for their kind support and assistance rendered to me during this research program. Big thanks to former Head of Department Søren FISKER [1] and Head of Department Lotte THØGERSEN [1] for being very flexible with my teaching obligations at VIA University College, Denmark during this study. Warm thanks to all my new colleagues at Aarhus University, Denmark and explicitly to former Head of Department Morten DAM RASMUSSEN [2] for assisting with the international cooperation and letting me work firstly in the Department of Biosystems Engineering and for the last year in the Department of Engineering. A special thanks to Head of Research Unit Ole GREEN [2] who was the initiator and overall responsible for this study, to PhD Fellow Vicent GASSO TORTAJADA [2] for shooting the stereo-microscopic images, to Research Assistent Ole JØRGENSEN for kind help with image recognition to M.Sc. Andres Villà HENRIKSEN [2] for his thorough editing assistance and to Department secretary Anja TORUP HANSEN [2] for her proof reading.

I have had the privilege to corporate and gain experience from a team of supervisors whom I now address as friends. The completion of this thesis would not have been possible without guidance from my main supervisor, Senior Scientist Claus Aage GRØN SØRENSEN [2] and co-supervisors: Senior Scientist Dionysis BOCHTIS [2], Professor Andrea SALANDIN [3], Post Doc Gilles GOUATY [4] and Ingénieur de Recherche Eric TOSAN [4] who sadly passed away before the project was completed. Your enthusiastic encouragement was gratefully appreciated and I cannot thank you enough.

I hereby want to thank all these nice people and others not mentioned by name for any assistance rendered to me during the last couple of years.

Last but not least thanks to my wonderful wife Anne-Mette who has supported me even though we were supposed to slow down a little bit at this stage of our life!

[1] Department of Civil Engineering, School of Technology and Business, VIA University College, Chr. M. Østergaards Vej 4, 8700 Horsens, Denmark.

[2] Aarhus University, Faculty of Science and Technology, Department of Engineering, Blichers Allé 20, 8830 Tjele, Denmark.

[3] Universidad Politechnica de Valencia, Spain. ETS Gestión en la Edificación, Universidad Politécnica de Valencia, c/Vera s/n E-46022 Valencia, Espania.

[4] Dept. GeoMod / Proj. ModItere Laboratoire d'InfoRmatique en Image et Systèmes d'information (LIRIS) UMR 5205 CNRS/INSA de Lyon/Université Claude Bernard Lyon/Université Claude Bernard Lyon 1/Université Lumière Lyon 2/Ecole Centrale de Lyon, France.

Notations

	INDICES
n_{obs}	number of scanned data sets for a natural geometry
n_τ	limit level of refinement
$k_\tau \in [0, n_\tau]$	level of refinement. (Master level: $k_\tau = 0$. Iterated levels: $k_\tau \geq 1$)
	GEOMETRIC DISCRETIZATION
Ω_τ	**Domain Representations**
Σ_Ψ	cluster
Ω_Ψ	subcluster
Ψ	object/species
Ω: V_τ, V^e, V	subdomains, volume segment, volume element, volume
$\partial^{(\cdot)}\Omega$	**Boundary Representations**
$\partial\Omega$: S_τ, $\mho$, F^e, S, A	surfaces: surface segment, planar surface segment, face element, surface area, planar area
$\partial^2\Omega$: C_τ, E^e, L, l	curves: curve segment, edge element, curve length, linear length
$\partial^3\Omega$: **V**, **T**, **N**, **B**, **d**	vectors: vertex, tangent, normal, binormal, rectifying vector
$\partial^4\Omega$: χ, ρ	scalars: generalized curvature, radius of curvature
$\kappa_\chi, \kappa_\tau, \tau_\tau$	segment curvature, (Frenet) curvature, (Frenet) torsion
$\rho_\chi, \rho_\kappa, \rho_\tau$	segment radius of curvature, radius of curvature, radius of torsion
$\partial^5\Omega$: τ, λ_ε, D_H, D_M, D_α	shape metrics: tortuosity, lacunarity, Hausdorff–Besicovitch dimension, Minkowski–Bouligand dimension, Rényi dimension

	Constellation Representations
$\{F\}$	Frenet frame
P_τ , $n_{\{F\}}$	tortuosity pole, pole valence
f_τ	frame index
$P_{\tau_{bi}}$	bi-pole
$M_{\tau_{bi}}$	bi-mesh
M_τ , M_τ' , $M_{\tau_{obs}}$, $M_{\tau_{phan}}$	tortuous mesh , first derivative of a tortuous mesh, observation mesh, phantom
M_τ^0, $M_\tau^{k_\tau}$, $M_\tau^{n_\tau}$	master mesh, iterated mesh, limit mesh
S^{k_τ}	multiresolution parametric subdivision operator
	Parameters
q , q_Δ	natural parameters, perturbation parameters
q^0 q_Δ^0	master parameters, master perturbation parameters
$q_{\|\Omega\|}^0$ $q_{\|\Omega\|_\Omega}^0$ $q_{\|\Omega\|_b}^0$	size parameters, size normalization parameters, dimension parameters
q_P^0 q_ξ^0 q_f^0	landmark parameters, location parameters, orientation parameters
q^{k_τ} $q_\Delta^{k_\tau}$	iterated parameters, iterated perturbation parameters
$q_P^{k_\tau}$ $q_\xi^{k_\tau}$ $q_f^{k_\tau}$	Iterated pole parameters, location parameters, orientation parameters
$Q = Q_\alpha p_\alpha + Q_\beta$	alpha-beta decomposition of Q
p_α	perturbation level
μ_β	beta mean value , i.e. the mean value of the decomposed Q
$\sigma_\alpha , \sigma_\beta$	alpha standard deviation, beta standard deviation
$r_{\alpha\beta}^2$	variance ratio
$\hat{q}_{\alpha\beta}$, $\hat{q}_\alpha$, $\hat{q}_\beta$	alpha-beta realization of Q , alpha realization of Q , beta realization of Q

Abbreviations

FEA

- finite element analysis

G^0, G^1, G^2

- vertex continuity, tangent continuity, curvature continuity

NURBS

- non uniform rational basis spline

IFS

- iterated function system

MPA

- multi-physics analysis

SA

- sensitivity analysis

TSW

- thousand seeds weight

PCA

- principal component analysis

PLS

- partial least squares

Prolog

This prolog is an informal appetizer to the PhD-study entitled "Natural Parameterization".

Figure 0.1. Four subdivision geometries resulting from four parametric settings of the exact same master mesh and two pictures of beet roots

Can nature be parameterized like ellipsoids and other volumetric objects?

In 2009, my friend Dr. Ole Green looked at the images in Figure 0.1. and posed this tricky question: *"Since we are able to parameterize complex but man-made subdivision geometries, do you think it is possible to develop a kind of "reverse parameterization" which enables us to find a unique set of "natural parameters" that can be used for parametric modeling of natural geometries, such as beet roots, as well?"*

This teasing question is the motivation for this study and the inspiration for challenging research in the years to come. When you take a look at the images above you see a sphere, an octahedron, a cup, and something that "looks almost like a beet root".

Surprisingly, these geometries are generated from the same six geometric "poles" which contain information on location vertices and orientation tangents. Following the idea of reverse parameterization, the question that emerges is: whether or not it is possible, by examining of a collection of beet roots, to identify the same six poles for every single object observed?

 - The answer is probably!

In other words, is it possible to develop a *"reverse parameterization procedure"* which can reveal a kind of *"parametric DNA"* of natural geometries*?*

In this study, some modest attempts to answer these questions and pursue these goals are introduced. The research includes: a systematic approach for parameter extraction of natural objects based on expert knowledge, a decomposition method for stochastic parameters which enables simple Monte Carlo simulation, and finally a novel parametric subdivision algorithm for imitation of rough geometries based on Frenet-Serret concepts and tortuosity. To control the approach, two new concepts are presented. The first concept, called the goodness of replication, controls the extraction of natural parameters from scanned objects. The second concept, called goodness of imitation, controls the reparameterization from the captured parameters back into new unique look-a-like phantoms.

Upon close inspection natural objects usually seem rough and irregular!

Figure 0.2. Stereomicroscopic images of wheat grains (Triticum aestivum) with rough and highly irregular surfaces

Compared to most man-made geometries, the big challenge of working with natural geometries is that they always possess rough characteristics (as seen in the above images). One key strategy used in natural parameterization is to let all irregularities be modeled through *controlled parameterization*. The parameters introduced are simple, measurable, and intuitive. It also allows for free form modeling with a high degree of flexibility.
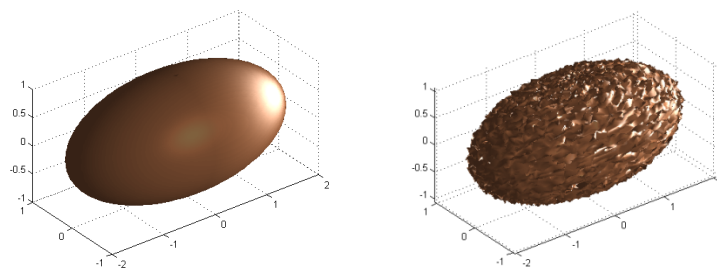
Parameterization of location and orientation

Figure 0.3 *Left:* **A smooth ellipsoid.** *Right:* **A rough ellipsoid with one perturbation DOF**

When an ellipsoid is parameterized by its center and its semi-axes, the center is said to provide information on *location* in space, whereas the semi-axes provide information on the objects *bounding dimensions* and *local orientation*. Mathematically, location and orientation are represented by *vectors*. Other domain properties such as volumes, cross-section moments of area, and curvatures, are defined by scalars. Important metrics such as tortuosity, lacunarity, the Hausdorff–Besicovitch[1] dimension, the Minkowski–Bouligand[2] (box counting) dimension, and others are all scalar properties of irregular geometries. Therefore, vectors and scalars are the fundamental building blocks used to model the size and the shape of any tortuous geometry, whether it be smooth or rough.

Degrees of freedom

The "smooth ellipsoid" in Figure 0.3 is defined by: three coordinates controlling the *location,* and three semi-axis controlling the *orientation* and *size*. The number of parametric degrees of freedom (DOF) is therefore six. To include roughness, at least one more parameter must be included. In the "rough ellipsoid" (see Figure 0.3, right), one additional parameter, called the perturbation level, is introduced to alter the appearance of the surface. This perturbation level randomly translates each of its smooth surface coordinates by simple Monte Carlo perturbations. In Figure 0.3 (right) these perturbations are realized by multiplying the perturbation level with a realization obtained from the uniform random number generator with zero mean and unit variance. As a result, the number of DOF of the rough geometry is now increased to seven, i.e., even a minor increase in the parametric DOF's for analytic geometries can change the appearance from smooth to rough. However, it is not likely that such a simple modification of analytic geometries can be used to imitate natural geometries appropriately. Therefore, more advanced imitation generators are needed in order to model natural objects.
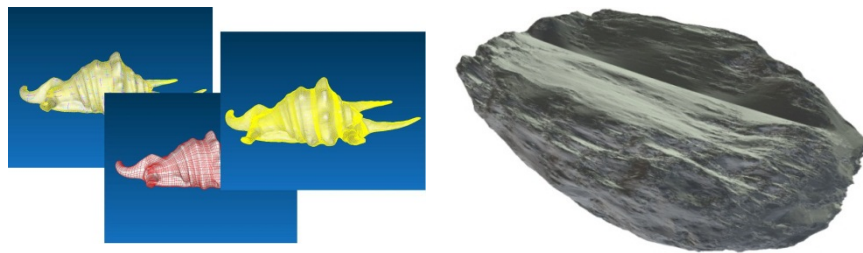
Figure 0.4. Left: Reconstruction by Non-uniform Rational B-spline Surfaces (NURBS) of a scanned model - GSI STUDIO® Geometry Systems, Inc. Right: IFS rough grain surface with complex texture, componed by an assembly of six fractal surfacic patches connected with G0 continuity (the edge on the top) or G2 continuity (making their boundaries indiscernible from one patch to the other), Dr. Gilles Gouaty, Université Claude Bernard Lyon 1, FRANCE

---

[1] Felix HAUSDORFF (1868 –1942), German mathematician. Abram Samoilovitch BESICOVITCH (1891 – 1970), Russian mathematician.
[2] Hermann MINKOWSKI (1864 - 1909), German mathematician and physicist. Georges Louis BOULIGAND (1889-1979), French mathematician.

Complex vs. intuitive parameterization

Over the past decade, NURBS has been developed into an advanced tool for irregular geometry modeling - see Figure 0.4 (left). However, in terms of parameterization, the number of DOF for NURBS models is likely to become very high for imitations like the one seen in the figure above (left). In todays advanced geometry software NURBS are the de facto mesh engine. However, another promising mesh engine is a parametric *subdivision* strategy known as Iterated Function Systems (IFS), see mesh Figure 0.4 (right). It controls the appearance of the geometries by manipulating a set of control points. In this way, it allows the modeler to induce highly irregular geometry patterns. Unfortunately, the parameters of parametric IFS are not directly measurable which means that when a model is generated its parameterization cannot be identified from simple measurements. Therefore, it is not straight-forward to obtain reverse parameterization. Furthermore, the fractal behavior, which is the beauty of the irregular geometries, makes it very difficult to anticipate the limit model from controlled parameters. At this stage, it seems difficult to avoid such modeling complexity and to let the IFS parameterization be simple and intuitive. A very impressive IFS based synthetic subdivision surface, which imitates the texture of a grain in surprising detail, is illustrated in Figure 0.4 (right). Such texture generations by IFS might be today's best answer for advanced modeling of rough surfaces. However, since the ambition is to model curves, surfaces, and solids from a unified approach based on a simple setup with *measurable parameters,* a special subdivision approach is developed during this study. Briefly, this approach is a tortuous variant of what is commonly called a Catmull–Clark split (Catmull & Clark, 1978). Like Catmull–Clark subdivision the tortuous approach starts from an initial mesh and decomposes it into new meshes which become more and more detailed for each step during recursive mesh refinements. The tortuous variant proposed here is called *Frenet subdivision* since its initial mesh is formulated from Frenet frames.

Frenet subdivision

One advantage of the novel Frenet subdivision scheme is its ability to generate meshes that imitate natural geometries from an initial master mesh with *low parametric DOF*. Another benefit is that, due to the use of measurable parameters, the *modeler* finds the parameterization process *intuitive and controllable*. However, the drawback is that the entire model is non-linear by nature and thus requires an iterative setup to carry out the Catmull-Clark splitting, a process which is quite CPU demanding.

Natural objects are unique and hard to imitate

Except for clones, natural objects are *unique*. This means that any imitation generated from parameters must possess the same underlying stochastic nature as the object itself. Therefore, imitations must be based on collected knowledge, and reflect this knowledge within the generated imitations. Consequently, the collection of statistical data and its influence on the reparameterization into imitations is significant for today, and tomorrow's, advances in natural parameterization.

To face the challenges, new algorithms have been developed and are summarized in the following section to give a first impression. The overall approach is called "natural parameterization". It is a two-way approach. In the first step, expert knowledge is used to extract parameters from natural objects. In the next step, the same parameters are *re-parameterized* into new, unique imitations. Statistically these imitations belong to the same family as the observed objects. The extraction is geometrically formulated by so-called **tortuosity poles,** which contain information on location as well as orientation. This information is for each pole linked is to the same nodal point in space. Pairs of such poles then form a so-called **tortuosity bi-pole** and this, in turn, forms a so-called **tortuosity bi-mesh**. The most fundamental mesh, which is composed by a finite number of bi-meshes, is called the "master mesh". It has the lowest number of DOF. This mesh is subdivided into denser meshes each containing more and more data. In the limit, it finally forms a so-called "goal mesh," denoted as an iterated limit mesh. Algorithmically, the mesh generation is performed by the novel **Frenet subdivision** scheme. This enables the generation of tortuous curves, surfaces and volumes in 3D. The extraction of the set of governing natural parameters is governed by a novel rule called **goodness of replication**. It governs the iterations so that the replication meshes have minimum tortuosity and small replication error. This rule is entirely deterministic and suits the parameter extraction process. However, to obtain "nature-like" imitations, a **stochastic decomposition variant of Reynolds averaging** called **"alpha-beta decomposition"** is introduced. This decomposition enables generation of parameterized geometries where the natural parameters are uncorrelated. To ensure a high efficiency of such stochastic imitations, another decision rule called **goodness of imitation** is introduced. It is an indirect approach introduced to ensure that the underlying stochastic nature of a natural geometry is also found in its imitations. The "new" imitations represent stochastic phantoms, i.e. computational phantoms that are deformable and size-shape customizable. The above principles and methods are based on well-established theory and include elements of calculus of variations, differential geometry, vector algebra, stochastic Reynolds averaging, biometrics, chemometrics, FE formulations and multivariate non-linear optimization.

Natural parameterization

Natural parameterization is a piloting approach towards modeling of multiresolution natural objects and it is encouraged by "reverse parameterization" fostered by Dr. Ole Green. However, this first version of the natural parameterization approach does not at all give a profound answer on reverse parameterization. It simply attempts to reveal some of the key problems and introduce a systematic set of parameterization procedures for modeling of natural objects and

Figure 0.5. A "synthetic" phantom   phenomena.

Natural parameterization is in its very beginnings and reverse parameterization poses a big challenge for future research.

1   INTRODUCTION

"Clouds are not spheres, mountains are not cones, coastlines are not circles, and bark is not smooth, nor does lightning travel in a straight line" (Mandelbrot, 1983).

1.1   CONTEXT

Today, high resolution scanners are able to capture the geometrical details of natural objects like never before. Using the latest multi-physics software, advanced geometrical models can be developed and use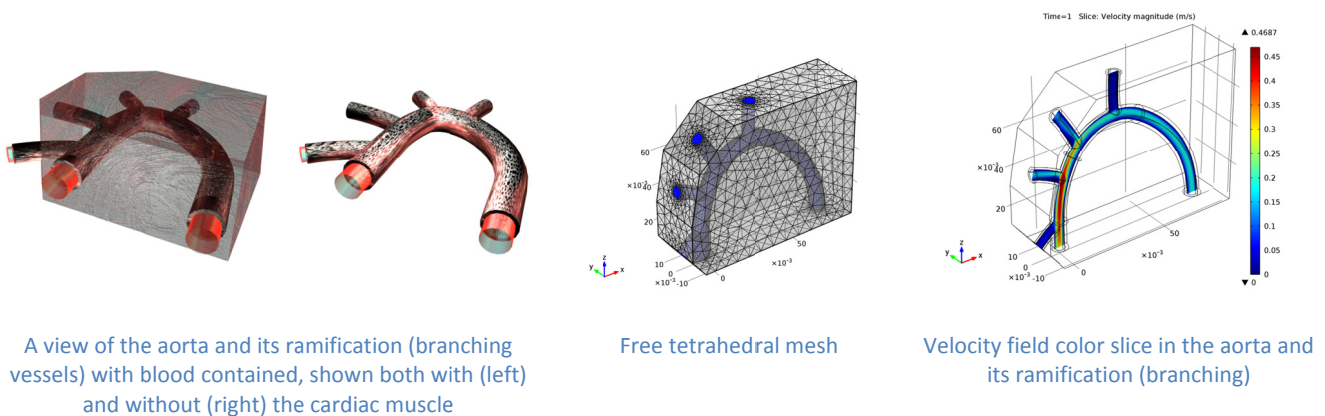d for sophisticated applications. The creation of detailed geometrical meshes using observations from objects that exhibit variation in space and time, represent the very wide contextual boundary of this study. At this stage, computational phantoms have only been modeled for anatomical parts of humans (Xu & Eckerman, 2010).

Computational Phantoms

A view of the aorta and its ramification (branching vessels) with blood contained, shown both with (left) and without (right) the cardiac muscle

Free tetrahedral mesh

Velocity field color slice in the aorta and its ramification (branching)

Figures and labels from: Fluid-Structure Interaction in a Network of Blood Vessels, COMSOL® Multiphysics 4.2a, 2012 – www.comsol.com

**Figure 1.1. Synthetic phantom of the aorta, 2012**

In Figure 1.1, a synthetic mesh of the human aorta, is defined and modeled by the COMSOL® Multiphysics software to investigate the interaction between blood flow and structural deformations. Such finite, element based, multi-physics is a reflection of today's state of the art natural modeling capabilities. However, the creation of the geometrical model of the natural objects, such as the aorta, is challenging since the blood boundary layer is essential to obtain realistic flow patterns. The geometry of this boundary layer is highly irregular and it is very complicated to model in detail. As a result, the physics of this layer is approximated and not modeled in high resolution. Such situations where details are crucial for accurate simulations represent the specific conceptual environment for this study. Obviously, geometric irregularities relate to the underlying stochastic nature of the object itself and therefore stochastic modeling becomes a specific conceptual ingredient in this study.

Today, irregular but smooth meshes are usually synthetic or semi-synthetic in the sense that they are based on nominal parameters found from fitted analytic geometries such as: spheres, ellipsoids, or percentile or mean

value parameters. However, in this study such synthetic meshes are perceived simply as a special case of realizations of stochastic parameters. Technically, synthetic parameter values are assumed to be achieved from parametric Monte Carlo simulations with no variance. Therefore, to obtain look-a-like phantoms there is a need to combine classical geometry modeling with stochastic data simulation. This means that the development of new advanced look-a-like phantoms must reflect not only the ability to model conventional irregular geometries but also tortuous geometries with natural or abnormal variations. Like natural objects, each look-alike phantoms must be simulated so it is unique. On the other hand, if a huge sample of these unique phantoms is simulated, then their stochastic variations must match the variations of the underlying natural object. In the following discussion, this problem is called an *imitation problem* and it highlights the theoretical context of this study.

Focus is shared between a detailed representation of highly irregular geometries and a general variation modeling for natural objects and phenomena. The development of algorithms for the creation of parametric phantoms with natural properties is also a major task. Since these algorithms are supposed to integrate with the latest multi-physics software they must also be designed so the modeler can apply and modify the generated phantoms during modeling. Despite the geometrical complexity, the setup must be designed to meet today's demand for free-form geometry modeling as known from Rhinoceros®, 3ds Max Design® and other software packages based on NURBS.

During the last few years, modeling of the first human body parts and biomasses has been performed using finite element based multi-physics software from synthetic phantoms (Anza, 2011), (Lazutkin, Harkara, & Husar, 2010) and (Lund, 2009). Furthermore, human-centered design is receiving increasing attention indicating that extended focus is on accurate modeling of natural geometries.
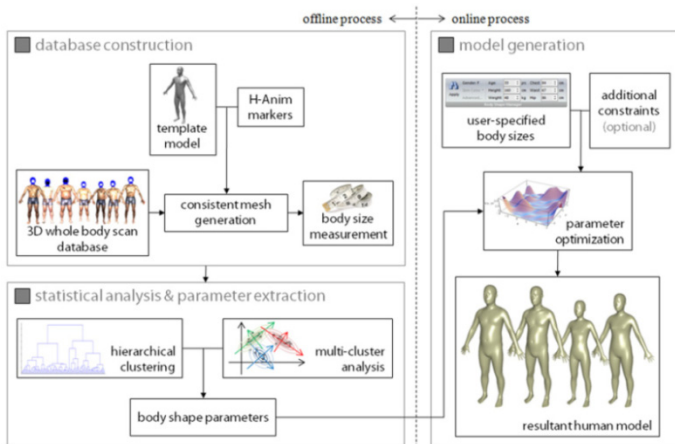
An overview of the proposed method.

Figure and Label from: (Baek & Lee, 2012)

Figure 1.2. The first approach for full body imitations, 2012

Especially within human-centered design, much effort has been placed on the development of accurate computational phantoms, which can be used to investigate the effect between the product and the human user.

The first full body approach for human surface generation was published a few months ago (Baek & Lee, 2012). In this novel Baek-Lee approach there are many key elements. First, a data base is created using whole body scans. Each body is fitted to a template model by a set of sixty-eight H-Anim, ISB[3] anthropometric markers[4] (of which seventeen new markers were proposed by the authors).

---

[3] ISB is an acronym for International Society of Biomechanics. See also isbweb.org.
[4] More details on H_Anim, ISB markers and other human body statistics is found in (van Sint Jan, 2007). See also h-anim.org.

Thereafter, the scanned data are treated by statistics and a set of body shape parameters is formed. This offline process is later followed by an online process where the extracted parameters are optimized to meet modeler's body-size specifications i.e., the resultant simulation of the human models allows for customizable full body phantom creation.

The research in human variation modeling started only thirteen years ago in 1999. The original work involved morphable modeling of 3D faces by (Blanz & Vetter, 1999). This first work by Blanz and Vetter, has been a main source of inspiration for subsequent research up until present day.
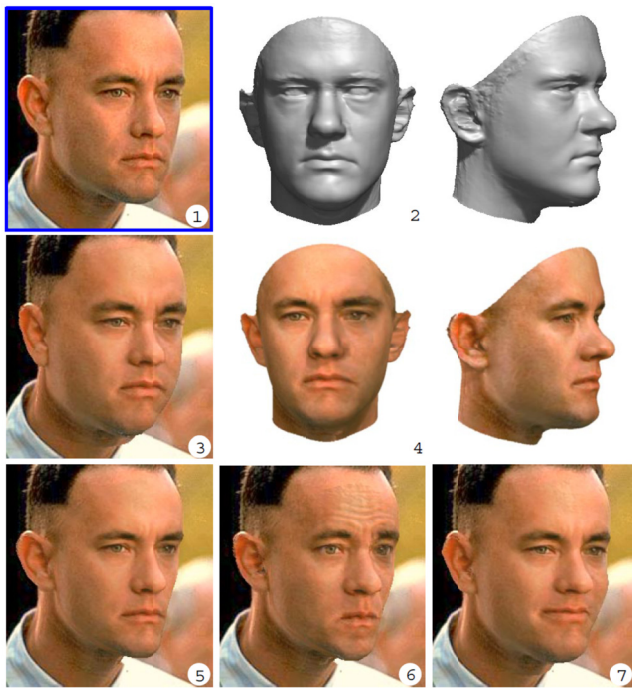
One key characteristic of variation modeling is that the meshing of new computational phantoms is based on the statistics from a sample of humans.

Matching a morphable model to a single image (1) of a face results in a 3D shape (2) and a texture map estimate. The texture estimate can be improved by additional texture extraction (4). The 3D model is rendered back into the image after changing facial attributes such as gaining (3) and losing weight (5), frowning (6), or being forced to smile (7).

Figure and label from (Blanz & Vetter, 1999).

Figure 1.3. The first approach for morphable modeling, 1999

A comprehensive review of the attempts to develop customizable phantoms based on samples was presented by (Baek & Lee, 2012). The review started with the initial contribution by Blanz & Vetter in 1999 and ended with their own approach in 2012. In these approaches from 1999-2012, the shape characteristics of human beings, often referred to as landmarks, attributes, or patterns, are hand-labeled. In other words, they are selected from expert knowledge. The characteristic vertices are stored in shape-vectors (coordinate arrays) and texture-vectors including RGB-color settings. Usually, such texture-vectors store one RGB-setting per vertex. Furthermore, segmentation is introduced to increase the expressiveness of the model, i.e. for human faces sub-regions such as eyes, nose, mouth and a surrounding area are assumed to be independent. During the reparameterization, these segments are generated individually by parametric combinations and finally blended at their borders.

However, to isolate attributes which are not expressible by simple manipulations is not a trivial task (Blanz & Vetter, 1999).

Novel approaches for creation of rough phantoms are needed

A literature search on rough phantom generation for soil, animals, biomasses, vegetation, fluid transport and material science revealed that approaches similar to the novel Baek-Lee method either do not exist, or can not be found in the published literature. Therefore, the idea is to develop a new approach for rough phantom generation which encorporates some of the methodic elements presented in the Baek-Lee approach, but is generic, in the sense that it is applicable for geometries from Biosystems engineering as well as other research areas too.

Advances in scanning technology

Despite the fact that a general approach has not been found for variation modeling of Biosystems engineering objects and phenomena, a variety of data are available from various scans of biomasses, vegetation, soil and others. Just as scans of human beings were a starting point for the Baek-Lee approach for smooth full body surfaces, existing scans of biomasses, vegetation, and soil are a very important starting point for the development of novel approaches for rough geometries. The steadily increasing level of meshing details resulting from ongoing advances in scanning technology is one explanation for the development of new variation centered design approaches. It appears that future achievements in stochastic phantom modeling will go hand in hand with the advances in scanning technology.

A novel mesh approach must handle both rough and smooth geometries

Various complex physical problems, which are estimated by macroscopic parameters, might be be better explained using micro- and Nano-scale models. This means that new geometrical meshing tools must allow for multiresolution geometry modeling. On the other hand, novel meshing approaches must still be able to handle conventional parameterization for comparative analysis and for validation of new results. They must also be able to incorporate standardized parameters for soil, biomasses, vegetation, atmospheric air, and other fluids i.e., new meshing approaches must be *customizable*.

: A brief introduction to selected scanning and meshing aspects are presented in chapter 1: "INTRODUCTION".

Ongoing experiments needs multi-physics verification

There is an immediate need for a new tool to assist the *verification* of novel Biosystems engineering developments by multi-physics modeling. For example, such model verification by computer simulations is planned to be included in a recent sensor development approach based on the impedance tube measurement of the acoustic transmission loss (TL) through seed clusters initiated by Ole Green, AU. This technique shows promising results for non-invasive detection of density and other parameters. However, its underlying multi-physics model is a challenge, since detailed rougness models must be included.

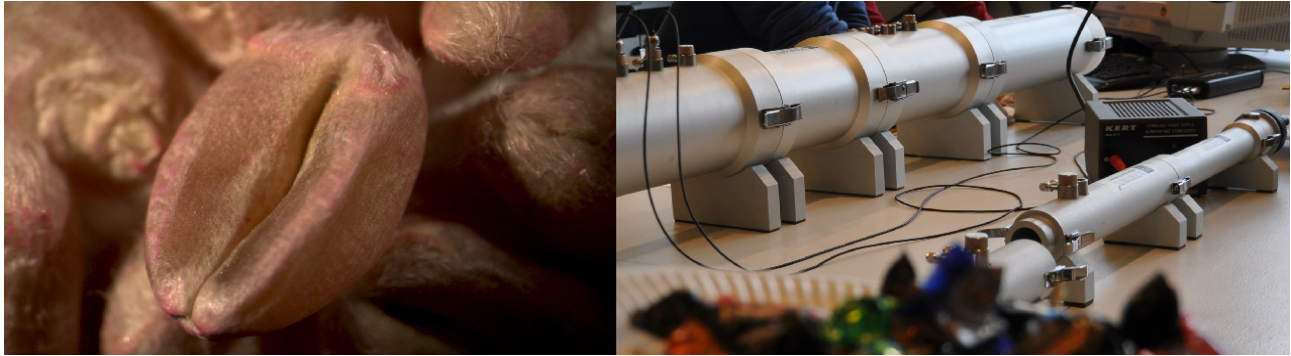Figure 1.4 (left) illustrates a stereo microscopic image of a single wheat grain on the top of other wheat grains.

Figure 1.4: Detailed multi-physics modeling of grain geometries might verify acoustic TL measurements, AU, 2010

The sound absorption coefficient spectra for such wheat grains (*Triticum aestivum*) and six other seed samples: oat (*Avena sativa*), barley (*Hordeum vulgare*), maize (*Zea mays*), sunflower (*Helianthus annuus*), soya bean (*Glycine max*) and canola (*Brassica napus*), are investigated by impedance tube measurements, see Figure 1.4 (right). The piloting experiments indicate that it is possible to identify density and other parameters from the sound absorption coefficient spectra and that PCA presents reliable seeds type grouping capabilities (Gasso-Tortaja et al., 2010). Additional transmission loss (TL) experiments for clay, sand, rice and others clusters of materials show similar results (Gasso-Tortajada, Dubasaru, Rojas, Brøchner, & Green, 2010).

The original starting point

However, existing physics models do not fully explain these surprising findings. A detailed computer simulation which mixes classical Biot theory for grain clusters is considered to be modeled as porous media (Biot, 1956; Biot, 1956). Acoustic energy transport through a model of a seed cluster with detailed surface irregularities might explain the surprising results better. Also, previous findings on the dependence between shape and reverberation time (Salandin, 2004) (p. 55-70) indicate that acoustic absorbtion is texture dependent. Therefore, detailed multi-physics simulation including complex geometries might reveal new explanaitions on experimental findings.

In fact, the development of a detailed multi-physics model for such particular porous media aiming at acoustic identification and classification of seeds was the original starting point of this study. The first multi-physics model was planned to be developed along with ongoing experiments (Gasso-Tortajada, Dubasaru, Rojas, Brøchner, & Green, 2010) on wheat grain clusters (*Triticum aestivum*). However, the development of a grain cluster model for multi-physics soon lead to a more general study on modeling of natural geometries and their parameterization. This general study on a generic approach for natural parameterization is what is reported and discussed in this thesis.

: The theory behind the novel natural parameterization approach is presented in chapter 2: "METHODS".

Validation by wheat grains cross-sections

A sample of the same type of wheat grains (Triticum aestivum) used in the aforementioned acoustic experiments was used to validate the novel parameterization approach.

According to the Food and Agriculture Organization of the United Nations (FAO) wheat is ranked as the world's number two food commodity. In terms of annual production, $650.2 \cdot 10^6$[MT] of grain was produced in 2010, following closely behind rice at $672.2 \cdot 10^6$[MT]. In Denmark, wheat is ranked number one with $5.05 \cdot 10^6$[MT] and barley second with $2.98 \cdot 10^6$[MT]. For more details see (FAOSTAT, 2010).

Within Biosystems Engineering, wheat grains are an important object of investigation. Two examples of recent investigations are: geometric parameters of wheat grain determined by image analysis (Fératlégil-Durmus et al., 2010) and changes in mitochondrial shape in wheat root cells exposed to mitochondrial poisons (Ponomareva & Polygalova, 2012).

In general, various seeds properties have been targeted for thorough investigation over the past decade. The physical properties of sweet corn seed (Zea mays saccharata Sturt.) was studied by (Coskun, Yalcin, & Ozarslan, 2006) and (Ahmadi, Mollazade, Khorshidi, Mohtasebi, & Rajabipour, 2009) determined some physical and mechanical properties of fennel seed (Foeniculum vulgare).

International seed measurement standards have also been developed, i.e., for size distribution by sieving the international standard (ANSI/ASAE S319.3, 1997) is today's normative reference.

Therefore, grains in general, and wheat grains in particular, were selected as a relevant validation object for this study.

A sample of cross-section images was captured of one hundred wheat grains (triticum aestivium) using a stereo microscope. They were used as the target for the methodic validation of the introduced approach called "natural parameterizaton".

: Details on the validation by wheat grain cross-sections are presented in chapter 3: "RESULTS".

1.2 THE PROBLEM DOMAIN

Geometric complexity and the tortuosity metric

A general observation in biometrics is that natural geometries seem to be smooth at low resolutions and highly irregular at high resolutions. Furthermore, natural geometries often form clusters, which from a macroscopic point of view, are often considered porous media. One important geometric characteristic of the air channels of porous media is *tortuosity*. It indicates the degree of irregularity of a curve segment and is simply defined as the ratio between the arc length of the segment and the chord it spans over. The inclusion of tortuosity was originally introduced in the study of porous media by (Biot, 1956). Such tortuosity effects are clearly geometric in nature and thus play a central role in this study. However, it is not only soil pore spaces that are tortuous (Moldrup, Olesen, Komatsu, Schjønning, & Rolston, 2001). Any curve embedded in a natural geometry exhibits tortuosity[5]. This observation has been validated by a number of investigations carried out over the last decade: (Bullitt, Gerig, Pizer, Lin, & Aylward, 2003), (Grisan, Foracchia, & Ruggeri, 2003; Grisan, Foracchia, & Ruggeri, 2008) , (Kou et al., 2012) and others.
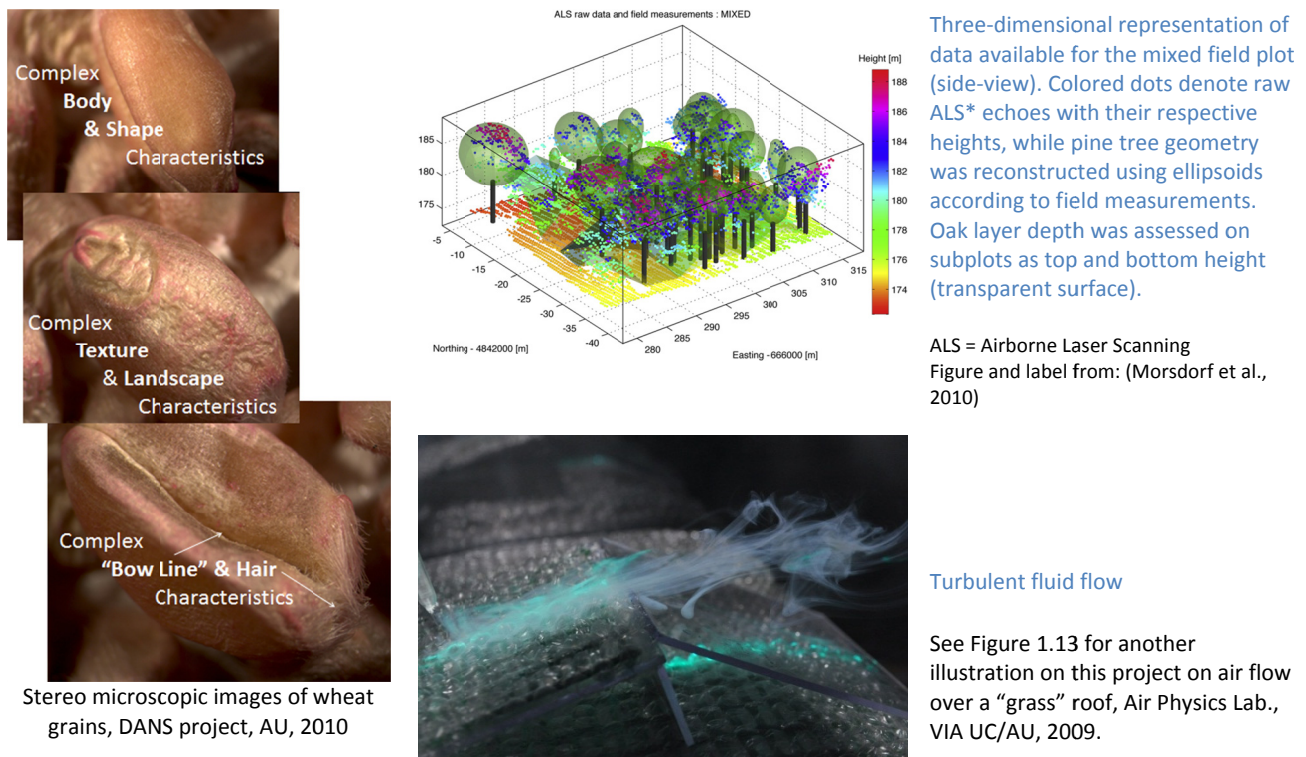

Complex
Body
& Shape
Characteristics

Complex
Texture
& Landscape
Characteristics

Complex
"Bow Line" & Hair
Characteristics

Stereo microscopic images of wheat grains, DANS project, AU, 2010

Three-dimensional representation of data available for the mixed field plot (side-view). Colored dots denote raw ALS* echoes with their respective heights, while pine tree geometry was reconstructed using ellipsoids according to field measurements. Oak layer depth was assessed on subplots as top and bottom height (transparent surface).

ALS = Airborne Laser Scanning
Figure and label from: (Morsdorf et al., 2010)

Turbulent fluid flow

See Figure 1.13 for another illustration on this project on air flow over a "grass" roof, Air Physics Lab., VIA UC/AU, 2009.

Figure 1.5: Complex natural surfaces (left), discrimination of vegetation (right, top) and turbulent flow (right, bottom)

---

[5] One exception with no tortuosity is an embedded curve through the middle region of a stationary liquid surface.

26

As it appears from Figure 1.5, the complexity of the three illustrations is a consequence of an underlying stochastic variation. Figure 1.5 (left) illustrates the geometrical complexity of wheat grain surfaces such as irregular body, shape, texture, micro-landscapes, characteristic "bow-line," and hair. Keeping in mind the beauty of fractals (Mandelbrot, 1983), the modeling of such complex geometries might be described by iterative recurrence relations. Figure 1.5 (right, top) illustrates that discrimination of vegetation from height and intensity information retrieved from airborne laser scanning is possible for three different vegetation strata in a multilayered ecosystem (Morsdorf et al., 2010). To obtain an even more accurate stratification than is possible with spheres, new irregular shapes might be useful. Figure 1.5 (right, bottom) displays an instant image of a turbulent flow over a "grass" roof. Today, such fluid flows are usually modeled by Reynolds' averaged vector fields as solutions to Navier-Stokes equations[6]. Perhaps these transport phenomena can be modeled alternatively by particle tracing simulations[7] in Nano- or micro-scale?
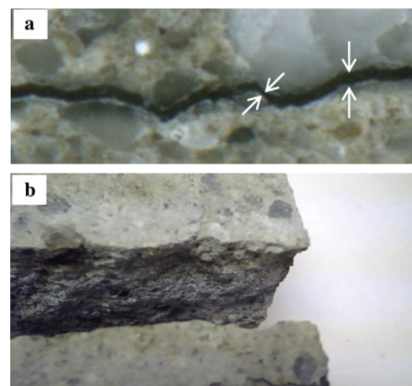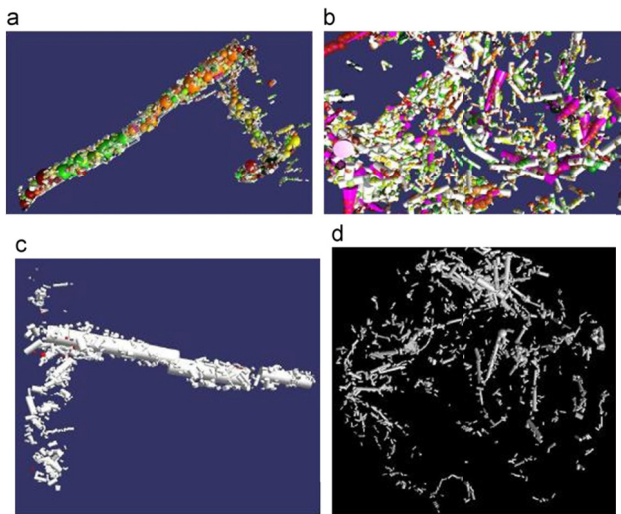
A thru-thickness crack in a mortar disk specimen showing: (a) crack width variability and crack tortuosity, (b) crack wall roughness.

Figure and label from: (Akhavan, Shafaatian, & Rajabipour, 2012)

Figure and label from (Ngom, Monga, Mohammed, & Garnier, 2011)

Optimal cylinders, truncated cones, and balls computed from the simply connected set of balls. (a) Cylinders computed from the MISS representation of the recomposed soil. Each chain is attached to a color. (b) Cylinders are colored in white and truncated cones are colored in mauve. (c) Cylinders and truncated are cones in grey and balls in red. (d) Cylinders, truncated cones and balls in gray

Figure 1.6: Geometry models of soil (left) and tortuous cracks (right)

The four illustrations (a-d) in Figure 1.6 (left) show geometric models of soil by means of generalized cylinders for complex 3D soil micro-structures, scale 3-5 [μm] (Ngom et al., 2011). In Figure 1.6 (right), a crack in a mortar disk specimen is illustrated (a, b). In general, such cracks are described by stochastic extreme value theory (Lamon, 2009) . However, future cracks might alternatively be modeled from irregular, incrementally updated, meshes with random roughness[8] characteristics.

---

[6] Navier Stokes equations are named after Claude-Louis Navier (1785-1836) and George Gabriel Stokes, 1st Baronet (1819-1903). These equations govern fluid flow models in continuum mechanics.

[7] Inspiration on tortuous flow field simulation might be found in the illustrations in Figure 2.19.

[8] Inspiration on rough curves might be found in the illustrations in Figure 2.21 and Figure 2.23 in Chapter 2.

Abnormalities

a) - Geometrical Deformity

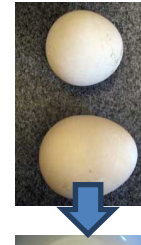Chicken Egg with a peculiar deformity, DK

b) – Extreme size and shape

One normal Eastern Bluebird egg, one small and one very big

c) -Surface color abnormality

Bluebird eggs have blood on them, and white streaks of feces

d) Interior double yolk impacts exterior shape

Khaki Campbell duck eggs

Local news paper article: Hans Wackers, Horsens Folkeblad, DK, Sep. 2011

Pictures (b), (c) and (d) are located 23rd May 2012 at URL: www.sialis.org/weirdeggs.htm

Figure 1.7: Geometrical abnormalities of eggs

Sometimes, natural geometries are observed in variants classified as abnormal. These abnormalities can appear as non-normal shapes (deformities)[9], as extreme size and shapes, as outer scars (scratches, holes, and cracks from mechanical impacts, diseases or other invasive natural objects) or as internal misconfigurations (such as missing, duplicate or triplicate regions or collapsed structures).

Stochastic phantoms must be flexible, detailed and natural at the same time

As seen from the above examples, many complex problems exist in Biosystems Engineering and the related sciences. Key problems relate to the detailed modeling of complex biomass and vegetation surfaces, turbulent fluid flow, various soil phenomena, and cracks in different materials. Abnormalities also are likely to create geometric modeling problems. These examples of well-known geometric modeling problems, along with other problems which will be discussed later, constitute the wide problem domain of this study.

Modeling techniques for sharp edges by subdivision, have been studied for some years (Zorin, Schröder, & Sweldens, 2006; Zorin, 2006). However, controlled parameterization of meshes with sharp edges and extraordinary points remains problematic. A novel approach to such roughness problems by parametric vertex-controlled IFS are under investigation in these years (Gouaty, 2009).

Mathematical formulation problems related to the modeling of sharp edges, extraordinary points, and other geometric irregularities as well as their controlled parameterization, extend the problem domain of this study even further. Moreover, a special theoretical question on about how to judge which phantom of a set of merely identically simulated phantoms is the best model of the original object must also be treated. The mathematical formulation and the algorithmic design, which ensure that created phantoms behave "naturally," are also key theoretical issues that need to be addressed.

---

[9] Inspiration on the modeling of ab-normal shape deformities might be found in the illustration in Figure 2.26 (right).

1.3   STATE OF THE ART

Scanning instruments, meshes for FEA and modeling constraints

Natural geometry modeling relies on scanning objects for subsequent discretization and meshing. As such, this method is centered on state of the art scanning instruments and meshing techniques that relate to the imaging of irregular geometries. This introduction is limited to scanning instruments used in Biosystems engineering and medical science and meshing techniques that have reportedly been applied to natural objects. Some geometrical properties related to the description of natural objects are also briefly presented and grouped.

Selected scanning instruments that are particularly relevant for data acquisition from natural objects are described in section 1.3.1 while meshes mainly dedicated to tortuous geometries are presented in section 1.3.2. Modeling constraints are outlined in 1.3.3 accompanied by a discussion of grouping by size, bounding, location and orientation representations, Frenet curvatures and torsion, special curvatures, Frenet planes, shape metrics, mechanical properties and landmarks.

1.3.1   Scanning Instruments

Scanners are non-invasive devices used to capture shape, color characteristics, and other properties of objects or the environment. The object or environment scanned is either 2D (planar), 3D (spatial) or 4D (spatial real-time). The data obtained are usable for construction of two- or three dimensional static or time-dependent three dimensional computational replication phantoms or two- or three dimensional physical phantoms respectively. Retrieved data are often stored as raw image data in pixels (for reflected surfaces), voxels (for penetrated volumes), or as a derived set of vertices forming a point cloud. Colors and other properties are either integrated in the storage data format or stored separately. In the following section, scanners are categorized based on their underlying measurement principle.

In relation to the formation of observation meshes, emphasis is placed on sensors designed for vector measurements. Relevant measurements include distance, location, orientation, and colors. However, for 4D representations time is also measured. The selected types of sensors for vector measurements include radars, laser scanners, image scanners, ultrasound and tomography. In the following a summary description of the measuring principles for this selection of sensors, planning of measurements, selection of measuring and data processing systems is given. Descriptions of non-penetrating devices such as lasers, radars, and image scanners are given in paragraphs 0-1.3.1.3. Paragraphs 1.3.1.4-1.3.1.5 provide an introduction to penetrating scanners, including 3D ultrasound and X-ray based tomography with focus on computed tomography (CT) and magnetic resonance (MR). Because the application field for this selection of scanners is extremely wide, the introduction concentrates on the imaging of highly irregular or complex (2D, 3D) geometries and irregular flow fields (4D). This introduction also pays special attention to emerging approaches and improvements in existing scanning systems.

1.3.1.1 Radars

A RADAR (acronym for RAdio Detection and Ranging) is an object-detection system that uses electromagnetic waves to measure distance, location, and change in position (velocity) of reflecting objects. Micro wave radiation is characterized by radio waves with a frequency range from 3[kHz] up to 300[GHz] and corresponding wavelengths that range from 100[km], to 1[mm]). Radars are useful for detection of macro-sized geometries with dimensions bigger than 1[mm]. Such geometries are usually detectable by the naked eye. The sensor is based on an antenna transmitting electromagnetic energy as pulses of radio waves. These waves are bounced off an object and returned. The reflected beam is captured by a dish, which concentrates the incoming radiation into a narrow volume so it becomes detectable by a receiver. The received energy level is significantly lower than the transmitted level. Direct measurment of the signal is performed by a time sensor, which is able to capture the elapsed time between the outgoing and incoming electromagnetic beam. The derived measure, i.e. the distance to the object, is then calculated as the product between the elapsed time and the constant propagation speed of light. It is assumed that the elapsed time is proportional to the distance. The antenna, receiver, and dish are usually mounted in one installation unit. Historically, the development of radar goes back to World War II.

Photo of the stabilized platform with the radar frame resting in the cradle. The roof hatch with the slanted radome is located above the cylindrical antenna shroud

Above: Figure and label from:
(Moran, 2012)

Right: Figure and label from:
(Sun & Weng, 2011)
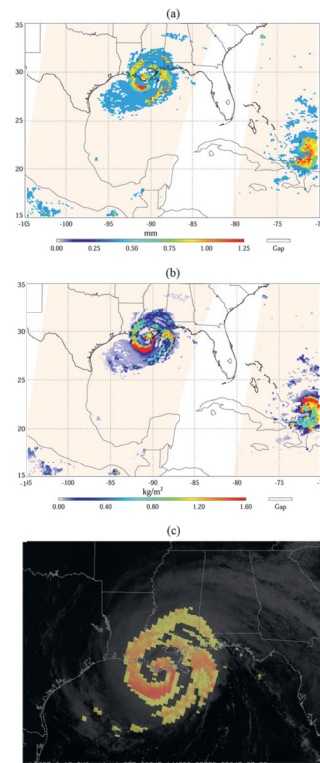
(a) SSMIS ice particle effective diameter, (b) SSMIS ice water path, and (c) *GOES-12* imager and SSMIS ice water path superimposed plot for Hurricane Gustav at the time of landfall at 1430 UTC 1 Sep. 2008.

Figure 1.8. Motion-stabilized shipboard radar (left). Ice water path (IWP) for Hurricane Gustav (Right)

Radars are often land-based, however, motion-stabilized shipboard radars, see Figure 1.8 (Moran 2012), and airborne radars (Koch, 2010) are also in operation. The review by (Koch, 2010), includes a profound overview on remote sensing in general and sensing for forest biomass assessment in particular. In a recent study, such

multi-parameter remote sensing data from radars was used to estimate above-ground biomass over cold and arid area (Tian et al., 2012). In Figure 1.8 (right), the ice water path (IWP) for Hurricane Gustav in 2008 is illustrated. Global quantitative measurements of ice cloud microphysical parameters, such as IWP and ice particle size in ice clouds, are crucial for understanding climate changes (Sun & Weng, 2011).

Many radar installations are designed to monitor different weather conditions including the motion of rain droplets, cloud formations, and many forms of precipitation (rain, sleet, snow, graupel and hail). For such meteorology measurements, weather surveillance radars (WSR) and Pulse-Doppler weather radars are often used (Brown & Lewis, 2005). The Pulse-Doppler is in fact a 4D system capable of detecting the spatial location and the radial range ROC. In general, the collected data are used for weather forecasting and prediction of extreme weather such as storms, hurricanes, rainfall, and more.

1.3.1.2 Laser scanners

A laser is an optical oscillator that emits a beam of electromagnetic radiation. Technically, a laser consists of a transmitter and a receiver of the beam and a scanning device. The term laser is an acronym for Light Amplification by Stimulated Emission of Radiation. The abbreviation LIDAR, which stands for Light Detection and Ranging, is used to specify its application for distance measuring. By such range determination, it is the distance to the first object the beam pulse meets on its path which is measured. LIDAR is applicable for formation of irregular point cloud representations of surfaces.

Like radars, laser scanners can be used for long distance object-detection but they can also be used for micro-distance measurements. A push broom scanner represents a long range sensor often used to capture satellite images of the earth. The latest developments in high resolution satellite images are significant because their remote images are utilized for accurate earth observations (Poli & Toutin, 2012).
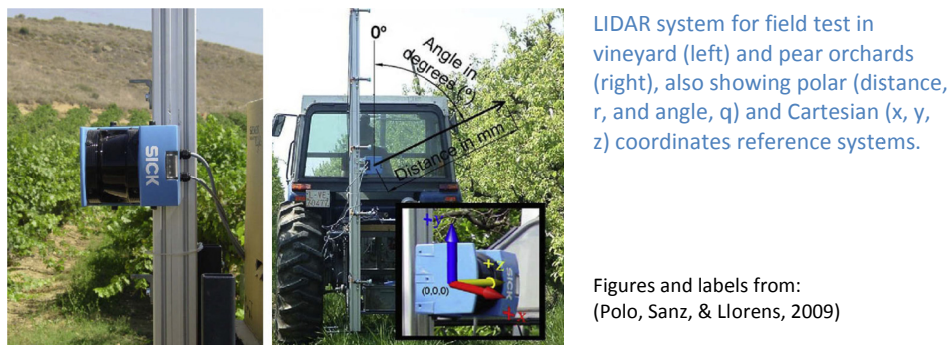

LIDAR system for field test in vineyard (left) and pear orchards (right), also showing polar (distance, r, and angle, q) and Cartesian (x, y, z) coordinates reference systems.

Figures and labels from:
(Polo, Sanz, & Llorens, 2009)

Figure 1.9. A tractor mounted scanning LIDAR for vegetative volume and area imaging

For middle-range distance measurements, terrestrial laser scanners (TLS) are used. TLS and light detection and ranging (LIDAR) represent standard sensing technology in various studies on natural objects and nature caused damages. In a comparative study within Biosystems engineering conducted by (Polo et al., 2009), a tractor mounted scanning LIDAR was used to measure volume and vegetative surface area of tree-row plantations (see Figure 1.9).

Recently LIDAR was also used in a monitoring study on biological crust in civil engineering structures (Gonzáles-Jorge, Gonzales-Aquilera, Rodriguez-Gonzalvez, & Arias, 2012). In a study by (Armesto-Gonzales, Riveiro-Rodríguez, & Riva-Brea, 2010) TLS was used to detect damages in historical buildings.

A review on airborne laser scanning (ALS) was carried out by (Wehr & Lohr, 1999), while a comprehensive introduction to range scanning has been given in the book "*Topographic laser ranging scanning*"(Shan & Toth, 2008).

The principle for laser scanner data acquisition for the TLS example is illustrated in Figure 1.10 below (left).
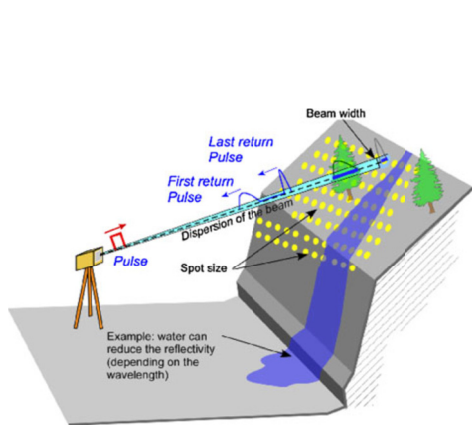
Principles of laser scanner data acquisition, showing the example of TLS

Figures and labels by (Jaboyedoff et al., 2012)
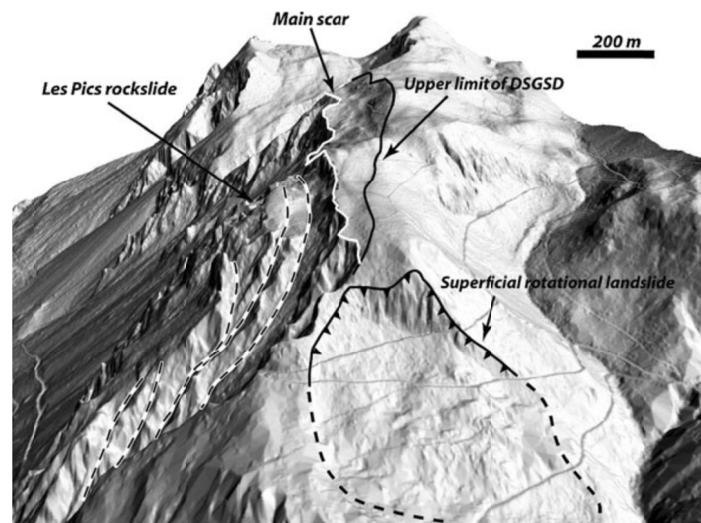
Hillshade view of the upper part of Les Pics instability (Muraz, Switzerland). Gravitational features as scarps, trenches and depressions forming the ''Les Pics DSGSD'' could be clearly identified. The real instability extend could be better defined using LIDAR-derived DEM than in aerial photographs or from topographic maps (Data from swisstopo)

Figure 1.10: Left: Terrestial laser scan (TLS). Right: LIDAR derived landscape discretization

Two major sensing techniques, interferometric synthetic aperture radar (inSAR) and light detection and ranging (LIDAR), are described thoroughly in a review on scanner technologies for landslides, rock fall, and debris-flow. It is mentioned that areas with water are critical due to reduced reflectivity. The data acquisition delivers a point cloud and the accuracy is typically ±1.5 cm with maximum distance 800-1000 m (Jaboyedoff et al., 2012).

A comprehensive overview and details relating to terrestrial laser scanning (TLS) can be found in *"Chapter 3 – Terrestrial Laser Scanners"* (Petrie & Toth, 2008) .

Image scanners are instruments that optically scan 2D and 3D objects. Conventional 2D objects include images, printed text, handwriting, while typical 3D objects include physical objects. However, natural objects such as fingerprints and other recognition objects are image scanned. In iris recognition, subtle infrared illumination is used to acquire detail-rich images of the complicated and random structure of the iris.

Today's image scanners are designed as flatbed or mechanically driven hand held devices. In flatbed designs, the object is stationary and the scanner moves, whereas in mechanically driven designs the object moves relative to the scanner. In hand-held designs, the device is usually moved around the object.

Since the beginning of this millennium, retinal images have been used for diagnosis and post-treatment checking.


Panel (a) shows the retinal image (000004ce.bmp) acquired at gestational age 236 days in a patient being screened for ROP[10]. Panel (b) shows the retinal image (00000513.bmp) acquired at gestational age 257 days, at which point the patient was judged to have reached threshold disease, and was treated. The increase in vessel width and tortuosity is clearly apparent.

(a)   (b)

Figure and label from: (Heneghan, Flynn, O'Keefe, & Cahill, 2002)

Figure 1.11: Image analysis used to measure changes in vessel width and tortuosity

In Figure 1.11, two retinal images of the same eye of a prematurely-born baby are captured at different stages of ROP[10]. In this study, tortuosity was used as an indicator for changes in the blood vessels, and a general approach for segmenting out vascular structures in retinal images and characterizing the segmented blood vessels was proposed (Heneghan et al., 2002).
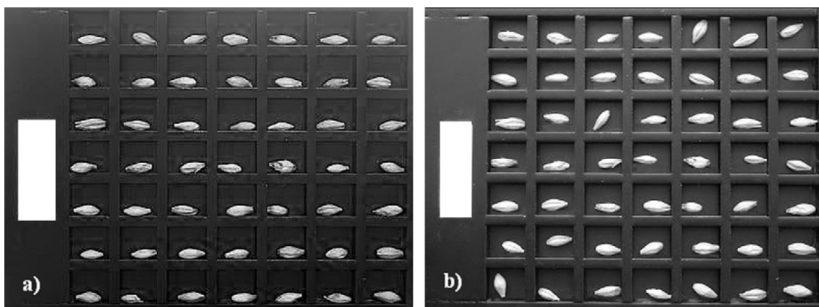

Lately, image analysis has been introduced as an indirect measurement of kernel weight, see Figure 1.12.

Images from the side (a) and front (b) views from the kernels.

Figure and label from (Amaral, Rocha, Goncalves, Ferreira, & Ferreira, 2009)

Figure 1.12: Image analysis used as indirect measurement of kernel weight

---

[10] ROP is an acronym for retinopathy of prematurity which is an eye disease that affects prematurely-born babies.

Figure 1.13. Air flow over "grass" roof
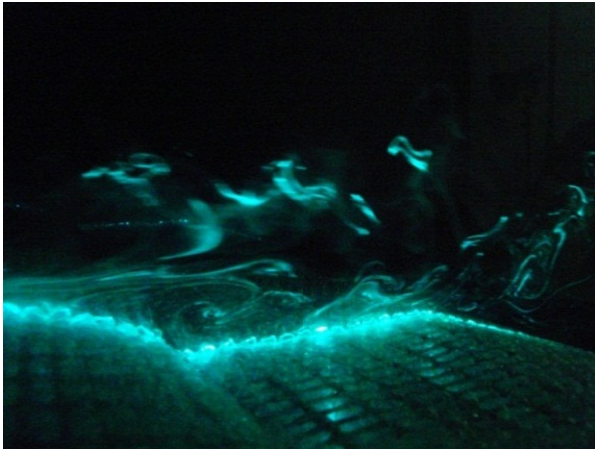
In Figure 1.13, the airflow in the neighborhood of a rough surface is captured at The Air physics lab, Aarhus University, Bygholm, Denmark, 2009. The surface is supposed to imitate grass on the roof of a building. The picture is captured by a high speed camera and represents one frame, whereas the picture in Figure 1.5 (right top) is a high-resolution still picture of the same "grass" roof. The air is supplied with smoke and the lighting is obtained by a laser sheet. High resolution particle tracing from such 4D data is almost impossible since the geometrical constellation of the velocity field is extremely difficult to mesh even with a single frame.

Multi-setups

(a) Optical tracker set-up, (b) IR camera unit.
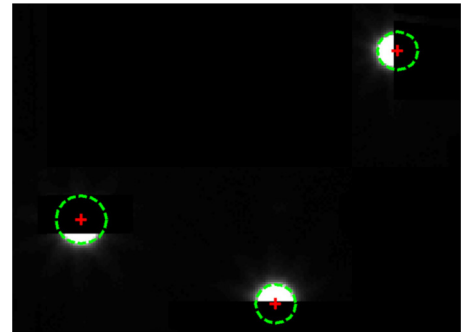
Detection of partially occluded spheres.

Figures and labels from (Barone, Paoli, & Razionale, 2012)

Figure 1.14. 3D shape measurements based on alignment of images captured by two digital cameras from detection of pre-positioned occluded sphere landmarks

In a recent study, (Barone et al., 2012) presented an automatic procedure for full 3D shape measurements based on alignment of images captured by two digital cameras from detection of pre-positioned landmarks (see Figure 1.14).

Ultra-high speed cameras are sometimes used in similar multi-setups.

A multi-vision setup is also employed in the following example where it is used to capture 3D point clouds for geometrical vegetation modeling.
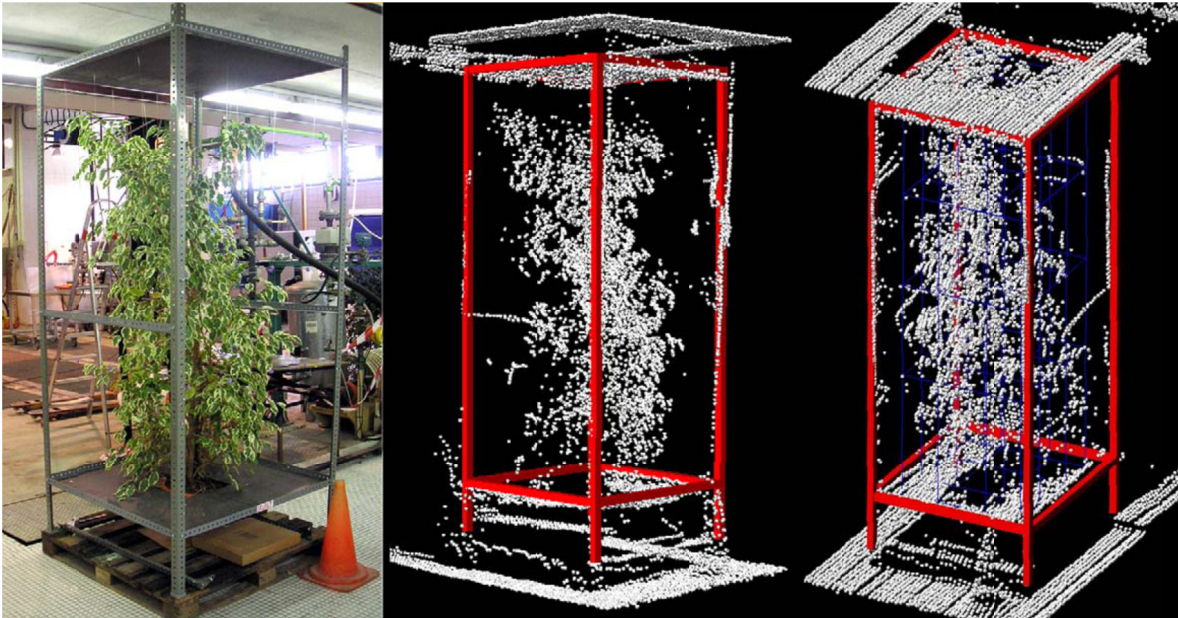
Photography (left) and two 3D images (corresponding to different views) of a *Ficus Benjamina Variegata*, obtained with a LMS200 laser scanner in a laboratory environment.   Figures and labels from (Rosell et al., 2009)

Figure 1.15. Point Clouds from laboratory tests of a 2D setup

In a study aimed at obtaining the 3D structure of tree orchards using LIDAR scanning, a 2D setup was first tested in the laboratory. For subsequent scanning of real crops in the terrain, a 2D setup based on a terrestrial LIDAR sensor was used to obtain vertical slices of continuous, as well as discontinuous, vegetation surfaces from two sides.

By using dedicated software, it was demonstrated that it was possible to construct 3D models from 2D scans of plants (Rosell et al., 2009). This, and other field-based measurements (Polo et al., 2009), indicate that current scanning technologies can enable field-based observation meshes represented by point clouds from treatment of 2D measurements.

Digital cameras mounted on microscopes enable imaging of surface geometries with micro-dimensions (Ponomareva & Polygalova, 2012). High-speed vision cameras are relevant for experiments involving 4D scanning of fluid flow, and for validation of CFD models. As with 3D imaging, simultaneous use of two or three high speed cameras is necessary for 4D imaging (Hwang, Dog, & Okamoto, 2005).

In the following two paragraphs, a brief introduction to penetrating scanning instruments, such as 3D ultrasound and tomography, is given.

3D ultrasound is a relatively new penetrating scanning technique developed and patented by Olaf von Ramm and Stephen Smith at Duke University in 1987 (United States Patent 4,694,435 - Sep15, 1987). Ultra sound waves are mechanical pressure waves with a frequency greater than 20[kHz] and a corresponding wavelength below 17[mm]. Such a small wavelength enables considerable penetrating power.

In contrast to ordinary 2D ultrasound, where waves are sent and reflected within the same angle orientation, 3D ultrasound sends out sound waves at different angles. 3D ultrasound produces volumetric images from where width, height and depth can be measured.

Ultrasonic has conventionally been used in obstetric ultrasonography (during pregnancy) to reconstruct the human fetus' surface of internal organs. However, animals such as cows and horses are also targets for ultrasound scanning.

Shapes of 3D transducers. (A) Bulb-shaped abdominal 3D transducer for humans. (B) Pole-shaped endo-vaginal 3D transducer for humans. (C) Actual size and shape of the bulb-shaped transducer compared to the anus and vagina of a thoroughbred mare.
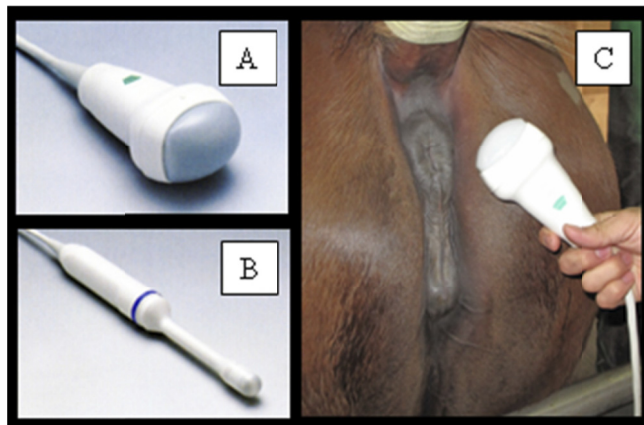
Figure and Label from: (Kotoyori et al., 2012)

Figure 1.16. Ultrasound transducers for humans used for imaging of the equine fetus

In Figure 1.16 A) and B), two standard ultrasound transducers normally used for human scans are illustrated. In a study exploring the possibility of using 3D ultrasound imaging, the same two transducers were used to examine imaging of the equine fetus C) for clinical applications (Kotoyori et al., 2012).

4D ultrasound is a time controlled extension of conventional 3D scans which allows for volumetric images. Compared to 3-dimensional ultrasound, where the streaming image lags due to computer construction time, 4D ultrasound is visible in real time.

Acoustic measurements in the audible range

Acoustic measurements in the audible range have been used for some years. A recent non-invasive experiment on eight different cultivars (Gasso-Tortaja et al., 2010) shows that acoustic measurement in the audible range (20[Hz]-20[kHz], 17[mm]-17[m] at 20[C^0]) can be an inexpensive tool for future bio-characterization.

1.3.1.5   Tomography

Tomography is an imaging technique based on penetrating electromagnetic waves. It is useful for mapping the interior of natural objects. The object is scanned in sections (cross-sections, slices) and the individual images (the tomograms) are composed into continuous representations by tomographic reconstruction.

A few devices (tomographs) such as CT and MR, which are used for imaging of natural objects with highly irregular geometry, are commented on in the following section.
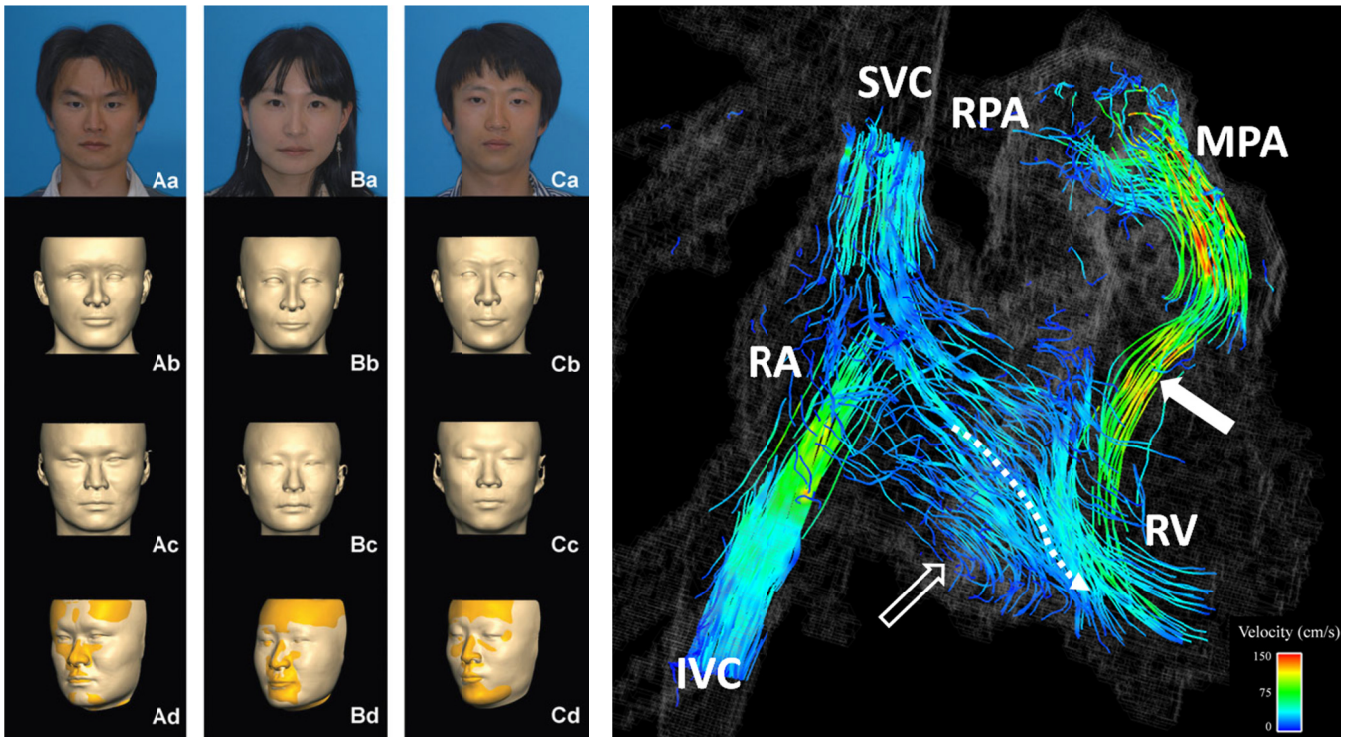
From the top row: facial photographs of subjects A, B, and C (Aa, Ba, and Ca), reconstructed faces (Ab, Bb, and Cb), scanned facial surfaces (Ac, Bc, and Cc), alignments each of the facial reconstruction, and corresponding scanned face (Ad, Bd, and Cd; gold-colored for the scanned faces, orange-colored for the reconstructions).corresponding scanned face (Ad, Bd, and Cd; gold-colored for the scanned faces, orange-colored for the reconstructions).
Figure and labels from (Lee, Wilkinson, & Hwang, 2012)

17 year-old female with Tetralogy of Fallot repaired with transannular patch at 2 years of age. Particle trace visualization during a right ventricular diastolic time frame demonstrates pulmonary regurgitation (closed arrow). The majority of the flow from the right atrium (RA) into the RV is directed abnormally toward the RV apex (curved dashed arrow) with a smaller vortex just beyond the tricuspid valve (open arrow).Color-coding was achieved with respect the absolute acquired velocities. SVC = superior vena cava; IVC = inferior vena cava; MPA = main pulmonary artery; RPA = right pulmonary artery.
Figure and labels from (François et al., 2012).

Figure 1.17. Left: Facial reconstruction employing cone beam CT from Live subject sculls. Right: MR Velocity mapping during a right ventricular diastolic time frame

Figure 1.17 (left) illustrates cone-beam computed tomography (CT scan) utilized for 3D forensic facial reconstruction from live subjects (Lee et al., 2012). In Figure 1.17 (right) an instant frame from a 4D magnetic resonance (MR) velocity mapping is shown. The impressive color coded fields are obtained by (François et al., 2012).

The previous two examples show that CT and MR are able to produce accurate representations of both hard and soft tissues of human beings. For biomasses, livestock animals, and many other natural objects, it is likely that such 3D/4D scans are able to replicate non-human nature with the same level of resolution.

In radiology, tomography is used to both diagnose and treat human body diseases. The illustrated reference book, "Squires's fundamentals of radiology" (Novelline & Squire, 2004), covers imaging techniques, normal radiological anatomy, and details body parts as well as the vascular and central nervous system and more. Advances in scanning technology enable more and more accurate meshing of natural objects such as human body parts, animals, biomasses, vegetation, soil, crack growth, landscape discretization and natural fluid flow phenomena and more.

Following this overview on scanning instruments, various well-known and relevant meshing techniques will be presented.


1.3.2 Meshes for FEA

In this study, meshes are perceived as discrete geometric representations of objects. Meshes are intended to be further modeled and investigated using finite element based multi-physics software. Finite element analysis is a numerical method for approximation of differential or integral equations. The key idea is to discretize the geometry of the object into smaller parts called elements. These elements are defined from a node point, called nodes, and specified through connectivities. Today there are many commercial FE-software packages on the market, however still at universities throughout the world FE-subroutines are used for teaching, research and development and tested by development software such as Maple®, Matematica®, Mathcad®, MATLAB® and others. Furthermore, new algorithms must comply with standard matrix programming. A detailed introduction to the programming of algorithms for finite element matrices can be found in (Shivaswamy, 2010) where MATHCAD® is used as the technical documentation language. For details on FE-algorithms programmed by MATLAB®, see the original work by (Kwon & Bang, 2000). A thorough introduction into automatic mesh generation for FEA can be found in (Zienkiewicz, Taylor, & Zhu, 2005). For an introduction into completeness and compatibility requirements for iso-parametric elements see (Ottosen & Petersson, 1992). Finally, for a detailed presentation on non-linear FEA, and to obtain a historic perspective, see the reference book by (Bathe, 1982) .

The first model for moisture transfer for drying grain was developed as an FE application within Biosystems engineering by (Lund, 2009). The model was developed within the software package COMSOL Multiphysics®. In COMSOL® and ANSYS® (and other multi-physics software), a discretization strategy for 3D solid elements enables inclusion of several different physics in the same model. Obviously, this physical discretization strategy affects the geometrical discretization and its core must be adopted into new meshing approaches. This is particularly relevant in Biosystems engineering where non-isothermal CFD, particle transport, thermodynamics and other bio-physical and bio-chemical phenomena are often mixed. Therefore, meshes designed for multi-physics modeling are given high priority. Storage wise, vertices of meshes are assumed to be stored in coordinate arrays, and incidences in connectivity arrays.

A phantom is a mesh represented with additional graphical features such as colors, lighting and opacity. This additional information is stored in corresponding arrays, which will not be discussed in further detail here.

Phantoms are used extensively as anatomical models and represent formalizations of natural objects. A comprehensive overview of anatomical phantoms is provided by The International Commission on Radiological Protection (ICRP) in the reference work "Handbook of anatomical models for radiation dosimetry," edited by (Xu & Eckerman, 2010) . This book summarizes the development in phantom creation and various phantom series up until 2010.
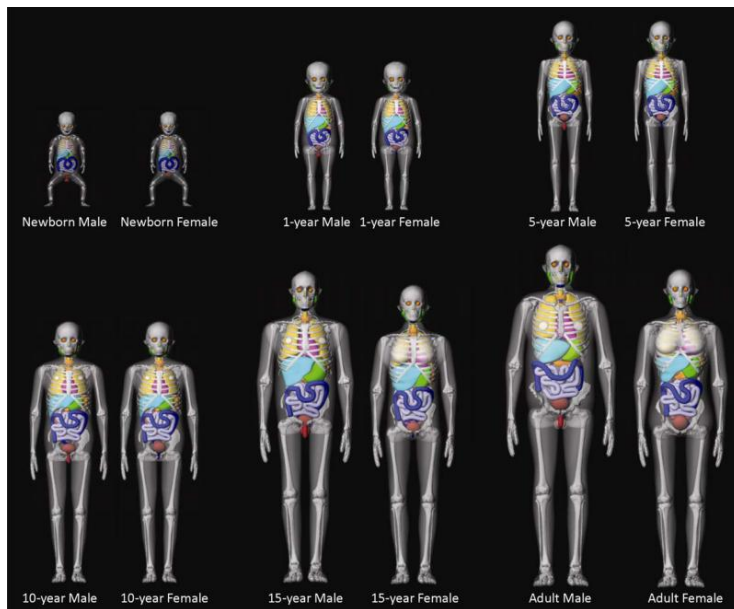
3D frontal views of the entire series of UF hybrid paediatric and adult phantoms. The body contours were made semi-transparent for better viewing of internal anatomy.

Figure and label from: (Lee et al., 2010)

Figure 1.18: The (UF) reference phantoms

Three main types of phantoms are in use: stylized phantoms which are equation based surface meshes, computational phantoms based on voxels, and finally hybrid phantoms which combine stylized and computational phantoms in a NURBS based mesh approach. Various phantom series such as the Pediatric Series (1 - 15 years old) developed at University of Florida (UF) are also included.

Recently, attention has been put on the development of supplementary pediatric phantoms of newborn patients (Wayson, 2012). All such phantoms are used as anatomical models for radiation dosimetry and to model standard persons i.e. reference man, reference woman, reference child and more (Lee et al., 2010) see Figure 1.18.

Equation-based stylized phantoms have been developed and used since the 1960s. Today's 3D voxel phantoms, based on NURBS surfaces, are developed with surprising detail and complexity. They play an essential role in today's dosimetry.

A stochastic phantom is a parametric deformable mesh based on a stochastic simulation. A customizable phantom is a stochastic phantom that can be manipulated to the modeler's specifications for height, width, volume and other geometric characteristics. The morphable human faces originally modeled by (Blanz & Vetter, 1999) represent one of the first examples of customizable phantoms.

1.3.2.1 Synthetic vs. Tortuous Meshes

The label *synthetic* is used to emphasize that a mesh is formed from analytic geometries such as NURBS or a nominal data set. Since most FE models concern man-made objects that are usually designed and manufactured from analytic geometries or NURBS, the majority of today's meshes are synthetic. The label *tortuous* emphasizes that a *mesh* is formed from data with an underlying random variation. Also, it is understood that a tortuous mesh is parametric and deformable in the sense that its size and shape is affected by changes in its parameters. Customizable meshes formed from scanned data or generated from statistical parameters are said to be tortuous. From a statistical point of view, a synthetic mesh differs from a tortuous mesh because the underlying data. For a synthetic mesh the underlying data is assumed to be *deterministic,* whereas it is assumed to be *stochastic* for a tortuous mesh.

1.3.2.2 Special Tortuous Meshes

All the derived meshes in the previous subsection 1.3.1 on scanning instruments, represent *observation meshe*s. An *observation mesh* is a tortuous mesh directly retrieved from the scanning of natural objects or phenomena. It is assumed that observation meshes are affected by natural or abnormal variations. This means that they vary from scan to scan of objects within the same class of objects. Observation meshes are used for description, identification, or classification of natural characteristics.

However, tortuous meshes can also be distinguished according to their creation process and thus can be labeled as replication or imitation meshes.

1.3.2.2.1 Replication Meshes

The label *replication* indicates that a mesh is fitted to a single observation mesh, i.e. it is an approximation to an existing geometric constellation anchored to one scan or one data file. Replication meshes include meshes achieved from digital shape reconstruction (DSR) (Goyal, Piya, Benjamin, Liu, & Ramani, 2012). Other replication meshes are based on polynomial approximation to edges from raw data such as pixel boundaries of images. The advanced technique used to fit a full 3D human scan to a template mesh by affine transformations (Allen, Curless, & Popovic, 2003) is also a replication mesh. The classification of characteristics from observation meshes is defined from existing domain, segment, or boundary elements. The meshes resulting from classification of characteristics are often referred to as atlas reconstructions or classification maps. In general, the aim of these meshes is to replicate the same attributes as observed from the underlying object.

(a)

(b)

(c)
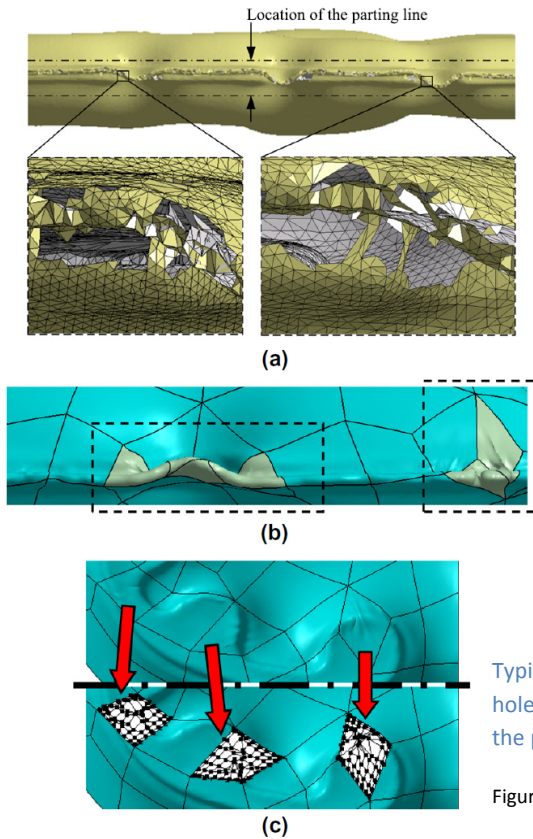
Recently, a new mathematical algorithm for automatic surface reconstruction, which enables practical restrictions on scanned points to be taken into consideration, is presented by (Lin et al., 2012). In this paper, some typical issues on surface construction are also outlined, see Figure 1.19. Recently, studies based on existing algorithms have been carried out and published in very different application areas: (Baroncini, 2012) studied the human hypothalamus from MRI and defined its atlas. (Pan & Skala, 2012), (Lin et al., 2012) focused on surface reconstructions and (Cham, Beckers, Spanhove, & Borre, 2012) classified Natura 2000 heathland in Belgium. Apart from the diversity in applications, it must be emphasized that in all of the mentioned replication mesh examples characteristics or attributes were directly or indirectly extracted from the observation mesh.

Typical issues in current surface reconstruction approaches: (a) complex holes near the parting line, (b) irregular and even wrinkled surfaces near the parting line, and (c) wrinkled surfaces near sharp regions.

Figure and label: (Lin, Huang, Lai, Tsai, & Ueng, 2012)

Figure 1.19. Surface reconstruction

In Biosystems engineering, species outline recognition is often used to recognize an unknown object and identify the species it belongs to based on the captured outline properties. Usually, the objects' characteristics are available as an image file and the identification is based on a trained backpropagation neural network (Rojas, 1996) or by characteristic landmark identifications or recognitions.
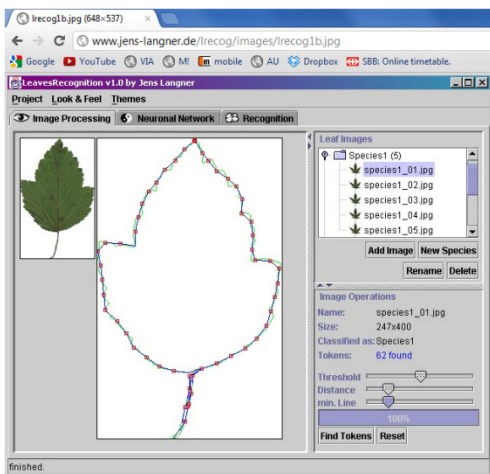
With the Leaves Recognition® v1.0 software, it is possible to extract the edge token from a leaf image as a polygon of pixel values. The subsequent identification procedure allows an unknown object to be specified as belonging to a particular species. This recognition procedure is based on a trained backpropagation network.

For more details see:

Jens Langner, Leaves Recognition v1.0. Neural Network based recognition system of leaf images. LightSpeed Communications GbR. Dresden Germany. 18 April 2006. Localized 21st March 2012 at www.jens-langner.de/lrecog/#2.1

41

The label *imitation* is used to stress that a mesh is generated from sample information of observation meshes. In general, an imitation mesh is formed from data that has been treated with chemometrics. Examples of immitation meshes are phantoms generated from random parameters and fitted to meet constraints within stochastic approaches (Blanz & Vetter, 1999), (Allen et al., 2003) and (Baek & Lee, 2012). Formally, a replication mesh represents a *deterministic fit,* whereas an imitation mesh represents a *simulation* based on realizations of parameters *modeled as random variables or stochastic processes*.

1.3.2.2.3   Examplifications on Synthetic vs Tortuous Replication and Imitation Meshes

EXAMPLIFICATIONS   The label "synthetic" is used for meshes purely formed from analytic geometries, fractals, scanned or man-designed buildings, machines, infrastructure, vehicles and more. The label "tortuous" simply means that the mesh is based on scanned data that reflects an underlying variation. The additional label "observation" emphasizes that the scanned objects are human beings, animals, vegetation, soil, landscapes and others. Also, geometric constellations of scanned cracking phenomena in materials are considered observation meshes, i.e. the data source for "synthetic" meshes is deterministic, whereas it is stochastic for "observation" meshes. The label "replication" indicates that a tortuous mesh is fitted to a single observation mesh such as various types of digital shape reconstruction, whereas the label "imitation" relates to a process where the new mesh is formed by stochastic data such as Monte Carlo generated location and orientation parameters. Technically, "replication" refers to a parameter extraction process whereas "imitation" refers to a reparameterization process. Note that none of the above labels reflect the degree of geometric irregularity they only characterize the data type or the meshing process.

1.3.2.3   Master Meshes
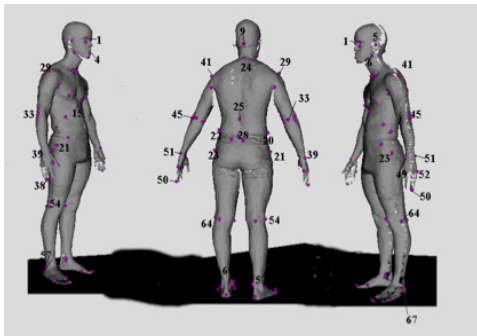
From Wikipedia Commons commons.wikimedia.org

A *master mesh* is a constellation of characterics, i.e. biometric points such as points of interest, special identifiers or other characteristic location and orientation patterns. In the following discussion, all such characteristics are defined as *landmarks.* The formation of landmark information into a parametric constellation used for further subdivision is described as a master mesh. Today, landmarks are commonly used for identification of parts of human body surface, see illustration to the left hand side.

Technically, master meshes are outcomes of manipulated observation meshes. They carry geometrical and color information adequate enough for an observer with relevant expertise to identify characteristics. Such manual identification is sometimes replaced with automatic detection procedures implemented as identification algorithms.

The expert knowledge is usually formalized by atlas or tables of anthropometric markers. The (CAESER, 2012) anthropometric database (Civilian American and European Surface Anthropometry Resource) contains 3D surface grid and color map information. This database also includes "The seventy-three Anthropometry

Landmarks" of the human body. Landmarks for iris scanning and fingerprints are other well-known examples. Recent studies indicate that automatic detection of landmarks for selected objects appears to be on the horizon in the near future. Recently, various emerging identification algorithms have been presented:

An automatic detecting approach based on spin images was presented by (Li & Zhong, 2012). A fast and automatic image-based registration of TLS data where key-point candidates are selected after comparison of each sample point to its eight neighbors and their characteristic location and orientation is derived from local image gradients and presented by (Weinmann, Weinmann, Hinz, & Jutzi, 2011). An Automated sparse 3D point cloud generation of infrastructure from video streams was introduced by (Fathi & Brilakis, 2011) . In this stereo vision-based method, surface data was captured using two video streams. The characteristic features were detected and matched from such pairs of stereo video frames.

However, automatic detection procedures still reflect expert knowledge about the object in the algorithmic definitions. However, it is likely that in future full-automatic detection, the need for expert knowledge will be reduced to a minimum.
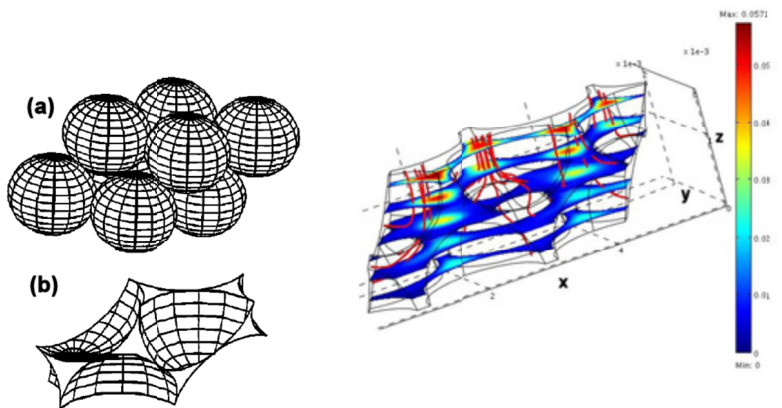
Formally, the constellation of the detectable characteristics is in itself regarded as a mesh. Location and orientation landmarks represent an initial coarse or sparse "master" for the shape of the object. If the master mesh is defined from anthropometric parameters defining height, width, length, radius, curvature or other metrics they are called parametric master meshes.

Often, a master mesh serves as a basis for the generation of rough or smooth models with higher mesh densities. In these situations, a discretization of the observation mesh is required. This discretization is performed using geometric primitives and, or subdivision. This will be further elaborated on in later sections.

Mesh creation from GUIs is usually synonymous with interactive manipulations of *geometric primitives.* These primitives are the building blocks for mesh creations. In multi-physics software such as COMSOL®, ANSYS® and others, the geometric primitives for 3D volume creation include: point, Bezier polygons, parametric curves & surfaces, block, cone, cylinder, sphere, ellipsoid, helix, hexahedron, pyramid, tetrahedron, torus and more. Furthermore, during the geometric design process, the objects are divided into domain, segments, and boundary elements that are further specified as homogenous entities with individual physical settings. In boundary representation, the topological elements are defined as follows. A face is a bounded portion of a surface, an edge is a bounded piece of a curve, and a vertex lies at a point. In terms of physical properties, each domain (or subdomain) is usually considered a solid, which has a unique setting.

However, in some situations relevant for natural geometries, the domain, segment, and boundary elements are not used to model solid matter but rather cavities filled with fluids (gasses or liquids). In one example (Monga 2009), air-filled pore spheres of soil were modeled using simple primitives. In this case balls were used as geometric primitives (see below). In a recent approach, generalized cylinders were introduced to model cavities by (Ngom, Monga, Mohammed, & Garnier, 2011). An important study on blood vessels by (Heneghan et al., 2002) also exemplifies liquid-filled cavities. In this study, vessels were modeled using line segments that were extracted from a RetCam® image (Clarity Medical Systems, Inc., Pleasanto, CA, USA), and tortuosity was calculated from constituent points of each vessel segment and used to detect changes in retinal vessels.

Boolean operations including Boolean difference, intersection, union, and complement, supplement built-in features in modern CAD software.

Figure 1.20 illustrates a COMSOL® Multiphysics model which indicates that flow phenomena in idealized pore spaces are realistically represented by the Navier-Stokes equations. In this study pore cells are defined from rhombohedral packing of spheres by Boolean operations (Viola, Zama, Tuller, & Mesini, 2009).

(a) Rhombohedral packing of identical spheres, and (b) unit pore cell.

Two joint rhombohedric cells with the inlet face on top.

Figures and labels from (Viola et al., 2009)

Figure 1.20: A synthetic mesh for flow through rhombohedric pore spaces constructed by Boolean operations on sphere primitives.

In the future more detailed meshes which include irregularly shaped pore cells with roughness and local discontinuities might influence the results significantly even when the central tortuosity of the flow path through the cells is kept at the same level.

A corresponding rhombohedral packing is often experimentally reproduced from uniform sands or glass beads having different porosities. Typical experimental parameters such as tortuosity, diffusivity, and permeability in the liquid and gaseous phases of soils have been used by (Moldrup et al., 2001). Also, transport studies of suspended particles (SP) in a saturated porous medium have also been studied (Benamar, Ahfir, Wang, & Alem, 2007). Such pore space problems, as well as other other special soil modeling problems, need to be supplemented by new multiresolution simulations in the future. One such example is related to complex pore spaces created by biological activity (Monga, 2009).

Mesh creation from imported data is a feature included in some software packages. In the following illustration the COMSOL® Multiphysics software package is used to illustrate the simple steps in such data import.
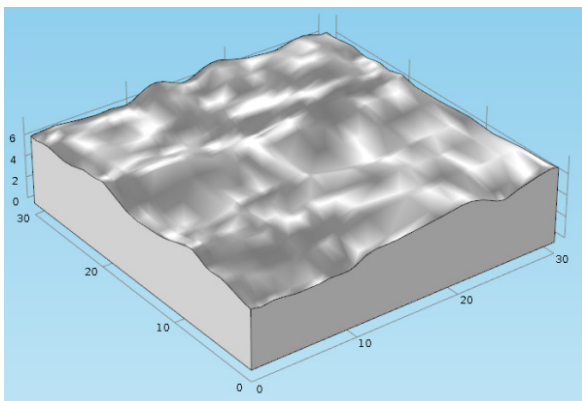
In Figure 1.21, a tortuous surface plot for the COMSOL® version 4.2a (2012) built-in file,

`rock_fracture_flow_aperture_data.txt,`

is illustrated. Like other advanced software packages, COMSOL® Multiphysics allows for parameterization of imported data files. The mesh based on the above data file is imported, interpolated, and finally used as a boundary surface for a 3D domain.

Figure 1.21: Tortuous observation mesh created from imported data, DANS Project, AU, 2011

The first book on Multiphysics modeling using COMSOL® has recently been published (Pryor, 2011). In this book a thorough introduction into Multiphysics is given, along with a huge number of meshing examples for self-studying.

In general, it might be expected that future software will allow for highly irregular geometry files to be imported, transformed into tortuous domains as observation meshes, and if relevant, utilized for further multi-physics analysis.

B-splines, (Basis-splines[11]), which are piecewise smooth polynomial functions defined from control points (sometimes referred to as de Boor points), are themselves used for mesh generation. Recently, a novel approach for smooth fitting of highly irregular surfaces using B-splines was presented by (Gálvez, Iglesias, & Puig-Pey, 2012). This flexible approach, based on genetic algorithms,[12] enables accurate fitting to point clouds even with complex discontinuities. Indirect parameterization of B-splines is performed from the control points.

---

[11] Nikolai Ivanovich Lobachevsky, Russian mathematician (1792 –1856) was one of the first who studied splines.

[12] Genetic Algorithms (GA) originated from the seminal work of John Holland in the 70s, republished in the book "Adaptation in Natural and Artificial Systems", (Holland, 1992)

NURBS stands for Non-Uniform Rational Basis Spline. The concept was pioneered by Bezier[13] and represents today's de facto technique for irregular meshing of smooth surfaces in 3D. At the Rhinoceros® home page (see link at 7.2) details on NURBS algorithms, as well as smooth and kinked curves, are provided in an intuitive manner. Kinked curves are used to model discontinuities. This means that NURBS based meshes also allow for highly irregular geometries including singularities. NURBS meshes are designed from "artificial" control points. In general, these control points are not directly measurable from observation meshes since they usually lie outside or inside the object.

Control points (as mentioned under B-splines) can be perceived as parameters efficient for shaping a mesh. However, meshes based on NURBS control points are not the answer when the goal is to use parameters that are intuitive and directly measurable from observation meshes. NURBS based meshing is the mathematical engine of the Rhinoceros® software and a feature in 3ds Max Design® as well as others. This type of software is designed for free form modeling, meaning that the mesh of control points can be flexibly adjusted in an intuitive manner by the modeler. Free-form modeling eases the geometry creation of both man-made objects, and models of natural objects, see Figure 0.4.

Implicit surfaces, also known as "metaballs", "blobbies" or "soft objects," are another starting point for smooth mesh generation. Let $f_{\text{implicit}} = f(x,y,z)$ define an implicit function in 3D. Then $f_{\text{implicit}} = 0$ defines a surface representation, whereas $f_{\text{implicit}} < 0$ defines the negative domain, i.e. the inside of the surface and $f_{\text{implicit}} > 0$ the positive domain, i.e. the outside. Implicit surfaces are used to interpolate irregular observation meshes with new smooth meshes. One of the first pioneering articles on implicit surfaces was published by (Savchenko, 1995). As for spline-based meshes, the parameterization of implicit functions is indirect

---

[13] Pierre Étienne Bézier (1910 –1999), French engineer at Renault was the pioneer behind today's NURBS.

Mesh creation from wizards is very efficient if the geometry is regular and parametrically definable from boundary polygons and holes.
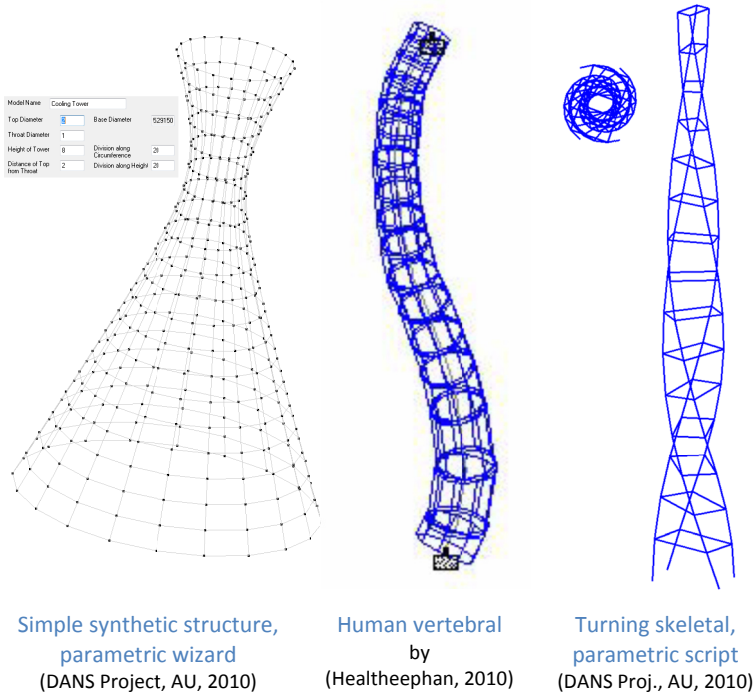

In Figure 1.22 (left), the built-in "Cooling Tower" wizard from the Staad.Pro® V8i 2012 software is used to illustrate a skeletal structure defined in cylindrical coordinates by six parametric inputs: top & throat diameter, height, distance from top, and divisions along circumference and height.

However, features such as translational repeat, rotational repeat, and mirroring are other semi-wizard based mesh generation procedures available in many commercial software packages.

Simple synthetic structure, parametric wizard
(DANS Project, AU, 2010)

Human vertebral by (Healtheephan, 2010)

Turning skeletal, parametric script (DANS Proj., AU, 2010)

In Figure 1.22 (middle) a model from a study by (Healtheephan, 2010) for the structural behaviour of human vertebral column using Staad.Pro® is illustrated.

Figure 1.22: Structural meshes

In this study on the deflections and forces in vertebrae produced in the vertebral column (spine) during the course of accidents, the geometry is modeled from different types of spinal curves and normal curvature values.

Mesh creation from super-element scripts is an alternative that gives full control over the actual mesh. A non-parametric input script is a code sequence, which is interpreted by the meshing software and transformed into a graphical mesh. These input scripts usually take advantage of super-element codes including super node arrays, connectivity arrays, and supplementary codes for subdivision specification.

The super-elements themselves are usually formed as quadrilateral or triangular surface elements. Such super elements are equivalent to the nodal elements formed by master meshes. However, parametric meshes can also be coded using a third-party programming language. As such, they are able to deliver input script code for the meshing software.

In Figure 1.22 (right), a turning skeletal structured coded as a MATLAB® script generates a new input script file ready made for Staad.Pro®. It demonstrates the user-flexibility in current mesh generation software across platforms. It also enables dedicated algorithms for irregular meshing to be separated from the FE-software, where the mesh is later used.

Subdivision is a meshing technique based on recursive subdivision, which gives finer and finer meshes from an initial coarse mesh. This coarse mesh can also be referred to as the control mesh, control points, control handles, control polygons, global mesh or master mesh. In the following section it is called a *master mesh* since it defines the key characteristics of the geometry. In other words, a master mesh represents the geometric basis constellation, which is the starting point for subsequent subdivision into finer and denser meshes. The new subdivision meshes are usually called *iterated* meshes. Each of these iterated meshes are specified at a specific level of refinement from the sequence of new subdivision meshes. At any step of recursive subdivision, iterated meshes are in fact the intermediate outcome. The ultimate (final, terminal or goal) mesh is the last iterated mesh in the sequence and is referred to as the *limit surface*. At the infinte, there is no longer any mesh (a finite set of polygons) but rather a continuous set of points. Master and iterated meshes are technical meshes used in a recursive formulation strategy. A comprehensive overview of recursive surface meshing is found in the book *"Subdivision Surfaces"* by (Peters & Reif, 2008). It provides details about the development of the various algorithms as proposed by (Deng & Ma, 2012). The following section includes a retrospective introduction related to irregular geometry modeling. It starts by highlighting the latest achievements and works backwards to the roots of subdivision.

A study including *scale dependency* and applications of subdivision geometry, affected by *multi-level scales,* was recently presented in a work by (Stotz, Gouaty, & Weinand, 2009). They showed that *transformation driven geometric design methods* can be applied to the architectural design of timber constructions through *controlled modification of the subdivision operators*. Usually, *subdivision surfaces* are treated as *spline surfaces with singularities,* as described by (Peters & Reif, 2008). A comprehensive overview with many applications on modeling with *multi-resolution subdivision surfaces* was presented by (Zorin, 2006). A special branch of subdivision is called Iterated Functions Systems (IFS). Mathematically, IFS represent a collection of contractive transformations. Details on IFS, and an approach to build fractals from subdivision schemes, can be found in (Schaefer, Levin, & Goldman, 2005). This and later approaches to generate fractals from subdivision are based on the work by (Goldman, 2004). Surprisingly, Goldman showed, using The de Casteljau subdivision algorithm,[14] that Bezier curves are also IFS attractors. This means that Bezier curves are fractals, since fractals are attractors (fixed points) of iterated function systems (Barnsley, 1988).

However, even before Goldman's findings, other attempts to form highly irregular meshes had been made. (Tobler, Maierhofer, & Wilkie, 2002) introduced a rule based on mesh growing where modification of vertex position at each subdivision level was defined at a local tangent plane. The basic idea of adding such small-scale geometry into the subdivision process is probably one of the most fundamental approaches for the generation of irregular natural objects. In principle, parameterization and small-scale control can be applied on a variety of subdivision schemes. (Guérin, Tosan, & Baskurt, 2001) gave a concise classification of a wide variety of representation methods based on the original data source. Furthermore, they introduced an *IFS based approximating method for both smooth and rough surfaces*. Such approximation seems relevant, in particular for natural object surfaces since they seem to always possess rough characteristics.

---

[14] De Casteljau's algorithm is a stable recursive method to evaluate polynomials developed by Paul de Casteljau (born 1930), French physicist and mathematician.

Unfortunately, the introduction of irregularity by perturbations can result in smoothing instead. In an article about the control of irregular geometries, (Dyn, Levin, & Micchelli, 1990) studied the impact from small perturbations and found that even a proper perturbation could increase the smoothness and thus provide a one-parameter class of schemes with better continuity properties. Therefore, special perturbations enhance smoothness, whereas huge vertex perturbations in other situations produce non-smooth fractal like geometries. It is a common experience that adding perturbations at one subdivision level, influences all subsequent levels. This makes it very hard to predict the limit geometry and even harder to make geometry simulations customizable in a controlled way. Irregularities were also studied in an article on the simplest possible subdivision schema for smoothing polyhedra (Peters & Reif, 1997). Here, the first convergence improvements at irregular points were integrated into the subdivision process. Also, studies of *the smoothness of the limit surface* were performed by (Peters & Reif, 1997). IFS based methods were originally introduced by (Barnsley, 1988) and sprung out of the original work on subdivision by (Doo & Sabin, 1978) and (Catmull & Clark, 1978). Other control-point based predecessors for curve and surface generation were introduced in the 70'ties by (Lane & Riesenfeld, 1977) , (Barnhill, 1974).

Still, the key ideas behind many of today's subdivision algorithms are based on the original work by Edwin Earl Catmull (born 1945) and James H Clark (born 1944). These key concepts are introduced hereafter.
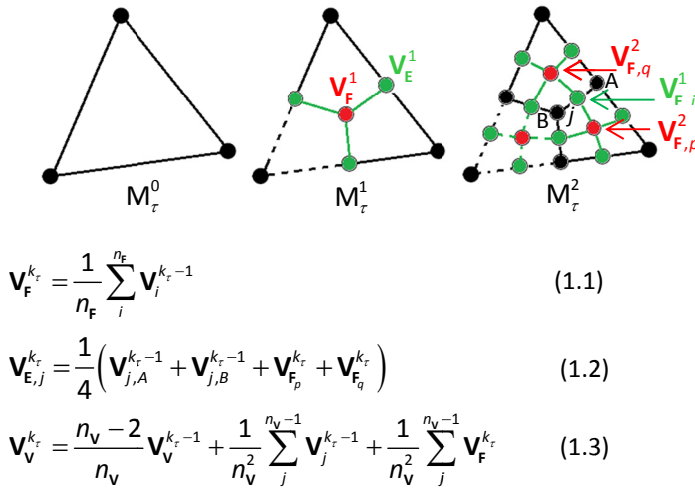
$$V_F^{k_\tau} = \frac{1}{n_F} \sum_i V_i^{k_\tau - 1} \tag{1.1}$$

$$V_{E,j}^{k_\tau} = \frac{1}{4}\left(V_{j,A}^{k_\tau - 1} + V_{j,B}^{k_\tau - 1} + V_{F_p}^{k_\tau} + V_{F_q}^{k_\tau} \right) \tag{1.2}$$

$$V_V^{k_\tau} = \frac{n_V - 2}{n_V} V_V^{k_\tau - 1} + \frac{1}{n_V^2}\sum_j^{n_V - 1} V_j^{k_\tau - 1} + \frac{1}{n_V^2}\sum_j^{n_V - 1} V_F^{k_\tau} \tag{1.3}$$

Figure 1.23: Catmull-Clark subdivision

In Catmull-Clark subdivision (Catmull & Clark, 1978), an arbitrary master mesh M_τ^0 formed by polygonal faces is used to iterate a new finer mesh $M_\tau^{k_\tau}$ by a recurrence relation $M_\tau^{k_\tau} = S^{k_\tau} M_\tau^{k_\tau - 1}$. Here $k_\tau = 1,...n_\tau$ is the level of refinement and n_τ is the ultimate level of refinement. S^{k_τ} is the subdivision operator which split every polygonal face into a number of new quadrilateral faces by manipulating the old vértices $V^{k_\tau - 1}$ so new face-vertices $V_F^{k_\tau}$ see (1.1), edge-vertices $V_E^{k_\tau}$ see (1.2) and vertex-vertices $V_V^{k_\tau}$ see (1.3) are generated.

From these iterated vertices, a new and finer quadrilateral mesh $M_\tau^{k_\tau}$ is then formed. Therefore, each face of this new mesh is bound by four edges and four vertices. Hereafter, the same recurrence relation is applied until a limit mesh $M_\tau^{n_k} = S^{k_\tau} M_\tau^{n_k - 1}$ is eventually created. This mesh possesses G^2 geometric continuity in the limit $(n_k \to \infty)$, except at some extraordinary vertices. In (1.1) n_F is the number of edges defining the face, i.e. the face valence and i is the index of vertices. In (1.2) and (1.3), j is the index for an edge defined from local A to local B , and n_V is the number of edges meeting at a vertex, i.e. the vertex valence.
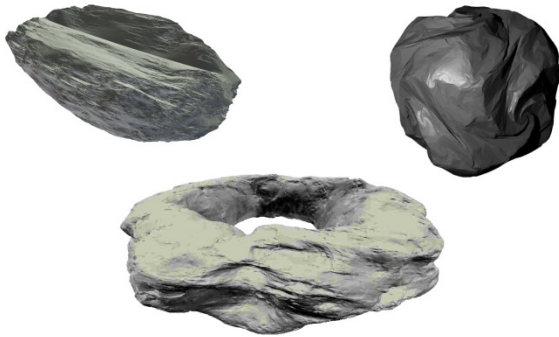
IFS meshes from: project ModItere, LIRIS, Université Claude Bernard, Lyon 1, France

Figure 1.24: Synthetic IFS meshes

One of the latest theoretical studies by (Gouaty, 2009) generalizes IFS to a level where the subdivision operators are *customizable,* i.e. the use of moving subdivisions points affect the geometry at each level of subdivision and therefore at smaller and smaller scales.

The "grain", "stone" and "ring," shown in Figure 1.24, represent synthetic 3D phantoms. In general, these multiresolution geometries are *fractal*. However, the generalization by Gouaty also allows for generation of smooth phantoms.

In a famous article by (Morse, Lawton, Dodson, & Williamson, 1985) it was demonstrated that some natural surfaces are fractal. Morse et al. showed that the distribution of arthropod body lengths was correlated with the fractal dimension of vegetation. This correlation indicates that geometry might play an important role in the study of diseases and insect attacks on seeds. A study on Hausdorff dimension and Diophantine Approximation by (Dodson & Kristensen, 2004) demonstrated that the fractal dimension also provides an indication of the size and complexity for packing of particles. Dodson and Kristensen also showed that the boundary of the Mandelbrot set has the Hausdorff dimension two. The packing of biological objects (such as seeds and vegetables and soil particles) is a very complex geometrical phenomenon that should be seen in a fractal perspective.

Inspiration might also be found in The von Koch snowflake curve. This curve, and other irregular curves, have been known for more than a hundred years. Details on these curves, and more, can be found in the fascinating book by (Barnsley et al., 1988) on fractal images. For multiresolution modeling, such iterated curves might become useful especially for natural geometries at micro and Nano-levels. In the reference book "The beauty of Fractal" by (Peitgen & Richter, 1986), a formalization of Julia sets and fractals was established. The computer graphical generations in the book were state of the art at that time. The spectacular images are still a source of inspiration for many scientists and for modeling of natural objects as well.

Benoit Mandelbrot developed the notion of a fractal and presented the iterative recursive nature of fractal generation in the famous work "The Fractal Geometry of Nature" (Mandelbrot, 1983). When natural objects like vegetation and landscapes are observed, fractal appearance is striking. The same conclusion is made when natural objects are observed under a microscope. Therefore, fractals seem to be a relevant tool for modeling of irregular and unpredictable geometries. However, as mentioned earlier, due to their built-in chaotic behavior it is hard to control fractal iterations in algorithms designed for systematic geometry generation.

1.3.3 Modeling Constraints

Geometrical and mechanical properties are today's key parameters for seed characterization (Coskun et al., 2006). Conventional seed measurement covers volume, thousand seed weight (TSW), moisture content (MC), and other mechanical properties. These parameters represent constraints and they are, themselves, parameters in stochastic phantom modeling. Therefore, they are expected to play a leading role in future flexible simulation modeling. Some geometrical and mechanical properties have been measured over the decades. They range from simple caliper measurements and laser scans, over geometrical models, to image analysis, acoustics, and other non-invasive measurements. In general, the geometry of any natural object is likely to be constrained by these properties. Therefore, in the following section selected properties relating to size, boundings, location and orientation, landmarks and shape are introduced.

1.3.3.1 Size Metrics

For stochastic phantom creation the following size properties seems to be the overall natural constraints.

- 1D: length l_1, width l_2, thickness l_3 diameter d and perimeter O_σ
- 2D: surface area S, cross-sectional area A_σ and projected area $A_\perp$
- 3D: Volume V.

Sometimes, also the following derived quantities are relevant:

- Geometric mean diameter (side length of the cube of equal volume): $d = \left(l_1 l_2 l_3 \right)^{\frac{1}{3}}$

- Equivalent diameter of projected area (diameter of the circle of equal area): $d_\perp = 2\pi^{-\frac{1}{2}} A_\perp^{\frac{1}{2}}$

- Spherical surface area (area of the sphere of equal volume): $A_s = \pi^{\frac{1}{3}} \left(6V \right)^{\frac{2}{3}}$

The use of size properties in phantom creation was included in one of the early studies on the space of human body shapes by (Allen et al., 2003). First human phantoms were generated with a required height and weight (=volume times homogenous density) and thereafter from feature-based editing adjusted to fit changes in the height and weight respectively. In the determination of reference phantoms, the size was found to be a constraining property for meshing (Wayson, 2012), (Lee et al., 2010).

In a recent study on one hundred kernels per seven different cultivar by (Fératlégil-Durmus et al., 2010), a FEA approach and formulas for ellipsoid seeds model was compared with digital image analysis on a number of standard parameters. Furthermore, the relative difference in volume and surface area between pycnometric measurement and ellipsoid approximation was determined. The size values approximated from the ellipsoid did not differ more than 10% and 4% from the pycnometric measurement respectively. As such, this study demonstrates that using 2D image analysis in combination with ellipsoid approximation is a suitable method for determining the size of grain as well as other parameters.

1.3.3.2   Bounding Metrics
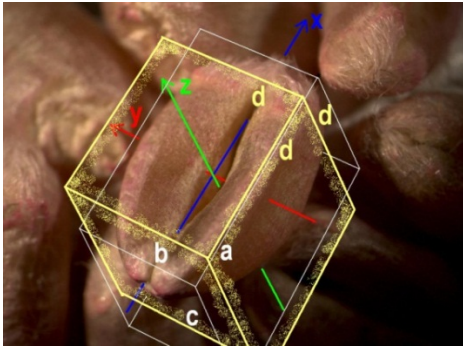
Feret bounding box (*axbxc*) and its geometric mean box (*dxdxd*), DANS Project, AU, 2009
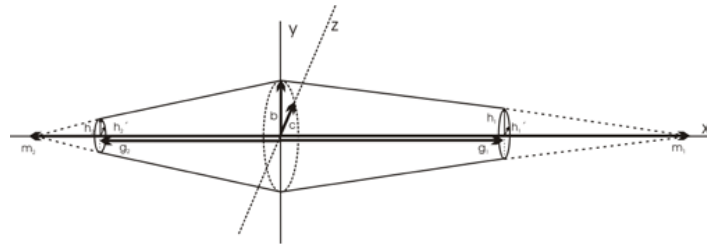
Model 4 – Combination of two cone frustums

Figure and label from: (Sykorova, Sarka, Bubnik, Schejbal, & Dostalek, 2009)

Figure 1.25: Feret bounding box (left) and analytic cone frustrums bounding model (right)

The following bounding metrics are likely to be relevant for geometrical bounding of natural geometries.

- Feret diameters[15]: $\{d_F\}$
- MinFeret: $d_{F_{max}} = \min\{d_F\}$
- MaxFeret: $d_{F_{min}} = \max\{d_F\}$
- Feret elongation: $d_{F_{max}} / d_{F_{min}}$

In image analysis it is common practice to use bounding rectangles. For analysis of 3D objects, bounding boxes $(a \times b \times c)$ are used, see Figure 1.25 (left). The Feret bounding box is defined by the following operations: First the overall MaxFeret diameter defines the first bounding dimension *a*, which then defines the first local coordinate of a Cartesian frame, i.e. $a \to x$. Then, the overall MaxFeret diameter of all cross-sections normal to the x-dir. defines the second bounding dimension *b* and thereby the second Cartesian coordinate direction, i.e. $b \to y$. Finally, the third bounding dimension *c* is defined as the MaxFeret in the third direction *z*. The measured size in terms of its geometric mean box (in yellow) is illustrated.

Parameters of analytic geometries are sometimes used as parametric boundings of natural objects, see Figure 1.25 (right). "Model 4" illustrates an analytic combination of two cone frustums out of a total of four models*. These models were used in a study by (Sykorova et al., 2009) that looked at the size distribution of barley kernels. It was concluded that "Model 4" provided the best approximation of the volume with all cultivars when the measured average crease depth was taken into consideration.

*("Model 1" - Symmetric combination of two parts of general ellipsoid and two cone frustums, "2" - Asymmetric combination of two parts of general ellipsoid and two cone frustums, and "3" - Combination of two parts of general ellipsoid and cone frustum).

---

[15] Feret diameter and various other measures of the size of irregularly shaped particles seen under a microscope are described in details by (Walton, 1948). Technically, the Feret Diameter is found at each identified point of the outher boundary of any geometry as the maximum distance from the actual point to all other points. The max/min Feret is the max/min distance between the set of all these Feret diameters.

In 3D geometry, the location of a point on a tortuous surface S_τ is defined by a vertex $\mathbf{V} \in \Re^3$, which is a vector in a global Cartesian reference frame $\{\mathbf{e}_X, \mathbf{e}_Y, \mathbf{e}_Z\}$. In the following section, two local frames of unit vectors, known as the Frenet-Serret frame and the Darboux frame for tortuous curves C_τ, are introduced. These classical frames are used in differential geometry to describe the orientation of tortuous curves embedded in surfaces S_τ. The French mathematicians Jean Frédéric Frenet (1816-1900) and Joseph Alfred Serret (1819 -1885) are referred to as co-discoverers of the Frenet-Serret formulas. In the following discussion, the Frenet-Serret formulas and derived Frenet-Serret concepts are referred to by the name 'Frenet' only and symbolized by $\{F\} = [\mathbf{T} \quad \mathbf{N} \quad \mathbf{B}]^\top$ (Ghommam, Mnif, Benali, & Derbel, 2009). A similar notation $\{D\} = [\mathbf{T} \quad \mathbf{t} \quad \mathbf{u}]^\top$ is used to indicate an orthonormal right-handed Darboux frame, which was originally introduced by the French mathematician Jean-Gaston Darboux (1842-1917). Although these frame notations are conceptually similar, they are not to be confused.

In this paper the Frenet notation is used solely. At a particular location $\mathbf{V}^*$ of an embedded curve $C_\tau \subset S_\tau$, the unit vectors $\mathbf{T}, \mathbf{N}, \mathbf{B}$ are assumed to form a triple of local basis vectors $\{\mathbf{e}_1^{\{F\}}, \mathbf{e}_2^{\{F\}}, \mathbf{e}_3^{\{F\}}\} = \{\mathbf{T}(\mathbf{V}^*), \mathbf{N}(\mathbf{V}^*), \mathbf{B}(\mathbf{V}^*)\}$ which defines the orientation of the embedded curve C_τ at $\mathbf{V}^*$. The triple of unit direction vectors is formed by: the tangent $\mathbf{T}$, the principal normal $\mathbf{N}$, and the binormal $\mathbf{B}$. The triple is sometimes called a trihedron and denoted as $\mathbf{TNB}$. In general, the triple is evaluated at a particular point $\mathbf{V}^* = C_\tau(s(t^*))$ of a tortuous space curve $C_\tau(s)$, defined by a parametric arc length function $s = s(t)$. By default, the normal $\mathbf{N}$ of a trihedron is said to define an instantaneous inward normal of C_τ at $\mathbf{V}^*$.

Frenet-Serret	Darboux

$$\{F'\} = \begin{bmatrix} \mathbf{T}' \\ \mathbf{N}' \\ \mathbf{B}' \end{bmatrix} = \begin{bmatrix} 0 & \kappa_\tau(s) & 0 \\ -\kappa_\tau(s) & 0 & \tau_\tau(s) \\ 0 & -\tau_\tau(s) & 0 \end{bmatrix} \begin{bmatrix} \mathbf{T} \\ \mathbf{N} \\ \mathbf{B} \end{bmatrix} \quad (1.4)$$

where
  $\kappa_\tau(s) > 0$ is the Frenet curvature and
  $\tau_\tau(s)$ is the Frenet torsion

$$\{D'\} = \begin{bmatrix} \mathbf{T}' \\ \mathbf{t}' \\ \mathbf{u}' \end{bmatrix} = \begin{bmatrix} 0 & \kappa_g(s) & \kappa_n(s) \\ -\kappa_g(s) & 0 & \tau_r(s) \\ -\kappa_n(s) & -\tau_r(s) & 0 \end{bmatrix} \begin{bmatrix} \mathbf{T} \\ \mathbf{t} \\ \mathbf{u} \end{bmatrix} \quad (1.5)$$

where
  $\kappa_g > 0$ is the geodesic curvature,
  $\kappa_n > 0$ is the normal curvature, and
  τ_r is the relative torsion (geodesic torsion)

The following relation rotates the Frenet frame into the Darboux frame

$$\begin{bmatrix} \mathbf{T} \\ \mathbf{t} \\ \mathbf{u} \end{bmatrix} = \begin{bmatrix} 1 & 0 & 0 \\ 0 & \cos\theta & \sin\theta \\ 0 & -\sin\theta & \cos\theta \end{bmatrix} \begin{bmatrix} \mathbf{T} \\ \mathbf{N} \\ \mathbf{B} \end{bmatrix} , \quad\quad\quad (1.6)$$

where θ is the unique angle which rotates $\mathbf{N}$ and $\mathbf{B}$ around $\mathbf{T}$ into $\mathbf{t}$ and $\mathbf{u}$ respectively. The Darboux vector $\mathbf{t}$ is the tangent normal and $\mathbf{u}$ the unit normal.

1.3.3.4   Frenet Curvature and Torsion

The Frenet curvature κ_τ is a measure of the rotation of the Frenet frame about the binormal **B**, whereas the Frenet torsion τ_τ measures the rotation of the Frenet frame about the tangent **T**. When the Frenet curvature and Frenet torsion are simple numbers; the 3D path defined by the Frenet-Serret equations forms a helix. If the torsion is positive, the helix is said to be right handed and left handed if the torsion is negative.

The curvatures used in the Frenet-Serret equations often are expressed in terms of their radii as: $\kappa_\tau = \rho_\kappa^{-1}$ and $\tau_\tau = \sigma_\tau^{-1}$, where ρ_κ is the *radius of Frenet curvature,* and ρ_τ is the *radius of Frenet torsion* respectively. Finally, the radius of curvature ρ_κ is the distance between the points called the *center of curvature* $\mathbf{V}_\kappa$, and a given vertex $\mathbf{V}_A$ which is located on the embedded tortuous curve.

$$\mathbf{V}_\kappa = \mathbf{V}_A + \rho_\kappa \mathbf{N} = \kappa_\tau^{-1} \mathbf{N} , \quad \kappa_\tau > 0 \tag{1.7}$$

1.3.3.5   Special Curvatures

In 1874, the French mathematician Marie Ennemond Camille Jordan generalized the Frenet-Serret Formulas to $\Re^n$ and introduced the concept of *generalized curvature.* $\chi_i(s)$, $i = 1,...n$. However, for natural geometries in $\Re^3$, only the first and second generalized curvatures are in use. The first curvature, the conventional Frenet curvature (or simply the *curvature)* is usually denoted by $\kappa_\tau = \chi_i(s)$, $i = 1$. It expresses the spatial rate of change of the tangent in direction of the normal $\kappa_\tau = \mathbf{N} \cdot \mathbf{T}'$. The second curvature, the *torsion*, is denoted by $\tau_\tau = \chi_i(s)$, $i = 2$. It expresses the negative spatial rate of change of the binormal in direction of the normal $\tau_\tau = -\mathbf{N} \cdot \mathbf{B}'$.

It must be mentioned that in conventional differential geometry other curvature metrics are in use. For example, in the neighborhood of a particular point of an analytic regular C^2-surface, an embedded Weingarten map exists (also known as the shape operator) (O'Neil, 1997). It is expressed using; a symmetric (3x3) matrix with a trivial eigenvalue corresponding to the Gauss normal; and two non-trivial eigenvalues defining the two *principal curvatures* κ_1, κ_2 oriented by the principal directions of the corresponding eigenvectors.

In relation to curvature invariance (see 2.2.12.5), it must also be emphasized that the *mean curvature* $\kappa_M = (\kappa_1 + \kappa_2)/2$ is not invariant to isometric scaling, whereas the *Gaussian curvature* $\kappa_G = \kappa_1 \kappa_2$ is. The Frenet curvature κ_τ is not invariant to isometric scaling either.

For further details on embedded Weingarten map and its implications on subdivision surfaces see (Peters & Reif, 2008). However, in relation to irregular geometry modeling in this study, only the first generalized curvature and the second generalized curvature will be included.
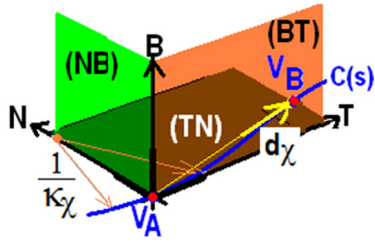
Figure 1.26: Frenet planes

Individually, the Frenet vectors can be interpreted as normals to three planes, called the *Frenet planes*, see Figure 1.26. Each of these Frenet planes is fully defined if only a single pair of Frenet vectors is given.

The special Frenet symbols, names and orthogonality characteristics are listed hereafter for convenience.

- $\{F\}^{N\times B}$ - The *normal plane* (NB) spanned by **N** and **B** perpendicular to **T** .

- $\{F\}^{B\times T}$ - The *rectifying plane* (BT) spanned by **B** and **T** perpendicular to **N** .

- $\{F\}^{T\times N}$ - The *osculating plane* (TN) spanned by **T** and **N** perpendicular to **B** .

At each particular point $\mathbf{V}^*$ on a tortuous surface, at least one tangent plane passing through that point is assumed to be definable. In general, many tangent planes with different normals exist at each point on a tortuous surface. In the following discussion, it is assumed that any Frenet rectifying plane $\{F\}^{B\times T}$ represents a particular plane amongst these tangent planes. In other words, any point $\mathbf{V}^{B\times T}$ on a rectifying plane $\{F\}^{B\times T}$ (see Figure 1.26) satisfies the following equation for a plane having the Frenet normal **N** as normal.

$$\{F\}^{B\times T}: \ (\mathbf{B}\times\mathbf{T})\bullet(\mathbf{V}^{B\times T}-\mathbf{V}^*)=0 \ , \ \ \mathbf{N}=\mathbf{B}\times\mathbf{T} \ \rightarrow \ \{F\}=\{\mathbf{T},\mathbf{N},\mathbf{B}\} \tag{1.8}$$

If the current vertex is designated as $\mathbf{V}_A = \mathbf{V}^*$ and a new vertex as $\mathbf{V}_B$ in the near neighborhood of A , then point B is said to be located in the positive direction of the embedded curve if its arc length function $s = s(t)$ increases from A to B . This implies that a positively oriented chord direction vector $\mathbf{d}_\chi$ exists which defines the new vertex $\mathbf{V}_B$ from the current vertex $\mathbf{V}_A$ as

$$\mathbf{V}_B = \mathbf{V}_A + \mathbf{d}_\chi \tag{1.9}$$

For an illustration of this chord direction vector $\mathbf{d}_\chi$ see Figure 1.26. Also, note the illustration of the first generalized curvature χ_1, i.e. the Frenet curvature $\kappa_\tau = \chi_1$. This curvature represents the reciprocal radius of curvature in the osculating plane (TN). This means that Frenet curvature is a direct measure for the shape variations along embedded curves.

1.3.3.7   Shape Metrics

Shape metrics are often used to characterize volumetric shapes such as: stone particles, grains, natural landscapes and others (Ahmadi et al., 2009; Fératlégil-Durmus et al., 2010; Sykorova et al., 2009; Mohsenin, 1970; Wadell, 1935). Some metrics that characterize the irregular distribution of point clouds, curve segments, and surfaces are given below.

Point, pixels or voxels distribution metrics

- Lacunarity and fractal dimensions λ_ε and D_f

*For further details on lacunarity and fractal dimensions as descriptors for the complex geometry of natural world landscapes see (Kirkpatrick & Weishampel, 2005). Various fractal dimensions are in use: Hausdorff–Besicovitch dimension D_H, the Minkowski–Bouligand dimension D_M, Rényi dimension D_α and others.

Curve segment distribution metrics

- Curve segment length (arc-length): L_τ
- Chord length[16]: l_χ
- Tortuosity, the distance metric (arc-chord ratio) : $\tau = L_\tau l_\chi^{-1}$

Tortuosity can be defined in a number of ways. However, it always measures the "twist" of a curve segment. In a study by (Hart, Goldbaum, Cote, Kube, & Nelson, 1997), the distance metric tortuosity was subtracted by one, as a result the tortuosity for a straight then becomes zero. In addition, six more tortuosity metrics were introduced to measure retinal vascular twist. The seven metrics were then used to classify the tortuosity of blood vessel segments and the tortuosity of blood vessel networks. One finding was that for automated classification the conventional (distance metrics) showed best performance.
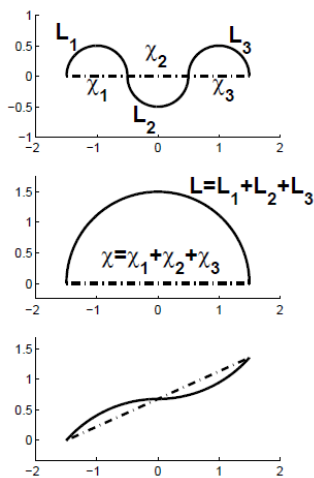
Figure 1.27: Turn Curves

(Grisan et al., 2008) have also proposed a novel tortuosity metric called the tortuosity density. The metric is based the idea of splitting a given 2D curve segment into a number of turn curves and then defining the irregularity as an average of each individual distance metric minus one over the entire segment.

The first two curves (top and middle panel) have very different tortuosity but the same Length L and chord length. The second and last curves (middle and bottom panel) have the same average angular difference despite their different tortuosity. The curve in the bottom panel has a curvature integral of π/2 whereas the one in the middle panel has curvature integral π, even if that in the bottom panel is clearly perceived as more tortuous.

Figure and label: (Grisan et al., 2008)

Note that tortuosity metrics are always constrained by two non-coinciding reference vertices which span the chord.

---

[16] The chord length notation using the Greek lowercase letter Chi as index is adopted from (Grisan et al., 2008).

Sometimes, the tortuosity metrics are also used as an abnormality metric. (Bullitt et al., 2003) measured the tortuosity of the intracerebral vasculature from MRA images and categorized the observed abnormalities into three classes of tortuosity abnormalities: Type I, Type II, and Type III.

It is often difficult to measure the tortuosity. However, some practical methods for measuring the tortuosity from binary or gray-tone tomographic reconstructions have been provided by (Gommes, Bons, Blacher, Dunsmuir, & Tsou, 2009).

Surface distribution metrics

- Shape index[a], (Koenderink, 2003): *SI*
- Sphericity of particle, (Wadell, 1935) $\Psi_\psi = \pi^{\frac{1}{3}} (6V)^{\frac{2}{3}} S^{-1}$
- Estimated sphericity (Mohsenin, 1970) $\hat{\Psi}_\psi = d_\perp d_{F_{max}}^{-1}$
- Circularity[b]: $\kappa_s = 4\pi A_\perp O_\perp^{-2}$

[a] Shape index (SI) is a curvature based number in the range [−1, +1] that is scale invariant. In a study by (Woodard, 2005), a novel approach for personal identification and identity verification using 3D finger surface features as a biometric identifier was proposed. In this work, the *SI* was used in a formula for a normalized correlation coefficient. It was then used to compute a match score.

Table 1.1: Shape Index (*SI*)

Shape index intervals and associated surface classes

Surface type	Interval
Spherical cup	[0, 0.125)
Trough	[0.125, 0.25)
Rut	[0.25, 0.375)
Saddle rut	[0.375, 0.5)
Saddle	[0.5, 0.625)
Saddle ridge	[0.625, 0.75)
Ridge	[0.75, 0.875)
Dome	[0.875, 1.0)
Spherical cap	1.0

Table and Label from (Woodard, 2005)

Also, in this study an explanatory table of the associated shape types with the actual range of *SI*-numbers was given, see reproduced table above. Note that *surface type* refers to a surface segment in $\mathfrak{R}^3$.

[b] Circularity κ_s is a value in the range [0, 1]. Only a circular desk has the value one. Recently, the circularity metric and the tortuosity measure play an important role in the description of a new shape descriptor for asymmetries in distribution of roughness (ADR). Besides circularity and tortuosity, this study also refers to a number of other shape metrics such as: Fourier descriptors; Zernike moments; moment invariants; and specific metrics such as convexity, sigmoidality, orientability and elongation.

As demonstrated, a large number of metrics exist for curve distribution and for the classification of shape patterns. Therefore, inclusion of such metrics in flexible modeling of natural objects is inevitable.

1.3.3.8   Mechanical Properties

Often mechanical properties impact the geometrical properties. A list of such selected mechanical properties, which are often referred to in studies on biomass and soil, is given below[17].

- Mass of kernel (particle mass) : m_Ψ
- Thousand seed weight (TSW): average kernel weight of 1000 kernels
- Estimated mean kernel mass: TSW
- Average bulk density (ABD), ρ_b
- True density of kernel (particle density), ρ_Ψ
- Average true volume: $m_\Psi \rho_\Psi^{-1}$
- Porosity (Mohsenin, 1970): $\phi = 1 - \rho_b \rho_\Psi^{-1}$
- Moisture content: MC
- Fineness Modulus: FM, See (ANSI/ASAE S319.3, 1997)
- : 2.00-4.00 [mm] – Fine aggregates – FM, typically around 3
- : 2.00-8.00 [mm] – Mixed aggregate – FM, typically around 5
- : 4.00-8.00 [mm] – Coarse aggregates – FM, typically around 7

More details can be found on many of these properties in a study by (Ahmadi et al., 2009) on Fennel Seed (Foeniculum vulgare). Ahmadi et al. showed that the dependency between moisture content and many of the geometrical and mechanical properties listed above was significant.

Apart from height and weight, the non-geometric property, *aging* was also included in a novel approach to the manipulation of stochastic phantoms taken by (Baek & Lee, 2012). This was made possible by allowing age to be included as one of the basic input variables for the PCA.

Therefore, novel approaches for modeling of natural objects must be able to handle interactions between various physical properties and the phantom geometry. In other words, new meshing approaches must be generic and flexible by nature!

---

[17] A comprehensive overview of many of the above properties related to seed measurements are found in (Ahmadi, Mollazade, Khorshidi, Mohtasebi, & Rajabipour, 2009).
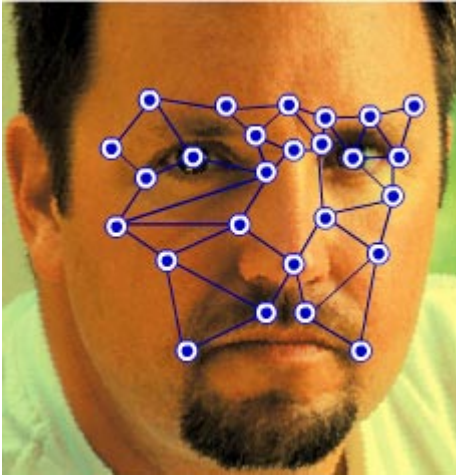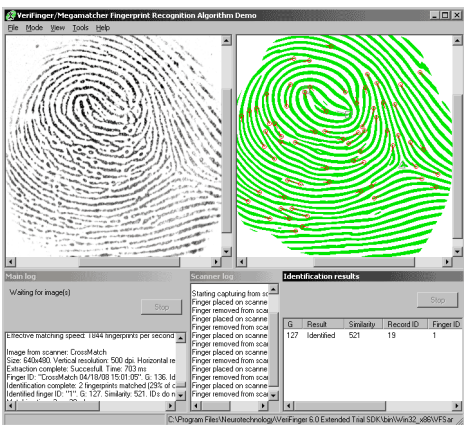
1.3.3.9   Landmarks

Image localized 13-06-2012 at URL:
www.questbiometrics.com/biometric-facial-recognition.html

Figure 1.28: Facial recognition

Sreendump from the VeriFinger®, NEUROtechnology

Figure 1.29: Fingerprint identification

In the following, the term landmark is used to cover biometric identifiers, vector based identifiers, and curvature and torsion based identifiers of natural objects and phenomena. A list dated from 1684 to 2006 of major developments in the theory and practice of biometrics is provided by (Caslon Analytics - biometrics, 2012). From this list the following key biometrics and their applications are extracted and presented in chronological order:

Fingerprints (since 1798), iris-based identification (since 1936), hand and voice identification (since 1976), computer recognition of faces (1977), retinal identification (since 1978) authentication by keystroke timing (since 1980) automatic signature verification (since 1983), Jeffreys' Restriction Fragment Length Polymorphism (RFLP) characterised as 'DNA Fingerprinting' (1984), forensic DNA profiling (since 1985), iris-recognition (1987), palmprint recognition (1998), biometric chips in passports (2005), and biometrics in national access card (2006).

In Figure 1.28, an example on facial recognition is reproduced. Note that this identification relies on facial traits forming a master constellation.

In Figure 1.29. (See 7.2 for a company link), an illustration on fingerprint identification using VeriFinger® is given. Note that the identification relies on location vertices and orientation tangents.

In Figure 1.30 (left), some facial landmarks are illustrated and in (right) A CAESER body scan mesh is shown. A comprehensive data base on anthropometric markers is provided by (CAESER, 2012). Meshing based on landmarks seems to be continously developing and future natural master meshes are likely to be based on an even more extended set of landmarks.
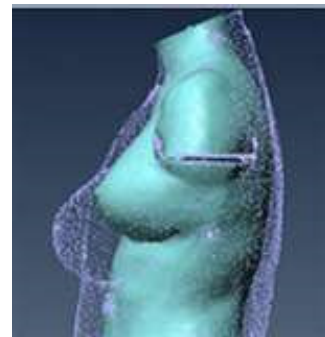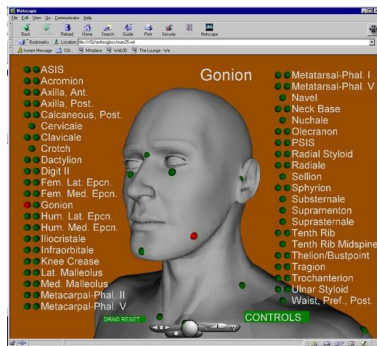

Figure 1.30: Facial Landmarks (left), partial body mesh (right)

LDX images of an osseous specimen with unfused epiphyses used for comparison between LDX and CT measurements, in frontal (left) and lateral (right) views.

Figure and caption from (Gheno, Nectoux, & Herbaux, 2012)

**Figure 1.31: Biometrics of lower extremity**

Biometrics of internatal organs and skeletal parts are also in use. One example is biometrics in the extremities.

In a study by (Gheno et al., 2012), the lower extremity using a biplanar low-dose X-ray (LDX) device in children and adolescents was examined. In two comparative measurements studies between a) LDX 3D and CT 3D and b) LDX 2D and 3D a total of seven biometric identifiers were studied:

- femoral length
- tibial length
- femoral mechanical angle
- femoral neckshaft angle
- tibial mechanical angle
- frontal knee angulation
- lateral knee angulation

It was concluded that: a) The 3D LDX were comparable with 3D CT; b) Differences were observed between LDX 2D and 3D for femoral mechanical angle, femoral neck-shaft angle, and tibial length.

New concepts introduced within stochastic geometry
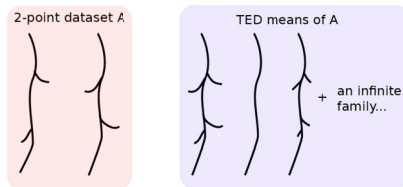
The infinite family of trees on the right are TED[19] means for the set of two trees on the left.

Figure and label from (Feragen et al., 2011)

Figure 1.32: Meshes for tree-studies

Stochastic geometry is a new research field which focuses on the modeling of random shape fluctuations[18]. It is a borderline mix of mathematics and statistics. New properties such as *means in spaces of tree-like shapes* have recently introduced (Feragen, Hauberg, Nielsen, & Lauze, 2011) see Figure 1.32.

Also, studies on point patterns might be a dicipline which can be adopted in Biosystems engineering models. A comprehensive set of notes on spatial point patterns investigated by the free ***R*** software package is provided by (Baddeley, 2010).

In future natural variation, modeling stochastic geometry might be a key player in the development of novel methods to analyze data from advanced bioimaging and for the introduction of statistical landmarks.

---

[18] For a reference list on latest publications and further information on stochastic geometry see *Annual Report* 2011, Centre for Stochastic Geometry and advanced bioimaging (CSGB) located at URL: http://csgb.dk/.

[19] TED is an acronym for (Tree) Edit Distance (Heumann & Wittum, 2009).

1.4 OBJECTIVE

1.4.1 The Research Gap

As described in the introduction, today's scientific stage allows researchers to observe the geometry of natural objects using advanced scanning technologies, and to fit meshes so that they nicely replicate the observed geometry. Advanced meshing approaches are customizable by free-form modeling, and result in surfaces with higher order geometrical continuity. Moreover, the novel Beck-Lee approach provides the opportunity for stochastic phantom modeling where new phantoms are simulated using statistics generated from measurements of full body surfaces. Beck-Lee phantoms are formed using a template so fitted phantoms match one or more mesh constraints such as: height, weight, or age. This simulation approach is state of the art in today's field of advanced phantom generation. It is based on standardized landmarks and full human body templates.

However, natural geometries for walnuts, grass, grains, cracks in soil, or trees, etc. are not smooth at all. They are very complex and are often characterized by rough irregular shapes or hair. Covered surfaces, and their interior, are often made up of tortuous pipes and interconnected sphere-shaped volumes. Even with the use of the most advanced meshing tools it is not an easy task to simulate a walnut, the flow pattern over a grass roof, or the cracks in the bark of a tree. Furthermore, it is not at all possible to simulate meshes in such a way that each new realization is a unique representation of the natural geometry itself. We are currently unable to produce rough phantoms which imitate the stochastic behavior of the underlying natural object in a systematic way.

It is this gap between today's deterministic or semi-deterministic geometry simulations and tomorrows advanced stochastic simulations that are capable of extreme detail, roughness, and flexibility, which are the focus of this study. Obviously, this very ambitious objective cannot realistically be achieved within the time frame of such a study. However, the hope is to contribute piloting algorithms, which will provide the basis for further research in simulation of stochastic phantoms. Such stochastic modeling approaches also point to the need for new mathematical formulations that include natural uniqueness, life-cycle changes, deformable structures, and other un-defined non-linear properties. Ultimately, new geometry generators must be designed as modeling tools for latest multi-physics software and integrated with existing FE algorithms.

1.4.2 Scope

In this study, the objective is to define a unified 3D approach for extraction of parameters from natural geometries for later use in the simulation of stochastic phantoms that imitate the stochastic behavior of a natural object. Methodically, the scope is to adopt and mix theoretical elements from, object-oriented programming, Finite Element Analysis (FEA), biometrics, subdivision, chemometrics, and optimization in a multidisciplinary approach. Coloring and lighting techniques that enhance the expressiveness of phantoms are beyond the scope of this study. The principal formulations are based on calculus of variations for enhanced expressibility and applicability. In the following, spatial descriptions built on fundamental concepts from differential geometry are combined with Cattmull-Clark subdivision. In terms of geometrical completeness, the aim is to include tortuous curves, surfaces, and solids. Curves will be described and illustrated with high degree of detail, and a high number of illustrations; surfaces with some detail, and some illustrations; and solids with little detail and no illustrations.

The key focus of this study is on the modeling and parameterization of *tortuous curves*.

1.4.3 Variables

The quantities that parameterize meshes are considered degrees of freedom variables (DOF-variables). Mesh based models are discretized into domain elements and boundary elements as in standard multi-physics software (like COMSOL® Multiphysics and others). Due to the complexity of the natural objects investigated in Biosystems engineering, the conventional discretization model needs to be extended to include static formulations, and also to support future time-dependent formulations. This means that extra variables need to be included that relate to: clusters and subclusters; as well as group objects and scalar objects such as curvature, torsion, and tortuosity.

1.4.4 Principles and Methods

Since natural objects are unique, direct validation of their imitations is not possible. Therefore, indirect validation, based on measurable indicators, is proposed as an alternative validation strategy. In the extension of such indirect validation, novel decision principles to control the parameter extraction and to handle the stochastic reparameterization are also needed. Beyond this uniqueness problem a further complication is the built-in complexity of natural geometries. A common funding is that natural geometries are highly resolution dependent. This means that the geometry of any natural object usually differs significantly when the object is seen under a microscope compared from when it is observed without magnification. To include this aspect, multiresolution parametric subdivision is chosen to facilitate detailed discretization. However, even though subdivision plays an important role in this study, the theoretical focus is on general parameterization methodology rather than subdivision details.

1.4.5 Strategy

In prolongation of the novel Baek-Lee approach, an alternative generic approach is proposed and described in details. It focusses on parameterization from independent landmark constellations for rough geometries. This approach for rough geometries is intended to be generic in the sense that all scanned objects that exhibit geometric variation from one object to another, or over time, are target for parameterization. The new approach does not intend to explain why some parameter constellations appear as a kind of "geometric DNA". It simply anticipates that such "geometric DNA" constellations are extractable under certain circumstances and that they act as a kind of parametric master template, similar to the human body template used by (Baek & Lee, 2012) . The idea is that these master meshes can be reused later as the source for simulation of look-a-like phantoms.

The outline strategy therefore consists of the following major parts:

- To develop a general methodology for parametric modeling of natural geometries and illustrate general features from 3D meshes in the "Methods" part (chapter 2),
- To apply and validate this parameterization methodology via a case study on one hundred wheat grain cross-sections in the "Results" part (chapter 3),
- To discuss the general approach incl. the case-study experiences, to list some un-answered questions discussion further research and give an outlook in the "Discussion & Outlook" part (chapter 4).
- To summarize general and specific achievements in the "Conclusion" part (chapter 5).

2   **METHOD**

2.1   INTRODUCTION TO METHODS AND PRINCIPLES

2.1.1   Key Aspects

In the following section, a novel approach called "*natural parameterization*" is introduced as a generic method to model geometries of rough natural objects using customizable multiresolution meshes. Smooth computational phantoms have been studied and controlled for decades (Xu & Eckerman, 2010), however, parametric human body shape modeling based on user-defined body size was non-existent until the novel Baek-Lee framework was proposed (Baek & Lee, 2012). Natural parameterization is very much in line with the Baek-Lee approach, however, the geometry modeling of parameterized variations and roughness means that natural parameterization aims at finding a geometric "master mesh" that is able to reflect the objects' "geometric DNA". Therefore, it has a different target. The input data for natural parameterization is gathered by scanning either a whole natural object, or parts thereof, in the same manor used for existing approaches to phantom creation. These input data are used for automatic identification of landmarks, which in turn enable further extraction of size and shape parameters. These extracted parameters are stored in a parametric bank for later stochastic phantom simulation. At the same time, the intention is to let the new parameterization be flexible and customizable. As such, scaling and user-defined size and shape requirements can be included in the simulation process. Abnormality modeling, life-cycles, and growth-modelling, are also enabled. Ultimately, the intention is to model natural uniqueness, growth, and aging in one unified approach.

The uniqueness of natural objects is a key challenge. Technically, two objects which belong to the same class of objects are said to possess the same properties. However, such observed value sets are never identical (except for clones, of course). This means that uniqueness can be perceived as a state-property of a natural mesh. Growth and aging on the other hand are time-dependent processes that require self-adjusting meshes with non-stationary topologies. This means that novel meshing strategies need to be extremely flexible and detailed while still remaining systematic enough to reflect characteristic mean-value processes. These demands are included in the new approach by letting the output mesh be a multiresolution computational phantom that is plausible to expert knowledge. Experts claim that any new phantom simulation belongs to the class of objects that it imitates. Unfortunately, conventional concepts such as the "goodness of fit" or "maximum likelihood," which require template information, cannot be used directly in the effort to measure how well generated unique objects imitate the original. Two new concepts that indirectly address this problem of "likeliness" are included in natural parameterization. The first concept on "goodness of replication" is introduced for parameter extraction based on replication of original objects. It defines how random parameters can be extracted from a single observation mesh. The second concept on "goodness of imitation" is introduced for the

simulation of "look-alike" phantoms from the extracted parameters so that samples of new phantoms (which are all unique) carry the same underlying stochastic behavior as samples of the observed object itself. This ensures that measurements of new unique phantoms will reflect the same stochastic characteristics as the natural objects they imitate. These two rules on "goodness of replication" and "goodness of imitation" constitute the theoretical base for the extraction of parameters as replication phantoms and simulation of new phantoms as imitations.

The newly generated natural imitations must include multi-resolution features to ensure a high level of detail. However, the level of detail is limited by the available input data and the computational capacity. Therefore, new "look-alike" phantoms can be modeled only by a finite number of degrees of freedom as defined by today's finite element analysis. Consequently, this novel approach is based on a finite set of parameters (the objects "geometric DNA") that are first extracted and then later reused for stochastic simulations of new objects.

In other words, the concept of natural parameterization introduces a forward operation for extraction of unique parameters from observations (parameter extraction), followed by a backward operation (reparameterization) that reuses these parameters to simulate "look-alike" phantoms with the same stochastic properties as the natural objects themselves.

2.1.2 Statement of Problem
Following the key aspects outlined in 2.1.1, the following central problems have been identified.

- How are parameters extracted from natural geometries so maximum "goodness of replication" is assured?
- How is reparameterization into "look-a-like" imitations generated with maximum "goodness of imitation"?
- How are such "parameter extraction" and "reparameterization" unified in one generic approach?

2.1.3 Solution Strategy
To answer the central problems defined in 2.1.2, the following strategies have been chosen.

- To properly define the two novel concepts on **"goodness of replication"** and **"goodness of imitation"** in an attempt to solve the two first central problems on parameter extraction and reparameterization as they have been stated in 2.1.2.
- To introduce a set of new algorithms which automate the parameterization and reparameterization process including size, bounding and landmark extraction, multiresolution parametric subdivision, systematic shape parameterization, stochastic decomposition, chemometrics, and Monte Carlo simulation of look-alike phantoms. By merging this set of algorithms into unified **"natural parameterization"** software having observation meshes, and using expert knowledge as input and stochastic phantoms as output an attempt is made to answer the third central problem in 2.1.2.

In the following section, notations are accompanied by illustrations symbolizing generic objects. Illustrations of tortuous geometries are based on vertices and faces generated by the MATLAB® built-in function `ellipsoid` and have been post processed by simple perturbations as described in ANNEX 5. Note that these phantom illustrations have not been generated by the novel subdivision algorithm presented later on.

2.1.4.1   Tortuous Meshes
Natural geometries are modeled by various types of tortuous meshes symbolized as M_τ.
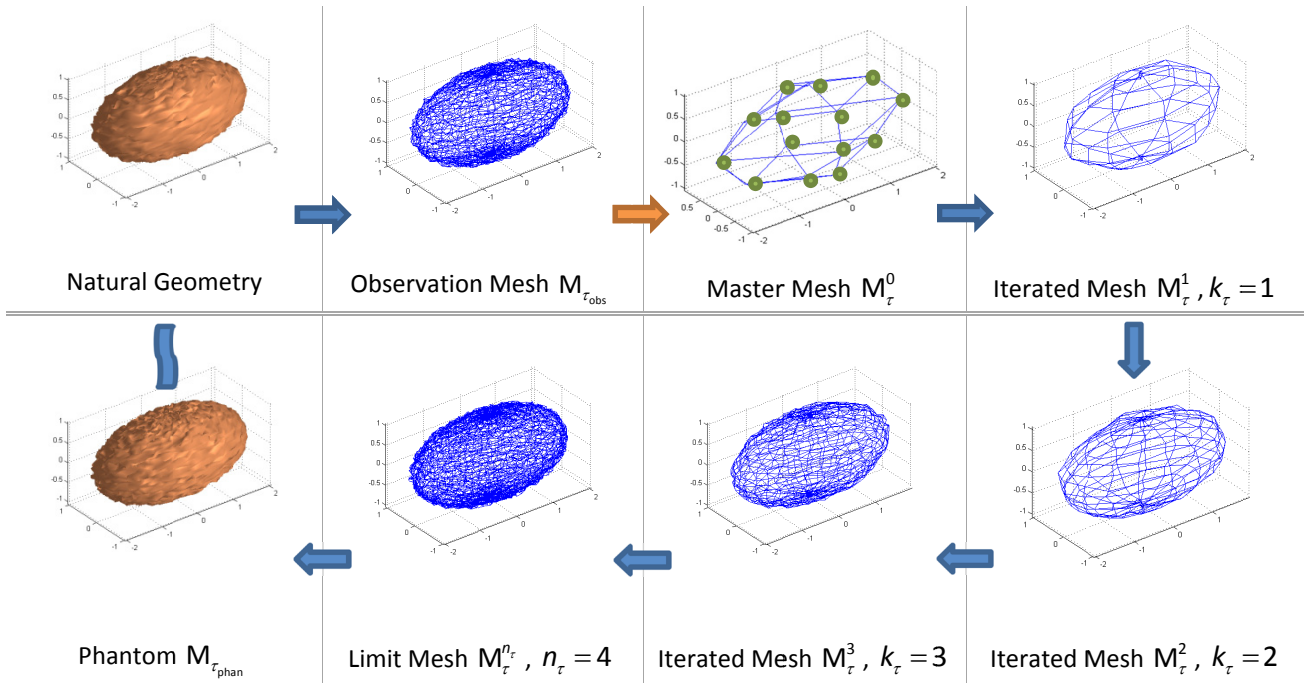
Figure 2.1: Tortuous meshes

The various mesh examples illustrated in Figure 2.1 are commented on in the following section. An observation mesh $M_{\tau_{obs}}$ is a digital representation of a scanned natural geometry. A master mesh M_τ^0 is a coarse parametric representation of the observation mesh, whereas a limit mesh $M_\tau^{n_\tau}$ is a finer representation generated from the master mesh. The level of refinement k_τ reflects the geometry's multiresolution characteristics up to the limit level of refinement n_τ, i.e. $k_\tau = 1,...,n_\tau$. An iterated mesh $M_\tau^{k_\tau}$ is the result of a subdivision process and is defined at intermediate levels of refinement $k_\tau = 1,...,n_\tau - 1$. A limit mesh $M_\tau^{k_\tau}$, $k_\tau = n_\tau$ is transformed into a phantom $M_{\tau_{phan}}$ that includes settings for graphics display such as: coordinate arrays for vertices; topology arrays for faces; as well as color, light and opacity data.

Replication vs. imitation phantoms

A replication phantom is developed to fit a single observation mesh, whereas an imitation phantom is based on reparameterization from a set of random variables or stochastic processes originally based on a sample of the natural geometry. Any phantom is supposed to contain enough information to be materialized into a physical model by a 3D printer or other machines.

2.1.4.2   Tortuous Elements

Geometrically, a mesh is formed by a constellation of mesh elements. These mesh elements can be divided into tortuous domains Ω_τ and tortuous boundaries $\partial\Omega_\tau$. The size of domain elements is symbolized by $\|\Omega_\tau\|$.

| Tortuous Domains Ω_τ | Cluster Σ_Ψ | Subcluster Ω_Ψ | Object/Species Ψ_Ω | Subdomain Ω |

| Tortuous Boundaries $\partial\Omega_\tau$ | Surface $\partial^1\Omega$ **(Tortuous)** | Curve $\partial^2\Omega$ **(Embedded)** | Vector $\partial^3\Omega$ (**Tangent**, **Normal**, **Binormal**) | Scalar $\partial^4\Omega$ **(Length, Curvature & Torsion)** |
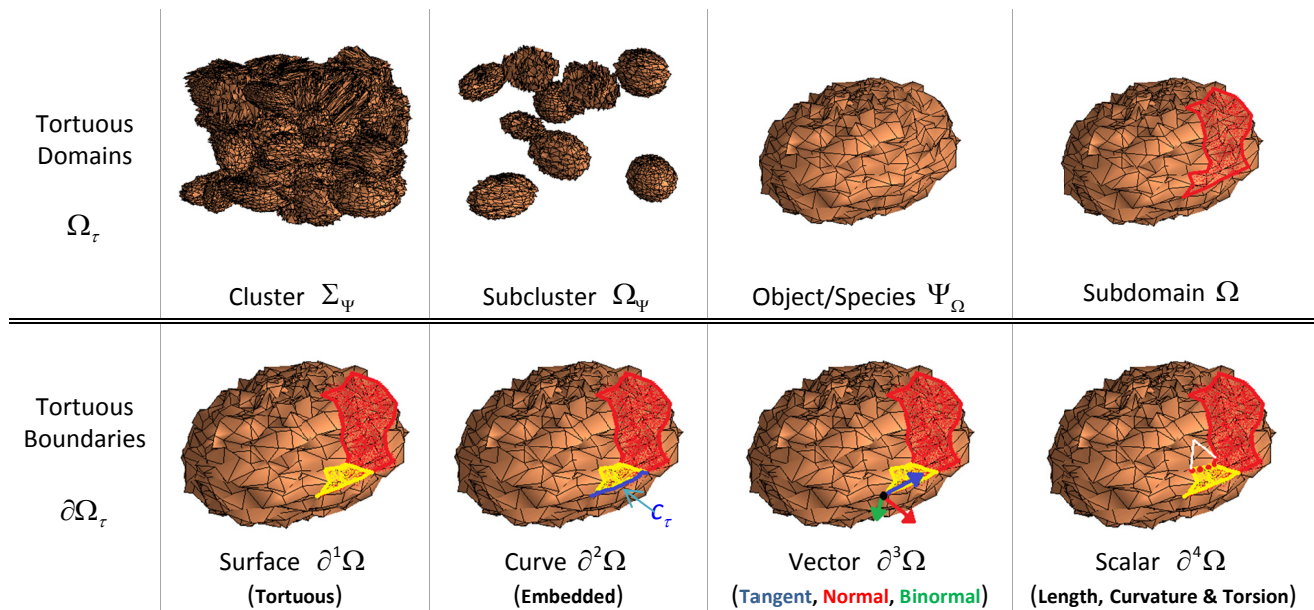
Figure 2.2: Tortuous mesh elements (domains and boundaries)

The element hierarchy presented in Figure 2.2 and Table 2.1 is adopted from COMSOL Multiphysics®3.5a 2011. However, the domain elements; *cluster, subcluster, object/species;* are added as well as the boundary element *scalar*. A scalar measure, called segment curvature, is also added to facilitate segment based subdivision. Furthermore, the boundary element "point" used in COMSOL Multiphysics® is replaced by "vector" to facilitate further distinction into *location vectors* and *orientation vectors*. In COMSOL Multiphysics®4.2a 2012 the term *subdomain* is changed to *domain*. However, the term subdomain is kept here to emphasize that it is used to subdivide an object/species volume into a finite number of discrete homogenous volume parts. The color codes blue (tangent), red (primary normal), and green (binormal), are adopted from the FE software package STAAD PRO® V8i-2012. They are used to identify the local axis of two-noded 3D members and triangular and quadrilateral plates and solids respectively.

Table 2.1: Classification and identification of mesh elements and their graphical description

Classification		Identification		Description	
Name	**Symbol**	**Name**	**Symbol**	**Discretization element(s)**	**Symbol (Plot)[20]**
Tortuous Domain	Ω_τ	Cluster	Σ_Ψ	Heterogeneous volumes	V^e (patch)
		Subcluster	Ω_Ψ	Homogenous volume subset	V^e (patch)
		Object[21]	Ψ	Heterogeneous subvolume set	V^e (patch)
		Subdomain	Ω	Homogenous subvolume	V^e (patch)
Tortuous Boundary	$\partial^{(\cdot)}\Omega$	Surface	$\partial^1\Omega$	Set of Face elements	F^e (surface/patch)
		Curve	$\partial^2\Omega$	Set of Edge elements	E^e (line/edge)
		Vector	$\partial^3\Omega$	Location vector	$\mathbf{V}$ (marker)
				Orientation vector	$\mathbf{T,N,B}$ (arrow/line)
		Scalar	$\partial^4\Omega$	Segment curvature	κ_χ
				Frenet curvature	κ_τ
				Frenet torsion	τ_τ
		Dimension	$\partial^5\Omega$	Tortuosity	τ
				Lacunarity	λ_ε
				Hausdorff–Besicovitch dimension	D_H
				Minkowski–Bouligand dimension	D_M
				Rényi dimension	D_α

---

[20] Plot functions refer to MATLAB®.
[21] For biological objects the term *object* is sometimes replaced by the term *species*.

Tortuous geometries

In general, tortuous geometries cover non-straight geometries that are either smooth, rough, or mixed smooth-rough.

Solids

Tortuous solids Ω_τ are constellations of volumetric segments V_τ discretized by volume elements V^e. Volume elements themselves are formed by face elements, i.e. $V^e \supseteq F^e$. A subdomain is a parametrically homogenous solid, whereas objects, subclusters, and clusters, are formations of such subdomains.

Surfaces

Tortuous curves $\partial^2\Omega$ are constellations of curve segments C_τ discretized by edge elements E^e. Edge elements are formed by tortuous constellation objects, called bi-meshes $M_{\tau_{bi}}$ (see 2.2.8), i.e. $E^e \supseteq M_{\tau_{bi}}$.

Curves

Tortuous curves $\partial^2\Omega$ are constellations of curve segments C_τ discretized by edge elements E^e. Edge elements are formed by tortuous constellation objects called bi-meshes $M_{\tau_{bi}}$ see 2.2.8, i.e. $E^e \supseteq M_{\tau_{bi}}$.

Location and Orientation Vectors

Vectors $\partial^3\Omega$ are used here solely to model location and orientation.

Location vectors are used for the representation of vertices. A vertex $\mathbf{V}$ is assumed to be an instant representation of a conventional parametric position vector, i.e. $\mathbf{V} = \mathbf{r}(t)$. In FEA, such location vectors are often referred to as nodal points or simply nodes.

Orientation unit vectors $\mathbf{T, N, B}$ are assumed to form a triple $\mathbf{TNB}$ of local basis vectors at a particular location $\mathbf{V}$ of an embedded curve c_τ, i.e. $\left\{ \mathbf{e}_1^{\{F\}}, \mathbf{e}_2^{\{F\}}, \mathbf{e}_3^{\{F\}} \right\} = \left\{ \mathbf{T(V), N(V), B(V)} \right\} = \left\{ \mathbf{T}^{\{F\}}, \mathbf{N}^{\{F\}}, \mathbf{B}^{\{F\}} \right\}$ where the individual vectors are assumed to be Frenet-Serret vectors. The set of Frenet-Serret orientation vectors is assumed to form a local orthonormal system $\mathbf{e}_i^{\{F\}} \cdot \mathbf{e}_j^{\{F\}} = \delta_{ij}$, where δ_{ij} is the Kronecker delta, and each frame is supposed to be right-handed, i.e. $\mathbf{e}_i^{\{F\}} \cdot \left(\mathbf{e}_j^{\{F\}} \times \mathbf{e}_k^{\{F\}} \right) = \varepsilon_{ijk}$, where ε_{ijk} is the Levi-Civita symbol.

When a natural surface is approximated by an analytic differentiable surface, its Frenet normal $\mathbf{N}^{\{F\}}$ is a vector perpendicular to the surface tangent plane at a particular location. When a differentiable scalar function $\tilde{f}_\tau$ in space is used to estimate a family of oriented level surfaces S_τ of $\tilde{f}_\tau$ for $\tilde{f}_\tau = const$, then from classical vector differential calculus the gradient of $\tilde{f}_\tau$ at a particular vertex $\mathbf{V}$ is known to be a normal to that surface. Therefore, a discrete Frenet normal for smooth surfaces can sometimes be thought of as a normal to such a surface tangent plane, i.e. $\mathbf{N}^{\{F\}} \approx -\nabla\tilde{f}_\tau(\mathbf{V}) / \left\| \nabla\tilde{f}_\tau(\mathbf{V}) \right\|$. However, from the point of view of differential geometry,

a tortuous geometry is often characterized by its *discontinuities,* which complicate the direct comparison between Frenet normals of smooth (continous) and rough (discontinuous) surfaces. Therefore, it must be emphasized that in a discrete mesh formulation, a Frenet normal is conceived as an orientation vector for an embedded curve passing through a vertex at that point. Consequently, many such Frenet normals are assumed to exist at the same time at one mesh vertex where different embedded curves pass through.

Scalars

The scalar functions $\kappa_\tau(s)$, $\tau_\tau(s)$, known as the natural equations for curvature κ_τ and torsion τ_τ respectively, are used to represent the variation in orientation. The variation is measured at a certain location of an embedded tortuous curve C_τ defined by the arc length function $s(t)$ at a particular parameter value t, i.e. $C_\tau = C_\tau(s(t))$.

An additional curvature called the segment curvature κ_χ is introduced to assist in the formulation of parametric subdivision, relative to a segment chord of a tortuous curve segment (see ANNEX 6.1). In general, the segment curvature is a Frenet type curvature.

Dimensions

Dimension descriptors such as Hausdorff–Besicovitch dimension, Minkowski–Bouligand dimension, Rényi dimension; and metrics such as tortuosity, lacunarity and others (see 1.3.3) are used to describe the *distribution* of geometric characteristics.

Tortuous Segments

EndEnd

BegEnd
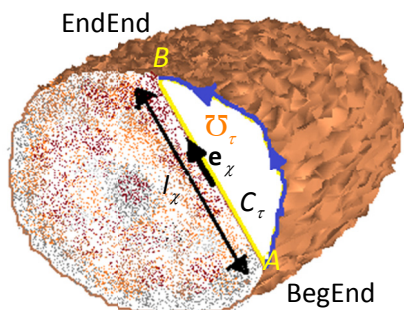
Figure 2.3: Tortuous segment (white)

A tortuous segment is symbolized by $\mho_\tau$. In Figure 2.3 such a planar tortuous segment is illustrated in white. It is defined as a region of a cross-section enclosed by the chord $C_\chi = \overline{AB}$ with length $l_\chi = \left\|\overline{AB}\right\|$, unit direction vector $\mathbf{e}_\chi$ and a directed tortuous curve C_τ. It is directed so that $A = C_{\tau_{BegEnd}}$ and $B = C_{\tau_{EndEnd}}$ [22]. To indicate the segments planar section properties conventional moments of area metrics are used. Typical metrics are area, centroid, centroid moments and principal moments. For further information on such natural indicator metrics for cross-sections see ANNEX 3.

---

[22] The special "BegEnd", "EndEnd" direction notation is taken from the FEM software package STAAD.Pro®V8i - 2012.

In accordance with (ISO 8000-2, 2009), the two set notations $x \in A$ and $A \ni x$ both mean that the member "x belongs to A". However, in the following discussion, both variants are used to emphasize two different kinds of data flow.

The notation $x \in A$ is used for parenting: "The child x is *set* to belong to the parent *A*" i.e. it is not possible to get x before A is created. The notation $A \ni x$ is used for grouping: "The group *A* is formed by the member x", i.e. x must exist before *A* can be created and set.

A similar data flow indication is implied from the two inclusion notations $B \subseteq A$ and $A \supseteq B$. They both mean that the subset B is included in A. The notation $B \subseteq A$ is used to indicate that B is a subset of the declared set A, whereas $A \supseteq B$ indicates that the declared set *A* is extended with, or formed by the subset *B*.

2.1.5   Main Hypotheses

The theory behind natural parameterization is founded on three hypotheses:

- Size and shape of natural geometries might be dependent but uncorrelated.
- Shape can be modeled by tortuous meshes from independent parameters.
- Amongst feasible meshes which all model the same natural shape, the particular mesh that possesses the smallest tortuosity is an extremal.

2.1.6   Principles & Methods

The two key concepts behind natural parameterization, namely the concept of *goodness of replication* and the concept of *goodness of imitation*, are formulated as variational problems (Dacorogna, 2004).

The nature of the first concept on goodness of replication (see 2.2.2) is deterministic. It is used to define an indirect replication method for the extraction of parameters from observation meshes (see 2.2).

The second concept on goodness of imitation is stochastic (see 2.4.3). It is used to control the imitation of new stochastic phantoms as a reparameterization of the extracted parameters.

As a bridge between parameter extraction and reparameterization a stochastic decomposition method is introduced for decomposition of random variables into semi-stationary and fluctuating parts (see 2.3.2). This decomposition is useful for Monte Carlo based stochastic simulation of the natural parameters.

The unified approach comprised of parameter extraction, stochastic decomposition, and reparameterization is the essence of a dedicated set of algorithms, called natural parameterization.

2.2 PARAMETER EXTRACTION

2.2.1 Replication Problems

Obs.:

$$\left\{ M_{obs_{\tau_i}} \right\}, i = 1, ..., n_{obs}$$

Rep.:

$$\left\{ M_{phan_{\tau_i}} \right\}, i = 1, ..., n_{obs}$$
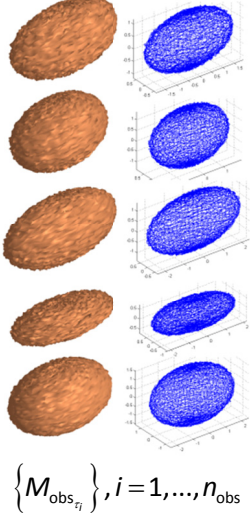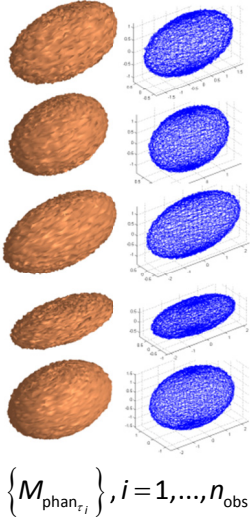
When the efficiency of replication is high it is difficult to differentiate between the observation and the replication meshes.

First, let a sample of n_{obs} objects from an observed class of objects be represented by a set of meses $\left\{ M_{obs_{\tau_i}} \right\}, i = 1, ..., n_{obs}$ in $\mathbb{R}^3$ called observation meshes. Thereafter, let a set of replications be generated as new meshes, called replication phantoms $\left\{ M_{phan_{\tau_i}} \right\}$, i.e. $M_{phan_{\tau_i}} \leftarrow M_{obs_{\tau_i}}, i = 1, ..., n_{obs}$. To measure the goodness of fit, a new measure $\eta_\tau \in [0;1]$ called the *efficiency of replication* is introduced as

$$\eta_\tau = 1 - \varepsilon_\tau ~, \tag{2.1}$$

where the complementary measure ε_τ is called the *fault of replication*.

Next, let a variational problem be defined as to minimize a tortuosity functional J_τ over a tortuous segment $\mho_\tau$ of a phantom M_{phan,τ_i} so the fault of replication ε_τ is constrained by an upper bound $\varepsilon_{\tau,upp}$ and a set of end conditions given by phantom parameters $\left\{ q^0_{M_{phan}} \right\}$ and observation parameters $\left\{ q^0_{M_{obs}} \right\}$.

$$\min J_\tau : \varepsilon_\tau (M_{phan}, M_{obs}) \le \varepsilon_{\tau,upp} \to 0 ~, ~~ \left\{ q^0_{M_{phan}} \right\} = \left\{ q^0_{M_{obs}} \right\} \tag{2.2}$$

Such a problem is called a *replication problem*. The set of meshes which satisfies the constraints in (2.2) are called *feasible replications* of the natural object. Compared to a conventional formulation of a variational problem, (2.2) loosens the stationarity criterion $\delta \{J_\tau\} = 0$ by a limit approach $\lim\limits_{\varepsilon_{\tau,upp} \to 0} \left| \delta \{J_\tau\} \right| \to 0$.

Finally, a particular mesh $\overline{M}_{phan}$ which has the minimum tortuosity τ amongst the feasible meshes with highest efficiency of replication is called a replication extremal to (2.2), i.e. $\overline{M}_\tau$ is a solution to the replication problem and its efficiency of replication is $\eta_\tau = 1 - \varepsilon_\tau (\overline{M}_{phan}, M_{obs})$.

Figure 2.4: Replication meshes are intended to "fit" the observations meshes with high efficiency of replication

In this first study, the definition for the fault of replication ε_τ in (2.2) is related to segment properties and is inspired by conventional CT scanning where sliced data sets are the typical output. These data sets carry information on planar geometries and their cross-sections. Therefore, metrics like moments of area (see ANNEX 3) and other metrics (see 1.3.3) are natural candidates as indicator parameters. A proposal for slice-based fault of replication modeling and its details is given in ANNEX 2.

2.2.2 Goodness of Replication

The concept behind the deterministic criterion outlined in 2.2.1 is referred to as *goodness of replication*. The goodness of replication concept ensures that the selected phantom mesh possesses the lowest tortuosity amongst all feasible meshes, even though other feasible meshes may have even higher efficiency of replication.

In general, feasible tortuous meshes are found by numerical procedures. However, an analytical solution can sometimes be found when the replication problem is simplified into a form called its *ordinary form*.

2.2.3 Ordinary Replication Problems

An ordinary replication problem is a problem where the fault of replication is identically zero. This simplification automatically implies that the stationarity condition must be fulfilled exactly.

$$\varepsilon_{\tau,\text{upp}} \equiv 0 \quad \rightarrow \quad \partial\{J_\tau\} = 0 \tag{2.3}$$

Therefore, an ordinary replication problem only contains equality constraints. In other words, an ordinary replication problem is a conventional variational problem for minimizing a tortuosity functional with a set of equality constraints. This implies that it can be solved with standard procedures from calculus of variations. Consequently, the smoothness criteria required by conventional variational problems must be fulfilled for ordinary replication problems. This smoothness requirement implies that an ordinary tortuosity functional J_τ must be expressed by an Euler-Langrage function of the form $L_\tau = L_\tau\left(\xi, \mathrm{M}_\tau, \mathrm{M}'_\tau\right)$, where variations of first order are taken into account. For an analytic geometry, first order analytic continuity is required $L_\tau \in C^1\left[\xi_A, \xi_B\right]$. For a discretized geometry, first order geometric continuity is required at discrete points $L_\tau \in G^1\left[\xi_A, \xi_B\right]$. However, in both situations the tortuosity functional can be defined by

$$J_\tau\{\mathrm{M}_\tau\} = \int_{\xi_A}^{\xi_B} L_\tau\left(\xi, \mathrm{M}_\tau, \mathrm{M'}_\tau\right) d\xi, \tag{2.4}$$

which is a real-valued functional J_τ with a definition set D_{J_τ}.

This functional represents a mapping from a set of tortuosity functions to the real numbers and is expressed by a definite integral of the mesh and its first derivative.

$$J_\tau \; : \; L_\tau \rightarrow J_\tau\{L_\tau\}, \quad L_\tau \in \mathrm{D}_{J_\tau}, \quad J_\tau\{L_\tau\} \in \mathbb{R} \; . \tag{2.5}$$

For these ordinary replication problems only a set of n equality constraints are relevant, i.e.

$$\int_{\xi_A}^{\xi_B} L_{\mho,i}\left(\xi, M_\tau, M_\tau'\right) d\xi = l_{\mho,i}, \quad i=1,...,n ,$$ (2.6)

where $l_{\Omega,i}$ are scalar constants indicating properties of the considered segment $\mho$.

According to the *fundamental lemma of the calculus of variations* (Dacorogna, 2004), a necessary condition to find a particular solution $\overline{M}_\tau$ amongst all *feasible solutions* M_τ is accomplished if the variation of the tortuosity functional J_τ becomes stationary $\delta\{J_\tau\}=0$ by satisfying the set of simultaneous Euler–Lagrange equations:

$$\frac{dL}{d\overline{M}_\tau} - \frac{d}{d\xi}\frac{\delta L}{\delta \overline{M}_\tau'} = 0 ,$$ (2.7)

where the function L in (2.7) is given by

$$L = L_\tau - \sum_{i=1}^{n_\lambda=1} \lambda_{\mho,i} L_{\mho,i}$$ (2.8)

Note that the extra coefficients $\lambda_{\mho,i}$ are determined from the side conditions.

2.2.4 Dido's Problem and the Reversed Dido's Problem

In the following section (see 2.2.4), some of the key aspects of parameter extraction and reparameterization are given a theoretical perspective by exploring a classical variational problem known as Dido's problem and a variant called the reversed Dido's problem. After this mathematical problem formulation, an analytic solution is derived in 2.2.4.3. Thereafter, as an entrance to numerical solution by parametric subdivision, some simple numerical solutions are briefly defined in 2.2.4.4 and a principle numerical solution is finally presented in 2.2.12.2.

2.2.4.1 Dido's Problem

In the following section, focus is on the classical variational problem known as Dido's problem and a variant called the reversed Dido's problem. The well-known analytical solution to Dido's problem and the solution to the reversed Dido's problem are important to consider because these solutions serve as the basis for numerical solutions. The introduced notation for tortuous meshes defined in 2.1.4 is applied on the classical Dido's problem as well.

Dido's problem is an isoperimetric area maximization problem defined in $\mathbb{R}^2$. Its tortuous subdomain Ω is an area and its boundary $\partial\Omega$ a tortuous curve C_τ. The historical formulation is as follows: "In Virgil's Aeneid, Queen Dido of Carthage must find the largest area that can be enclosed by a curve of fixed length" (Stone & Goldbart, 2002). Mathematically, Dido's problem describes how to maximize the area of a region with a fixed perimeter. Its formulation as a variational problem is often termed the isoperimetric problem (Ashbaugh & Benguria, 2010).
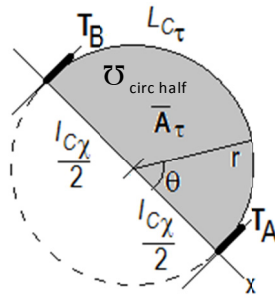
Figure 2.5: The solution to Dido's area-maximization problem is a half circle

Mathematically, Dido's variational problem is defined as finding a particular curve $\overline{C}_\tau$ amongst a set of feasible curves $\{C_\tau\}$ which maximizes the area $\overline{A}_\tau$ (called the functional) between the curve with fixed arc length L_{C_τ} and the chord C_χ with fixed chord length l_{C_χ}.

In a polar (r,θ) coordinate system, with the polar axis parallel to the chord and the pole located at the midpoint of the chord, the planar area A_τ to be maximized is given by the functional

$$J_{A_\tau} = \int_0^\pi \frac{1}{2} r^2(\theta) d\theta \qquad (2.9)$$

and the constraining arc length by

$$L_{C_\tau} = \int_0^\pi \sqrt{r^2(\theta) + r'^2(\theta)} d\theta \qquad (2.10)$$

The problem can be solved by calculus of variations and its well-known solution expresses that the extremals are represented by curves which form circles with tangents $\mathbf{T}_A, \mathbf{T}_B$ perpendicular to the chord at the ends (A,B). The extremal curve $\overline{C}_\tau$ is a half circle $\mho_{\text{circ half}}$.

2.2.4.2   The Reversed Dido's Problem

Now, let Dido's problem be "reversed" in the sense that the "reversed" task is to find a particular curve $\overline{C}_\tau$ amongst a set of feasible curves $\{C_\tau\}$ which minimizes the arc-chord tortuosity given by $\tau = \dfrac{L_{C_\tau}}{l_{C_\chi}}$ when the area A_τ is kept fixed at an observed value A_{obs} between the curve with arc length L_{C_τ} and the chord C_χ with the given length l_{C_χ}.

Furthermore, let the chord ends be bound at the same distance $l_{C_\chi}/2$ to its middle point. The problem is described in rectangular coordinates $x = x(t), y = y(t)$, where t is a parameter. The vector $\mathbf{r} = \mathbf{r}(t) = (x(t), y(t))$ is a position vector representing the points on any feasible curve C_τ.

74
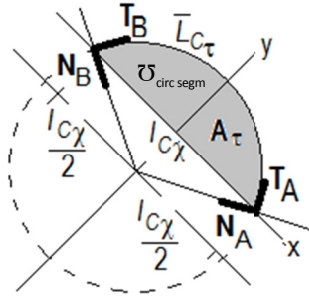
Figure 2.6: The analytic solution to the reversed Dido's problem is a circular segment

The reversed Dido's problem is solved analytically (see 2.2.4.3) as well as by a principle numerical solution, see 2.2.12.10.

2.2.4.3   Analytical Solution to the Reversed Dido's Problem

It is shown in ANNEX 4 that the analytical solution to the reversed Dido's problem which infact is an ordinary replication problem represents a circular segment $\mho_{\text{circ segm}}$ centered at

$$(x,y) = (0, -\sqrt{\frac{1}{\lambda^2 l_{C_\chi}^2} - \frac{1}{4}l_{C_\chi}^2}),$$ (2.11)

where λ is a constant. The extremals are circular segments as expected. However, note that additional geometrical information on the ends of the extremals can be extracted from this solution. At the chord ends (A,B) the curve is specified by its end tangents $\mathbf{T}_A, \mathbf{T}_B$, end normals $\mathbf{N}_A, \mathbf{N}_B$, and embedded end curvatures $(\kappa_A, \kappa_B) = (\kappa_\tau, \kappa_\tau)$.

2.2.4.3.1   Shape Indicators

An additional observation from the analytical solution (2.11) is that geometrically the area A_τ can be regarded simply as a descriptive quantity acting as a shape indicator since it implicitly provides information on whether a solution to the reverse Dido's problem is almost feasible or far away from being feasible. To simulate a feasible geometrical shape of a natural object is by nature impossible since nature is unpredictable. However, some *shape indicators* of the simulated natural geometry (like the area) can be used to indicate whether the simulated shape is feasible or not. It is assumed that goodness of replications is measured implicitly by comparing such indicator values from the replicated meshes with the observed meshes. The differences between such indicator metrics are the segment faults $\varepsilon_{\mho,i}^{k_\tau} \ \forall i \in [1; n_\mho]$. In this study, the indicator metrics $m_\mho$ used are: area, moments of area, perimeter, and other standard cross-section properties. This implicit formulation of goodness of replication is the key stone for the formulation of numerical solutions.

2.2.4.4 Simple Numerical Solutions

Now, a simple solution to a reversed Dido's problem is demonstrated by very simple means. From a numerical point of view, feasible curves $\{C_\tau\}$ can be simulated by any curve generator that enables random perturbations and at the same time fulfills the boundary conditions of the problem. Geometrically, such feasible curves are represented by polyline meshes M_τ.
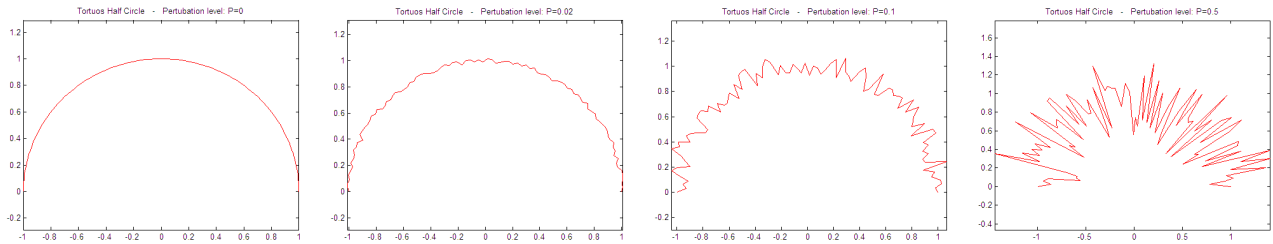
Figure 2.7: The four generated curves are feasible solutions to the reversed Dido's problem of finding a curve with a fixed segment area of π/2 and a chord that equals two.

In accordance with the concept of goodness of replication, the curve (left) is a feasible curve which possesses the smallest tortuosity and a high efficiency of replication. Therefore, it is selected as the extremal, i.e. the numerical solution. Also, it is noted that it converges towards the analytic half-circle solution. Curve generators that include random perturbations can sometimes be realized by very simple Monte Carlo simulations of some iterated parameters of the mesh like the tortuous ellipsoid in 2.1.4.

2.2.4.5 Advanced Numerical Solutions

It must be emphasized that when the concept of goodness of replication is applied on the reversed Dido's problem it ensures that the numerical solution, after a number of iterations, converges towards the analytical solution if the approximating curve[23] has a proper parameterization. Aspects of such advanced parameterizations are defined in the following section.

A novel approach, which intends to include such features, will now be introduced. This novel approach has its roots in the above problem and has been designed so that it is still able find an answer that converges towards the analytical solution of the reversed Dido's problem. Unfortunately, problems including complex geometries such as tortuous curves, surfaces, and solids require advanced numerical solutions that are often difficult to control.

2.2.5 Tortuous Mesh Generators

In this paragraph, focus is on the development of a new subdivision based tool to generate complex tortuous geometries. The strategic approach is to combine classical subdivision theory with a special parameterization technique based on Frenet vectors. The novel mesh engine presented is called *Frenet subdivision* and it is defined as a multi-resolution parametric variant of the classical Catmull-Clark approach. The dedicated purpose

---

[23] For a brief introduction to basic perturbation modeling, see ANNEX 5 where the example-algorithm behind Figure 2.7 is defined. This simple approximating curve is based on a half circle and its perturbations are created as radial variations. However, controlled perturbation modeling of more complex geometries requires extended flexibility and generality of the parametric setup.

for Frenet subdivision is to generate rough geometries that can be manipulated by a set of parameters, which are measurable and intuitive. Furthermore, it is developed to include perturbation modeling as a tool to model extreme conditions such as natural abnormalities. When Frenet subdivision is used in conjunction with the concept of goodness of replication it is finally shown that the novel algorithm iterates a numerical solution to the reversed Dido's problem which matches the analytical solution.

Definitions and outline

A tortuous mesh generator is an algorithm which is able to generate tortuous meshes. For 3D geometries the generators introduced are designed to generate tortuous **curves**, **surfaces** or **solids**. However, most details are put on the tortuous curve generator since it also forms the basis for the surface and solid generators. One milestone is to explicitly include orientation vectors $\partial^3\Omega$ and curvatures $\partial^4\Omega$. In paragraph 2.2.12, a *tortuous curve generator* for edges $\partial^2\Omega$ is defined. Based on this curve generator, paragraph 2.2.13 defines a *tortuous surface generator* for faces $\partial^1\Omega$. Finally, in paragraph 2.2.14, a general *tortuous volume generator* for tortuous domains Ω_τ such as subdomains Ω, species Ψ_Ω, subclusters Ω_ψ and clusters Σ_ψ is introduced. First the various generators are presented in a deterministic formulation. Subsequently, in 2.3 these mesh generators are extended to include stochastic simulations as well. This occurs in conjunction with an introduction of the concept of goodness of imitation 2.4.3. The above geometry generators have a common theoretical basis, which is described in this sub-section. Key elements are tortuosity poles, bi-poles and bi-meshes. In the following subsection the parameterization aspects are described.

2.2.6   Tortuosity Poles
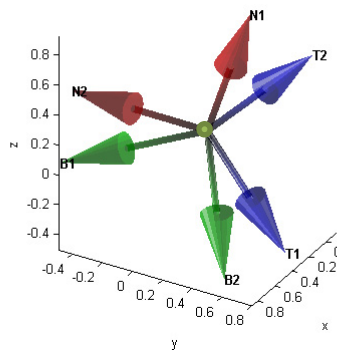
Figure 2.8: Random tortuosity pole located at the origin V= (0, 0, 0) with pole valence equaling two

Let the tortuous boundary $\partial\Omega_\tau$ at a location of a tortuous mesh be defined from vector elements $\partial^3\Omega \supseteq \left\{[\mathbf{V,T,N,B}]^T\right\}$ and scalar elements, i.e. curvatures $\partial^4\Omega \supseteq \{\boldsymbol{\chi}\}$. The superset containing such vector and scalar elements is called a *tortuosity pole* P_τ. A tortuosity pole is therefore a hybrid primitive composed of boundary elements of different order.

$$P_\tau \supseteq \left\{ \partial^3 \Omega, \partial^4 \Omega \right\} \qquad (2.12)$$

Note that the composition of vector elements $\partial^3 \Omega$ of a tortuosity pole, i.e. the quadruple consisting of one location vector and three orientation vectors, is identical to the well-known composition of the Darboux trihedron (or *trièdre*) $\{D\} = \begin{bmatrix} \mathbf{V} & \mathbf{T} & \mathbf{t} & \mathbf{u} \end{bmatrix}^T$ for embedded curves, see (1.5). However, the orientation of a tortuosity pole is not defined from the unit normal and the tangent normal as for Darboux frames but uses the Frenet principal normal vector and the Frenet binormal vector instead. Furthermore, a tortuosity pole does not require all its elements to be present. Algorithmically, a tortuosity pole is simply a dynamic information container which stores one location vector and one or more orientation vectors from a finite number of Frenet frames. Also, their natural equation values (conventional curvature and torsion) taken at that point are stored. The number of Frenet frames that are active during a meshing operation at a current level of refinement is called the *pole valence* $n_{\{F\}}$ at that level.

At minimum, a tortuosity pole must contain one location vector, i.e. a vertex and at least one orientation vector, i.e. a Frenet unit vector. The minimum pole valence is therefore one. The introduced curvature vector $\boldsymbol{\chi}^T = \begin{bmatrix} \kappa_\chi & \kappa_\tau & \tau_\tau \end{bmatrix}$ is formed from the segment curvature $\kappa_\chi \in \delta^4 \Omega$ (see ANNEX 6.2) and the two generalized curvatures $\chi_j \in \delta^4 \Omega, j = 1,2$ derived at the pole vertex for the particular Frenet frame. In the following the notations $\kappa_\chi \in \chi_0$, $\kappa_\tau = \chi_1$ and $\tau_\tau = \chi_2$ are in use for segment curvature, conventional curvature and conventional torsion respectively. The segment curvature supplements the two generalized curvatures $\chi_j \in \delta^4 \Omega, j = 1,2$ and is used for segment based extrapolation of a new pole. Details on the segment curvature can be found in ANNEX 6.1.

The three curvatures $\kappa_\chi, \kappa_\tau, \tau_\tau$, which form the vector $\boldsymbol{\chi}$, are called *curvature coordinates* and are assumed to be given. However, if the segment curvature is not explicitly defined it is estimated (see ANNEX 6.1). In the following discussion, all coordinates encompassed in $\mathbf{V,T,N,B,\chi}$ for a tortuosity pole are therefore referred to simply as the *pole coordinates*. In matrix notation, a tortuosity pole that includes only one Frenet frame, i.e. $n_{\{F\}} = 1$ is conveniently organized into a five-by-three coordinate array.

$$P_\tau = \begin{bmatrix} \mathbf{V}^T \\ \mathbf{T}^{\{F\}T} \\ \mathbf{N}^{\{F\}T} \\ \mathbf{B}^{\{F\}T} \\ \boldsymbol{\chi}^T \end{bmatrix} \qquad (2.13)$$

In general, the pole valence of a tortuosity pole is greater than one. The listing number in which a frame appears in the frame list is called its frame index $f_\tau \in \left[1, \, n_{\{F\}} \right]$.

Simplest form
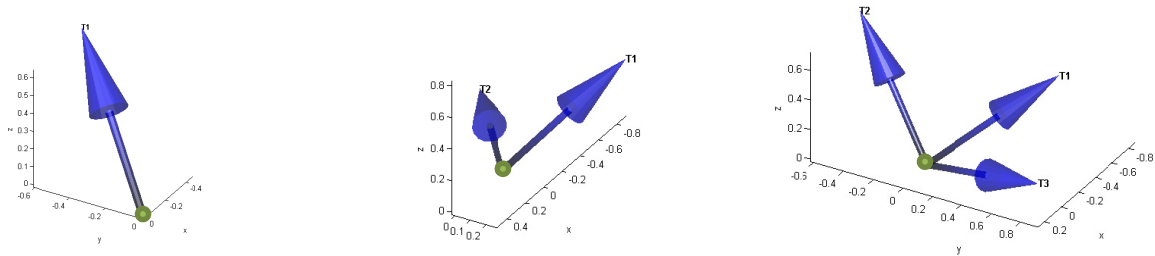
Figure 2.9: Random tortuosity poles in their simplest form with valence=1, 2, 3 (Left, Middle, Right)

When a tortuosity pole is solely defined from its pole vertex **V** and Frenet tangents $\mathbf{T}^{\{F\}}$ it is said to be in its simplest form.

However, still more than one tangent can be included in the pole. In Figure 2.9 three random tortuosity poles with three different pole valences are illustrated.

2.2.7 Bi-Poles

A constellation of two tortuosity poles $P_{\tau,A}$ and $P_{\tau,B}$ is called a bi-pole. A master bi-pole ($k_\tau = 0$) is symbolized as $P^0_{\tau,AB} = \left\{ P^0_{\tau,A}, P^0_{\tau,B} \right\}$. A bi-pole is an oriented constellation since any orientation vector for a Frenet frame $\mathbf{T}^{\{F\}} \mathbf{N}^{\{F\}} \mathbf{B}^{\{F\}} \in \delta^3 \Omega$ bound to a tortuosity bi-pole is said to be "negatively" oriented if its scalar product with the chord direction vector $\mathbf{e}_\chi$ is negative.
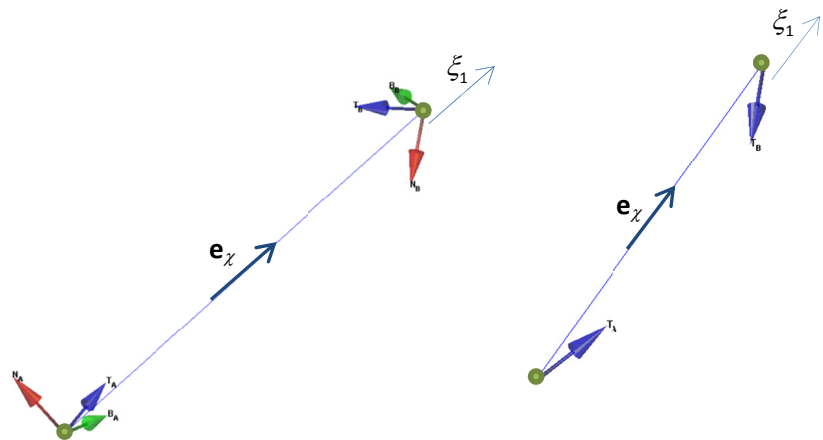
Figure 2.10: Ordinary bi-pole (left). Bi-pole in its simplest form (right)

2.2.7.1   Bi-pole directionality

A bi-pole direction vector $\mathbf{d}_\chi = (\mathbf{V}_B - \mathbf{V}_A)$, see (1.9), controls the positive direction of a local coordinate axis ξ_1 along the segment chord $\overline{AB}$ by a unit chord vector $\mathbf{e}_\chi$ defined as:

$$\mathbf{e}_\chi = \frac{\mathbf{d}_\chi}{\|\mathbf{d}_\chi\|}. \qquad (2.14)$$

Any vector related to a bi-pole is said to be positively directed if its inner product with the chord vector is not negative.

Algorithmically, this positiveness is expressed from a number $r_{\langle,\rangle}$. For an arbitrary Frenet vector, $\mathbf{e}^{\{F\}}$ is defined as

$$r_{\left\langle \mathbf{e}_\chi, \mathbf{e}^{\{F\}} \right\rangle} = \begin{cases} +1, & \left\langle \mathbf{e}_\chi, \mathbf{e}^{\{F\}} \right\rangle \geq 0 \\ -1, & \left\langle \mathbf{e}_\chi, \mathbf{e}^{\{F\}} \right\rangle < 0 \end{cases} \qquad (2.15)$$

EXAMPLE 1   Positive bi-pole tangent

Let a chord unit vector be given as $\mathbf{e}_\chi = \begin{bmatrix} 0 & 0 & 1 \end{bmatrix}$ and a Frenet tangent at a bi-pole EndEnd as $\mathbf{T}_B^{\{F\}} = \begin{bmatrix} \sqrt{2}/2 & 0 & \sqrt{2}/2 \end{bmatrix}$. Then the tangent $\mathbf{T}_B^{\{F\}}$ is said to possess positiveness relative to the bi-pole since the inner product $\left\langle \mathbf{e}_\chi, \mathbf{T}_B^{\{F\}} \right\rangle = \sqrt{2}/2$ is a non-negative number.

2.2.8   Bi-Meshes

Definition: A constellation object formed solely by a master bi-pole $P_{\tau,AB}^0 = \left\{ P_{\tau,A}^0, P_{\tau,B}^0 \right\}$ and two frame indices $\left\{ f_{\tau,A}^0, f_{\tau,B}^0 \right\}$ is called a master bi-pole mesh $M_{\tau,bi}^0 \ni \left\{ P_{\tau,AB}^0, f_{\tau,A}^0, f_{\tau,B}^0 \right\}$, or simply a *master bi-mesh*. Furthermore, an *iterated bi-mesh* $M_{\tau,bi}^{k_\tau} \ni \left\{ P_{\tau,AB}^{k_\tau}, f_{\tau,A}^{k_\tau}, f_{\tau,B}^{k_\tau} \right\}$ is the outcome of a subdivision process and defined at a specific level of refinement k_τ.

In FE terminology, such a bi-mesh constitutes a two-noded element where the poles $P_{\tau,A}^0$ $P_{\tau,B}^0$ are said to be located at the "BegEnd" *A* and the "EndEnd" *B* respectively. From a subdivision point of view bi-meshes serve as the source to iterate new tortuosity poles, i.e. $M_{\tau_{bi}}^{k_\tau - 1} \rightarrow P_{\tau_{bi}}^{k_\tau}$, $\forall k_\tau$.

This iteration process and its requirement for adjustment of sign of tangents is described hereafter.

The following bi-meshes are assumed to be locally end convexive. This means that their end normals always show positiveness relative to the bi-mesh.

$$r_{\left\langle \mathbf{e}_\chi, \mathbf{N}_A^{\{F\}} \right\rangle} \equiv r_{\left\langle -\mathbf{e}_\chi, \mathbf{N}_B^{\{F\}} \right\rangle} \equiv +1 \, . \tag{2.16}$$

However, when applying the Frenet-Serret formulas on tortuosity bi-mesh based extrapolation, see ANNEX 7, the Frenet frames are adjusted so the orientation tangents are also positive.

This means that any tangent is directed so it has a positive projection on the bi-mesh chord. The adjustments are defined as:

$$\mathbf{T}_A = r_{\left\langle \mathbf{e}_\chi, \mathbf{T}_A^{\{F\}} \right\rangle} \mathbf{T}_A^{\{F\}}, \quad \mathbf{T}_B = r_{\left\langle -\mathbf{e}_\chi, \mathbf{T}_B^{\{F\}} \right\rangle} \mathbf{T}_B^{\{F\}} \tag{2.17}$$

$$\mathbf{N}_A \equiv \mathbf{N}_A^{\{F\}}, \quad \mathbf{N}_B \equiv \mathbf{N}_B^{\{F\}} \tag{2.18}$$

$$\mathbf{B}_A = \mathbf{T}_A \times \mathbf{N}_A, \quad \mathbf{B}_B = \mathbf{T}_B \times \mathbf{N}_B, \tag{2.19}$$

These adjusted vectors are called bi-mesh orientation vectors. In Figure 2.9 the illustrated bi-mesh is identical to its corresponding bi-mesh since its tangent and normal vectors need no adjustments.

The illustration (left) represents a general bi-mesh whereas the illustration (right) represents a bi-mesh in its simplest form.

2.2.8.2   Frame formation from a rectifying vector

In situations where a full frame with normal and binormals is required, it can alternatively be formed from its simplest form by a rectifying vector $\mathbf{d}_C$ as

$$\mathbf{N} = -\left(\mathbf{T} \times \mathbf{d}_C \right) / \left\| \left(\mathbf{T} \times \mathbf{d}_C \right) \right\|, \quad \mathbf{B} = \mathbf{T} \times \mathbf{N} \tag{2.20}$$

Note that the rectifying vector used must not be parallel to the tangent.

2.2.9   The Recurrence Relation

$M^0_{\tau_{bi}}$
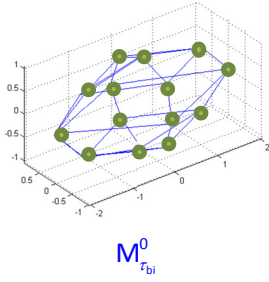
In this paragraph a parametric recurrence relation algorithm which is able to iterate tortuous bi-meshes $M^{k_\tau}_{\tau_{bi}}$ in $\mathbb{R}^3$ from master bi-meshes $M^0_{\tau_{bi}}$ in $\mathbb{R}^3$ is introduced. In general, this algorithm is able to generate tortuous meshes which model curves, surfaces, solids or mixed geometries when dedicated subdivision rules are applied. However, the simplest bi-mesh variant which is described first in this paragraph generates tortuous curves only.

Mathematically, the algorithm having as central part the following recurrence relation:

$$M^{k_\tau}_{\tau_{bi}} = S^{k_\tau}_{\tau_{bi}} M^{k_\tau -1}_{\tau_{bi}} \qquad (2.21)$$

The notation used in (2.21) is taken and combined from (Warren & Schaefer, 2004) and (Zorin, 2006). Specifically, in this relation the iterations are initiated from a *master bi-mesh* $M^0_{\tau_{bi}}$ with adjusted bi-mesh vectors, see (2.17) to (2.19). The master mesh is assumed to be parametrically generated from its master parameters before the iteration process (2.21) is started.

The iterations in (2.21) are said to "run" over $k_\tau = 1, ..., n_\tau$ and to "terminate" at the limit level of refinement n_τ.

Recursively, it predicts new tortuosity bi-poles from preceding tortuosity bi-meshes and adjusts them into bi-meshes. At each recursion the prediction of new tortuosity poles is based on a sequence of *extrapolations, interpolations* and *pole translations* which are parametrically controlled.

The subdivision operator $S^{k_\tau}_{\tau_{bi}}$ for bi-meshes controls the iterations at any level of refinement and each mesh $M^{k_\tau}_{\tau_{bi}}$ at any intermediate level $k_\tau = 1, ..., n_\tau - 1$ represents a new set of tortuosity poles, bi-poles and bi-meshes. In FE terminology the limit mesh $M^{n_\tau}_{\tau_{bi}}$ for $k_\tau = n_\tau$ is a mesh which includes an ordered set of two-noded edge elements formed by an ordered sequence of vertices **V**. However, it will be shown that a limit mesh $M^{n_\tau}_{\tau_{bi}}$ also can be designed to include **TNB** triples and curvatures **χ**.

Furthermore it will be shown that in terms of geometric continuity a limit mesh $M^{n_\tau}_\tau$ in general possess explicit G^1 continuity and asymptotically G^2 continuity.

The recurrence relation (2.21) is defined to form a multiresolution parameteric approach and operationalized by a new subdivision technique which is built on systematic parameterization. Therefore, the systematic parameterization is described prior to the actual subdivision approach.

2.2.10 Parameterization

The set of parameters that control the recurrence relation (2.21) are, as a whole, called natural parameters. In this subsection all parametrical details for these natural parameters are provided. First, some general parameterization aspects are introduced followed by dedicated parameterization of tortuosity pole based geometries.

To represent the degrees of freedom of any natural geometry, a set of independent parametric quantities q, called natural parameters, are now going to be defined in detail. They define (in full or in part) a multiresolution mesh that is able to model the object with the same underlying stochastic nature as observed from the natural geometry itself since they are extracted from observation meshes M_{obs} of the natural object.

Theoretically, natural parameters are considered generalized coordinates.[24] Their observed values and statistical parameters are assumed to be stored in a parametric bank.

Master parameters and iterated parameters

In (2.21), the subset of natural parameters used to control the master bi-meshes $M_{\tau_{bi}}^0$ are called *master parameters* q^0. The subset used to control the iterated bi-meshes $M_{\tau_{bi}}^{k_\tau}$ are called *iterated parameters* q^{k_τ}. Natural parameters q are formed by master parameters q^0 and iterated parameters q^{k_τ} respectively.

$$q \ni \left\{ q^0, q^{k_\tau} \right\} \tag{2.22}$$

Master parameters q^0 are discussed in detail in paragraph 2.2.10.1 and iterated parameters q^{k_τ} in 2.2.10.3. To allow for customized perturbation modeling, additional sets of modification parameters q_Δ^0 for master parameters and a set $q_\Delta^{k_\tau}$ for iteration parameters are included too. These additional parameters are called *perturbation parameters* and are intended for deterministic or pseudo-stochastic modeling only.

Since natural parameters are an indirect representation of the model they can be regarded as a parametric template of the object. However, the interpretation of such a parametric template is henceforth included in what is understood as a parametric bi-mesh.

During the iteration of a tortuous bi-mesh, i.e. $M_{\tau_{bi}}^{k_\tau} = S_{\tau_{bi}}^{k_\tau} M_{\tau_{bi}}^{k_\tau - 1}$, the subdivision operator $S_{\tau_{bi}}^{k_\tau}$ is first used to control the master mesh $M_{\tau_{bi}}^0$ through master parameters q^0. Thereafter, at subsequent levels of refinement $k_\tau = 1, ..., n_\tau$ it controls the iterated meshes $M_{\tau_{bi}}^{k_\tau}$ by iterated parameters q^{k_τ}.

To provide an immediate overview of master parameters q^0, iterated parameters q^{k_τ}, and perturbation parameters, a list is presented in Table 2.2.

---

[24] In the classical meaning as they were originally introduced in Lagrangian mechanics by Joseph-Louis Lagrange in 1788

Table 2.2: Natural parameters are divided into master, iterated and perturbation parameters

Parametric Main-Classes		Parametric Sub-Classes		Description
Name	**Symbol**	**Name**	**Symbol**	
Master parameters	q^0	q_Δ^0 — Size parameters	$q_{\|\Omega\|}^0$	Used to to control the size through a transformation of observation vertices $\mathbf{V}_{obs} \in M_{obs}$ from global coordinates to centered dimensionless coordinates.
		Landmark parameters	q_P^0	Used to to control location and orientation of master poles P_τ^0 in bounding coordinates $\xi_1^0, \xi_2^0, \xi_3^0$.
Iterated parameters	q^{k_τ}	$q_\Delta^{k_\tau}$ — Location parameters	$q_\xi^{k_\tau}$	Used to control the locations for iterated tortuosity poles $P_\tau^{k_\tau}$ after local axis $\xi_1^{k_\tau}, \xi_2^{k_\tau}, \xi_3^{k_\tau}$ by translations from one location C to another C'.
		Orientation parameters	$q_\chi^{k_\tau}$	Used to define the extrapolation of Frenet frames from segment ends. A subsequent non-parametric bi-mesh interpolation predicts a new tortuosity pole.

The following sections describe master parameters and iterated parameters in two separate paragraphs.

2.2.10.1   Master parameters

Parameterization of bi-meshes $M_{\tau_{bi}}^0$ is the process of redefining the coordinates of the tortuosity poles from a bi-mesh mesh $M_{\tau,bi}^0 \ni \left\{ P_{\tau,A}^0, P_{\tau,B}^0, f_{\tau,A}^0, f_{\tau,B}^0 \right\}$ into a form that is expressible by master parameter q^0. Here, this parameterization is performed by reference, i.e. all tortuosity pole elements are defined relative to a length reference l_{q^0}. Three types of master parameters are used: size parameters (see 2.2.10.2.1), landmark parameters (see 2.2.10.2.2) and master perturbation parameters (see 2.2.10.2.3).
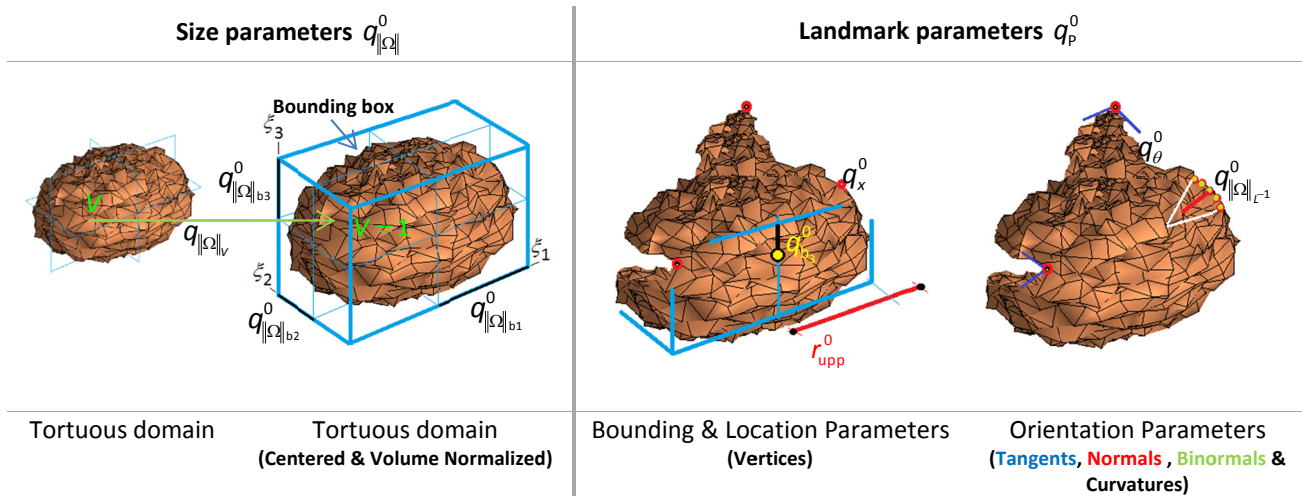
Figure 2.11: Parameterization by size and landmark parameters

A simple length reference called the *upper semi range* is used to achieve non-dimensional references for bounding box based parameterization. This semi range is a nominal length value defined to be bigger than the maximum semi-range of the bounding box found amongst all sample objects, see Figure 2.11. This nominal value, called the upper bounding semi-range r_{upp}^0, is loosely defined by claiming that the probability of exceeding it for any box dimension in any extended sample is very small, i.e.

$$\Pr\left[\max r_{b_i}^0 > r_{upp}^0\right] \to 0 , \quad \forall i \in \left\{1,..., n_{obs}\right\} , \tag{2.23}$$

Where $r_{b_i}^0$ is the observed maximum bounding box dimension for sample object i.

2.2.10.2   Natural parameter range

The upper semi-range is a simple way to let the modeler define the realization limits for natural parameters. In this presentation, natural parameters are defined within one-sided positive ranges $q \in [0,1]$ or double-sided ranges $q \in [-1,1]$.

NOTE   Technically, the modeler can define the upper semi-range by an "n-sigma" definition or as a nominal value. This means that the distributions for natural parameters in principle are finite. However, if the variation of a natural parameter is modeled by an infinite distribution, normalization by upper semi range might exclude extreme value realizations not present in the sample. Therefore, such extreme values resulting from natural abnormalities are intended to be modeled by a separate set of parameters called perturbation parameters. These perturbation parameters are allowed to include values beyond the natural limits through controlled incrementations. In this presentation such perturbation parameters are included in synthetic phantom generations.

2.2.10.2.1   Size parameters

Size parameters $q_{\|\Omega\|}^0$ are introduced to normalize and define the overall size of domain objects (cluster, subcluster, object and subdomain). Size parameters form a sub-set of master parameters, i.e. $q^0 \supseteq \left\{q_{\|\Omega\|}^0\right\}$ and they might be non-linearly related to the shape of the geometry. However, size and shape is assumed to be uncorrelated.

Size normalization parameters

Size normalization parameters are used to normalize vertex coordinates of observation meshes by first integrals, i.e. $\int d\Omega$.

EXAMPLE 2   The well-known first integrals of volume V, cross-section area A and arc length L are:

$$V = \int d\Omega_V = \int_V dV(\xi_1,\xi_2,\xi_3) \quad A = \int d\Omega_A = \int_A dA(\xi_1,\xi_2) \quad L = \int d\Omega_L = \int_C ds(\xi_1) \tag{2.24}$$

Here, and in the following example, such first integrals are assumed to represents regular geometrical properties with non-negative values. In general, observation meshes in $\mathbb{R}^3$ are size normalized by volume. Its volume parameter is therefore defined as

$$q^0_{\|\Omega\|_{V_i}} = \frac{Gx_{j_i}}{V_i^{1/3}} \quad , \quad j \in \{1,2,3\}, \ \forall i , \tag{2.25}$$

where Gx_{j_i} is the jth global coordinate of a vertex from observation mesh $M_{\text{obs},i}$, $i \in \{1, ..., n_{\text{obs}}\}$ with volume V_i. The volume parameter is a simple coordinate scaling factor. However, for observation meshes in $\mathbb{R}^2$ or $\mathbb{R}^1$ the size parameterization can be based on area or arc length references respectively.

$$q^0_{\|\Omega\|_{A_i}} = \frac{Gx_{i,j}}{A_i^{1/2}} \quad , \quad q^0_{\|\Omega\|_{L_i}} = \frac{Gx_{i,j}}{L_i^{1/1}} \quad , \quad \forall i \tag{2.26}$$

This size normalization transfers the geometry from data coordinates in observation space $Gx_j, j=1,2,3$ into dimensionless bounding coordinates $x_j, j=1,2,3$ in parametric space. When curvatures are in use, it must be noted that they are not invariant to isometric size scaling and their physical dimension is L^{-1}.

EXAMPLE 3   Curvatures are reversely scaled.

If a curvature κ is not extracted from a size normalized mesh but from the global mesh then its value in size normalized coordinates can be found from its global coordinates as

$$\kappa_{\text{normalized}} = \frac{\kappa_{\text{global}}}{q^0_{\|\Omega\|}} . \tag{2.27}$$

Dimension parameters

After size normalization the dimensions of the bounding box are usually defined by the half of its length, breadth and height. These dimension parameters are symbolized as $q^0_{\|\Omega\|_{b1}}, q^0_{\|\Omega\|_{b2}}, q^0_{\|\Omega\|_{b3}}$ respectively, and represent simple proportions of the actual bounding dimensions. The bounding box and dimension parameters are illustrated in Figure 2.11. Dimension parameters indicate locale size of bounding dimension in contrast to size parameters, which indicate global size scaling in terms of volume. Sometimes natural geometries are characterized by their dimensions. This means that apart from indicating local dimension, these parameters are also candidates to be used for classification.

In conclusion, it must be emphasized that dimension parameters are simple scaling factors that, in principle, are defined in size-normalized rectangular coordinates $x_j, j \in \{1,2,3\}$. Of course, dimension parameters obtain the same values if they are determined from global coordinates instead.

2.2.10.2.2 Landmark parameters

Landmark parameters q_P^0 are introduced to control the geometric constellation of master poles P_τ^0 from a finite number of degrees of freedom[25]. They represent a sub-set of the master parameters i.e. $q^0 \ni \{q_P^0\}$. In this approach, it is assumed that expert knowledge is used to identify characteristic geometric quantities such as characteristic vertices, Frenet vectors, and curvatures from a set of observation meshes. If the same set of characteristics from every single observation mesh in the sample can be identified, then such characteristics are called landmarks.

NOTE   In the introduction landmarks from iris scanning, finger prints, face recognition and more are mentioned. However, in relation to natural parameters, the identification of landmarks in some situations is solely defined from the convex hull of the natural geometry or from its bounding box. In such situations it is possible to identify landmarks automatically by extreme value identification relative to the convex hull or bounding vertices. Examples of such are landmarks identified by tortuosity poles from the maximum distance to the convex hull and poles where the bounding box is constrained to a normal or poles with extreme curvature or torsion.

Master location parameters

Master location parameters q_x^0 are landmarks that are used to parameterize vertices located on the edge of the bounding box, or those landmarks inside the bounding box. These parameters are defined in rectangular bounding coordinates $x_j, j \in \{1,2,3\}$ as

$$q_{x_j}^0 = \frac{x_{i,j}}{r_{\text{upp}}} \quad , \quad \forall i \ , \ j \in \{1,2,3\}, \quad q_P^0 \ni \{q_x^0\} \quad , \tag{2.28}$$

Where r_{upp} is the upper semi-range. The landmark bounding and location parameters are said to define the vertices of a master mesh by a set of local rectangular dimensionless coordinates $\{\xi_1^0, \xi_2^0, \xi_3^0\}$, referred to as bounding coordinates.

Landmark orientation parameters

In situations where orientation vectors such as tangents, normals, and binormals are useful for parameterization, they can be defined from angular coordinates. Since only unit orientation vectors are considered here, they are defined by spherical coordinates $\theta \in \{1, \vartheta, \varphi\}$. Therefore, these coordinates can be normalized relative to an upper angle semi range

$$q_{\theta,i}^0 = \frac{\theta_i}{r_{\theta,\text{upp}}} \quad , \quad \forall i \ , \quad q_P^0 \ni \{q_{\theta,i}^0\} \ , \quad \theta_i \in (-\pi, \ \pi] \quad , \tag{2.29}$$

---

[25] It is assumed above that landmark parameters are extracted after the origin of the size normalized coordinates is translated to the bounding centroid and the standard `atan2` function is used for the angle determination. Hereby the mean values of the orientation parameters can be restricted to the range from minus one to plus one.

where q_θ^0 are landmark orientation parameters, and $r_{\theta,\text{upp}}$ is the upper angular semi range which is set to $r_{\theta,\text{upp}} = \pi$.
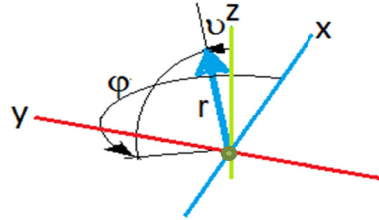
Figure 2.12: Spherical coordinates for orientation vectors

Since orientation is independent of the radial component (see Figure 2.12), only two angle coordinates $\{\vartheta,\varphi\}$ are needed for parameterization of tangents, normals, and binormals.

$$x = r\sin(\vartheta)\cos(\varphi) \tag{2.30}$$

$$y = r\sin(\vartheta)\sin(\varphi) \tag{2.31}$$

$$z = r\cos(\vartheta) \tag{2.32}$$

NOTE   To supplement orientation vectors, curvature and torsion are sometimes relevant as orientation measures. Like orientation vectors, curvature and torsion are also candidates for parameterization by upper ranges. However, in this presentation curvature and torsion are kept as non-normalized parameters derived from osculated circle fitting of embedded curves of the observation mesh.

2.2.10.2.3   Master perturbations

A master perturbation q_Δ^0 is a modification of one, or more, size or landmark parameters. Master parameters are assumed to be modified incrementally as a whole, in groups, or individually. Size normalization and dimension parameters are incremented by size perturbation parameters. Modifications of landmark parameters are performed as translations or rotations for location and orientation parameters respectively. In general, master perturbations are an alternative subset used to customize the master parameters.

Master perturbations allow the modeler to control the master shape and abnormality modeling. It also opens for the opportunity to model time dependent shape changes included in lifecycles, kinematics, and more. In this study, the master parameters are used as customizable design parameters.

Table 2.3: Master Parameters - Overview

Parameter Classification			Parameter Identification		Parameter Description
	Name	**Symbol**	**Name**	**Symbol**	$k_\tau = 0$
S I Z E	size normalization parameters	$q^0_{\|\Omega\|_\Omega}$	length normalization parameter	$q^0_{\|\Omega\|_L}$	Controls the size normalization of geometries in $\mathbb{R}^1$ by a length reference
			area normalization parameter	$q^0_{\|\Omega\|_A}$	Controls the size normalization of geometries in $\mathbb{R}^2$ by an area reference
			volume normalization parameter	$q^0_{\|\Omega\|_V}$	Controls the size normalization of geometries in $\mathbb{R}^3$ by a volume reference
	dimension parameters	$q^0_{\|\Omega\|_b}$	first dimension parameter	$q^0_{\|\Omega\|_{b1}}$	Controls the relative bounding dimension in the first direction
			second dimension parameter	$q^0_{\|\Omega\|_{b2}}$	Controls the relative bounding dimension in the second direction
			third dimension parameter	$q^0_{\|\Omega\|_{b3}}$	Controls the relative bounding dimension in the third direction
L A N D M A R K S	landmark location parameters	q^0_ξ	first master location parameter	$q^0_{\xi_1}$	Controls the location of pole vertices in the first axis direction
			second master location parameter	$q^0_{\xi_2}$	Controls the location of pole vertices in the second axis direction
			third master orientation parameter	$q^0_{\xi_3}$	Controls the location of pole vertices in the third axis direction
	landmark orientation parameters	q^0_θ	first master orientation parameter	$q^0_{\theta_1}$	Controls the orientation of free frame tangents, normals and binormals in the first angle direction
			second master orientation parameter	$q^0_{\theta_2}$	Controls the orientation of free frame tangents, normals and binormals in the second angle direction
P E R T U R B.	landmark perturbation parameters	q^0_Δ	size perturbation parameters	$q^0_{\|\Delta\Omega\|}$	Controls the customization of size
			location perturbation parameters	$q^0_{\Delta\xi}$	Controls the customization of the location of coordinates
			orientation perturbation parameters	$q^0_{\Delta F}$	Controls the customization in orientation of tangent, normal, binormal and curvature coordinates

Table 2.3 gives an overview of the master parameters and their subsets.

2.2.10.3 Iterated parameters

The iterated parameters q^{k_τ} will now be defined as the second subset of the natural parameters, i.e. $q^{k_\tau} \in q$, $k_\tau = 1, ..., n_\tau$. As for master parameters, iterated parameters q^{k_τ} are used to control the location and orientation of the geometry. However, iterated parameters in particular, are designed to control the interior shape spanned by the master poles.

The parameterization of a tortuos curve which is spanned and iterated from a master bi-mesh is now introduced to include up to nine different parameters. Three of theses parameters, which are designed to control the location $q_\xi^{k_\tau}$, are called *iterated location parameters*. The six remaining parameters $q_f^{k_\tau}$ are called *iterated orientation parameters*. The six orientation parameters $q_f^{k_\tau}$ operate with three parameters at each end of the bi-mesh. More specifically, they are associated with a particular frame index of a tortuosity pole. For a bi-mesh they operate at the "begin end" with the frame index f_{BegEnd}, and at the "end end" with the frame index f_{EndEnd}.

2.2.10.3.1 Iterated location parameters

The location of a new tortuosity pole found from a bi-mesh subdivision is assumed to be controlled by the subdivision operator. However, often it is relevant to modify the pole vertices using a set of location parameters. Here, these location parameters, which define simple pole translations, are modeled by a set $q_\xi^{k_\tau}$ of up to three parameters for each level of refinement. More details on parametric location modification are given in ANNEX 11. The iterated location parameters are organized as

$$\mathbf{q}_\xi^{k_\tau} = \begin{bmatrix} q_{\xi_1} & q_{\xi_2} & q_{\xi_3} \end{bmatrix}^{k_\tau}, \quad q \in [-1,1], \quad n_{\text{DOF}} = 3 \tag{2.33}$$

Formally, this set of individual parameters is termed *iterated location parameters,* since they specify the change in location coordinates of a tortuosity pole. However, the idea is to define the iterated location parameters as a control set for the entire iteration process. This is obtained by defining a degrees of freedom array to control the on/off impact at each level of refinement.

$$\xi_{\text{DOF}} = \begin{bmatrix} \xi^1_{1_{\text{DOF}}} & \xi^1_{2_{\text{DOF}}} & \xi^1_{3_{\text{DOF}}} \\ \xi^2_{1_{\text{DOF}}} & \xi^2_{2_{\text{DOF}}} & \xi^2_{3_{\text{DOF}}} \\ . & . & . \\ \xi^{k_\tau}_{1_{\text{DOF}}} & \xi^{k_\tau}_{2_{\text{DOF}}} & \xi^{k_\tau}_{3_{\text{DOF}}} \\ . & . & . \\ \xi^{n_\tau}_{1_{\text{DOF}}} & \xi^{n_\tau}_{2_{\text{DOF}}} & \xi^{n_\tau}_{3_{\text{DOF}}} \end{bmatrix} \tag{2.34}$$

The individual degrees of freedom values are represented as Booleans. Furthermore, to accomplish individual pole translations, each new tortuosity pole should be assigned with its individual length reference l_{q_ξ}, see ANNEX 11.

2.2.10.3.2 Iterated orientation parameters

Iterated orientation parameters are designed to control the orientation of the TNB frame of a new tortuosity pole.

These orientation parameters are formed as a set of up to six iterated parameters $q_f^{k_\tau}$ per bi-mesh, as defined in detail in ANNEX 9.

This six-tuple of parameters is conveniently organized into an array $\mathbf{q}_f^{k_\tau}$, formed by a concatenation of two 3x1 arrays (one from each pole) of a bi-mesh with "TripleTriple" numbers of degrees of freedom.

$$\mathbf{q}_f^{k_\tau} = \begin{bmatrix} \mathbf{q}_{f_A} & \mathbf{q}_{f_B} \end{bmatrix}^{k_\tau} = \begin{bmatrix} q_{\mathbf{T}_A} & q_{\mathbf{N}_A} & q_{\mathbf{B}_A} & q_{\mathbf{T}_B} & q_{\mathbf{N}_B} & q_{\mathbf{B}_B} \end{bmatrix}^{k_\tau}, \quad q \in [0,1], \quad n_{\mathrm{DOF}} = 6 \tag{2.35}$$

The iterated orientation parameters indirectly control the extrapolation of new control-frames during a bi-mesh subdivision process.

In summary, the parameters for the tangent, the curvature and the torsion influence the orientation of the new subdivided poles.

The higher the values for these parameters, the more impact the iterated orientation parameters have on the final TNB orientation. On the contrary, if the orientation parameters are all zero, they have no TNB impact on the orientation of the new pole.

2.2.10.3.3 Iterated perturbations

As for iterated location parameters, an additional set of orientation perturbation parameters $q_\Delta^{k_\tau}$ can be defined at each level of refinement to provide the modeler with tools for modeling synthetic phantoms.

Technically, this process is often identical to location modeling. However, modelers in perturbation modeling are free to design arbitrary parameter values even outside the range defined in (2.33).

An overview of the influence of iterated location and orientation parameters on new iterated subdivision poles is given in the following table.

Table 2.4: Iterated Parameters

Parameter Classification		Parameter Identification		Parameter Description
Name	Symbol	Name	Symbol	$k_\tau \geq 1$
Iterated location parameters	$q_\xi^{k_\tau}$	First iterated location parameter	$q_{\xi_1}^{k_\tau}$	Controls the translation of an iterated pole in the first local axis direction
		Second iterated location parameter	$q_{\xi_2}^{k_\tau}$	Controls the translation of an iterated pole in the second local axis direction
		Third iterated location parameters	$q_{\xi_3}^{k_\tau}$	Controls the translation of an iterated pole in the third local axis direction
Iterated orientation parameters	$q_f^{k_\tau}$	First iterated orientation parameter	$q_{\mathbf{T}_A}^{k_\tau}, q_{\mathbf{T}_B}^{k_\tau}$	Controls the influence from the segment curvature from the ends of a bi-mesh chord
		Second iterated orientation parameter	$q_{\mathbf{N}_A}^{k_\tau}, q_{\mathbf{N}_B}^{k_\tau}$	Controls the influence from the conventional curvature from the ends of a bi-mesh chord
		Third iterated orientation parameter	$q_{\mathbf{B}_A}^{k_\tau}, q_{\mathbf{B}_B}^{k_\tau}$	Controls the influence from the conventional torsion from the ends of a bi-mesh chord
Iterated perturbation parameters	$q_\Delta^{k_\tau}$	Iterated location perturbation parameters	$q_{\Delta\xi}^{k_\tau}$	Controls the customized perturbation of the iterated location parameters
		Iterated orientation perturbation parameters	$q_{\Delta f}^{k_\tau}$	Controls the customized perturbation of the iterated orientation parameters

COMMENTS   The three-tuple of location parameters represented by the array $\mathbf{q}_\xi = \begin{bmatrix} q_{\xi_1}, q_{\xi_2}, q_{\xi_3} \end{bmatrix}$ simply translates the tortuosity pole into a new location in local segment coordinates. This is almost identical to "the local frame at a vertex" introduced by (Tobler et al., 2002). In the original work by (Overveld, 1990), a parameter set including four parameters $\{a, b, \alpha, \beta\}$ for the cubic Bezier curve was introduced. The Overveld parameter b can be compared with q_{ξ_2}. Usually, the parameter q_{ξ_2} is referred to as the control for normal translations and it controls translations directed by the normal. The three-tuple of orientation parameters $q_f = (q_\mathbf{T}, q_\mathbf{N}, q_\mathbf{B})$ at each end controls the influence on the shape from the curvature coordinates included in the tortuosity poles at these ends. The first orientation parameter $q_\mathbf{T}$ controls how much the segment curvature influences the shape in the region between the central part and one of the ends. The Overveld parameter a is comparable with $q_\mathbf{T}$. The second orientation parameter $q_\mathbf{N}$ controls the influence of the conventional curvature close to that end. The third parameter $q_\mathbf{B}$ controls the influence from the conventional torsion near that end. As for master perturbations, the iterated perturbation parameters $q_\Delta^{k_\tau}$ are introduced to accommodate life-cylce modeling and other time or stage dependent phenomena.

2.2.11   Frenet Subdivision

In this paragraph a simple geometric approach for the generation of a new iterated tortuosity pole $P_{\tau,C}^{k_\tau}$ is introduced. First, a geometric construction is introduced to give a simple overview of the vector compositions. A detailed description of the Frenet subdivision algorithm follows.

2.2.11.1   Geometric Construction of Frenet Subdivision

A special property of Frenet subdivision is that it can be defined from a simple vector construction where a new tortuosity pole "C" at the level of refinement k_τ is defined from two existing tortuosity poles "A" and "B" at the previous level of refinement $k_\tau - 1$.
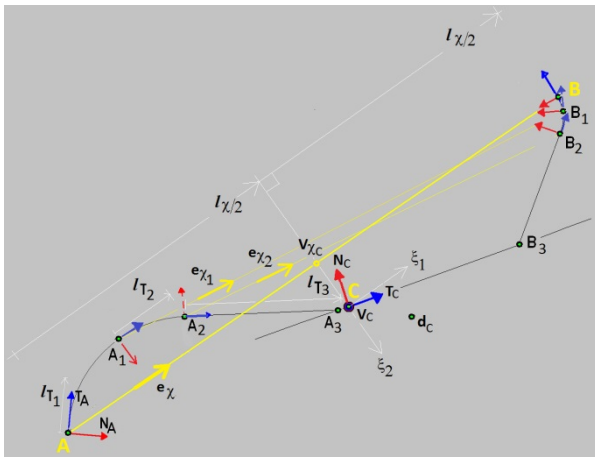
From each end "A" and "B" two new control poles "A1" and "B1" are extrapolated with respect to the torsion and curvature at these ends. Then, from these new poles two more control poles "A2" and "B2" are extrapolated from the curvatures only. Finally, two other control poles "A3" and "B3" are extrapolated from the tangents at "A2" and "B2" respectively. A chord between "A3" and "B3" is then constructed and the orientation **TNB**$_C$ of a new tortuosity pole at "C" is now defined from the direction of the chord and a "rectifying vector" denoted "$\mathbf{d}_C$" using the cross products.

Figure 2.13: Geometric Construction of a new tortuosity pole at "C" between "A" and "B"

Finally, the location vertex $\mathbf{V}_C$ is found as the intersection between the plane through the center of the bi-mesh chord "A1B1" and the new chord "A3B3". This pole location $\mathbf{V}_C$ can then be further translated into a new position C' if desired. From a parametric perspective, the **TNB** extrapolations are controlled by orientation parameters, whereas the **TNB** translations are controlled by location parameters. After this standardized iteration process both orientation and location can be further customized by perturbation parameters.

2.2.11.2   Algorithmic Construction of Frenet Subdivision

Let it be assumed that a bi-mesh $M_{\tau_{bi}}^{k_\tau - 1}$ is given at a "previous" level of refinement $k_\tau - 1$ with chord $\overline{AB}$. Then, a new tortuosity pole $P_{\tau,C}^{k_\tau}$, at a central location C between the chord-planes through A and B, is formed by three successive parametric constructions. This enables multiresolution subdivision and ensures approximate G^2 continuity in the limit. Therefore, the multiresolution subdivision which is going to be defined is a natural descendant of the approach introduced by (Tobler et al., 2002).

However, the approach introduced here includes Frenet-Serret frames explicitly. Infact, this justifies the name Frenet-Serret subdivision which can be even further shortened to "Frenet subdivision".

In brief, the methodic steps which are going to be defined in details in the following can be outlined as:

Multiresolution parametric Frenet subdivision $M_\tau^{k_\tau} = S_\tau^{k_\tau} M_\tau^{k_\tau-1}$

is initiated from a **master mesh** M_τ^0 and at each step $k_\tau \geq 1$ it is iterated by

extrapolations	followed by	**interpolations**	and finalized by	**pole translations**.

➔ After n_τ steps this results in a new **limit mesh** $M_\tau^{n_\tau}$ with asymptotic $\boldsymbol{G^2}$ **continuity.**

➔ This limit mesh can be used for **FEA** or transformed into a graphical representation called a **phantom.**

NOTE   In this setup $S_{\tau_{bi}}^{k_\tau}$ is a multiresolution parameteric subdivision operator, which algorithmically controls the subdivision process at every level.

Multiresolution aspects

In multiresolution iterations, the iterated parameters are applied with different settings at relevant levels of refinement. Multiresolution is in general non-homogenous. However, in special situations (which are in general unlikely for natural geometries) *the same settings* for iterated parameters are applied at all levels of refinement. Such homogenous multiresolution settings are especially usefull in synthetic modeling.

Extrapolations

From each end of the chord $\overline{AB}$ a sequence of parametric extrapolations $A_1 \to A_2 \to A_3$, $B_1 \to B_2 \to B_3$, controlled by the iterated orientation parameters $[q_T, q_N, q_B]^T_{k_{\tau,A}}$, $[q_T, q_N, q_B]^T_{k_{\tau,B}}$, define two new control vertices V_{A3}, V_{B3}, which then form a new chord $\overline{A_3B_3}$. See ANNEX 9 for more details on extrapolations.

Interpolations

The new chord $\overline{A_3B_3}$, and a rectifying direction vector $\mathbf{d}_C$, control the interpolation of a new central tortuosity pole $P_{\tau,C}^{k_\tau} = [V_C T_C N_C B_C \chi_C]^T$. Its subdivision vertex V_C, is defined as the intersection between the normal plane through V_{χ_C} and $\overline{A_3B_3}$. The normal and binormal are defined as $N_C = -T_C \times \mathbf{d}_C \to B_C = T_C \times N_C$, where the vector $\mathbf{d}_C$ lies in the rectifying plane and is called the rectifying vector. To define the orientation vectors it must be a real valued vector non-parallel to the tangent. Unless actual information on the curvatures is available all curvature coordinates of χ_C are set equal to zero, i.e. $\chi_C^{k_\tau} = [0 \quad 0 \quad 0]^T$, $k_\tau = 1,...,n_\tau - 1$. However, the two segment curvatures at the limit level of refinement ($\tilde{\kappa}_{\chi_A}^{n_\tau}$, $\tilde{\kappa}_{\chi_B}^{n_\tau}$) are estimated from osculating circles at any

level. At the limit level of refinement $k_\tau = n_\tau$, the embedded curvature is estimated as their average i.e.

$\boldsymbol{\chi}_C^{n_\tau} = \begin{bmatrix} 0 & \tilde{\kappa}_\tau^{n_\tau} & 0 \end{bmatrix}^T$, $\tilde{\kappa}_\tau^{n_C} = 0.5(\tilde{\kappa}_{\chi_A}^{n_\tau} + \tilde{\kappa}_{\chi_B}^{n_\tau})$. See ANNEX 10 for further details on subdivision pole interpolation.

Pole translations

Finally, the interpolated pole $\mathrm{P}_{\tau,C}^{k_\tau}$ at C is translated into a new location C'. This translation is controlled by iterated location parameters $\begin{bmatrix} q_{\xi_1}, q_{\xi_2}, q_{\xi_3} \end{bmatrix}^{k_\tau}$ at the current level of refinement $k_\tau = 1,...,n_\tau$.

Limit iterations

When pole translations are avoided at the last levels of refinement, i.e. $q_{\xi_1}^{k_\tau} = q_{\xi_2}^{k_\tau} = q_{\xi_3}^{k_\tau} = 0$; $k_\tau \in (..., n_\tau - 3, n_\tau - 2, n_\tau - 1, n_\tau]$, the estimated limit curvature $\tilde{\kappa}_\tau^{n_\tau}$ becomes a better estimate of the target curvature. The estimated pole triple $\mathbf{T}_C \mathbf{N}_C \mathbf{B}_C$ also becomes a better estimate of the target Frenet frame $\mathbf{T}_C^{\{F\}} \mathbf{N}_C^{\{F\}} \mathbf{B}_C^{\{F\}}$ when the number of non-perturbed limit-iterations increases

$$\lim_{n_\tau^- \to \infty} \left(\mathbf{T}_C \mathbf{N}_C \mathbf{B}_C \right)^{n_\tau} \to \left(\mathbf{T}_C^{\{F\}} \mathbf{N}_C^{\{F\}} \mathbf{B}_C^{\{F\}} \right)^{n_\tau}, \qquad \lim_{n_\tau^- \to \infty} \frac{(\tilde{\kappa}_{\chi_A}^{n_\tau} + \tilde{\kappa}_{\chi_B}^{n_\tau})}{2} \to \kappa_\tau^{n_\tau} \qquad (2.36)$$

The corresponding center of curvature $\mathbf{V}_\kappa$, is defined from the second local base vector $\mathbf{e}_{\xi_2}^{n_\tau}$ as

$$\mathbf{V}_\kappa = \mathbf{V}_C - \frac{1}{\kappa_\tau^{n_\tau}} \mathbf{e}_{\xi_2}^{n_\tau}, \; \kappa_\tau^{n_\tau} > 0, \qquad \mathbf{e}_{\xi_2}^{n_\tau} = \frac{\mathbf{V}_C - \mathbf{V}_{\chi/2}}{\left\| \mathbf{V}_C - \mathbf{V}_{\chi/2} \right\|}, \quad \left\| \mathbf{V}_C - \mathbf{V}_{\chi/2} \right\| > 0 \qquad (2.37)$$

In a situation where the curvature is zero, or the central vertex lies on the chord, i.e. $\left\| \mathbf{V}_C - \mathbf{V}_{\chi/2} \right\| = 0$, the second base vector $\mathbf{e}_{\xi_2}^{n_\tau}$ is defined from a prediction rule based on the control poles $\{ \mathrm{P}_{\tau,A3}, \mathrm{P}_{\tau,B3} \}$ or, alternatively, it is generated as a random unit vector not parallel to $\mathbf{e}_{\xi_1}^{n_\tau}$.

Graphical representations

The limit mesh can be used for FEA or transformed into an appropriate[26] graphical representation.

---

[26] In this presentation, curves are plotted by the the MATLAB® graphics objects `line` or by arrows. Later, triangulated surface plots are handled by the MATLAB® `patch` object. Future volumetric displays are planned to be handled by a combination of these two graphics objects or by the dedicated MATLAB® `slice` object.

Construction of subdivision bi-meshes

In this paragraph, details for algorithmic implementation of the Frenet subdivision approach are given.

Algorithmically, at any recurrence level $k_\tau = 1,...,n_\tau$, Frenet subdivision is defined by a non-linear mapping $P_{\tau,C}^{k_\tau} \leftarrow \left\{ P_{\tau,A}^{k_\tau-1}, P_{\tau,B}^{k_\tau-1} \right\}$ as described in Table 6.1 below. The input is assumed to be initiated from a master bi-mesh $M_{\tau_{bi}}^0 \ni \left\{ P_{\tau_A}^0, P_{\tau_B}^0 \right\}$, and the minimum input includes at least one vertex **V** and one tangent **T** at each of the two tortuosity poles $\left\{ P_{\tau_A}^0, P_{\tau_B}^0 \right\}$ as well as an optional rectifying vector $\mathbf{d}_C$. Furthermore, it is assumed that the chord unit vector $\mathbf{e}_\chi$, and the first local axis $\mathbf{e}_{\xi_1}$, coincide i.e. $\mathbf{e}_{\xi_1} = \mathbf{e}_\chi$. The local (ξ_1, ξ_2, ξ_3)-frame forms an orthonormal right handed base i.e. $\mathbf{e}_{\xi_3} = \mathbf{e}_{\xi_1} \times \mathbf{e}_{\xi_2}$.

However, this local frame is first defined after the central interpolation vertex $\mathbf{V}_C$ is found, and before pole translations are applied. The rectifying vector $\mathbf{d}_C$ is used to define the central orientation triple $\mathbf{T}_C \mathbf{N}_C \mathbf{B}_C$. However, if the rectifying vector $\mathbf{d}_C$ it is not defined it can be estimated at the limit level of refinement as $\mathbf{d}_C^{n_\tau} \approx -\mathbf{e}_{\xi_1}^{n_\tau} \times \mathbf{e}_{\xi_2}^{n_\tau}$, see (2.37).

The theoretical background is given in ANNEX 5 - ANNEX 9. Within these annexes, details are given for the nine prediction functions included in parametric Frenet subdivision.

An overview of these nine prediction functions are given here:

Prediction functions	Parametric Scope	
Three extrapolation prediction functions: $\hat{f}_{F_B}$ $\hat{f}_{F_N}$ $\hat{f}_{F_T}$	$\hat{f}_{F_B}\left(q_\mathbf{B}^{k_\tau}\right)$, $\hat{f}_{F_N}\left(q_\mathbf{N}\right)$, $\hat{f}_{F_T}\left(q_\mathbf{T}\right)$	See 2.2.11.3
Three interpolation prediction functions: $\hat{f}_{G^2}$ $\hat{f}_{G^1}$ $\hat{f}_{G^0}$	Non-parametric	See 2.2.11.4
Three pole translation prediction functions: $\hat{f}_{H_1}$ $\hat{f}_{H_2}$ $\hat{f}_{H_3}$	$\hat{f}_{H_1}\left(q_{\xi_1}\right)$, $\hat{f}_{H_2}\left(q_{\xi_2}\right)$, $\hat{f}_{H_3}\left(q_{\xi_3}\right)$	See 2.2.11.5

Briefly summarized, the *extrapolation functions* $\hat{f}_F$, are developed by applying the mean value theorem on the Frenet formulas. The extrapolation functions are used to generate three control poles from each end of a bi-mesh.

The *interpolation functions* $\hat{f}_G$, are defined by geometrical averaging of vectors and used to define orientation and location of a new iterated tortuosity pole.

The *pole translations* $\hat{f}_H$, are defined as simple orthogonal translations of the new pole to obtain a new location. The extrapolation and perturbation prediction functions are controlled by iterated parameters whereas the interpolation is non-parametric.

To initiate a Frenet subdivision process a master bi-mesh is required.

"EndEnd"

"BegEnd"
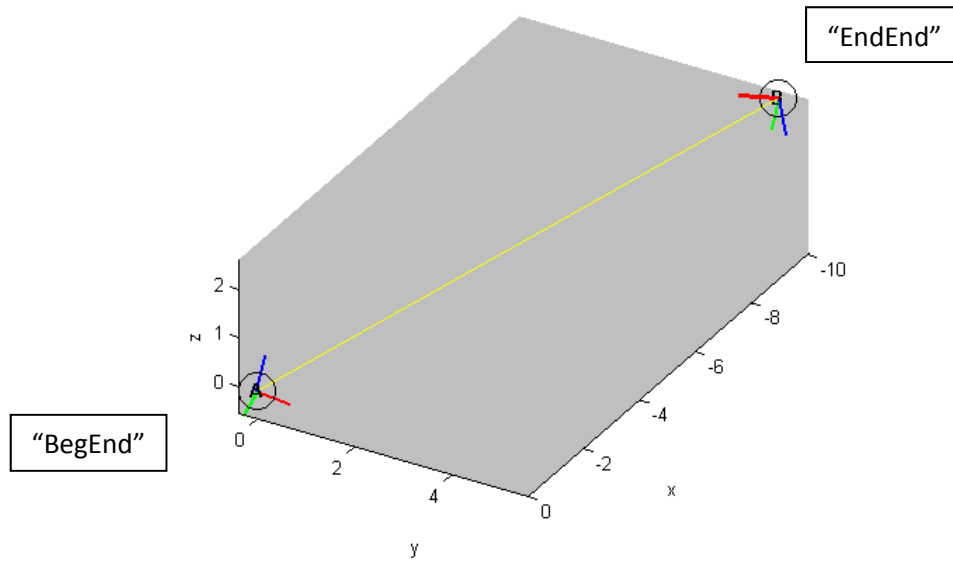
Figure 2.14: Initiation of a parametric bi-mesh subdivision

Figure 2.14 and Table 2.5 illustrate the initiation of a bi-mesh subdivision process, i.e. $k_\tau = 0$.

Note that a bi-mesh is defined by two particular frame indices of the two tortuosity poles respectively. Also note that curvature and torsion are explicitly included in the two selected frames at the BegEnd and at the EndEnd respectively.

Table 2.5: Bi-mesh constellation for a tortuous curve

Edge	Vertex	Frenet vectors	Curvatures	Bi-mesh	Chord	Chord vector
$j=1$	$\mathbf{V}_A$	$\mathbf{T}_{A,1}, \mathbf{N}_{A,1}, \mathbf{B}_{A,1}$	$\mathbf{\chi}_{A,1}$	$M^{k_\tau}_{\tau_{bi}} \ni \left\{ P^{k_\tau}_{\tau,A}, P^{k_\tau}_{\tau,B}, f^{k_\tau}_{\tau,A}, f^{k_\tau}_{\tau,B} \right\}$	$\overline{AB}$	$\mathbf{e}^0_{\chi,1} = \dfrac{(\mathbf{V}_B - \mathbf{V}_A)}{\|\mathbf{V}_B - \mathbf{V}_A\|}$
	$\mathbf{V}_B$	$\mathbf{T}_{B,1}, \mathbf{N}_{B,1}, \mathbf{B}_{B,1}$	$\mathbf{\chi}_{B,1}$			

In the following paragraphs extrapolations, interpolations, and pole translations are defined one by one.

2.2.11.3 Extrapolations

Let a tortuosity master pole at a node A be given as $P_{\tau,A_n}^{k_\tau} = \left[\mathbf{V}_{A_n} \mathbf{T}_{A_n} \mathbf{N}_{A_n} \mathbf{B}_{A_n} \mathbf{\chi}_{A_n} \right]^{\mathsf{T}}$. A prediction rule that

determines a new tortuosity pole $P_{\tau,A_n}^{k_\tau} = \left[\mathbf{V}_{A_n} \mathbf{T}_{A_n} \mathbf{N}_{A_n} \mathbf{B}_{A_n} \mathbf{\chi}_{A_n} \right]^{\mathsf{T}}$ in the neighborhood of A_n, is called a Frenet

extrapolation at the k_τ level of refinement. When a maximum of three successive extrapolations are performed, i.e. $n \leq 3$, the successive extrapolation is called near-field. Otherwise, when $n > 3$, it is called a far-field extrapolation. If the parameterization is based directly on the arc length function, it is called direct Frenet extrapolation. If it is based on quantities that indirectly define the arc length function, then it is called Frenet extrapolation by reference.

Extrapolations defined in this paragraph for bi-meshes are all near-field extrapolations and are based on the six parameters $q_{\mathbf{T}_A}, q_{\mathbf{T}_B}, q_{\mathbf{N}_A}, q_{\mathbf{N}_B}, q_{\mathbf{B}_A}, q_{\mathbf{B}_B}$ previously defined in An overview of the influence of iterated location and orientation parameters on new iterated subdivision poles is given in the following table.

Table 2.4. Furthermore, every single parameterization is applied *by reference* from one of three length references $l_{q_{\mathbf{B},A}}, l_{q_{\mathbf{N},A}}, l_{q_{\mathbf{T},A}}$. The general background theory for Frenet extrapolation and the applied prediction functions is given in ANNEX 9.

In the approach that follows, Frenet extrapolations are represented by three prediction functions $\hat{f}_{F_{\mathbf{B}}}$ $\hat{f}_{F_{\mathbf{N}}}$ $\hat{f}_{F_{\mathbf{T}}}$.

They sequentially generate three new tortuosity bi-mesh estimates $\left(P_{\tau_{A1}}, P_{\tau_{B1}} \right), \left(P_{\tau_{A2}}, P_{\tau_{B1}} \right), \left(P_{\tau_{A3}}, P_{\tau_{B3}} \right)$, from the

two tortuosity master poles $P_{\tau_{A0}}, P_{\tau_{B0}}$. This Frenet subdivision DOF-setup is called "TripleTriple" since it is defined from three parameters at the "BegEnd" and the "EndEnd" respectively.

$$\left(P_{\tau_{A1}}, P_{\tau_{A2}}, P_{\tau_{A3}} \right) = \hat{f}_{F_{\mathbf{T}}} \left(\hat{f}_{F_{\mathbf{N}}} \left(\hat{f}_{F_{\mathbf{B}}} \left(P_{\tau_{A0}}, l_{q_{\mathbf{B},A}} \right), l_{q_{\mathbf{N},A}} \right), l_{q_{\mathbf{T},A}} \right) \tag{2.38}$$

$$\left(P_{\tau_{B1}}, P_{\tau_{B2}}, P_{\tau_{B3}} \right) = \hat{f}_{F_{\mathbf{T}}} \left(\hat{f}_{F_{\mathbf{N}}} \left(\hat{f}_{F_{\mathbf{B}}} \left(P_{\tau_{B0}}, l_{q_{\mathbf{B},B}} \right), l_{q_{\mathbf{N},B}} \right), l_{q_{\mathbf{T},B}} \right) \tag{2.39}$$
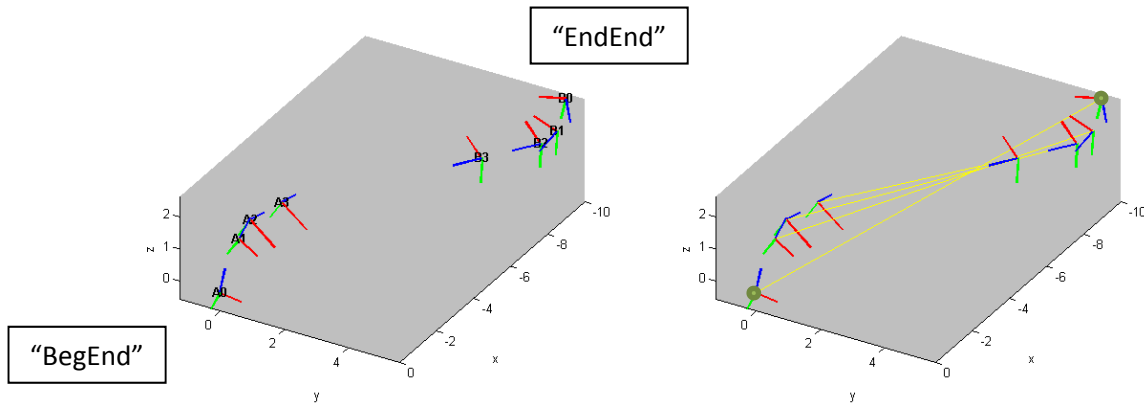
Figure 2.15: The extrapolations for a Frenet Subdivision. DOF-model: 'TripleTriple'. Right: with chords.

Figure 2.15 illustrates three such Frenet extrapolations from each end of the bi-mesh, initiated from two tortuosity master poles $P^0_{\tau_A}, P^0_{\tau_B}$.

Left: Plot poles are labeled $\left(A_0, A_1, A_2, A_3\right), \left(B_0, B_1, B_2, B_3\right)$ respectively.

Right: The master chord and the three new control chords are also illustrated.

During the extrapolations, the information on curvature coordinates is reduced at each step.

$$\hat{f}_{F_B} : \boldsymbol{\chi}_1 = \begin{bmatrix} \kappa_\chi & \kappa_\tau & \tau_\tau \end{bmatrix}^\mathsf{T} \;\rightarrow\; \hat{f}_{F_N} : \boldsymbol{\chi}_2 = \begin{bmatrix} \kappa_\chi & \kappa_\tau & 0 \end{bmatrix}^\mathsf{T} \;\rightarrow\; \hat{f}_{F_T} : \boldsymbol{\chi}_3 = \begin{bmatrix} \kappa_\chi & 0 & 0 \end{bmatrix}^\mathsf{T} \tag{2.40}$$

The embedded curvatures are therefore formed at the two control points *A3, B3* as

$$\partial^4 \Omega_{A3} \supseteq \left\{ \boldsymbol{\chi}_{A3} \right\}$$

$$\partial^4 \Omega_{B3} \supseteq \left\{ \boldsymbol{\chi}_{B3} \right\}$$

Finally, the two new control poles are formed as

$$P_{\tau_{A3}} \supseteq \left\{ \partial^3 \Omega_{A3}, \partial^4 \Omega_{A3} \right\}$$

$$P_{\tau_{B3}} \supseteq \left\{ \partial^3 \Omega_{B3}, \partial^4 \Omega_{B3} \right\}$$

It is rational to use a unified prediction function, which is called Frenet extrapolation $\hat{f}_F$, to incorporate the three previously defined functions as nested functions.

As such, the predictions of the two extrapolated control poles $P_{\tau_{A3}}, P_{\tau_{B3}}$ are expressible as:

$$P_{\tau_{A3}} = \hat{f}_F \left(P_{\tau_A}, l_{q_{TA}}, l_{q_{NA}}, l_{q_{BA}} \right) \qquad \text{("BegEnd" extrapolations)} \tag{2.41}$$

$$P_{\tau_{B3}} = \hat{f}_F \left(P_{\tau_B}, l_{q_{TB}}, l_{q_{NB}}, l_{q_{BB}} \right) \qquad \text{("EndEnd" extrapolations)} \tag{2.42}$$

2.2.11.4   Interpolations

Let two tuples of tortuosity poles be given such as $\left(P_{\tau_{A,1}}, \ldots P_{\tau_{A,m}} \right), \left(P_{\tau_{B,1}}, \ldots P_{\tau_{B,n}} \right)$, $(m,n) \in \mathbb{Z}_+^2$. Then, a prediction rule which determines a new central tortuosity pole (complete or in parts) is called a Frenet interpolation.

The Frenet interpolations defined in this paragraph are all non-parametric. The background theory is given in ANNEX 10.

The applied interpolations are divided into three parts. They are represented by the three interpolation functions $\hat{f}_{G^0}, \hat{f}_{G^1}, \hat{f}_{G^2}$, which sequentially generate a complete tortuosity pole estimate P_{τ_C} as

$$ P_{\tau_C} = \hat{f}_{G^0} \left(\hat{f}_{G^1} \left(\hat{f}_{G^2} \left(P_{\tau_A}, P_{\tau_{A3}},\ P_{\tau_B}, P_{\tau_{B3}},\ \mathbf{d}_C \right) \right) \right). \tag{2.43} $$
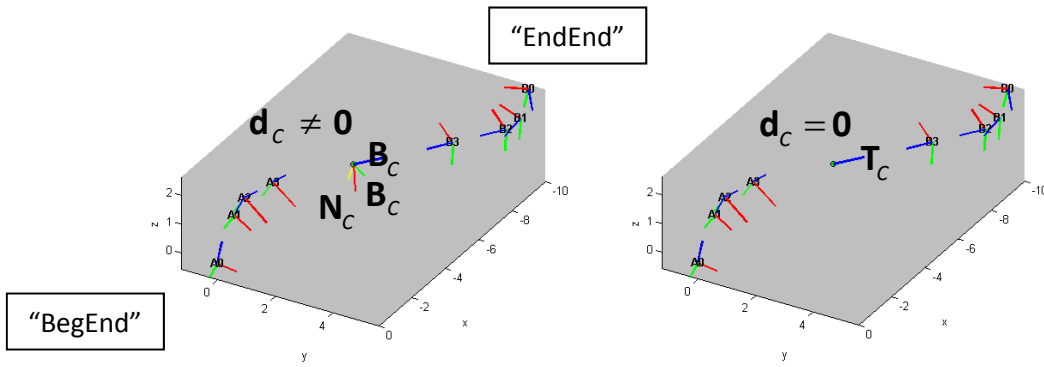
Figure 2.16: The interpolation in the second step of Frenet subdivision.

In Figure 2.16 the rectifying vector $\mathbf{d}_C$ is yellow. *Left:* When the rectifying vector is represented by a regular unit vector, $\mathbf{d}_C \neq \mathbf{0}$, a full Frenet frame $\mathbf{T}_C \mathbf{N}_C \mathbf{B}_C$ is predicted.

Right: However, when the rectifying vector is a null vector, $\mathbf{d}_C = \mathbf{0}$, only the Frenet tangent $\mathbf{T}_C$ is predicted.

The first function $\tilde{f}_{G^2}$ relates to G^2 continuity and predicts the normal $\mathbf{N}_C$ and the binormal $\mathbf{B}_C$ in the interior of the chord $\overline{A_3 B_3}$. However, zero normal and binormal vectors are returned if the rectifying vector is a zero vector.

The function $\tilde{f}_{G^1}$ relates to G^1 continuity. It predicts the tangent, $\mathbf{T}_C$, as a unit vector along the chord $\overline{A_3 B_3}$.
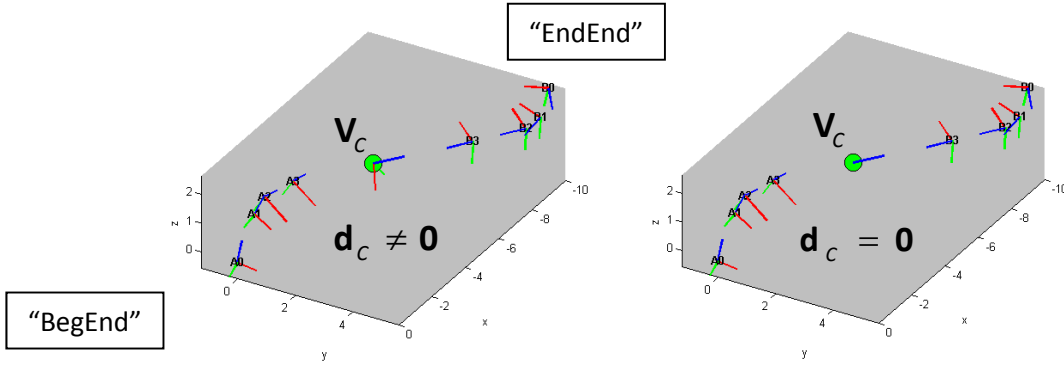
Figure 2.17: Non-parametric *location* interpolation in the second step of Frenet subdivision.

The function $\tilde{f}_{G^0}$ relates to G^0 continuity. As illustrated in Figure 2.17 above, it predicts a central vertex, $\mathbf{V}_C$ (marked in green), in the central plane of the chord $\overline{A_3 B_3}$.

Conclusively, location and orientation vectors depend on the existence of the rectifying vector as follows:

$$\mathbf{d}_C \neq \mathbf{0}: \quad \partial^3 \Omega \supseteq \left\{ \left[\mathbf{V}_C \; \mathbf{T}_C^{\{F\}} \; \mathbf{N}_C^{\{F\}} \; \mathbf{B}_C^{\{F\}} \right]^\mathsf{T} \right\} \tag{2.44}$$

$$\mathbf{d}_C = \mathbf{0}: \quad \partial^3 \Omega_C \supseteq \left\{ \left[\mathbf{V}_C \; \mathbf{T}_C^{\{F\}} \; \mathbf{0} \; \mathbf{0} \right]^\mathsf{T} \right\} \tag{2.45}$$

Furthermore, if the rectifying vector is a zero vector at the limit level of refinement n_τ, the limit curvature is approximated as the average of the segment curvatures for $P_{\tau_{A3}}, P_{\tau_{B3}}$ respectively.

$$\mathbf{d}_C^{n_\tau} = \mathbf{0}: \quad \partial^4 \Omega_C \supseteq \left\{ \left[\mathbf{0} \; \tilde{\kappa}_\tau^{n_\tau} \; \mathbf{0} \right]^\mathsf{T} \right\} \tag{2.46}$$

Otherwise, curvature coordinates are all set to zero.

Finally, the new interpolated pole is formed as

$$P_{\tau_C} \supseteq \left\{ \partial^3 \Omega_C, \partial^4 \Omega_C \right\}.$$

It is rational to use a unified prediction function, which is called Frenet interpolation $\hat{f}_G$, to incorporate the three previously defined functions as nested functions. In this case, the prediction of a non-perturbed tortuosity pole P_{τ_C} is expressible as:

$$P_{\tau_C} = \hat{f}_G \left(P_{\tau_A}, P_{\tau_{A3}}, P_{\tau_B}, P_{\tau_{B3}}, \mathbf{d}_C \right). \tag{2.47}$$

2.2.11.5 Pole translations

Let a tortuosity pole be given at a node C such as P_{τ_C}. A prediction rule that translates this tortuosity pole into a new location at node C' is called a pole translation.

Pole translations defined in this paragraph are all based on the three location parameters q_{ξ_1} q_{ξ_2} q_{ξ_3}, previously defined in Table 2.4. The parameterization is applied by reference from the three length references $l_{q_{1,ref}}, l_{q_{2,ref}}, l_{q_{3,ref}}$ respectively. Furthermore, the length parameters are defined from individual bounding factors k_{ξ_i}, $i \in \{1,2,3\}$ as

$$l_{q_{\xi 1}} = q_{\xi_1} l_{q_{1,ref}}, \quad l_{q_{\xi 2}} = q_{\xi_2} l_{q_{2,ref}}, \quad l_{q_{\xi 3}} = q_{\xi_3} l_{q_{3,ref}}, \qquad l_{q_{i,ref}} = k_{\xi_i} l_\chi, \quad i \in \{1,2,3\}, \tag{2.48}$$

where l_χ is the bi-mesh chord length.

The background theory for the length references $l_{q_{i,ref}}$, and the prediction functions is given in ANNEX 11. Bounds for the individual bounding factors k_{ξ_i}, $i \in [1,2,3]$ used in the preceding examples and illustration are given in ANNEX 12.2.
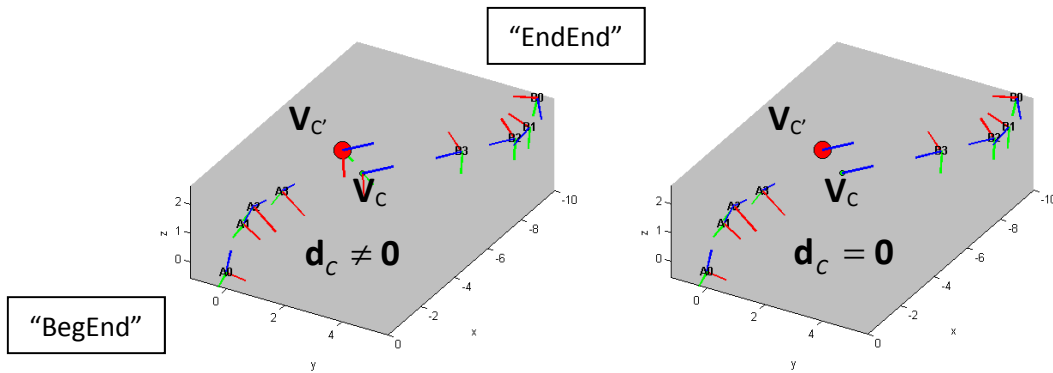
Figure 2.18: Location parameters translate the interpolated pole from a known location C to a new location C'

The third and final subdivision step includes three pole translations $\hat{f}_{\xi_1}$ $\hat{f}_{\xi_2}$ $\hat{f}_{\xi_3}$ which translate the central tortuosity pole to a new location $\mathbf{V}_{C'}$ in space from three orthogonal increments. The translations are oriented corresponding to the respective local coordinate axes see Figure 2.18.

$$P_{\tau_{C'}} = \hat{f}_{H_3}\left(\hat{f}_{H_2}\left(\hat{f}_{H_1}\left(P_{\tau_C}, l_{q_{\xi_1}}\right), l_{q_{\xi_2}}\right), l_{q_{\xi_3}}\right) \tag{2.49}$$

The theory provided in this paragraph supports the use of bi-mesh subdivision as the basis for more complex multi-pole modeling of tortuous curves, surfaces, and solids. This will be further described in the following sub-sections.

2.2.12 Tortuous Curves

In this sub-section, details on tortuous curve generation by Frenet subdivision are given. First parametric subdivision examples based on iterated Frenet extrapolations are presented. Next, these simulations are extended with pole translations. Thereafter, reduced degrees of freedom non-parametric subdivision, order & invariance, simplest form, null form, geometric continuity and finally a principle numerical solution to the reverse Dido's problem are presented.

2.2.12.1 Parametric Subdivision

The various demonstration curves are generated on the basis of input data sets where the variance of each parameter is zeroed. The tortuous demonstration curves generated are all synthetic.

EXAMPLE 4   Refinement process for synthetic curve generation with Frenet extrapolations.

The bi-mesh array used for simulations throughout this example is the same and set to:
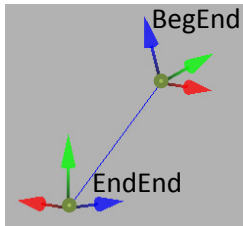
$$
M_{\tau_{bi}} = \begin{array}{l} V \\ T \\ N \\ B \\ X \end{array}
\begin{bmatrix}
0.45 & -0.40 & 0 & -0.35 & 0.50 & 0.00 \\
0.00 & 0.31 & 0.95 & 0.00 & -1.00 & 0.00 \\
-1.00 & 0.00 & 0.00 & 1.00 & 0.00 & 0.00 \\
0.00 & -0.95 & 0.31 & 0.00 & 0.00 & 1.00 \\
0.00 & 2.00 & 1.00 & 0.00 & 1.00 & 2.00
\end{bmatrix}
$$
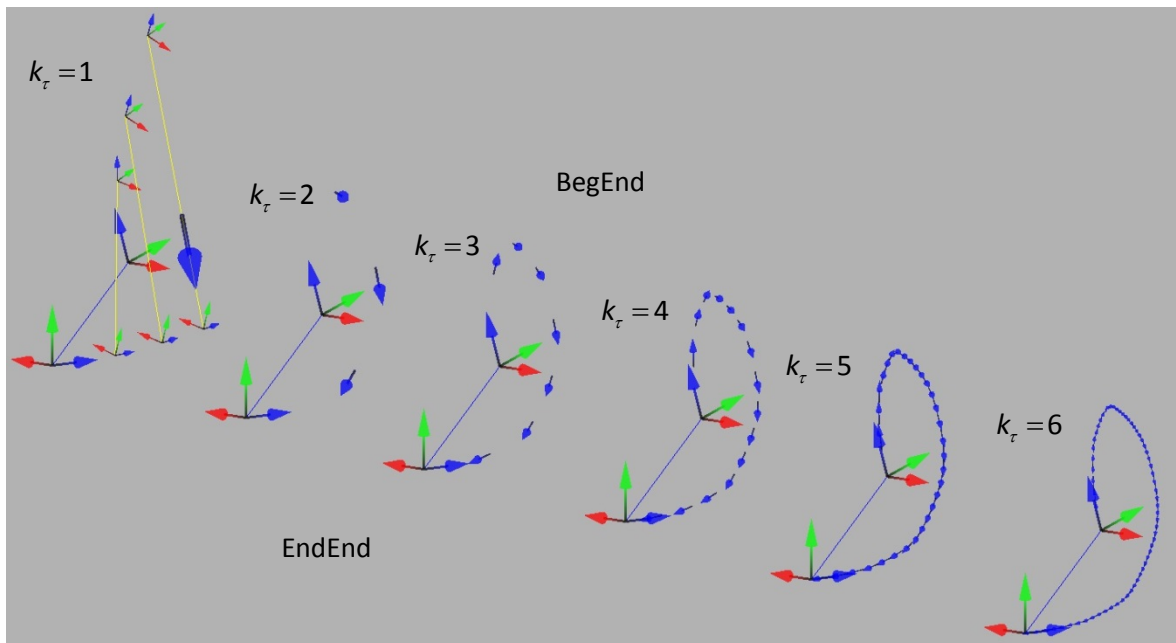
Figure 2.19: Tortuous curve refinement, n_τ = 6. Left: At k_τ = 1 the "TripleTriple" extrapolations are indicated

NOTE   The synthetic curve is generated from master tortuosity poles in their simplest form where the normal and binormal vectors are defined by a vertical rectifying vector. The normals are defined from (2.20) and sign adjusted by (2.15).

In Figure 2.19 a full "TripleTriple" extrapolation is illustrated. On the far left, the individual Frenet extrapolations are indicated. Each of the yellow chords represents the basis for the subsequent extrapolation, like the illustrations provided in ANNEX 12.3. In order to illustrate the refinement process, the tangents (in blue) are subsequently plotted for each level of refinement $k_\tau = 1, 2, ..., 6$.

Additionally, five different sets of iterated orientation parameters are now going to be applied. Individually, each of these sets is used to control the impact from the actual TNB vectors at the ends of the bi-mesh. Geometrically, "low" TNB impact means that the influence from the end conditions on the iterated shape of the curve is low. Similarily, "high" impact indicates that the TNB vectors influence the shape of the curve and especially the fitting in the neighborhood of the ends to the TNB vectors and the curvature and torsion to a high degree. The previous tortuous curve in Figure 2.19 was simulated with "medium" TNB impact. The five sets of orientation parameters, which are going to be used further, are reproduced in the table below.

Table 2.6: Five data sets for the orientation parameters

N°	"TripleTriple" Orientation Parameters	TNB Impact Descriptor
	$\{q_{T_{BegEnd}}, q_{N_{BegEnd}}, q_{B_{BegEnd}},\ q_{T_{EndEnd}}, q_{N_{EndEnd}}, q_{B_{EndEnd}}\}$	$\forall k_\tau$
1	{0.05, 0.05, 0.05, 0.05, 0.05, 0.05}	"low"
2	{0.25, 0.25, 0.25, 0.25, 0.25, 0.25}	"medium low"
3	{0.50, 0.50, 0.50, 0.50, 0.50, 0.50}	"medium"
4	{0.75, 0.75, 0.75, 0.75, 0.75, 0.75}	"medium high"
5	{0.95, 0.95, 0.95, 0.95, 0.95, 0.95}	"high"
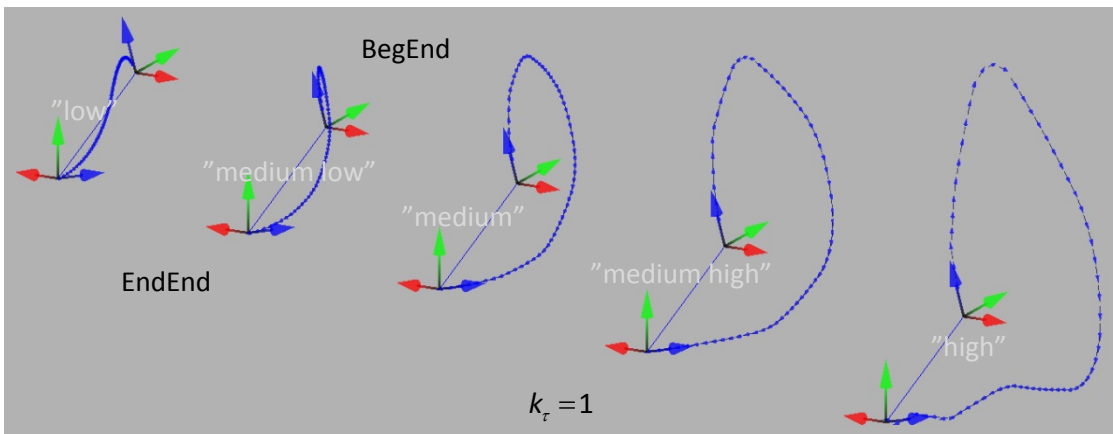
Figure 2.20: Tortuous curves with different TNB impact but the same bi-mesh.

Left to right: "low", "medium low", "medium", "medium high" and "high" TNB impact

EXAMPLE 5   Refinement process for synthetic curve generation with pole translations.

Pole translations parameterized by location parameters are controlled by the degrees of freedom array defined in (2.34). In this example, six individual runs with three degrees of freedom, defined at different levels of refinement, are performed. The same bi-mesh data as for the preceeding example is used with "medium" TNB impact factor. The degrees of freedom arrays are listed in the table below. The data in the list follows the general syntax in (2.34) and the plotted orientation parameters are equally specified.

$$\xi_{\mathrm{DOF}} = \begin{bmatrix} \xi^1_{1_{\mathrm{DOF}}} & \xi^1_{2_{\mathrm{DOF}}} & \xi^1_{3_{\mathrm{DOF}}} \\ \xi^2_{1_{\mathrm{DOF}}} & \xi^2_{2_{\mathrm{DOF}}} & \xi^2_{3_{\mathrm{DOF}}} \\ \cdot & \cdot & \cdot \\ \xi^{k_\tau}_{1_{\mathrm{DOF}}} & \xi^{k_\tau}_{2_{\mathrm{DOF}}} & \xi^{k_\tau}_{3_{\mathrm{DOF}}} \\ \cdot & \cdot & \cdot \\ \xi^{n_\tau}_{1_{\mathrm{DOF}}} & \xi^{n_\tau}_{2_{\mathrm{DOF}}} & \xi^{n_\tau}_{3_{\mathrm{DOF}}} \end{bmatrix} \qquad q_{\xi_1} = q_{\xi_2} = q_{\xi_3} = 0.10$$

Table 2.7: DOF-arrays for illustration of the $\xi_1\xi_2\xi_3$ location impact. (Note: Run 1 is defined with $n_{\mathrm{DOF}\xi} = 0$)

Run 2				Run 3				Run 4				Run 5			
0	0	0		0	0	0		0	0	0		1	1	1	$k_\tau = 1$
0	0	0		0	0	0		1	1	1	$k_\tau = 2$	0	0	0	
0	0	0		0	0	0		0	0	0		0	0	0	
0	0	0		1	1	1	$k_\tau = 4$	0	0	0		0	0	0	
0	0	0		0	0	0		0	0	0		0	0	0	
1	1	1	$k_\tau = 6$	0	0	0		0	0	0		0	0	0	
0	0	0		0	0	0		0	0	0		0	0	0	
0	0	0		0	0	0		0	0	0		0	0	0	

Figure 2.21: Tortuous curves based on the same bi-mesh with location impact at different levels.

It appears clearly from the runs that the location impact at high level of refinement has a small global effect on the overall shape, but a high local impact (see Run 2). At lower levels of refinement, the global effect increases whereas the local effect diminishes (see Run 3, 4 & 5). (The appearances recall Fourier decomposition).

2.2.12.2 Tortuous Curve Fields

Geometrically, the generation of tortuous curves C_τ by Frenet subdivision is designed to ensure explicit G^1 continuity at any level of refinement and asymptotic G^2 continuity at the limit level of refinement n_τ. The estimation of natural variations is controlled by a set of iterated parameters $\{q_{\partial\Omega}\}$ see 2.2.10.3. To ensure multi-resolution capability, iterated parameters are made customizable at any level of refinement $k_\tau = 1,\ldots, n_\tau$. In terms of conventional parametric subdivision terminology, the novel Frenet subdivision scheme includes six intermediate control vertices $\left(\mathbf{V}^{k_\tau}_{\tau,A1}, \mathbf{V}^{k_\tau}_{\tau,A2}, \mathbf{V}^{k_\tau}_{\tau,A3}, \mathbf{V}^{k_\tau}_{\tau,A2}, \mathbf{V}^{k_\tau}_{\tau,B1}, \mathbf{V}^{k_\tau}_{\tau,B3}\right)$ that are manipulated at each level of refinement by a six-tuple of iterated parameters $\left(q_{\mathbf{T}_A}, q_{\mathbf{N}_A}, q_{\mathbf{B}_A}, q_{\mathbf{T}_B}, q_{\mathbf{N}_B}, q_{\mathbf{B}_B}\right)$ and a three-tuple of iterated pole translation parameters $\left(q_{\xi_1}, q_{\xi_2}, q_{\xi_3}\right)$. Typically, tortuous curves are represented by one of the following representations.

A location field, i.e. a poly-line of a vertex sequence

$$\mathbf{V}_\tau = \left\{\mathbf{V}^0_{\tau,A},\ldots,\mathbf{V}^{k_\tau-1}_{\tau,A},\mathbf{V}^{k_\tau}_{\tau,C},\mathbf{V}^{k_\tau-1}_{\tau,B},\ldots,\mathbf{V}^0_{\tau,B}\right\}, \tag{2.50}$$

An orientation field of tangents, i.e. a field of tangent vectors of a tortuous curve

$$\mathbf{T}_\tau(\mathbf{V}_\tau) = \left\{\mathbf{T}^0_{\tau,A},\ldots,\mathbf{T}^{k_\tau-1}_{\tau,A},\mathbf{T}^{k_\tau}_{\tau,C},\mathbf{T}^{k_\tau-1}_{\tau,B},\ldots,\mathbf{T}^0_{\tau,B}\right\}, \tag{2.51}$$

An orientation field of normals

$$\mathbf{N}_\tau(\mathbf{V}_\tau) = \left\{\mathbf{N}^0_{\tau,A},\ldots,\mathbf{N}^{k_\tau-1}_{\tau,A},\mathbf{N}^{k_\tau}_{\tau,C},\mathbf{N}^{k_\tau-1}_{\tau,B},\ldots,\mathbf{N}^0_{\tau,B}\right\}, \tag{2.52}$$

An orientation field of binormals

$$\mathbf{B}_\tau(\mathbf{V}_\tau) = \left\{\mathbf{B}^0_{\tau,A},\ldots,\mathbf{B}^{k_\tau-1}_{\tau,A},\mathbf{B}^{k_\tau}_{\tau,C},\mathbf{B}^{k_\tau-1}_{\tau,B},\ldots,\mathbf{B}^0_{\tau,B}\right\} \tag{2.53}$$

A Frenet field including all orientation vectors of the tortuosity poles.

From an object oriented programming point of view, any new bi- mesh $\mathbf{M}^{k_\tau}_{\tau_{bi}}$ is formed by a *parent* bi-mesh $\mathbf{M}^{k_\tau-1}_{\tau_{bi}} \ni \left\{\mathbf{P}^{k_\tau-1}_{\tau,A}, \mathbf{P}^{k_\tau-1}_{\tau,B}\right\}$ by generating a new central *child* pole $\left\{\mathbf{P}^{k_\tau}_{\tau,C}\right\}$ into the sequence of tortuosity poles as $\left\{\mathbf{P}^{k_\tau-1}_{\tau,A}, \mathbf{P}^{k_\tau}_{\tau,C}, \mathbf{P}^{k_\tau-1}_{\tau,B}\right\}$. This new constellation is then subdivided into two new bi-poles $\left\{\mathbf{P}^{k_\tau-1}_{\tau,A}, \mathbf{P}^{k_\tau}_{\tau,C}\right\}$ and $\left\{\mathbf{P}^{k_\tau}_{\tau,C}, \mathbf{P}^{k_\tau-1}_{\tau,B}\right\}$, which are used to form two new parent bi-meshes $\mathbf{M}^{k_\tau}_{\tau_{bi}} \ni \left\{\mathbf{P}^{k_\tau-1}_{\tau,A}, \mathbf{P}^{k_\tau}_{\tau,C}\right\}$ and $\mathbf{M}^{k_\tau}_{\tau_{bi}} \ni \left\{\mathbf{P}^{k_\tau}_{\tau,C}, \mathbf{P}^{k_\tau-1}_{\tau,B}\right\}$. At every intermediate state the new poles are used to define subsequent poles. Later it is illustrated how bi-meshes are parametrically manipulated.

2.2.12.3 Reduced Degrees Of Freedom

The introduced model has nine parameters, which gives extensive control over the subdivision and allows for detailed roughness simulations. Sometimes, it is relevant to reduce the degrees of freedom. A few comments on reducing the degrees of freedom (DOF) are given in ANNEX 12.4.

2.2.12.4 Non-parametric Subdivision

In a non-parametric form $n_{\text{DOF}}^{k_\tau} = 0$, the generated shape from Frenet subdivision can be interpreted as a pendant to an analytical shape function known from FEA. This can be realized by letting all parameters be substituted by constants, i.e.:

$$n_{\text{DOF}}^{k_\tau} = 0 \rightarrow \left(q_{\xi_1}, q_{\xi_2}, q_{\xi_3}, q_{\mathbf{T}_A}, q_{\mathbf{N}_A}, q_{\mathbf{B}_A}, q_{\mathbf{T}_B}, q_{\mathbf{N}_B}, q_{\mathbf{B}_B} \right) =$$
$$\left(Const_{\xi_1}, Const_{\xi_2}, Const_{\xi_3}, Const_{\mathbf{T}_A}, Const_{\mathbf{B}_A}, Const_{\mathbf{N}_A}, Const_{\mathbf{T}_B}, Const_{\mathbf{B}_B}, Const_{\mathbf{N}_B} \right) \qquad (2.54)$$

In this special situation, Frenet subdivision can act like an analytic two-noded non-linear C^2-shape function $N(\xi)$ with second order geometric continuity in the limit. However, such a Frenet shape function $N_\tau(\xi)$ requires a master bi-mesh $\text{M}_{\tau,\text{bi}}^0$ as input whereas a conventional two-noded C^2-shape function requires end position vectors $\mathbf{r}_A, \mathbf{r}_B$ and their derivatives $\mathbf{r}_A', \mathbf{r}_A''$, $\mathbf{r}_B', \mathbf{r}_B''$ as input.

$$n_{\text{DOF}}^{k_\tau} = 0 \quad \rightarrow \quad N_\tau\left(\xi, \text{M}_{\tau_{\text{bi}}}^0 \right) = \lim_{m_\tau \rightarrow \infty} \left(\text{M}_\tau^{k_\tau} = S_{\tau_{\text{bi}}}^{k_\tau} \text{M}_\tau^{k_\tau - 1} \right)$$
$$\approx N\left(\xi, \mathbf{r}_A, \mathbf{r}_A', \mathbf{r}_A'', \mathbf{r}_B, \mathbf{r}_B', \mathbf{r}_B'' \right), \quad N_\tau \in G^2, \quad N \in C^2 \qquad (2.55)$$

For more details on analytic FE shape functions see (Shivaswamy, 2010).

2.2.12.5 Order and invariance

A master mesh defined solely by vertices $\left\{ [\mathbf{V}]^{\mathsf{T}} \right\}$ is said to be of the zeros order. Master meshes which also include tangents $\left\{ [\mathbf{V}, \mathbf{T}]^{\mathsf{T}} \right\}$ are of first order. Such first order meshes are defined from tortuosity poles in their simplest form. Master meshes including normals and curvatures $\left\{ [\mathbf{V}, \mathbf{T}, \mathbf{N}, \mathbf{B}, \boldsymbol{\chi}]^{\mathsf{T}} \right\}$ are said to be of second order.

Conventional zero-order master meshes are not included in this presentation. Frenet subdivision from first order master meshes is invariant to any coordinate transformation.

Frenet subdivision from second order master meshes is invariant to translations and rotations, but not to scaling since curvature is size dependent. Therefore, for general second order models size normalization is required.

2.2.12.6 Simplest form

Especially for a first order master mesh, Frenet subdivision is said to represent a mesh generator in its simplest form when each iterated location parameter q_ξ goes towards zero, i.e.

$$q_\xi = \left\{ q_{\xi_1}, q_{\xi_2}, q_{\xi_3,} \right\} \rightarrow \left\{ 0,0,0 \right\} \tag{2.56}$$

At the same time, the orientation parameters q_f are all defined as ones

$$q_f = \left\{ q_{\mathbf{T}_A}, q_{\mathbf{N}_A}, q_{\mathbf{B}_A}, \ q_{\mathbf{T}_B}, q_{\mathbf{N}_B}, q_{\mathbf{B}_B} \right\} = \left\{ 1,1,1, \ 1,1,1 \right\} \ . \tag{2.57}$$

2.2.12.7 Null form

A parametric Frenet Subdivision generator is said to be in its null form if all of its iterated parameters are zeroed, i.e.

$$q_f = \left\{ q_{\mathbf{T}_A}, q_{\mathbf{N}_A}, q_{\mathbf{B}_A}, \ q_{\mathbf{T}_B}, q_{\mathbf{N}_B}, q_{\mathbf{B}_B} \right\} = \left\{ 0,0,0, \ 0,0,0 \right\} \ . \tag{2.58}$$

In this special situation the output mesh is is represented by bi-mesh chords, i.e. straight line segments. Such curves might be usefull for man-made objects but it is unlikely to be usefull for natural object modeling.

2.2.12.8 Geometric continuity
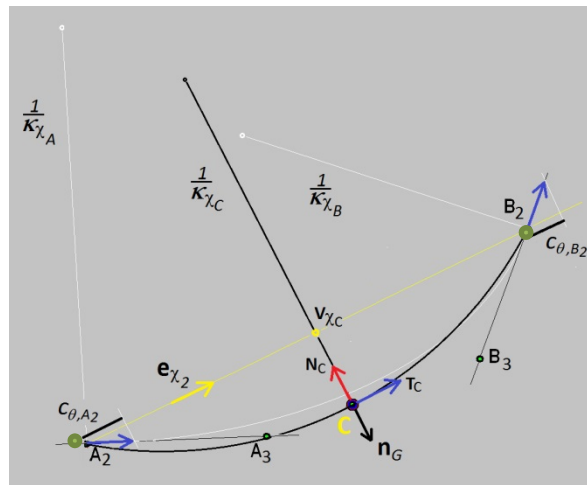
Figure 2.22: Frenet Subdivision possess asymptotic G^2 continuity

The Frenet subdivision algorithm for tortuous curves is designed to possess explicit G^1 continuity at $k_\tau = 1, ..., n_\tau$ and asymptotic G^2 continuity at the limit level of refinement $k_\tau = n_\tau$ under the following assumptions.

Let it be assumed that three poles $\left(P^{n_\tau}_{\tau,A_2}, P^{n_\tau}_{\tau,C}, P^{n_\tau}_{\tau,B_2} \right)$ at the limit level of refinement $k_\tau = n_\tau$ exist. Let their average direction cosine and direction sine for the tangent directions relative to the chord be defined from

$$c_{\theta_2,\text{avg}} = \frac{\mathbf{T}_{A_2} \bullet \mathbf{e}_{\chi_2} + \mathbf{T}_{B_2} \bullet \mathbf{e}_{\chi_2}}{2} = \frac{c_{\theta,A_2} + c_{\theta,B_2}}{2} \rightarrow s_{\theta_2,\text{avg}} = \sqrt{1 - c^2_{\theta_2,\text{avg}}} \ . \tag{2.59}$$

Further, let it be assumed that in the limit $n_\tau \rightarrow \infty$, the vertices and tangent vectors of these three poles share the same osculating Frenet plane $\{F\}^{\mathbf{T}_2 \times \mathbf{N}_2}$ and that an osculating circle exists, which fits these three poles exactly i.e. $c_{\theta_2,\text{avg}} = \mathbf{T}_{A_2} \bullet \mathbf{e}_{\chi_2} = \mathbf{T}_{B_2} \bullet \mathbf{e}_{\chi_2}$. Then, at any finite level of refinement $n_\tau \in Z_+$, the interpolation of the limit central pole $P^{n_\tau}_{\tau,C}$ is designed to possess explicit embedded G^1 continuity and approximate embedded G^2 continuity. However, in curve regions where no singularities are generated, approximate G^2 continuity is obtained by defining an estimate of the central curvature as

$$\tilde{\kappa}^{n_\tau}_{\tau_C} = \frac{2\sqrt{1 - c^2_{\theta_2,\text{avg}}}}{l_{\chi_2}} \ . \tag{2.60}$$

In other words, when Frenet subdivision is applied in its simplest form, the generated geometry asymptotically goes towards a circular segment, which is indeed the solution to the reversed Dido's problem, see 2.2.4. This means that Frenet subdivision in its simplest form generates discrete geometries that possess minimum tortuosity at a scale corresponding to the limit level of refinement. Naturally, curve generation with only G^0 continuity can be designed. The modeling of singularities is a feature which is incorporated in Frenet subdivision through multi-valence modeling.

Explicit G1 continuity is obtained by defining the rectifying plane as an approximation to an analytic rectifying plane:

$$\mathbf{N}_C \simeq -\mathbf{n}_G : M_\tau(\mathbf{T}_C) \ni P_{\tau,C}(\mathbf{T}_C) \mapsto \frac{\mathbf{T}_C \times (\mathbf{T}_C + \Delta\mathbf{T}_C)}{\|\mathbf{T}_C \times (\mathbf{T}_C + \Delta\mathbf{T}_C)\|}, \tag{2.61}$$

where the central normal $\mathbf{N}_C$, and the analytic Gauss normal $\mathbf{n}_G$ are equal up to sign.

NOTE   When a local radial axis is in use as ξ_2 it is oriented in the same direction as the Gauss normal $\mathbf{n}_G$.

Approximate G² continuity is assured by assigning the vertex field in the neighborhood of $\mathbf{V}_C$ to the same approximate rectifying plane:

$$\lim_{\Delta\mathbf{v}_C \rightarrow 0} \frac{((\mathbf{V}_C + \Delta\mathbf{V}_C) - \mathbf{V}_C) \bullet \mathbf{N}_C}{\|(\mathbf{V}_C + \Delta\mathbf{V}_C) - \mathbf{V}_C\|} = 0 \tag{2.62}$$

The approximate central normal $\mathbf{N}_C$ is asymptotically perpendicular to the vertex field $\mathbf{V}(M_\tau)$ in the neighborhood of $\mathbf{V}_C$ and still an approximation to the Gauss normal $\mathbf{N}_C \simeq -\mathbf{n}_G$.

In the current osculating Frenet plane $\{F\}^{\mathbf{T} \times \mathbf{N}}$ through $\mathbf{V}_C \in P^{n_\tau}_{\tau,C}$ the limit value for the secant curvature used to form a new central tortuosity pole C is given by

$$\lim_{n_\tau \to \infty} \kappa^{n_\tau}_{\chi,C} = \frac{2\sqrt{1-\left(c^{n_\tau}_{\theta_2,\mathrm{avg}}\right)^2}}{l^{n_\tau}_{\chi,2}} = \frac{2s^{n_\tau}_{\theta_2,\mathrm{avg}}}{l^{n_\tau}_{\chi,2}} \tag{2.63}$$

However, this only holds if Frenet subdivision is applied in its simplest form at the many last levels of refinement.

$$k_\tau \in \left[...,n_\tau -2, n_\tau -1, n_\tau\right] \tag{2.64}$$

NOTE   It must be stressed that the central secant curvature in (2.63) represents a single curvature related to one specific osculating plane through the bi-meshes of a tortuous limit mesh (see Figure 2.22).

2.2.12.9   Multi-Valence Curves
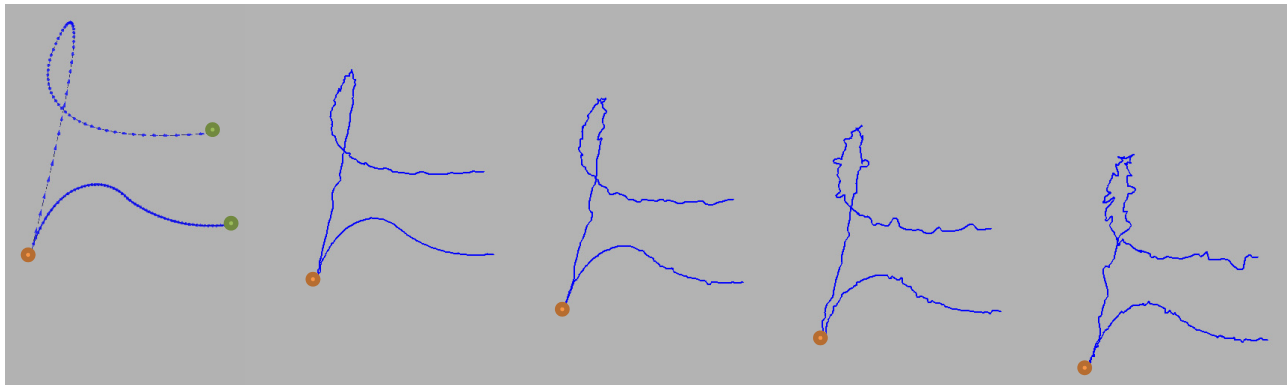
Figure 2.23: Tortuous curves with increasing roughness. The orange tortuosity pole has valence two

Figure 2.23 illustrates a series of tortuous curves based on there poles (one orange and two green). The orange pole has the valence two, which is used to form a discontinuity. Note that this discontinuity is modeled by two frames that share the same tangent. The curve furthest to the left is generated by Frenet subdivision in its "simplest form". From left to right: Theses curves are generated by adding increasing random roughness as synthetic pole translations.

2.2.12.10   A Principle Solution to the Reversed Dido's Problem

As will be demonstrated by the following principle example, a numerical solution to the reverse Dido's problem (see 2.2.4) can be found by multiresolution parametric Frenet subdivision.

EXAMPLE 6   A principle solution to the reversed Dido's problem

Let a reversed Dido's problem be defined numerically by a chord with length $l_\chi = 2$, centered at the origin, along the first axis of a global Cartesian coordinate system. The two observation vertices $(\mathbf{V}_A^T, \mathbf{V}_B^T)_{obs}$ are assumed to be given. Furthermore, the enclosed area in the osculating plane of the observed curve is defined to be $\pi / 2$. Sets of feasible curves are generated by parameteric Frenet subdivision. To illustrate the capability of Frenet subdivsion, and to give an impression of the numeriacal convergence, some selected plots are given. Parametric location modeling is first illustrated for location parameters alone, then for orientation parameters alone, and finally for some mixed selections for location/orientation parameterization. Finally, the particular curve which possesses the minimum arc-chord tortuosity, i.e. the replication extremal, is selected as the solution. Numerically, the problem is defined from a replication problem (2.2) where the fault of replication is bound by the fixed observation area $A_{obs} = \pi / 2$ as

$$\varepsilon_\tau(M_{obs}, M_{phan}) = \varepsilon_\tau(A_{obs}, A_{phan}) = \frac{\left| A_{phan} - A_{obs} \right|}{A_{obs}} \leq \varepsilon_{\tau,upp} \tag{2.65}$$

Fullfilling the side conditions $\left\{ q_{M_{phan}}^0 \right\} = \left\{ q_{M_{obs}}^0 \right\}$ for the two end vertices and their vertical tangents means that the numerical phantom has the same values as for the observed geometry.

$$\left\{ q_{M_{phan}}^0 \right\} = \left\{ q_{M_{obs}}^0 \right\} \;\rightarrow\; (\mathbf{V}_A^T, \mathbf{V}_B^T)_{phan} = ([1,0,0],[-1,0,0]), \quad (\mathbf{T}_A^T, \mathbf{T}_B^T)_{phan} = ([0,0,1],[0,0,1]) \tag{2.66}$$

More specifically, the bi-mesh for the phantom curve which is intended to be generated by Frenet subdivision, is specified as

$$M_{\tau,bi}^0 = \left\{ P_{\tau_A}, P_{\tau_B} \right\}, \tag{2.67}$$

where its two tortuosity poles are

$$P_{\tau_A} = \begin{bmatrix} \mathbf{V}_A^T \\ \mathbf{T}_A^T \\ \mathbf{N}_A^T \\ \mathbf{B}_A^T \\ \mathbf{X}_A^T \end{bmatrix}, \quad P_{\tau_B} = \begin{bmatrix} \mathbf{V}_B^T \\ \mathbf{T}_B^T \\ \mathbf{N}_B^T \\ \mathbf{B}_B^T \\ \mathbf{X}_B^T \end{bmatrix}. \tag{2.68}$$

Note that the two vertices $\mathbf{V}_A^T, \mathbf{V}_B^T$ are fixed due to the nature of the reversed Dido's problem. In principle, the tangents $\mathbf{T}_A^T, \mathbf{T}_B^T$ are variables, whereas the master normals, binormals are not in focus here as variables. The curvature is however kept active, i.e. their identical values are defined as one divided by the radius of curvature, which equals one in this situation. Tangent variability is already illustrated in EXAMPLE 5. Therefore, tangents are here kept fixed with the values defined in (2.66). Thus, the parameterization includes only iterated parameters. Furthermore, this is a planar problem, and due to symmetry considerations only two degrees of freedom are considered.

"q_ξ = location parameter"

$q_{\xi_2} = -0.75$ $q_{\xi_2} = +0.75$

$n_\tau = 8$

ξ_{DOF}

```
[0 1 0;
 0 1 0;
 0 1 0;
 0 1 0;
 0 1 0;
 0 1 0;
 0 1 0;
 0 1 0]
```

```
[0 0 0;
 0 1 0;
 0 1 0;
 0 1 0;
 0 1 0;
 0 1 0;
 0 1 0;
 0 1 0]
```

```
[0 0 0;
 0 0 0;
 0 1 0;
 0 1 0;
 0 1 0;
 0 1 0;
 0 1 0;
 0 1 0]
```

```
[0 0 0;
 0 0 0;
 0 0 0;
 0 1 0;
 0 1 0;
 0 1 0;
 0 1 0;
 0 1 0]
```

```
[0 0 0;
 0 0 0;
 0 0 0;
 0 0 0;
 0 1 0;
 0 1 0;
 0 1 0;
 0 1 0]
```

```
[0 0 0;
 0 0 0;
 0 0 0;
 0 0 0;
 0 0 0;
 0 1 0;
 0 1 0;
 0 1 0]
```

```
[0 0 0;
 0 0 0;
 0 0 0;
 0 0 0;
 0 0 0;
 0 0 0;
 0 1 0;
 0 1 0]
```

DIRECTION OF CONVERGENCE
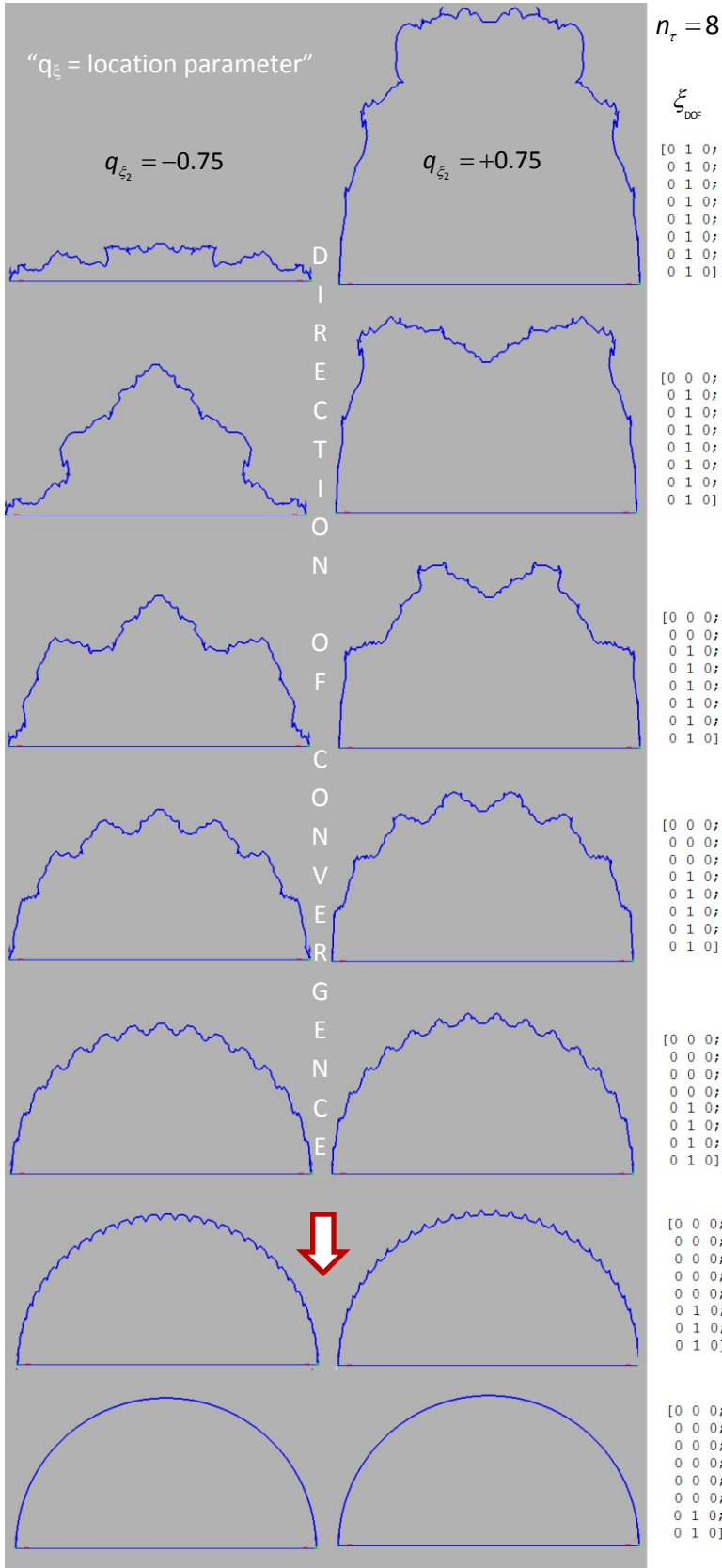
These are: the location parameter for the second local axis q_{ξ_2} (see plots in Figure 2.23) and the orientation parameter for tangential impact q_T (see plots in Figure 2.24) which is supposed to have the same value for both ends. The iteration space is limited to:

$$\left(q_{\xi_2}, q_T\right) \in \left([-1.00, 1.00] \times [0.00, 1.00]\right)$$
$$\rightarrow n_{DOF}^{k_\tau} = 2$$

However, only a small number of the high but finite numer of generated curves are reproduced here. The few curves displayed are supposed to illustrate the numerical convergence towards the solution. The following value sets are used for the illustrations:

$$q_{\xi_2} \in \{-0.75, +0.75\}$$
$$q_T \in \{0.05, 0.25, 0.50, 0.75, 0.95\}$$

The accompanying location and orientation bounds, are defined in accordance with ANNEX 12.2.

In this example, the 2nd local axis is defined to be identical with the global 2nd axis, i.e. all pole translations are performed in the vertical direction.

The numerical replication problem includes only two degree of freedom. The limit level of refinement is selected to eight. Expressed in terms of the set of iterated parameters this gives:

$$\left\{q_{\xi_1}, q_{\xi_2}, q_{\xi_3}, \ q_{T_A}, q_{N_A}, q_{B_A}, \ q_{T_B}, q_{N_B}, q_{B_B}\right\} =$$
$$\left\{0, q_{\xi_2}, 0, \ q_T^*, 1, 1, \ q_T, 1, 1\right\}, \ n_\tau = 8$$

Figure 2.24: Convergence towards a solution to the reversed Dido's problem from a single location parameter

Figure 2.25: Convergence towards a solution for the reversed Dido's problem from orientation parameters
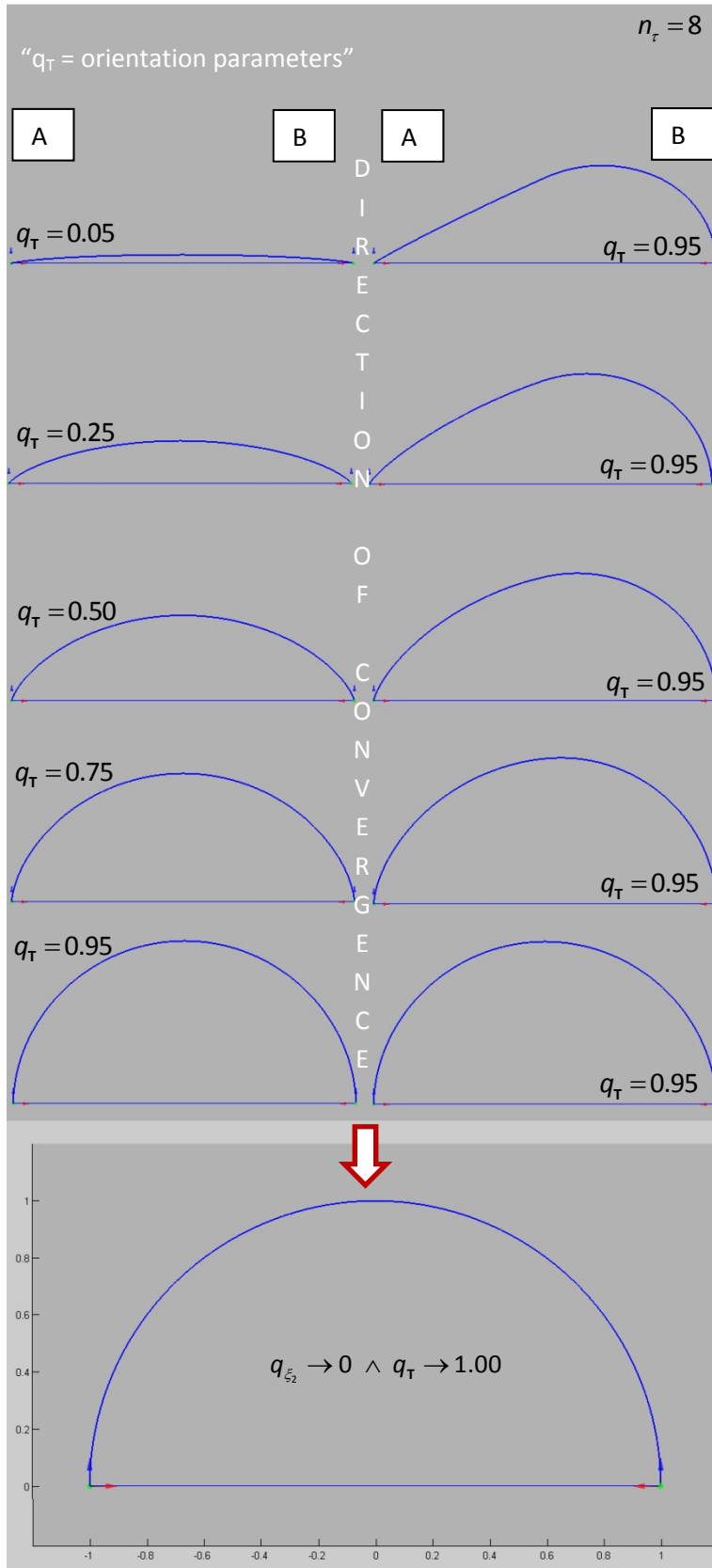
*The plots for the various values of the location parameter q_T also include a series of assymetric runs where the parameter on the far right is fixed at $q_T = 0.95$. The other end is impacted by the values from the list above. These extra plots are included to illustrate that in many situations prior knowledge on symmetry is not likely to be apparent. Therefore, the assymetric plots indicate that in such situations an extra degree of freedom must be incorporated:

$$\{0, q_{\xi_2}, 0, \; q_{T_A}, 1, 1, \; q_{T_B}, 1, 1\} \rightarrow n_{DOF}^{k_\tau} = 3$$

where $q_{\xi_2} = 0$, see Figure 2.24.

In principle, Figure 2.24 and Figure 2.25 illustrate separately, and as a whole, the direction of convergence for a multivariate optimization problem iterated by a dedicated replication algorithm.

Conclusive remarks

The reversed Didos problem can be given a numerical solution by finding a single curve amongst a high number of generated curves which possess the smallest tortuosity, i.e. a curve which satisfies a replication problem with a high efficiency of replication. Specifically, when multiresolution parametric Frenet subdivision is used as curve generator then in the limit the numerical solution converge when its parameter set goes towards:

$$\{q_{\xi_1}, q_{\xi_2}, q_{\xi_3}, \; q_{T_A}, q_{N_A}, q_{B_A}, \; q_{T_B}, q_{N_B}, q_{B_B}\} =$$
$$\{0,0,0, \; 1,1,1, \; 1,1,1\}, \quad n_\tau \rightarrow \infty$$

Multiresolution parametric Frenet subdivision is designed in its "simplest form" to generate solutions to the type of variational problems defined as reversed Didos problems.

2.2.13 Tortuous Surfaces

In this sub-section, details on tortuous surface generation by Frenet subdivision are given.
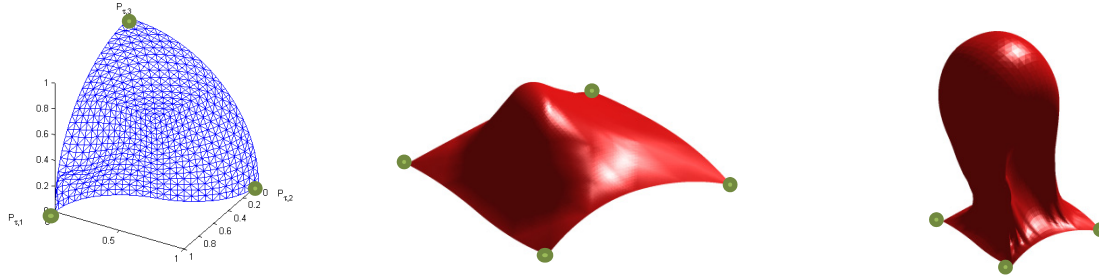
Figure 2.26: Tri-mesh (left). Quad-mesh with medium location perturbation (middle) and large (right) at $k_\tau = 1$

Tortuous surfaces are generated in two variants. One variant is based on a master *tri-mesh* (see Figure 2.26, left) and the other variant on a master quad-mesh (see Figure 2.26, middle and right). A tri-mesh includes three edges whereas a quad-mesh includes four edges. The subdivision scheme for any surface is initiated from such a master tri- or quad-mesh mesh M_τ^0. The target at each iteration step is to iterate new tortuosity poles $\left\{ P_{\tau_c}^{k_\tau} \right\}, \forall k_\tau$ from the preceding tri- or quad mesh. This means that the subdivision principle is the same as for the tortuous curve generator.

During iteration, some of the new tortuosity poles are defined from the first subdivision of the master edges. These new poles are called *edge poles* whereas other new poles at the interior are called *face poles*. The definition of the face poles is not straightforward. In general, the individual tortuous curves used to form the interior shape do not intersect at one single point (see Figure 2.29 and Figure 2.33). Therefore, the face poles are found by solving the following minimization problem. Find a vertex $\mathbf{V}_{C_\beta}$ of a new pole P_{τ_β} so that the sum of squared distances d_β between any of the vertices of the n_j tortuous curves $C_{\tau,j}$, $j \in \left[1, n_j \right]$ is minimized.

$$\mathbf{V}_{C_\beta}: \quad \min \sum_{j=1}^{n_j} d_{\beta,j}^2 = \min \sum_{j=1}^{n_j} d(\mathbf{V}_C, C_{\tau,j})^2 \tag{2.69}$$

The index beta is used to indicate that the n_j curves are all generated by Frenet subdivision in its simplest form. The new pole P_{τ_β} is said to be beta-iterated and it is defined as a new tortuosity pole with vertex $\mathbf{V}_{C_\beta}$. Its pole tangents are adopted directly from the involved curves in their "simplest form." However, its normals, binormals, and curvatures are left undefined. To take into account this numerical error, the new pole P_{τ_β} is anticipated to carry a small part of the variance of the overall statistical dispersion modeled by the location parameters q_{ξ_β} of that pole (see 2.3.22).

With the exception of the perturbations introduced in the red quad-surfaces at the first level of refinement $k_\tau = 1$, the three meshes are generated with Frenet subdivision in its simplest form at all levels of refinement.

Even in its simplest form Frenet subdivision can be used to shape various geometries. Figure 2.27 illustrates an irregular surface called, the "paper mache mouth," so called because of its appearance. This surface is generated from ten tortuosity poles in their simplest form using a tri-mesh constellation. The patch graphics in in this model have been added at each master tri-mesh individually.

The shadows on the triangular inter-edges make the skin look like paper marche.

Figure 2.27: The "paper marche mouth" is created by Frenet subdivision in its simplest form

The following section introduces a parametric subdivision algorithm, which is able to generate discretized surfaces, as illustrated in Figure 2.26, from a tortuous tri-pole (left) or quad-pole (middle, right) master mesh in $\mathbb{R}^3$. Mathematically, the algorithm is an extension of Frenet subdivision for tortuous curve generation. As a central part, the following recurrence relations for tri-pole and quad-pole meshes are used:

$$M_\tau^{k_\tau} = S_{\tau_{\mathrm{tri}}}^{k_\tau} M_\tau^{k_\tau - 1} \tag{2.70}$$

$$M_\tau^{k_\tau} = S_{\tau_{\mathrm{quad}}}^{k_\tau} M_\tau^{k_\tau - 1} \tag{2.71}$$

Specifically in these relations, the iterations are initiated from a master *tri-mesh* $M_{\tau_{\mathrm{tri}}}^0 \ni \left\{ P_{\tau_A}^0, P_{\tau_B}^0, P_{\tau_D}^0 \right\} = \left\{ P_{\tau_1}^0, P_{\tau_2}^0, P_{\tau_3}^0 \right\}$ (see Figure 2.28) or a master *quad-mesh* $M_{\tau_{\mathrm{quad}}}^0 \ni \left\{ P_{\tau_A}^0, P_{\tau_B}^0, P_{\tau_D}^0, P_{\tau_E}^0 \right\}$ (see Figure 2.33) respectively. The subdivision operators $S_{\tau_{\mathrm{tri}}}^{k_\tau}$ and $S_{\tau_{\mathrm{quad}}}^{k_\tau}$ can control the iterations at any level of refinement.

In the following section, the blue tri-mesh in Figure 2.26 (left) is used to describe how the multi-resolution tri-pole based subdivision operator $S_{\tau_{\mathrm{tri}}}^{k_\tau}$, and the multi-resolution quad-pole based operator $S_{\tau_{\mathrm{quad}}}^{k_\tau}$, controls the iterations.

Multi-resolution parametric surfaces

For natural geometries, it is unlikely that meshing from tortuosity poles, in their simplest form and with a low number of degrees of freedom, is able to model irregular rough surfaces with a high level of detail. Therefore, surface models based on multi-resolution parametric Frenet subdivision will be introduced.

More specifically, in the formulation of the master mesh, it is anticipated that at least a single parameter at one level of refinement exists.

2.2.13.1 Tri- and Quad Mesh Subdivision Surfaces

The final phantom mesh $M_{phan} = M_\tau^{n_\tau}$ represents a constellation of tortuosity poles. The vertex-face constellation is graphically illustrated by patches (see Figure 2.26). From an object oriented programming point of view, any new set of tortuosity poles $M_\tau^{k_\tau} \ni \left\{P_{\tau,C}^{k_\tau}\right\}$ are created as a child object of its parent constellation of tri-meshes or quad-meshes. At preceding levels of refinement, quad-meshes are also subdivided into quad-meshes. However, at the limit level of refinement quad-meshes are finally subdivided into tri-angulated patch for graphics display. At each level of refinement, the tortuous curve generator generates edges. The rectifying vectors $\left\{\mathbf{d}_C\right\}_{tri}$ or $\left\{\mathbf{d}_C\right\}_{quad}$ are assumed to be pre-defined or are estimated during the iterations. Tri-meshes are generated from a refinement approach. This approach is comprised of the formation of a tri-pole master constellation, followed by a subdivision into quadrilaterals as illustrated in the following series of figures.
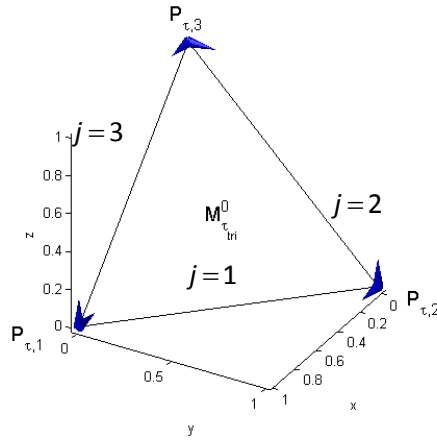
Figure 2.28: Master tri-mesh

Let a master tri-mesh $M_{\tau_{tri}}^0 \ni \left\{P_{\tau_1}^0, P_{\tau_2}^0, P_{\tau_3}^0\right\}$ be defined from three master poles and their connectivities to three oriented segment chords as illustrated in Figure 2.28 and specified in Table 2.8

Table 2.8: Tri-mesh for a tortuous surface

Edge	Vertex	Frenet vectors	Curvatures	Master bi-mesh	Chord	Chord vector
$j=1$	$\mathbf{V}_A$	$\mathbf{T}_{A,1}, \mathbf{N}_{A,1}, \mathbf{B}_{A,1}$	$\boldsymbol{\chi}_{A,1}$	$M_{\tau_{bi,1}}^0 \ni \left\{P_{\tau_A}^0, P_{\tau_B}^0,\right\}$	$\overrightarrow{AB}:$	$\mathbf{e}_{\chi,1}^0 = \dfrac{(\mathbf{V}_B - \mathbf{V}_A)}{\|\mathbf{V}_B - \mathbf{V}_A\|}$
	$\mathbf{V}_B$	$\mathbf{T}_{B,1}, \mathbf{N}_{B,1}, \mathbf{B}_{B,1}$	$\boldsymbol{\chi}_{B,1}$			
$j=2$	$\mathbf{V}_B$	$\mathbf{T}_{B,2}, \mathbf{N}_{B,2}, \mathbf{B}_{B,2}$	$\boldsymbol{\chi}_{B,2}$	$M_{\tau_{bi,2}}^0 \ni \left\{P_{\tau_B}^0, P_{\tau_D}^0\right\}$	$\overrightarrow{BD}:$	$\mathbf{e}_{\chi,2}^0 = \dfrac{(\mathbf{V}_D - \mathbf{V}_B)}{\|\mathbf{V}_D - \mathbf{V}_B\|}$
	$\mathbf{V}_D$	$\mathbf{T}_{D,2}, \mathbf{N}_{D,2}, \mathbf{B}_{D,2}$	$\boldsymbol{\chi}_{D,2}$			
$j=3$	$\mathbf{V}_D$	$\mathbf{T}_{D,3}, \mathbf{N}_{D,3}, \mathbf{B}_{D,3}$	$\boldsymbol{\chi}_{D,3}$	$M_{\tau_{bi,3}}^0 \ni \left\{P_{\tau_D}^0, P_{\tau_A}^0\right\}$	$\overrightarrow{DA}:$	$\mathbf{e}_{\chi,3}^0 = \dfrac{(\mathbf{V}_A - \mathbf{V}_D)}{\|\mathbf{V}_A - \mathbf{V}_D\|}$
	$\mathbf{V}_A$	$\mathbf{T}_{A,3}, \mathbf{N}_{A,3}, \mathbf{B}_{A,3}$	$\boldsymbol{\chi}_{A,3}$			

Thereafter, let three new tangents be defined at the three corners as the average of the existing tortuosity pole tangents.
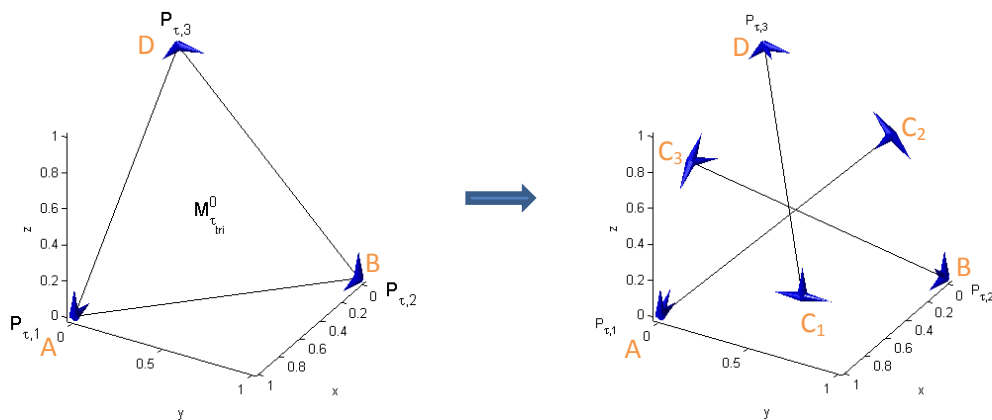
Figure 2.29: Master tri-mesh ABD, $k_\tau=0$ (left) subdivided into new poles ABDC$_1$C$_2$C$_3$, $k_\tau=1$ (right)

During the first iteration, a tri-pole constellation is extended by new orientation vectors at the existing poles as well as three new central poles C$_1$C$_2$C$_3$ at the middle of each of the master edges. The original poles ABC are extended with new tangents based on an average of the existing tangents. The three new tangents $\mathbf{T}_{C_1}$, $\mathbf{T}_{C_2}$, $\mathbf{T}_{C_3}$ of the central poles $P^1_{\tau_{C,1}}$ $P^1_{\tau_{C,2}}$ $P^1_{\tau_{C,1}}$ located at the three edges $j=1,2,3$ are defined from rectifying vectors $\mathbf{d}^1_{\tau_{C,1}}$ $\mathbf{d}^1_{\tau_{C,2}}$ $\mathbf{d}^1_{\tau_{C,3}}$, or they are estimated as the average of the tangents from the two adjacent master edges. At this stage the constellation represents a (six-noded) tortuous triangular element. In the following section a new central pole, called a beta-iterated tortuosity pole, will be defined.

Beta-iterated tortuosity poles
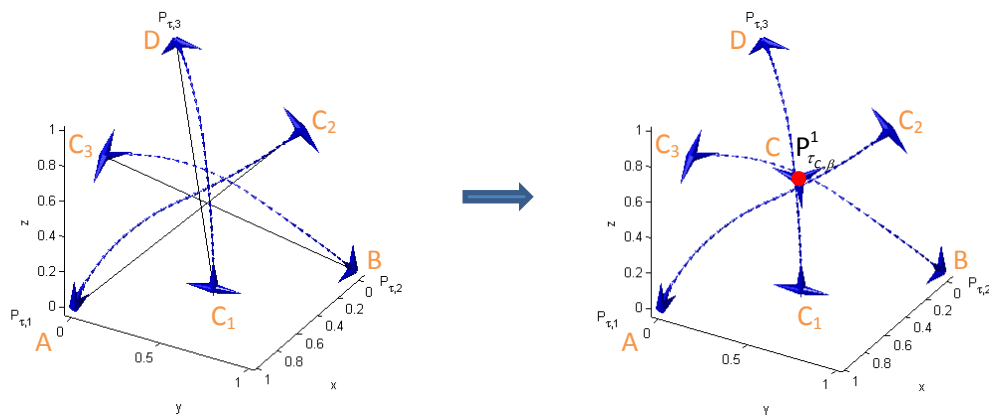
Figure 2.30: Tortuous curves C$_1$D, C$_2$A, C$_3$B (left). One new β-iterated tortuosity pole at $k_\tau=1$ (right)

From the three new poles $P^1_{\tau_{C,1}}$ $P^1_{\tau_{C,2}}$ $P^1_{\tau_{C,3}}$, which are connected by the chords $\overline{C_1 D}$ $\overline{C_2 A}$ $\overline{C_3 B}$, three new bi-meshes are used to generate three new curves (left) and to define the beta-iterated tortuosity pole $P^1_{\tau_{C,\beta}}$ (right) from (2.69). Hereby, four poles $P^1_{\tau_1}, P^1_{\tau_2}, P^1_{\tau_3}, P^1_{\tau_{C,\beta}}$ with $n^{\{F\}} \geq 3$ and three poles $P^1_{\tau_{C,1}}, P^1_{\tau_{C,2}}, P^1_{\tau_{C,3}}$ with $n^{\{F\}} \geq 2$ are formed.
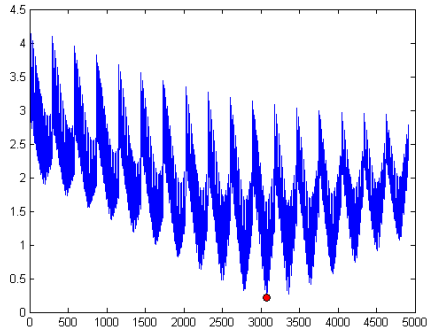
Figure 2.31: Full $|\beta|$-distance array

Figure 2.30 illustrates the values of the full distance for the three interior curves which are used to define the interior beta-iterated tortuosity pole $P^1_{\tau_{C,\beta}}$. In Figure 2.31, the abscissa holds the array indices for the pole combinations from the three curves. It is based on a subdivision by a local level of refinement set to five. This gives four thousand nine hundred and thirteen combinations. The ordinate holds the corresponding beta values defined by (2.69).

The plot of the full distance array clearly indicates that many local minima exist, even for curves generated by Frenet subdivision in its simplest form. The global solution index (marked in red) is used to locate $P^1_{\tau_{C,\beta}}$ at the centroid of the corresponding vertices, see Figure 2.30 (right) and Figure 2.32.

NOTE   Fundamentally, the beta-iteration is defined as a Catmull-Clark split (Catmull & Clark, 1978). However, since the surfaces are not regular tri- and quad faces the splitting relies on an iteration, which converges towards a singular vertex $\mathbf{V}_{C_\beta}$ for each split point rather than an NURBS based rule. This built-in non-linearity complicates the later imitation modeling by stochastic simulations. Later, in the stochastic parameterization, see 2.3.2.2, these "small" beta-perturbations are taken into account in the general stochastic formulation.
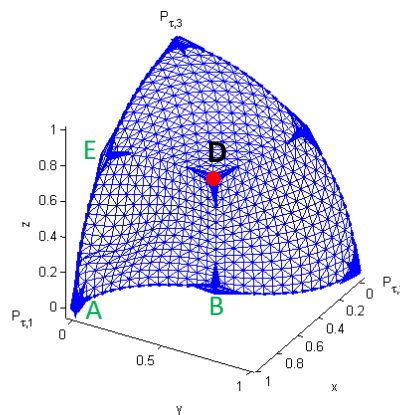
Figure 2.32: The seven tortuosity poles at $k_\tau = 1$ in solid blue and its triangular patch representation at $n_\tau = 5$

To obtain the iterated tri-mesh $n_\tau = 5$, seen in Figure 2.32, further subdivision for $k_\tau > 1$ is based on three quad-poles formed by the seven tortuosity poles $P^1_{\tau_1}, P^1_{\tau_2}, P^1_{\tau_3}, P^1_{\tau_{C,1}}, P^1_{\tau_{C,2}}, P^1_{\tau_{C,3}}, P^1_{\tau_C}$ at $k_\tau = 1$.

Quad-pole meshes are generated from a refinement approach which comprises formation of a master quad-mesh followed by a subdivision into four new quad-pole constellations. The subdivision process is finalized by a triangulation at the limit level of refinement see Figure 2.32.
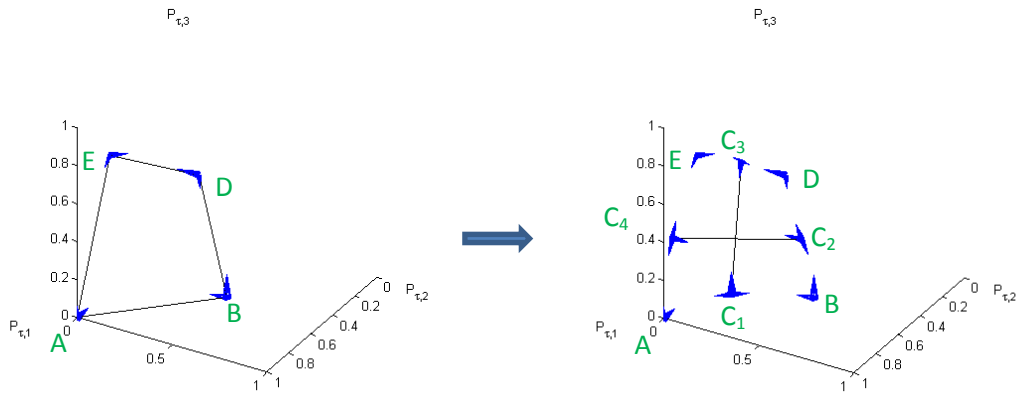
Figure 2.33: Quad-Pole ABDE (left) subdivided into four new central poles $C_1C_2C_3C_4$ (right)

Let a master quad-pole mesh $M^0_{\tau_{quad}} \ni \left\{P^0_{\tau_A}, P^0_{\tau_B}, P^0_{\tau_D}, P^0_{\tau_E}\right\}, n^{\{F\}} \geq 2$ be defined by four master poles and their four segment chords $\overrightarrow{AB} : \overrightarrow{BD} : \overrightarrow{DE} : \overrightarrow{EA}$, as specified in Table 2.9 and illustrated in Figure 2.33. (Note that this quad-pole is assumed to be a child of the master tri-pole in Figure 2.32, (left)).

From the quad-pole master mesh (Figure 2.33, left), one Frenet subdivision for each of the four sides (right) generates four new tortuosity poles. As a result, two new bi-meshes $\left\{P^0_{\tau,C1}, P^0_{\tau,C3}\right\}$, $\left\{P^0_{\tau,C2}, P^0_{\tau,C4}\right\}$, with $n^{\{F\}} \geq 2$, are formed. The settings so far represent an eight-noded tortuous quadrilateral master element.
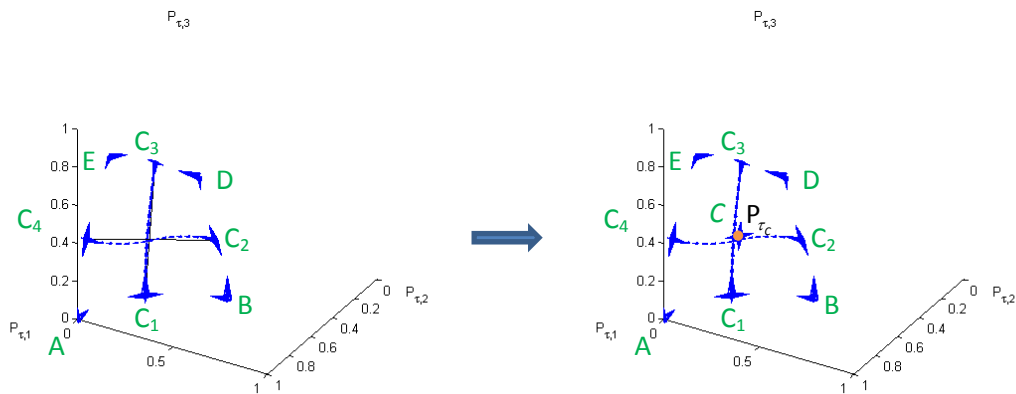
Figure 2.34: Tortuous curves $c_{\tau,1\text{-}3}$ and $c_{\tau,2\text{-}4}$ (left). One new interior tortuosity pole at C (right)

Subsequently, two bi-meshes $\left\{P_{\tau_{c,1}}, P_{\tau_{c,3}}\right\}$, $\left\{P_{\tau_{c,2}}, P_{\tau_{c,4}}\right\}$, with chords $\overrightarrow{C_1C_3}$ $\overrightarrow{C_2C_4}$ (Figure 2.34 left) and rectifying vectors, are used to iterate a new interior tortuosity pole $P^{k_\tau}_{\tau_c}, k_\tau < n_\tau$ at C, with $n^{\{F\}} \geq 2$, by Frenet subdivision (see Figure 2.34 right). This process results in four new master quad poles.

All details for the quad pole constellations are given in the following table:

Table 2.9: Quad-pole constellation for a tortuous surface

Edge	Vertex	Frenet vectors	Curvatures	Master bi Pole	Chords	Chord vector
$j=1$	$\mathbf{V}_A$	$\mathbf{T}_{A,1},\mathbf{N}_{A,1},\mathbf{B}_{A,1}$	$\mathbf{\chi}_{A,1}$	$M^0_{\tau_{bi,1}} \ni \left\{P^0_{\tau_A},P^0_{\tau_B}\right\}$	$\overrightarrow{AB}:$	$\mathbf{e}^0_{\chi,1}=\dfrac{\left(\mathbf{V}_B-\mathbf{V}_A\right)}{\left\|\mathbf{V}_B-\mathbf{V}_A\right\|}$
	$\mathbf{V}_B$	$\mathbf{T}_{B,1},\mathbf{N}_{B,1},\mathbf{B}_{B,1}$	$\mathbf{\chi}_{B,1}$			
$j=2$	$\mathbf{V}_B$	$\mathbf{T}_{B,2},\mathbf{N}_{B,2},\mathbf{B}_{B,2}$	$\mathbf{\chi}_{B,2}$	$M^0_{\tau_{bi,2}} \ni \left\{P^0_{\tau_B},P^0_{\tau_D}\right\}$	$\overrightarrow{BD}:$	$\mathbf{e}^0_{\chi,2}=\dfrac{\left(\mathbf{V}_D-\mathbf{V}_B\right)}{\left\|\mathbf{V}_D-\mathbf{V}_B\right\|}$
	$\mathbf{V}_D$	$\mathbf{T}_{D,2},\mathbf{N}_{D,2},\mathbf{B}_{D,2}$	$\mathbf{\chi}_{D,2}$			
$j=3$	$\mathbf{V}_D$	$\mathbf{T}_{D,3},\mathbf{N}_{D,3},\mathbf{B}_{D,3}$	$\mathbf{\chi}_{D,3}$	$M^0_{\tau_{bi,3}} \ni \left\{P^0_{\tau_D},P^0_{\tau_E}\right\}$	$\overrightarrow{DE}:$	$\mathbf{e}^0_{\chi,3}=\dfrac{\left(\mathbf{V}_E-\mathbf{V}_D\right)}{\left\|\mathbf{V}_E-\mathbf{V}_D\right\|}$
	$\mathbf{V}_E$	$\mathbf{T}_{E,3},\mathbf{N}_{E,3},\mathbf{B}_{E,3}$	$\mathbf{\chi}_{E,3}$			
$j=4$	$\mathbf{V}_E$	$\mathbf{T}_{E,4},\mathbf{N}_{E,4},\mathbf{B}_{E,4}$	$\mathbf{\chi}_{E,4}$	$M^0_{\tau_{bi,4}} \ni \left\{P^0_{\tau_E},P^0_{\tau_A}\right\}$	$\overrightarrow{EA}:$	$\mathbf{e}^0_{\chi,4}=\dfrac{\left(\mathbf{V}_A-\mathbf{V}_E\right)}{\left\|\mathbf{V}_A-\mathbf{V}_E\right\|}$
	$\mathbf{V}_A$	$\mathbf{T}_{A,4},\mathbf{N}_{A,4},\mathbf{B}_{A,4}$	$\mathbf{\chi}_{A,4}$			
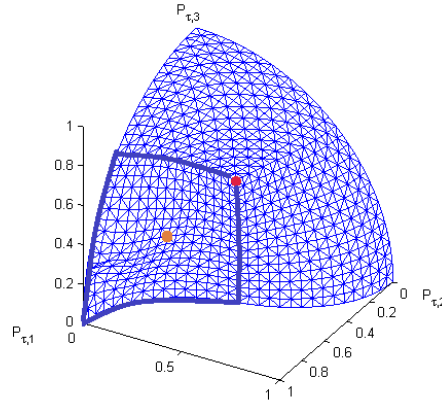
Figure 2.35: Quad-pole meshes are transformed into triangular patch graphics at the limit level n_τ

For further quad subdivision, the strategy illustrated in Figure 2.34 and Figure 2.35 is simply repeated for $k_\tau \in \left(...,n_\tau-2,n_\tau-1,n_\tau\right)$. Finally, at the limit level of refinement, where $k_\tau=n_\tau$, each of the generated quadrilaterals are subdivided into eight non-tortuous triangular faces sharing the same pole $P^{n_\tau}_{\tau_C}$.

As will subsequently be demonstrated, texture (i.e. irregularities and roughness) modeling is performed as master perturbations, as iterated perturbations, or as a mixture of both.

2.2.13.3   Master perturbations

Single-perturbation modeling

Frenet subdivision allows for master shape modeling by simple master perturbations. The constellation of a master mesh is modified through master perturbations. This means that one or more of the tortuosity pole components $(\mathbf{V},\mathbf{T},\mathbf{N},\mathbf{B},\mathbf{\chi})$, of one or more tortuosity poles, are manipulated. For constellations defined by master parameters, these parameters are manipulated instead of the actual vertices.
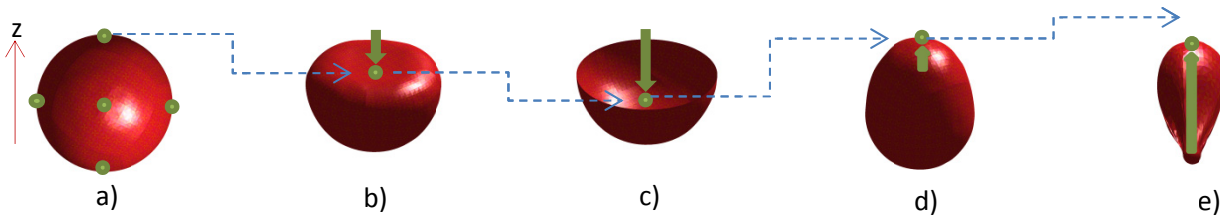
Figure 2.36: A six-poled master sphere (a) and four vertical master perturbations (b-e)
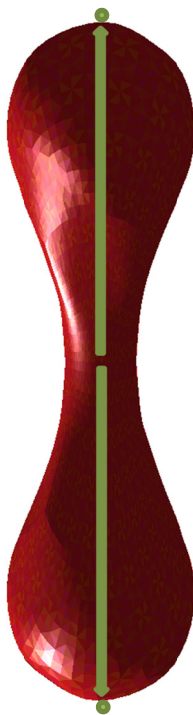
Figure 2.36 illustrates the impact from a vertical master location perturbation of the top pole (marked in green), of a six-poled master sphere (a). The impact from four different perturbations is illustrated for two downward and two upward perturbations respectively. All mesh generations are performed from Frenet subdivision in its simplest form. The actual perturbations are applied as follows: (b): downward, (c): significantly downward, (d): upward and (e): significantly upward.

Multi-perturbation modeling

Figure 2.37 shows the same six-poled master sphere as above but now with two vertical perturbations. The vertical perturbation at the top is similar to the perturbation in the image on the far right side of Figure 2.36. The second perturbation at the lower pole is of the same size, however, it is performed in the opposite direction (Here, this is in the downward direction).

As demonstrated, perturbation modeling is a free form tool that can be used by the modeler for single perturbations as well as for multi-perturbation modeling.

Figure 2.37: Double perturbations of the six-poled master sphere. One upward perturbation and one downward

2.2.13.4   Iterated perturbations

Multi-resolution modeling

Frenet subdivision allows for iterated perturbation modeling. In such modeling the iterated poles are manipulated directly by the modeler though the degrees of freedom array (2.34) applied at the beta-iterated poles.

$$k_\tau = 0 \qquad k_\tau = 1 \qquad k_\tau = 2 \qquad k_\tau = 3 \qquad k_\tau = 5$$
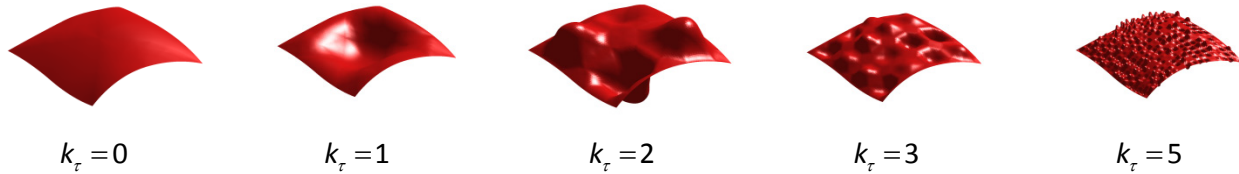
Figure 2.38: Random perturbations applied on a master quad-mesh at different levels of refinement

(Compare with the curves in Figure 2.21)

Surface perturbations are controlled by iterated perturbation parameters. As with curves, they are defined using local coordinate axes, see (2.34). For surfaces, the local axes are usually based on a common rectifying plane defined in the near neighborhood of a beta-iterated tortuosity pole. As an example, the first local axis is defined from one of the embedded curve tangents. The second axis is then oriented as the Gauss normal of the rectifying plane, defined by all or some of the embedded curves. Finally, the third axis is given as a cross product of the two.

At this stage it is too early to make definite conclusions about which local coordinate system is most useful. It is likely, that for each curve, surface, or volume of a natural object a prefered choice of local coordinates exists which would potentially optimize the modeling of its characteristic patterns.

2.2.13.5   Limit Curvatures of Tortuous Surfaces

During the last levels of refinement, when Frenet subdivision is applied in its simplest form, a limit tortuosity pole $P_{\tau_C}^{n_\tau}$ automatically specifies a unique approximate Gauss normal $\mathbf{n}_G \simeq -\mathbf{N}_C$. More precisely, the limit edges connected to this pole lie in the embedded osculating planes which all share the same normal. In the limit, the individual edges connected to the tortuosity pole possess asymptotic G^2 continuity. However, the distinct curvatures for each osculating plane must not to be confused with the analytic principal curvatures.

Obviously, particular regions designed to reflect geometric discontinuity by multi-valence poles with different orientation frames, do not fall into the category of regions where G^2 continuity exists in the limit.

2.2.14 Tortuous Solids

This paragraph explores how a tortuous solid generator can be defined using Frenet subdivision. Further details on the generation of solids by Frenet subdivision will be revealed in future studies and does not form an integral part of this study. Therefore, no illustrations are provided in this introduction to tortuous solid modeling. The following considerations are presented solely to complete the description of natural parameterization as a general tool for modeling tortuous curves, surfaces, and solids.

Here, subdivision from two mesh constellations called tetra-meshes and hexa meshes are described. For both subdivision approaches the separation into beta-simulations followed by alpha simulations occurs in the same way as for tortuous surface modeling. It is assumed that a solid observation mesh exists and that it has been discretized into a tetrahedral mesh.

In Frenet subdivision each tetrahedron represents a volume element made up of six edges and four faces. In principle, the subdivision scheme for volume follows the same strategy as for curves and surfaces since it is initiated from a master mesh M_τ^0 that can be subdivided into finer and finer iterated meshes $M_\tau^{k_\tau}$, $k_\tau = [1, n_\tau]$. The target at each level of refinement is to find a new set of central poles $\{P_{\tau_c}\}$. These poles are used to form new volumetric constellations defined as hexa-elements. Each new hexa-element includes twelve edges and eight faces. In Frenet subdivision each of these edges and faces are assumed to model tortuous curves and tortuous surfaces respectively. As such, the volumetric element that is formed represents a tortuous variant of the well-known quadrilaterally faced hexahedron. After each recurrence each hexahedron is subdivided into eight new hexahedrons. At the limit level of refinement the hexa-mesh is finally formed back into tetrahedrons for FEA based solid postprocessing.

Proposed algorithms

The following section proposes a parametric Frenet subdivision algorithm, which is able to generate a discretized solid as a tortuous mesh $M_\tau \ni \{P_\tau\}$ in $\mathbb{R}^3$. Mathematically, the algorithm is a logical extension of the tortuous curve and tortuous surface generators defined in 2.2.12 and 2.2.13 respectively. As a central part of the formula, the following recurrence relations are used:

$$M_\tau^{k_\tau} = S_{\tau_{\text{tetra}}}^{k_\tau} M_\tau^{k_\tau - 1} \tag{2.72}$$

$$M_\tau^{k_\tau} = S_{\tau_{\text{hexa}}}^{k_\tau} M_\tau^{k_\tau - 1} \tag{2.73}$$

Tetra-meshes

Tetra- meshes are subdivided from a refinement approach that involves the formation of a master tetra-pole constellation followed by a subdivision into new hexa-pole constellations at the first level of refinement.

Let a tetra-pole mesh $M_{\tau_{\text{tetra}}}^0 \ni \left\{P_{\tau_A}^0, P_{\tau_B}^0, P_{\tau_D}^0, P_{\tau_E}^0\right\}, n^{\{F\}} \geq 3$ be defined by four master poles with valence three that are inter connected with six oriented segment chords. At each of these six chords, six centrally located *edge poles* $\left\{P_{\tau_{E1}}^1, P_{\tau_{E2}}^1, P_{\tau_{E3}}^1, P_{\tau_{E4}}^1, P_{\tau_{E5}}^1, P_{\tau_{E6}}^1\right\}$ are defined as the first subdivision of the corresponding tortuous curves.

Subsequently, four new *face poles* $P_{\tau_{C,1}}^1$ $P_{\tau_{C,2}}^1$ $P_{\tau_{C,3}}^1$ $P_{\tau_{C,4}}^1$, which are centrally located at each of the four faces of the tri-mesh, are beta-iterated. The settings so far represent a (fourteen-noded) *tortuous tetrahedral master element*, i.e. four poles located at the master poles, six edge poles centrally located at the master edges and four face poles beta-iterated at the four triangular faces. Finally, a new central *volume pole* $P_{\tau_C}^1$ is estimated using the four face poles $P_{\tau_{C,1}}^1$ $P_{\tau_{C,2}}^1$ $P_{\tau_{C,3}}^1$ $P_{\tau_{C,4}}^1$ and the four opposing master poles. This new beta-iterated volume pole has valence $n_{\{F\}} = 4$. The new volume pole and the fourteen existing poles are then formed into four new hexahedra. As will be described, each hexahedron can be further subdivided into new and finer hexa-meshes.

Hexa-meshes

Hexa-meshes are subdivided using a refinement approach comprised of the formation of a master hexa-mesh, followed by a subdivision into new finer hexa-meshes. At the limit level of refinement, these meshes are eventually subdivided into sixteen tetrahedrons per hexahedron for FEA postprocessing.

Let a hexa-pole mesh $M_{\tau_{\text{hexa}}}^1 \ni \left\{P_{\tau_A}^1, P_{\tau_B}^1, P_{\tau_D}^1, P_{\tau_E}^1, P_{\tau_F}^1, P_{\tau_G}^1, P_{\tau_H}^1, P_{\tau_I}^1\right\}$ be defined from eight master poles with valence three and its internal connectivities by twelve corresponding bi-meshes. First, twelve edge poles $\left\{P_{\tau_{E1}}^2, P_{\tau_{E2}}^2, P_{\tau_{E3}}^2, P_{\tau_{E4}}^2, P_{\tau_{E5}}^2, P_{\tau_{E6}}^2, P_{\tau_{E7}}^2, P_{\tau_{E8}}^2, P_{\tau_{E9}}^2, P_{\tau_{E10}}^2, P_{\tau_{E11}}^2, P_{\tau_{E12}}^2\right\}$ are defined like for the tetrahedron bi-meshes. Then, the six new face poles $P_{\tau_{C,1}}^2$ $P_{\tau_{C,2}}^2$ $P_{\tau_{C,3}}^2$ $P_{\tau_{C,4}}^2$ $P_{\tau_{C,5}}^2$ $P_{\tau_{C,6}}^2$, are beta-iterated at at each of the six quadrilateral faces. The settings so far represent a (twenty-six-noded) *tortuous hexahedral element.* This means that twelve edge poles, six face poles, and eight master poles, centrally located at the master edges as well as six central face poles have been generated. Finally, a new central volume pole $P_{\tau_C}^2$ is estimated using three bi-meshes formed by opposite pairs of the six face poles $P_{\tau_{C,1}}^2$ $P_{\tau_{C,2}}^2$ $P_{\tau_{C,3}}^2$ $P_{\tau_{C,4}}^2$ $P_{\tau_{C,5}}^2$ $P_{\tau_{C,6}}^2$. The new tortuosity pole has the pole valence $n_{\{F\}} = 3$.

From this volume pole and the twenty-six existing poles, eight new hexa-meshes are formed. In subsequent subdivision $k_\tau = 3, \ldots, (n_\tau - 1)$, these hexahedrons are subdivided into new and finer hexa-meshes following the same procedure. At the limit level of refinement $k_\tau = n_\tau$ four new bi-meshes are formed from the diagonals of the hexahedron. Eventually, a central volumetric pole $P_\tau^{n_\tau}$ is beta-iterated from these bi-meshes. The new pole has the valence four. This central pole is ultimately used as a common pole for the formation of sixteen non-tortuous volumetric tetra-elements. The total mesh of these tetra-elements can then be imported and postprocessed by FE-based multiphysics software.

2.2.15 SUMMARY – Parameter Extraction

Let a set of observation meshes $\{M_{obs}\}$ be examined by experts and then let a three step parameterization chain be defined as follows. First, all vertices of each observation mesh are size normalized and set of size parameters $\{q^0_{\|\Omega\|}\}$ are obtained. Then, landmark parameters $\{q^0_P\}$, defined by expert knowledge, are identified. Subsequently, a set called master parameters are formed as $\{q^{k_\tau}\}$. Constellations, defined by tortuosity poles and segments, are then organized into a master mesh. From these master meshes, iterated parameters $\{q^{k_\tau}\}$ are finally extracted using Frenet subdivision in accordance with the concept of goodness of replication.

The parameter extraction chain

Bounding, Segmentation and Subdivision → **The Master Mesh**
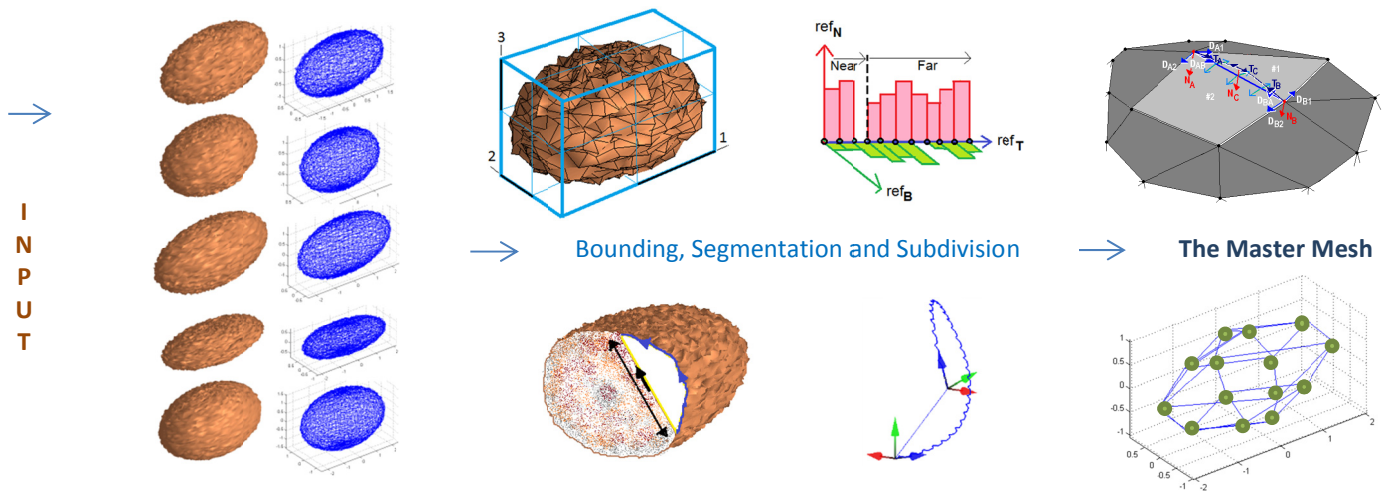
Figure 2.39: The parameter extraction process

The overall parameter extraction chain is defined as

$$\{M_{obs}\} \rightarrow \{q^0\} \rightarrow \{q^{k_\tau}\} , \quad \{q\} \ni \{q^0, q^{k_\tau}\} \tag{2.74}$$

The outcome of a parameter extraction process is a set of natural parameters $\{q\}$. These natural parameters are formed by a subset of master parameters $\{q^0\}$ and a subset of iterated parameters $\{q^{k_\tau}\}$.

Formalization of parameter extraction through Frenet subdivision

The following section summarizes the application of the concept of goodness of replication to Frenet subdivision and highlights some of the most important achievements.

Let it be assumed that the observations of a sample of natural objects are organized in observation meshes $\{M_{obs}\}$ in $\mathbb{R}^3$. Further, let it be assumed that these observation meshes are replicated by phantoms $\{M_{phan}\}$, which have been generated by multiresolution parametric Frenet subdivision after applying the concept of goodness of replication. Finally, let it be assumed that there exists a unique set of natural parameters q in $\mathbb{R}^1$ which are determined from observations.

These parameters are real valued quantities, determined for each single object during its replication, and represent the *DOF variables* of the model. The natural parameters are divided into two subsets:

The first subset, called *master parameters* $\{q^0\} \in q$, control the *size, bounding dimensions,* as well as the location and orientation of *landmarks.*

The second subset, called *iterated parameters* $\{q^{k_\tau}\} \in \{q\}$, control the tortuous *shape* of the subdomains by curves, surfaces, and volumes generated by Frenet subdivision (see Table 2.4).

Frenet subdivision is a general approach for tortuous mesh generation. It enables the parameterization of meshes that can be generated in the limit with explicit G^1 continuity and asymptotic G^2 continuity. However, the simulated tortuous mesh $M_\tau^{n_\tau}$ at the limit level of refinement is retransformed by an affine transformation into its original coordinates as a phantom M_{phan}.

$$M_\tau^{n_\tau} \to M_{phan} \qquad\qquad (2.75)$$

The parameterization is performed in order to achieve minimum tortuosity of the mesh, in accordance with the concept on goodness of replication.

Tortuosity poles as the basis for mesh generators

Operationally, Frenet subdivision is controlled by a master mesh, M_τ^0. The master mesh is expressed in terms of natural parameters q, which are further divided into master parameters q^0 and iterated parameters q^{k_τ}. Technically, these operations are defined by tortuosity poles, which are paired into bi-poles. Each of these bipoles is then used to define bi-meshes from selected frames of the tortuosity poles.

All in all, various constellations of tortuosity poles can be formed as the starting point for meshing.

A few such master pole constellations are in use:

- Master bi-poles are used to represent constellations of two tortuosity poles forming one edge.
- Master tri-poles and quad-poles represent constellations of three or four tortuosity poles forming one face with three or four edges respectively.
- Master tetra-poles and hexa-poles represent constellations of four or eight tortuosity poles forming four or six faces with four or twelve edges respectively.

Tortuous mesh generators are developed with the following characteristics:

- Tortuous curve generators are based on bi-meshes and simulate tortuous meshes of line elements having location vectors, orientation vectors, and curvatures as children.
- Tortuous surface generators are based on tri-poles or quad-poles and simulate tortuous meshes of face elements having tortuous curves as children.
- Tortuous solid generators are based on tetra-poles or hexa-poles and simulate tortuous meshes of volume elements having tortuous surfaces as children.

The concept of goodness of replication applied to Frenet subdivision is a deterministic approach dedicated to parameter extraction. The following paragraph focuses on how to reuse these extracted parameters for stochastic simulations.

In a multi-resolution parameter extraction process, the iterated parameters are extracted at relevant levels of refinement only.

$$q^{k_\tau} = \left\{ q_\xi^{k_\tau}, q_f^{k_\tau} \right\} \ , \ \forall k_\tau \in \left\{ k_{\tau_{relevant}} \right\} = \left\{ k_{1_{relevant}}, ..., k_{n_{relevant}} \right\} \ , \ n_{relevant} \in \left[1, n_\tau \right] \tag{2.76}$$

2.3 STOCHASTIC PARAMETERIZATION

In this section, the set of natural replication parameters is used as a sample for modeling corresponding random variables from stochastic processes. It is assumed that these natural parameters can be stored in a data bank, which is continuously updated so objects are better and better described over time (see paragraph 2.3.1). A stochastic decomposition approach, relevant for parametric subdivision, is introduced in paragraph 2.3.2. Following this, a strategy for stochastic simulation of natural objects is formulated based on Monte Carlo simulation (see 2.4.1). Finally, a novel concept called goodness of imitation is introduced as a criterion for "stochastic fitting" (see 2.4.3). It is intended to ensure that the stochastic variations of newly simulated phantoms do not differ significantly from the variations observed in the real objects.

2.3.1 The Bank of Natural Parameters

The set of natural parameters $\{q\}$ resulting from replication are assumed to be the outcome of experiments and they are modeled as random variables $Q: \{q\} \rightarrow Q$. Both the first moment (the mean μ_Q) and the second central moment (the variance σ_Q^2) are assumed to exist for each variable. The probability density function (PDF) for each parameter is also required for later Monte Carlo simulation.

If a parameter is observed by association through another parameter, such as the time, it is assumed to be modeled by an indexed set $\{Q(t) , t \in T\}$ of random variables $Q(t)$. These variables are all defined by the same sample space Ω_q, with the index t belonging to an index window T. Such statistics are stored in what is called a *bank of natural parameters,* or simply a *parametric bank,* symbolized as $\widehat{Q}(t)$. The general analysis of the parametric bank by multivariate data processing, i.e. chemometrics, is not covered by this study. However, a piloting principal component analysis (PCA), for detection of outliers from parameters in the wheat grain case study of cross-sections, is reproduced in ANNEX 22-23.

2.3.2 Stochastic Decompositions

This paragraph discusses the rationale for decomposing the natural parameters from the parametric bank into both a steady, and a fluctuating component, during the imitation process of natural geometries. Based on the well-known Reynolds decomposition, an altered version, called alpha-beta decomposition, is introduced. This altered decomposition allows for small variations to be included in the steady component. It is important to notice that the previously defined master meshes now are seen as geometrical constellations, which are parametrically invariant to geometrical dependencies. This means that although size, form, and shape may be dependent, the parameters used for modeling are assumed to be independent and therefore uncorrelated. This assumption is also assumed to be valid for all types of natural parameters, i.e. all types of master parameters and iterated parameters.

2.3.2.1 Reynolds Decomposition

The historic Reynolds decomposition[27], named after Osborne Reynolds (23 August 1842 – 21 February 1912) and introduced in 1851 by Sir George Gabriel Stokes, 1st Baronet FRS (13 August 1819–1 February 1903), represents a stochastic decomposition. It is frequently used in an Eulerian description to decompose stochastic fluid flow into two parts as

$$Q = Q' + \mu_Q , \tag{2.77}$$

where $Q = Q(t = t^\Theta)$ is the stochastic field vector defined at a particular instant t^Θ of the parameter, t (usually time). $Q' = Q'(t = t^\Theta)$ is the time dependent *fluctuation* modeled as a random variable with zero mean $\mu_{Q'} = 0$ and μ_Q its time average over an appropriate time window.

2.3.2.2 Alpha-beta Decomposition

For surface modeling by Frenet subdivision, the numerical complication in the determination of the beta factor (see (2.69)) must be accounted for. This numerical difficulty, which arises from lack of information, introduces an error. In an attempt to compensate for this error, the use of dedicated stochastic decomposition is introduced. More specifically, a variant of Reynolds decomposition is proposed.

It will be illustrated that for extreme value modeling there is a general need for flexible decomposition tools that allow for pseudo-stochastic parametric subdivision.

Let it be assumed that a stochastic process of a natural parameter $Q(t)$ is extracted from a natural object and made available from a parametric bank $\widehat{Q}(t)$, i.e.

$$Q(t) \leftarrow \widehat{Q}(t) , \tag{2.78}$$

where $\{Q(t) , t \in T\}$ is an indexed set of random variables $Q(t)$. These variables are all defined on the same sample space Ω_q with the index t [28] from an index window T.

Further, let it be assumed that $Q(t)$ is defined with mean value function $\mu_Q(t)$ and variance function $\sigma_Q^2(t)$.

---

[27] In latest CFD software Reynolds-decomposition is used to form the so-called time averaged RANS equations which is an abbreviation for Reynolds-averaged Navier–Stokes equations (ANSYS®14, 2012). For further details on RANS and a general introduction to Computational Fluid Dynamics (CFD) and the finite volume method see (Versteeg H.K. & Malalasekera W., 2007).

[28] For natural objects the index t might represent the time in a life-cycle or an index for a natural evolution stage.

Then, at an instant $t = t^\Theta$, an *alpha-beta decomposition* of $Q = Q(t = t^\Theta)$ is introduced as a simple linear combination of two independent random variables[29]:

$$Q = Q_\alpha p_\alpha + Q_\beta \ , \qquad (2.79)$$

In (2.79), the variable Q_α is called the alpha variable, p_α is called the perturbation level, and Q_β is called the beta variable. The multiple $Q_\alpha p_\alpha$ usually models the dominant fluctuations, whereas Q_β models the non-dominant (small) fluctuations, i.e. Q_β is usually semi-steady. The alpha variable Q_α is defined as a dimensionless random variable with zero mean $\mu_\alpha = 0$, and a variance of one $\sigma_\alpha^2 = 1$. It represents a standardized random variable, whereas Q_β is defined with a real valued mean μ_β and a variance σ_β^2 which is usually smaller than p_α^2. The perturbation level p_α reflects the standard deviations of the dominant variations. Therefore, it has the same physical dimension as Q.

$$\dim p_\alpha \equiv \dim Q \qquad (2.80)$$

The mean value for Q is now defined as

$$\mu_Q = \mu_\alpha p_\alpha + \mu_\beta = \mu_\beta \ , \qquad \mu_\alpha \equiv 0 \qquad (2.81)$$

Since the two decomposed random variables are independent, i.e. $\mathrm{Cov}\left[Q_\alpha, Q_\beta\right] = 0$, the variance for Q is

$$\sigma_Q^2 = \sigma_\alpha^2 p_\alpha^2 + \sigma_\beta^2 + 2 p_\alpha^2 \mathrm{Cov}\left[Q_\alpha, Q_\beta\right] = \left(1 + r_{\alpha\beta}^2\right) p_\alpha^2, \quad \sigma_\alpha^2 \equiv 1, \qquad (2.82)$$

where the (small) factor

$$r_{\alpha\beta}^2 = \frac{\sigma_\beta^2}{p_\alpha^2} \ll 1 \qquad (2.83)$$

is denoted the *variance ratio*. It defines the ratio between the non-dominant and the dominant standard deviations of the fluctuations, i.e. $r_{\alpha\beta} = +\sqrt{r_{\alpha\beta}^2} = \sigma_\beta p_\alpha^{-1}$.

However, any variable $Q = Q_\alpha p_\alpha + Q_\beta$ where its alpha component stabilizes around a zero mean, i.e. $\mu_\alpha \to 0$, can be represented by two alternative input parameters. They are: the perturbation level p_α, and the variance ratio $r_{\alpha\beta}^2$. In accordance with (2.81) and (2.82), the simple transformation from original to alpha-beta decomposed input parameters is given by:

---

[29] In this presentation techniques for the determination and convolution of the PDFs for the two decomposed parts are not covered. However, if the PDF for the original variable follow the normal (or Gaussian) distribution then both decomposed parameters follow the normal distribution. In the following, it is anticipated that the PDF used are well-defined and mathematically modeled as a function $f_Q(q)$ with a set of input parameters as arguments. As an example the normal (or Gaussian) distribution for a variable Q requires the two input parameters: mean value and standard deviation and is symbolized as $f_Q(q) = f_Q(\mu_Q, \sigma_Q)$.

$$\mu_\beta \equiv \mu_Q \,, \qquad p_\alpha = \frac{\sigma_Q}{\sqrt{1+r_{\alpha\beta}^2}} \,. \tag{2.84}$$

Note that alpha-beta decomposition is statistically identical to the wellknown Reynolds decomposition when the variance ratio $r_{\alpha\beta}^2$ is zero.

From a simplified geometric point of view, the statistical mean location μ_β of the semi-steady factor Q_β affects the *central appearance* of the underlying natural geometry, whereas its standard deviation σ_β, affects its small deviations around this central appearance. The dominant statistical dispersion is governed by the dominant fluctuation multiple $Q_\alpha p_\alpha$, which affects both the variations of the current shape, and ts local dimensions. Technically, alpha-beta decomposition enables customized imitation modeling since the modeler can control the two parts either by the variance ratio or by the perturbation level. Because the alpha and beta parts are also independent, the realizations q_α, q_β can be simulated either by two independent runs, or, by scaling from one run using the original (non-decomposed) input parameters. As mentioned earlier, in principle the perturbation level is an instrument proposed for application as a technical tool to handle numerical errors induced by beta-simulations of new tortuosity poles of surfaces and solids. Furthermore, the perturbation level is a rational factor in synthetic phantom generation where data is not available for a full stochastic imitation. In these situations, the modeler may need to supplement the data set with deterministic or semi-deterministic values. Then during subsequent simulations, the perturbation level can be changed and the immediate effect on the generated phantom can be inspected. In fact, this type of synthetic modeling is evident in all of the examples and illustrations, including perturbation modeling, throughout this presentation.

EXAMPLE 7   Alpha-beta decomposition of a location parameter for a surface generated by Frenet subdivision

Let it be assumed that parameter extraction by Frenet subdivision from observations of a surface, result in a set of natural parameters. In this example, one particular location parameter is in focus. Now, assume this parameter to be modeled by a random variable. If Frenet subdivision is applied during parameter extraction then, in accordance with (2.69), the location is found from a minimization of a distance error. This error varies in two ways: along the local directions, and from replication to replication. This error is represented as a random error-vector. One of its error-components is assumed to be modeled as a random variable Q_β .
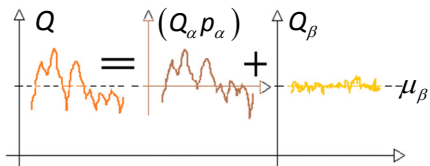
After having performed a high number of replications for similar surfaces, estimates for its mean μ_β and variance σ_β^2 are assumed to exist. Furthermore, during the many replications, a mean value $\left(\mu_\alpha p_\alpha\right)$ and variance $\left(\sigma_\alpha p_\alpha\right)^2$ are assumed to be extractable from alpha replications where the actual alpha location parameter is modeled as a variable $\left(Q_\alpha p_\alpha\right)$.

Consequently, if $\left(\mu_\alpha p_\alpha\right) \to 0$ and $\sigma_\alpha^2 \equiv 1$, the location parameterization through alpha-beta composition can be said to reflect an alpha-beta decomposition $Q = Q_\alpha p_\alpha + Q_\beta$ with variance ratio $r_{\alpha\beta}^2 = \sigma_\beta^2 \left(\sigma_\alpha p_\alpha\right)^{-2}$ and perturbation level $p_\alpha = \sigma_\beta r_{\alpha\beta}^{-1}$.

In other situations, synthetic modeling can be based on statistical information that is deterministically manipulated. This type of geometry generation is called pseudo-stochastic perturbation modeling. For this type of modeling, the perterbution level is not restricted to its usual limitations. Rather, it can be defined freely to fulfill modeler's requirements. It is not seen as a strict PDF input parameter, but as a tuning factor for forced extreme value generations. Furthermore, since the perturbation level is allowed to go beyond its natural limits, it allows the modeler to simulate forced natural abnormalities in all their forms. This is, for example, the case for geometrical forms that appear with extremely small probability and which are unlikely to be realized, even if the simulation includes a high number of runs. For an example of modeling extreme values, compare the abnormal egg illustrated in a), Figure 1.7: Geometrical abnormalities of eggs, with the synthetic (i.e. pseudo-stochastic) simulation in Figure 2.26 (right).

2.4   REPARAMETERIZATION

This section begins by focusing on stochastic simulation of master and iterated parameters for the generation of imitation meshes (see 2.4.1). Hereafter, a novel concept called "goodness of imitation" is introduced to accommodate stochastic simulations from natural parameters (see 2.4.3).

2.4.1   Stochastic Simulations

Realization of any random variable Q, from a numeric random number function* is denoted as $\hat{q}$. By applying alpha-beta decomposition on Q, a realization $\hat{q}$ can then be seen as the outcome of a Monte Carlo simulation generated in two tempi as

$$\hat{q} = \hat{q}_\alpha p_\alpha + \hat{q}_\beta , \tag{2.85}$$

where the simulation of the beta factor is run first, i.e.

$$\hat{q}_\beta \leftarrow \hat{f}_{Q_\beta}(\mu_Q, r_{\alpha\beta} p_\alpha) \tag{2.86}$$

and the simulation of the alpha factor is run next, i.e.

$$\hat{q}_\alpha \leftarrow \hat{f}_{Q_\alpha}(0,1) . \tag{2.87}$$

The total run $\hat{q} = \hat{q}_\alpha p_\alpha + \hat{q}_\beta$ is called an alpha-beta simulation. Individually, the first run $\hat{q}_\beta$ is called the beta-simulation and the second run $\hat{q}_\alpha$ the alpha-simulation.

In general, various rules can be applied for any parameterization. In the following algorithm, location parameters are resimulated at level of refinement where they are active. The values of orientation parameters at the first level are kept active at all of the subsequent levels of refinement.

Alternatively, when the non-decomposed input parameters (μ_Q, σ_Q) are available, and beta-simulations are not required, then the parameter simulation can be performed simply as

$$\hat{q} \leftarrow \hat{f}_Q(\mu_Q, \sigma_Q) \tag{2.88}$$

This simplified simulation strategy (2.88) holds for curves generated by Frenet subdivision.

*NOTE   A "hat" over a PDF such as $\hat{f}_Q(\cdot)$ is used to emphasize that it is a random number function[30] for that PDF.

---

[30] Random number functions are provided by various software packages. In the MATLAB® 2012a Statistics Toolbox the `betarnd` (Beta random numbers), `binornd` (Binomial random numbers), `chi2rnd` (Chi-square random numbers) represent the first three random number generators from a long list of such built-in functions. Up till three input parameters are in use for some of the MATLAB® built-in random number generators.

EXAMPLE 8   Principle pseudo-stochastic simulation of rough half-circle by post-perturbations

Figure 2.40: Principle of pseudo-stochastic simulations of rough half-circle at three different perturbation levels
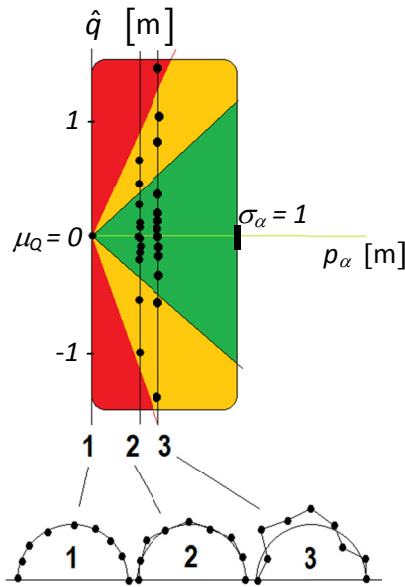
Let an approximation of a half circle geometry be alpha-simulated by a Frenet subdivision, i.e. $r_{\alpha\beta} = 0.0$ at the levels $k_\tau = 1,...,3$. This means that the total number of simulated vertices in the approximating polyline is $n_i = 2^{k_\tau} + 1 = 2^3 + 1 = 9$. Let it be further assumed that the radial perturbation of each of the corresponding nine vertices is modeled by the same Gauss distributed random variable Q with an estimated mean value of $\mu_Q = 0 [m]$. The rough half-circles are simulated by varying the perturbation levels from one simulation to another: $p_\alpha \in \left[p_{\alpha,1} = 0, \ p_{\alpha,2}, \ p_{\alpha,3} \right] [m]$.

Since the variance ratio is set to zero $r_{\alpha\beta} = 0.0$, the stochastic decomposition here is identical to the conventional Reynolds decomposition.

Therefore, geometric simulations based on alpha-beta decomposition give exactly the same results as simulations based on Reynolds decomposition for the same underlying random variable. However, the perturbation level assists in the modeling of arbitrary rough geometries and acts as a tool to generate pseudo-stochastic realizations when little or no statistical information is available. By setting all variance values to zero, purely deterministic geometry generation can be performed as well.

In conclusion, alpha-beta decomposition can be said to be a unified technical tool that enables simulations to be run in a variety of ways; from full stochastic simulation of rough surfaces, to pseudo-stochastic perturbation simulation, to purely deterministic geometry generation.

NOTE   The naming "alpha-beta" refers to the interpretation of the alpha-beta decomposition as a crowd of lines passing through a point $\left(0, \mu_\beta \right)$ and points $\left(1, \hat{q}_\alpha \right)$ in a $\left(p_\alpha, \hat{q} \right)$ realization space where $\hat{q}_\alpha$ represents the "slope" for each realization and μ_β, the "constant" when $r_{\alpha\beta} = 0.0$. Therefore, realizations can intuitively be displayed in a $\left(p_\alpha, \hat{q} \right)$ diagram as in Figure 2.40.

134

2.4.2 Imitation Problems

A parametric master mesh is said to be "badly-shaped" if its parameters are not mutually independent, i.e. if geometric symmetries or anti-symmetries are not decoupled despite the fact that they are not statistically correlated. In this sub-section it is the aim to develop a unified decision rule to test the following hyphothesis:

- "The stochastic behavior of the alpha-beta simulated imitation mesh does not differ significantly from the stochastic behavior of the underlying natural object".

It will be demonstrated how alpha-beta decomposition is integrated into such a decision rule. Mathematically, the formulation of this rule is formed by what is called an *imitation problem*.

Let it be assumed that the underlying observation domain (cluster, subcluster, object or subdomain) is size normalized (see 2.2.10.2.1). To measure the goodness of imitation a new measure $\eta_{imi} \in [0,1]$, called the *efficiency of imitation,* is introduced as $\eta_{imi} = 1 - \alpha_{two}$. The factor α_{two} is a significance level for a two-sample test which compares the distribution of values in two data vectors. Furthermore, let it be assumed that a sample of observation meshes $\{M_{\tau, obs_i}\}, i = 1, ..., n_{obs}$ and a set of alpha-beta simulated phantoms $\{M_{\tau, \alpha\beta_i}\}, i = 1, ..., n_{phan}$ exist at predefined levels of refinement $k_\tau \in [1, ..., n_\tau]$. Further, let there exist two $n_\mho$-tuples of indicator metrics for each segment. One set $m_{\mho_{obs}} = \left(m_{\mho_{obs,1}}, ..., m_{\mho_{obs,n_{obs}}} \right)$ represents indicators for the observation mesh segments, whereas the other set $\hat{m}_{\mho_{\alpha\beta}} = \left(\hat{m}_{\mho_{\alpha\beta,1}}, ..., \hat{m}_{\mho_{\alpha\beta,n_{phan}}} \right)$ represents indicators for the phantom. Similarily, let there exist two $n_\mho$-tuples of first integrals. One set $\int d\Omega_{obs} = \left(\int d\Omega_{obs,1}, ..., \int d\Omega_{obs,n_{obs}} \right)$ represents first integrals for the observation meshes, whereas the other set $\int d\Omega_{\alpha\beta} = \left(\int d\Omega_{\alpha\beta,1}, ..., \int d\Omega_{\alpha\beta,n_{phan}} \right)$ represents first integrals for the phantoms. A stochastic meshing process is said to imitate the underlying object if:

a) The distribution of the alpha-beta simulated phantom indicators $\hat{m}_{\mho_{\alpha\beta,i}}$ for the mesh segments does not differ significantly from the distribution of the observed indicators $m_{\mho_{obs}}$ in a two-sample test.

b) The distribution of first integrals of the alpha-beta simulated phantoms $\int d\Omega_{\alpha\beta}$ does not differ significantly from the distribution of the first integrals of the observed meshes $\int d\Omega_{obs}$ in a two-sample test.

These two conditions are unified and incorporated in the following variational problem:

$$\min J_{|\beta|}: \quad \frac{\alpha_{two}}{1 - h_{imi}} \le \alpha_{two_{upp}} \quad , \quad \forall i \in 1, ..., n_{\alpha\beta}, \ h_{imi} \ne 1, \quad \quad (2.89)$$

where $J_{|\beta|}$ is the beta functional, $\alpha_{two_{upp}}$ is an upper limit for the significance level,[31] and h_{imi} is an imitation test factor defined in ANNEX 15.

---

[31] The efficiency of imitation is said to be "high" if α_{two} is not bigger than five percent.

A low value for the imitation test factor ensures that the overall size is well represented. This means that the used master mesh is not badly shaped in respect to average size replication. The test parameter h_{imi} is used to identify significant differences between the distribution of a set of indicator metrics for the real object, and its imitations. If the test factors equal zero for all compared pairs of imitation metrics, the shape dispersion of the imitations does not differ from the shape dispersions of the real objects. (For more details see ANNEX 15).

2.4.3   Goodness of Imitation

The numerical testing of the two criterions included in (2.89) is the essence of what is referred to as the concept of goodness of imitation. It is designed to ensure that imitated meshes do not differ significantly from the original geometry in terms of location and dispersion. In general, the dual purpose is to stabilize the mean shape of the domain while at the same time to controlling boundary variations. As with the concept of goodness of replication (see 2.2.2), the concept of goodness of imitation is built on indirect comparisons of indicators, i.e. it is indicative only.

2.4.4   SUMMARY – Reparameterization

Reparameterization is the process of generating phantoms that imitate a natural object. By reusing the parameters from a bank of natural parameters, alpha-beta simulation aims to imitate the underlying stochastic nature of the natural object. By applying the concept of goodness of imitation it is assured that the reused master mesh represents a feasible model. The following process chain defines the entire reparameterization process from a parameterized master mesh to its stochastic phantoms.

The Master Mesh
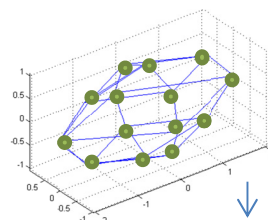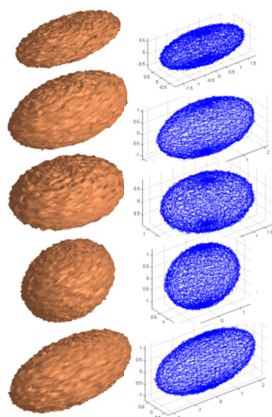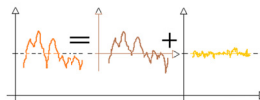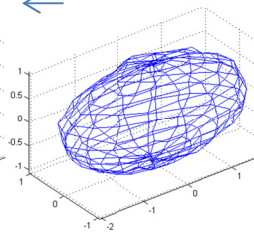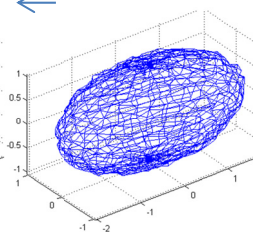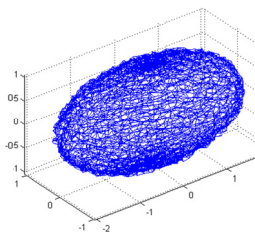
Figure 2.41: The reparameterization process

136

Mathematically, the reparameterization process illustrated in

Figure 2.41 can be defined as

$$\{q\} \to \{Q_\alpha p_\alpha, Q_\beta\} \to \{\hat{q} = \hat{q}_\alpha p_\alpha + \hat{q}_\beta\} \to \{M_\tau^0\} \to \left(\{M_{\tau_{phan}}\} \leftarrow \{M_{\tau,\alpha\beta}^{n_\tau}\} \leftarrow \bar{S}_\tau \{\bar{M}_\tau^0\}\right) \qquad (2.90)$$

In (2.90) it is assumed that a set of master meshes $\{M_\tau^0\}$ and their natural parameters q are size normalized and extracted from a set of observation meshes $\{M_{\tau_{obs}}\}$. Thereafter, these natural parameters q are modeled as a set of random quantities $\{Q\} \to \{q\}$, which belong to some stochastic processes $\{Q(t)\}$. They are treated by chemometrics and for each degree of freedom their statistics are stored in a parametric bank $\widehat{Q}(t)$.

Later, they are redrawn $Q \leftarrow Q(t) \leftarrow \widehat{Q}(t)$ for stochastic simulations. It is anticipated that each of these random DOF quantities Q are decomposed into two artificial random variables Q_α, Q_β by alpha-beta decomposition $Q = Q_\alpha p_\alpha + Q_\beta$. Here, Q_α is the alpha factor, p_α the perturbation level, and Q_β the beta factor. The decomposet variables are then Monte Carlo simulated and a set of realizations all defined as $\hat{q} = \hat{q}_\alpha p_\alpha + \hat{q}_\beta$ are formed. The master parameters are used to form a realization of the master mesh $\{\hat{q}\} \to \{M_\tau^0\}$. Subsequent alpha-beta iterations of this master mesh, controlled by the iterated parameters, form the limit mesh $\{M_{\tau,\alpha\beta}\}$.

The algorithmic determination of the alpha-beta iterations, and the following reparameterization into stochastic imitations, is controlled by an imitation problem. This imitation problem is mathematically formulated as a variational problem.

Technically, some of the imitated phantoms are not feasible imitations and must be rejected. However, the remaing set of feasible stochastic phantoms are said to be good imitations of the underlying object.

Finally, by size re-normalization these imitations can be transformed into a set of physical phantoms $\{M_{\tau_{phan}}\}$.

2.5 NATURAL PARAMETERIZATION

2.5.1 The Overall Validation Dilemma

Unfortunately, phantoms imitating natural objects can never be directly validated since natural objects are unique. Therefore, phantom validation can only be performed indirectly. In natural parameterization, such indirect validation is performed by a comparative analysis of measurable properties. For example, if the natural object is represented by an observation mesh, then properties such as length, width, height, surface area, cross-section moments of area, volume, tortuosity metrics, and others can be compared to the same metrics of the generated phantom. However, even when big samples of natural objects are investigated and compared to corresponding phantoms, the comparison will only be a *statistical indicator*.

2.5.2 Key Elements and Historical Roots

The conglomerate of parameter extraction, stochastic decomposition, and reparameterization is what lies in this piloting concept called natural parameterization. The fundamental idea behind the approach is founded on a long scientific tradition of two-way approaches[32]. However, natural parameterization is not as sophisticated as some of the famous historical two-way approaches fostered by famous scientist such as Gottfried Wilhelm von Leibniz, Sir Isaac Newton, Jean Baptiste Joseph Fourier and Pierre-Simon, marquis de Laplace. In natural parameterization the first step is extraction of geometric data (i.e. parameter extraction) from natural objects. The second step is stochastic simulation of the same object as imitations (i.e. reparameterization). However, a statistical interface including parametric decomposition is required to bridge the two steps. This involves reducing an infinite set of quantities of the natural object to a finite set, which is then reused to generate imitations of the original set. Methodologically, it is based on the same discretization strategy, which is one of the fundamentals behind the Finite Element Method (FEM). FEM discretization has been used since the 40s (Courant, 2007), (Stein, 2009) and ever since to refine models of primarily "man-made objects". However, in natural parameterization, the search aims to identify a *feasible set of parametric quantities* for natural objects, which can be organized as a unique *geometric constellation in* a *normalized space for later reparameterization and generation of new phantoms* in the *original space*. Any natural geometry is assumed to carry its own feasible parameter set, referred to as the *master mesh* (or the parametric DNA) of that object. These unique master meshes are the source for generation of multi-resolution "look-a-like" imitations of the natural objects themselves. Technically, the stochastically generated *meshes* represent *imitations*. The set of procedures used to obtain this parameterization, starting with the *observation* of natural objects to the transformation of final imitations into *computational phantoms,* are unified into one two-way algorithm with an interfacing parametric bank.

---

[32] The fundamental idea behind many historical two-way approaches is to introduce a "forward" operation and a "backward" operation. In the forward operation the original problem which is defined in its original space is simplified into a new but simpler problem in a new space. Reversely, during the "backward" operation an inverse method is used to produce a solution in the original domain from the simplified problem. This idea is fostered and applied by famous scientists in various scientific areas during the last centuries: The inventors of modern calculus Gottfried Wilhelm von Leibniz (1646 – 1716) and Sir Isaac Newton (1643 – 1727) introduced a "forward" process of finding the derivative of a function and termed it differentiation and an accompanying "backward" operation anti-differentiation today known as integration. In signal analysis, Jean Baptiste Joseph Fourier (1768 – 1830) introduced the Fourier transform as a "forward" process decomposing a function in a time-domain into a set of oscillatory functions in a frequency domain. The accompanying "backward" operation known as Fourier inversion recovers a function in its time domain from its Fourier transform. In differential calculus Pierre-Simon, marquis de Laplace (1749 – 1827) introduced a "forward" operation known as the Laplace transform which replaces an original function f defined in a t-domain of a certain problem with a new and simpler function F defined in a new domain known as the s-domain. After solving the simpler problem for F in the new s-domain one uses a "backward" operation, the inverse Laplace *transform*, to find a solution for the problem of f in the original t-domain.

In this chapter, the novel method called natural parameterization has been introduced as an approach for parameter extraction from natural geometries and later reparameterization by stochastic simulation into "look-a-like" imitations. In Figure 2.42 the seven steps in natural parameterization are illustrated for a symbolic natural object in 3D:

Natural parameterization is a two-way approach based upon a "forward" operation and a "backward" operation. Its "forward" operation, called *parameter extraction,* retrieves geometric *size* and *shape* information from an *observation mesh* of a natural object in *original space* and transforms this information into a *master mesh* in a non-dimensional *parametric space*. The "backward" operation, called *reparameterization,* regenerates *imitation meshes* of the original observation meshes back into the original space from the information stored in the parametric bank. Imitation meshes can be materialized into *physical models* or *computational phantoms*, called *phantoms*. Finally, the concept of goodness of imitation is used to decide if the meshing approach used imitates the underlying stochastic behavior with a good efficiency of imitation or not. If the meshing approach is not rejected then it is said to be a *natural tortuosity generator* of that object. This means that from the set of independent and uncorrelated natural parameters it models an underlying natural object with a good efficiency of imitation.

Between the forward parameter extraction process and the backward reparameterization process, *parametric decomposition* is applied. In this intermediate process it is verified that parameters are un-correlated or almost uncorrelated. If parameters are found to be correlated, another mesh approach must be applied. After this, decomposition acts as a starting point for *random number generations*. The data can be used for both mean value simulations, as well as stochastic perturbation modeling. To ensure *continuous knowledge building,* the extracted parameters are continuously *saved and updated* in a *bank of natural parameters*.

Table 2.10: Typical reparameterizations

Class	Mesh ID		Description
Name	Tag	Symbol	Mater and Iterated Parameters
Replication Phantom	One-to-one	M_{phan}	$\left\{q_{phan}^0\right\}=\left\{q_{obs}^0\right\}$, $\left\{q_{phan}^{k_\tau}\right\}=\left\{q_{obs}^{k_\tau}\right\}$
	Mean value	$E\left[M_{phan}\right]$	$\left\{q_{phan}^0\right\}=\left\{E\left[q_{obs}^0\right]\right\}$, $\left\{q_{phan}^{k_\tau}\right\}=\left\{E\left[q_{obs}^{k_\tau}\right]\right\}$
Imitation Mesh	Beta	$M_{\tau_\beta}^{n_\tau}$	$\left\{q^0\right\}=\left\{q_\beta^0\right\}$, $\left\{q^{k_\tau}\right\}=\left\{q_\beta^{k_\tau}\right\}$
	Alpha-beta	$M_{\tau_{\alpha\beta}}^{n_\tau}$	$\left\{q^0\right\}=\left\{q_{\alpha\beta}^0\right\}$, $\left\{q^{k_\tau}\right\}=\left\{q_{\alpha\beta}^{k_\tau}\right\}$
Stochastic Phantom	Beta	M_{phan_β}	$\left\{q_{phan}^0\right\}=\left\{q_{obs_\beta}^0\right\}$, $\left\{q_{phan}^{k_\tau}\right\}=\left\{q_{obs_\beta}^{k_\tau}\right\}$
	Alpha-beta	$M_{phan_{\alpha\beta}}$	$\left\{q_{phan}^0\right\}=\left\{q_{obs_{\alpha\beta}}^0\right\}$, $\left\{q_{phan}^{k_\tau}\right\}=\left\{q_{obs_{\alpha\beta}}^{k_\tau}\right\}$
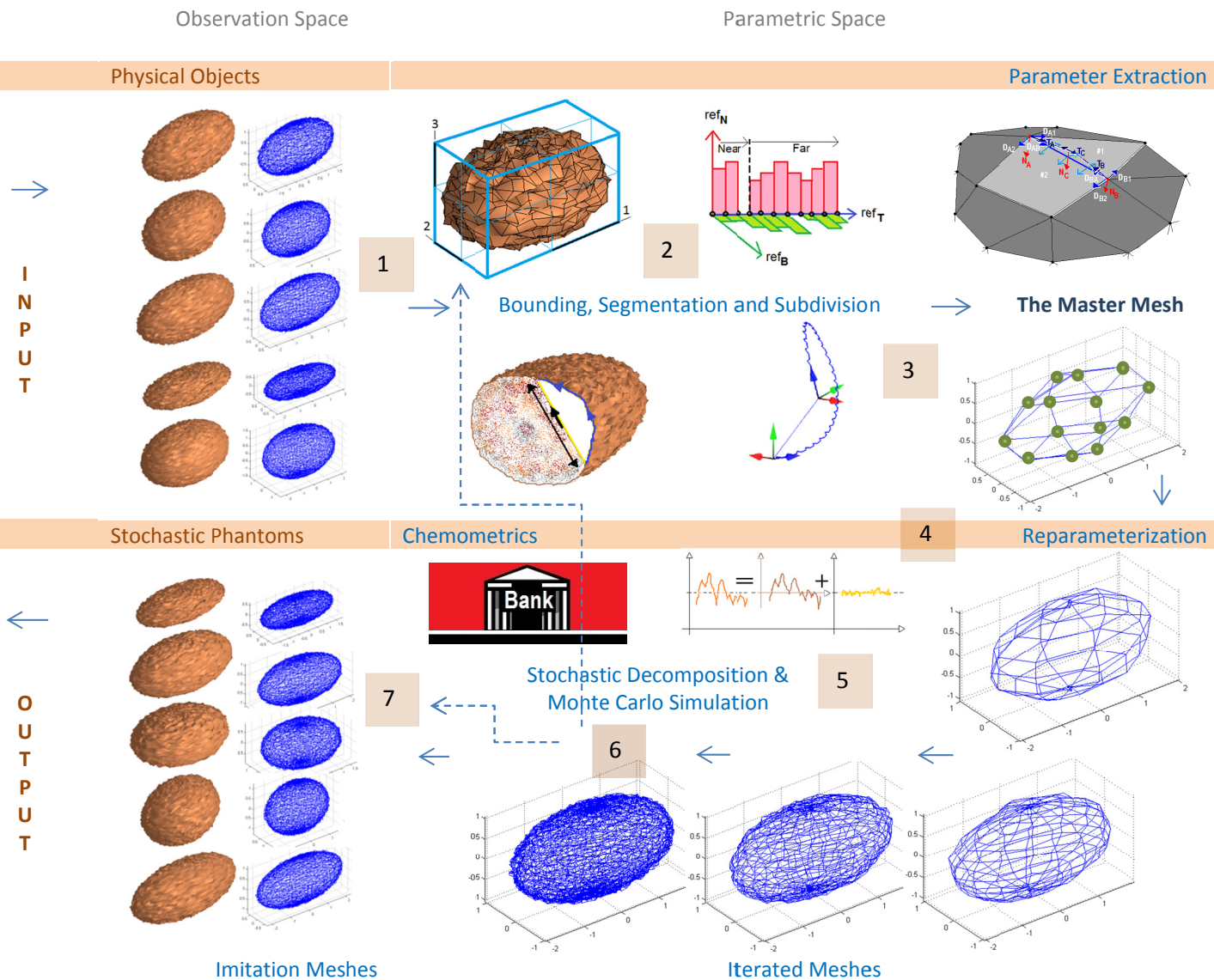
Figure 2.42: The seven steps in natural parameterization

1. A pre-processing procedure forms the observation meshes in the observation space.
2. Size and landmark parameters are identified and extracted to form the set of master parameters.
3. Iterated parameters are extracted according to the concept of goodness of replication. Together the master parameters and the iterated parameters form the set of natural parameters, which define the master mesh.
4. Master and iterated parameters are stored and accumulated over time in a parametric bank. Alpha-beta decomposition and chemometrics is applied and stochastic master meshes are formed in the parametric space.
5. The modeler is able to customize the parametric master meshes by adjusting properties such as length, volume, and more. Also, pseudo-sochastic perturbations can be applied for extreme value or abnormality modeling.
6. New imitations are then generated from the customized master mesh by reparameterization. Monte Carlo simulation is used and the set of imitation meshes are tested in accordance with the concept of goodness of imitation. The procedure 1-6 is repeated if high efficiency of imitation is not achieved.
7. Finally, the new meshed are transformed back to the observation space as stochastic phantoms. These "new" phantoms are ready made for graphical representation, further FE post-processing, or 3d-printing.

Mathematically, natural parameterization evolves from a classical *variational problem* known as "Dido's Problem". After a simple reformulation, a "reversed" Dido's problem is shown to be suitable for the understanding of replications from imitation parameters and the use of tortuosity metrics as functionals. Later, this deterministic approach is extended into cover stochastic parameters, which are decomposed into semi-stationary and fluctuating parts. The beta part is essential for mesh generation, which builds on tortuous Frenet subdivision for surfaces and solids. Therefore, numerical treatment of biometrics, FEA, subdivision, optimization, and chemometrics all complement each other in a unified algorithm for *natural parameterization.*

Software packages used for the development of algorithms

A number of commercial software packages for algorithm development, plots, and formula deployment have been used in this first approach. All algorithms were developed within the MATLAB® R2012A (www.mathworks.com) environment. Testing of code fragments was performed by MathCad 15 2012 (www.adeptscience.com), and color codes for Frenet directions and other de facto FE notations were adopted from STAAD PRO V8i 20012 (www.bentley.com).

In chapter 3, the natural parameterization approach is applied in a case study on a sample of one hundred wheat grain cross-sections.

3 RESULTS

3.1 PARAMETER EXTRACTION

In the following case study the natural parameterization approach was applied on a sample of wheat grains in accordance with the method outlined in Chapter 2. For reasons of simplicity, the objective of this piloting case study was to apply the approach on an object/species with a *single characteristic landmark*. Mechanical or physical properties were not modeled, i.e. only geometry was in focus. Details on geometric discretization of wheat grains are found in ANNEX 17. Wheat grains are described in 1.1 and the sampling of one hundred grains in 3.1.2. The natural parameterization approach is applied in its three main parts: First parameter extraction in 3.1, then chemometrics in 3.2 and finally reparameterization in 3.3.

Figure 3.1: Sampling of one hundred grains

3.1.1 The Bow-line

In this results chapter, grain of wheat (Triticum aestivum) was used as a case study object for the validation of the natural parameterization approach. Experts and farmers state that wheat grains possess one characteristic geometric landmark known as the "bow-line". This means that the number of free landmarks is restricted to one – which makes wheat grains particularly simple objects for shape identification.

3.1.2 Sampling of one hundred wheat-grains

From a cluster Σ_Ψ of wheat grains (*Triticum aestivum*) with impurities, a subcluster Ω_Ψ was taken, cleaned, and stored in a plastic bag. From this bag one hundred objects/species $\{\Psi_\Omega\}$ were drawn randomly to form a sample without impurities (see Figure 3.1).

NOTE   Evidently, this single data set is not sufficient for a general validation of the method. In the future, more application objects are planned to be studied for enhanced validation and for improvements of the approach.

3.1.3 Materials and Data Preprocessing

3.1.3.1 Samples preparation

Figure 3.2: Wheat grain cross-section

Using a scalpel, each of the wheat grains was cut in the middle region, perpendicular to the natural longitudinal axis of the grain. Thereafter, each grain was positioned on the microscope base perpendicular to the lens direction. The lighting settings were adjusted individually to obtain a fairly contrasted outline. Then a high-resolution image was shot. In the case where the contrast was not satisfactory, the procedure was repeated with altered settings.

3.1.3.2 Equipment Specification

The photos were captured using a stereo-microscope with the following specifications:

- Leica MZ 125 with 12.5:1 zoom and Res.: 16x_4d mounted with a digital camera:
- Leica CLS 100 X: Res.: 150x150 points per inch.
- Pixels: 2088x1550.
- Image format: JPEG.
- Localized 26 March 2012 at URL: http://www.leica-microsystems.com/products/stereo-microscopes-macroscopes/.

The digital representations of each of the wheat grain cross-sections, taken with the stereo-microscope, were assembled into a collection of one hundred JPEG images. Furthermore, various test photos of sub-samples from the one hundred wheat grain cross-sections were captured using a flatbed scanner with the following specifications:

- Canon CanoScan 5600F
- Optical Resolution: 4800 x 9600 dpi.
- Adjustable Resolution: 25-19200 dpi.
- Localized 21 March 2012 at URL:
  http://www.canon.dk/For_Home/Product_Finder/Scanners/Flatbed_with_Film_Scanning/canoscan_5600F/index.aspx?specs=1

Digitalized Data

A001.JPG

A011.JPG

A100.JPG

Figure 3.3: Selection of three cross-section images from the sample of one hundred stereo-microscopic images[33]

---

[33] The one hundred image files captured by the stereo-microscope are named: "A001.jpg ... A100.jpg" respectively.

In Figure 3.3, a selection of three such cross-section images captured by the stereo-microscope (see 3.1.3.2) are illustrated. Note that the cross-section outline is very diffuse in every image. The following section includes comments on the complications arising from automatic outline detection by image recognition.

Figure 3.4: Light Background

Figure 3.5: Dark Background

Background Settings

The images to the left illustrate a selected cross-section with different background settings. The images were captured by flatbed scanner. Further images of a subset of cross-sections are given in ANNEX 18.

In Figure 3.4 the cross-section image was captured with a light background by letting the flatbed cover be closed. In this situation shadows are captured.

In Figure 3.5 the cross-section image was captured with a dark background by letting the flatbed cover be open. In this situation no shadows are captured.

However, none of the scanned cross-sections are free of self-distortion in the sense that the background constitutes regions of the natural object itself. This means that the grey-color intensity is not uniquely defined by the outline boundary and the background, but by non-outline regions and the background.

Figure 3.6: Self-distortion

Self-Distortion

In general, capturing a section plane of a natural geometry without capturing surfaces from other parts of the geometry with almost the same grey-scale intensity is not possible.

As seen, the cross-section images are distorted by the object's own natural background. In Figure 3.6 it is seen that self-distortion for wheat grain cross-sections occurs at the external boundary.

However, self-distortion is also observed in the interior of the cross-section. Therefore, to enhance the ability of achieving a contrasted outline, post treatment might be required for automatic outline recognition.

In the following section, post-treatment by coloring of the cross-sections is briefly commented on.

Figure 3.7: Water Color
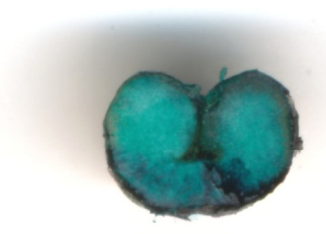
Figure 3.8: Correction Fluid

Post-coloring

To achieve a more contrasted outline, post-treatment by coloring is applied to the cross-section surface. The result of two treatments, one with water coloring and the other with correction fluid, was captured by flatbed scanner.

In Figure 3.7, the result from a first water coloring treatment is illustrated. Note that the water coloring is absorbed differently across the section. Unfortunately, some interior dark regions produce the same grey-color intensity as the bran outline. Therefore, this strategy does not improve the contrast conditions significantly. On the contrary, it disturbs the outline. Water coloring was therefore rejected as post-treatment.

A second post-treatment with standard liquid fluid was then applied manually. However, due to the small dimensions (2.5 – 4.5 mm) it was difficult to apply the liquid fluid without also marking geometry regions outside the actual cross-section, see Figure 3.8. Therefore, the contrasted outline is not improved by this post-coloring either.

In conclusion, post-coloring wheat grain cross-sections using either of the two coloring methods applied was not useful. It did not improve the separation between the interior and exterior regions

Piloting outline detection was performed with MATLAB® Image Processing Toolbox. However, the relatively poor contrast between the grain outline and the surroundings is problematic; see Figure 3.9 and Figure 3.10. The extracted data are not at all representative for the natural edges observed by the human eye.

Figure 3.9: White background

Figure 3.10: Black background

Table 3.1: The Influence from the Threshold Level

B001	B001_80	B001_100	B001_120	B001_140	B001_160
B002	B002_80	B002_100	B002_120	B002_140	B002_160
B003	B003_80	B003_100	B003_120	B003_140	B003_160
B004	B004_80	B004_100	B004_120	B004_140	B004_160
B005	B005_80	B005_100	B005_120	B005_140	B005_160
B006	B006_80	B006_100	B006_120	B006_140	B006_160
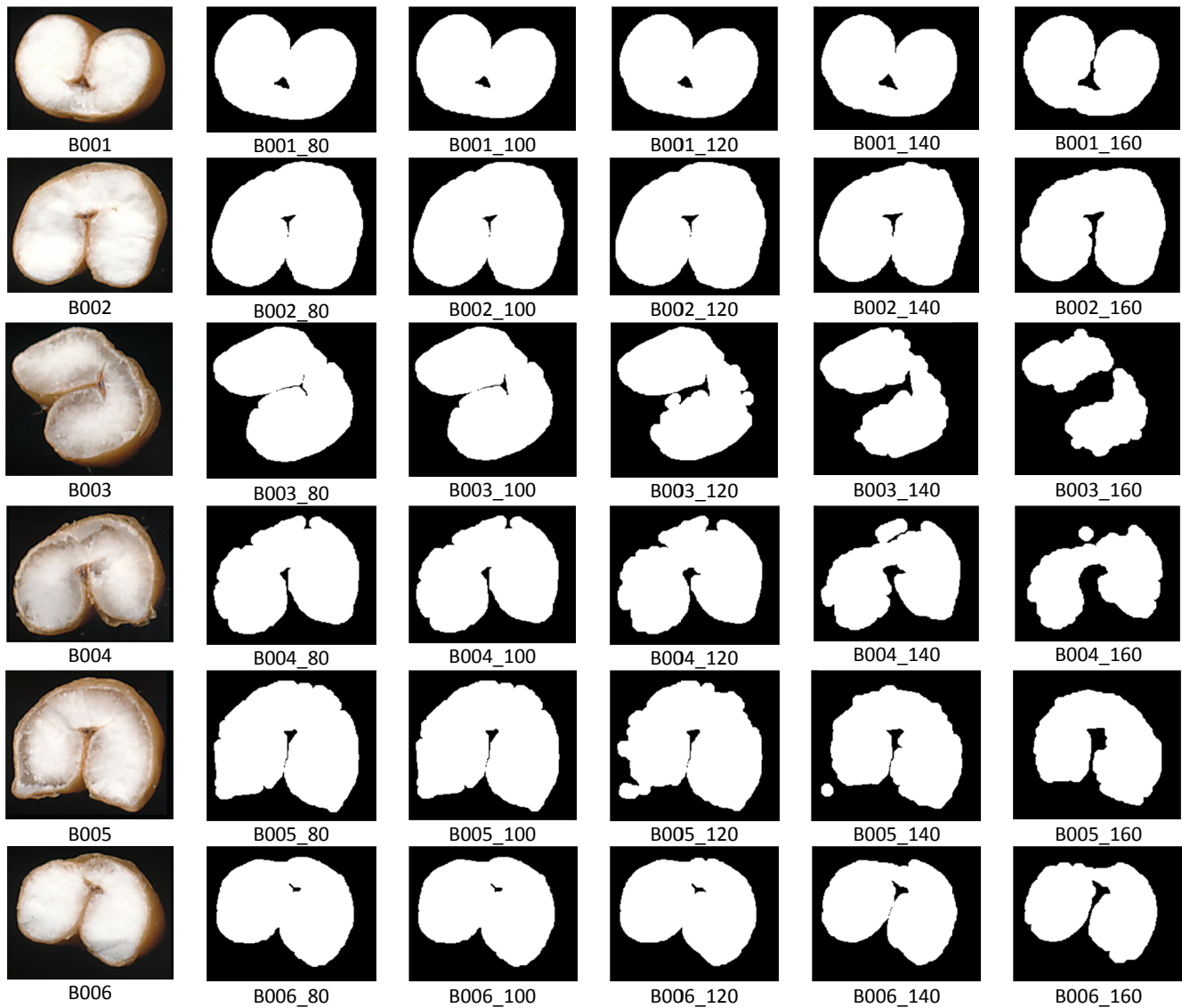
NOTE   Originally, it was intended to use a standard image recognition procedure. However, standard software that was able to identify a satisfactory outline was not found. For the wheat grain cross-sections examined, the variations in color do not vary significantly enough to perform robust and automatic outline recognition. Results from such a promising detection procedure by (Jørgensen, O. 2012, AU) are reproduced in ANNEX 20. However, the correct outline was detected more precisely, by manual inspection (using the human eye).

3.1.3.4 Observation Vertices

From the stereomicroscopic images, the 2D cross-section outline is observed and manually fitted by a set of n_V polygonal vertices $\mathbf{V}_{obs}$, i.e. $\mathbf{V}_{obs} = (x_i, y_i) \in \mathbb{R}^2$, $i = 1, ..., n_V$.
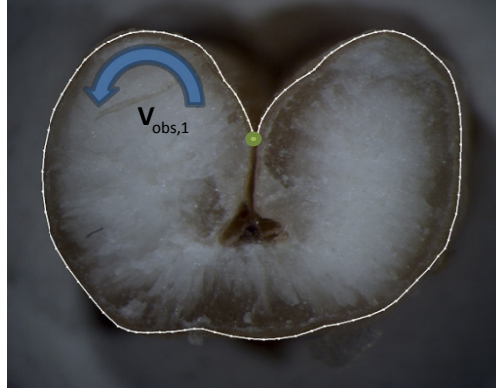
Figure 3.11: The cross-section outline is illustrated by a closed polygon

As indicated in Figure 3.11, the numbering is performed counter clock-wise. The number of vertices fitted to each polygon varies due to variations in the irregularity of the shape and the manual fitting process. The number of polygon vertices lies in the range: $n_V \in \left[n_{V_{obs,min}}, n_{V_{obs,max}} \right] = [75, 137]$.

3.1.3.5 Observation Tangents and Normals

Oriented tangents $\mathbf{T}_{obs}$ (blue) and inward normals $\mathbf{N}_{obs}$ (red) are determined from the polygon directly*. The orientation of tangents is governed by the counter clock-wise numbering of the vertices $\mathbf{V}_{obs}$.

*Normals are automatically found by MATLAB® as patch graphics vertex normals after the polygon are transformed into a strip of quadrilateral patches by adding mirrored vertices in the out-of-plane direction.

Figure 3.12: Tangents and normals

3.1.3.6 The Observation Mesh

Conclusively, a tortuous observation mesh $M_{\tau_{obs}}$ is formed from the vertices, tangents, and normals:

$$M_{\tau_{obs}} \ni \{\mathbf{V}, \mathbf{T}, \mathbf{N}\}_{obs}$$

For each wheat grain its tortuous mesh is stored along with its image data.

3.1.4 Landmarks

For grains of wheat, the aim is to develop one or more dedicated algorithms that are able to identify subjective characteristics, as stated by farmers and other experts. These routines are crucial to obtain a robust and objective identification from subjective information. Such landmark identification algorithms must be able to identify the same set of characteristics for all sample objects. At this stage, subjective landmark information is assumed to rely on experience, i.e. expert knowledge.

3.1.4.1 The bow line Landmark

The characteristic bowline (marked in blue in Figure 3.13) is a unique landmark for wheat grains. Therefore, this landmark is used as a starting point for automatic parameter extraction. However, the bounding window depends on the raw data frame and an automatically recognizable domain frame.

Figure 3.13: The bow-line landmark for wheat grains

3.1.5 Bounding Window

3.1.5.1 Bounding Frame

The choice of a unique reference frame for natural geometries is a study in itself. In general, the idea is to identify a frame from simple measurements of the sample objects. However, at this stage, generalizations cannot be made. The limited experiences gained from examination of wheat grains are the only background for the following comments.

The digitalized data are measured in a global data frame. Here, this global vector base $\{\mathbf{e}_1, \mathbf{e}_2, \mathbf{e}_3\}_{global}$ is measured in pixels. The third dimension is included as a pseudo direction to ensure a base in $\mathbb{R}^3$. Within this global frame, an identification algorithm is designed that can define a dedicated local *bounding frame* in $\{\mathbf{e}_1, \mathbf{e}_2, \mathbf{e}_3\}_b$ in $\mathbb{R}^3$ from the digitalized data. First, the orientation of the domain is identified and then its origin is fixed. Finally, within this local frame, a boundary window is defined.

NOTE   In general, it must be assumed that a number of such domain frames are to be defined. However, when expert knowledge exists, the number of relevant frames might be restricted to a small set. A robustness test of the applied bounding identification algorithm might reveal if the selected bounding frame is appropriate or not.

Computationally, it must be checked that the same identification algorithm is able to identify a unique domain frame and thereafter a unique bounding window for all objects in the sample.
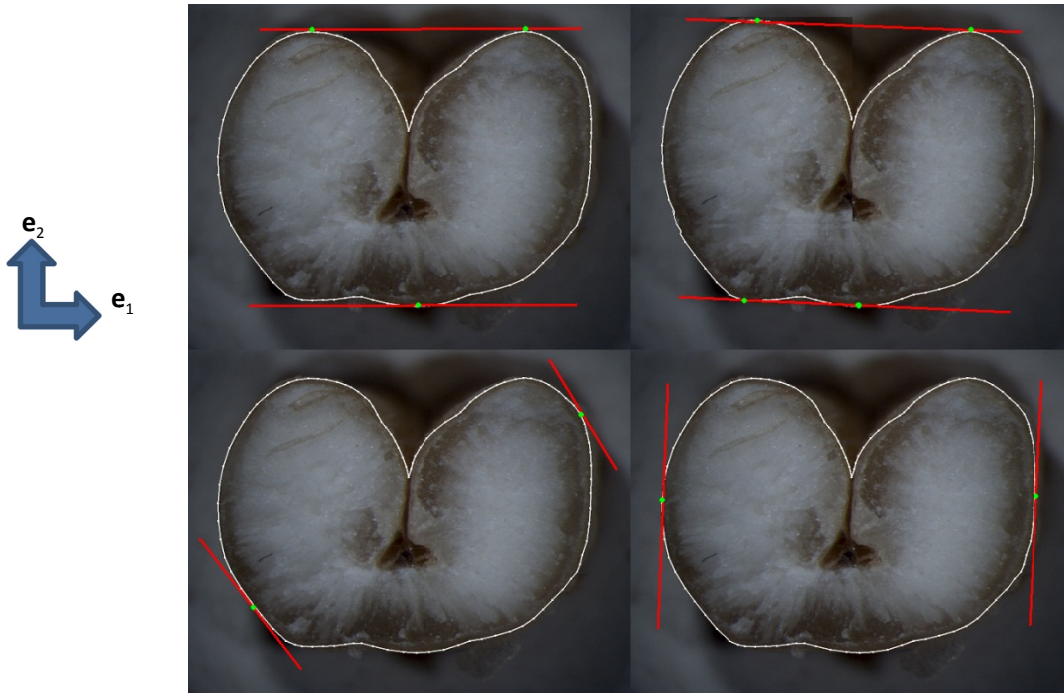
Figure 3.14: Anti podal pairs constellations. *Top left* is used to orientate the bounding frame from the raw frame.

In the identification algorithm applied, originally four different *anti podal pairs* constellations are considered to automatically identify the orientation of the domain frame. See Figure 3.14, where the orientation of the global frame $\{e_1, e_2, e_3\}_{global}$ is indicated in blue to the left of the images. As seen, all constellations envisaged are measurable by a Vernire caliper, by laser, by image recognition, or by using other methods. However, they are not equally relevant. Figure 3.14 (*top left)* illustrates a configuration where three vertices form two parallel bounding lines, i.e. it is a minimum distance bounding where the upper bounding line is bridging the characteristic bow. Figure 3.14 *(top right)* illustrates another minimum bounding. However, it is not likely to find lines touching four points quite so often. Therefore, the image on the top right is seen as a special situation. The image on the *bottom left* of figure 3.14 illustrates the maximum bounding lines i.e. the Feret diameter (maximum caliper). However, for a cross-section of wheat grains, the maximum Feret diameter does not capture special characteristics of the bow. The image on the *bottom right* of figure 3.14 represents the minimum of the maximum podal pair distances. This constellation also does not capture special bow characteristics.

The anti podal pairs constellation, illustrated *top left* in Figure 3.14, is therefore chosen for the sample of wheat grain cross-sections to identify the orientation of the bounding frame $\{e_1, e_2, e_3\}_b$.

NOTE   Here, the unique bounding frame is established for a cross-section outline from an anti podal pairs constellation. However, different techniques might be applied for different domains of natural objects.

Figure 3.15: Convex hull used as the frame for of landmark identification by distance

Figure 3.16: Three feasible segments identified from the convex hull. Top segment with max distance is used.

From Figure 3.15 and Figure 3.16 it is evident that a convex hull can be used to identify a finite set of characteristic segments where the distance from the convex hull to the vertices of the polygon is largest. The particular segment with the largest distance to its polygon vertex amongst the set of distances is identified as the characteristic edge. In Figure 3.17 it is illustrated that this edge is spanning like a "bridge over the bow".

For all objects in the sample, it is checked by inspection that the correct bowline is identified. It was found that for the sample investigated the applied decision rule was robust.
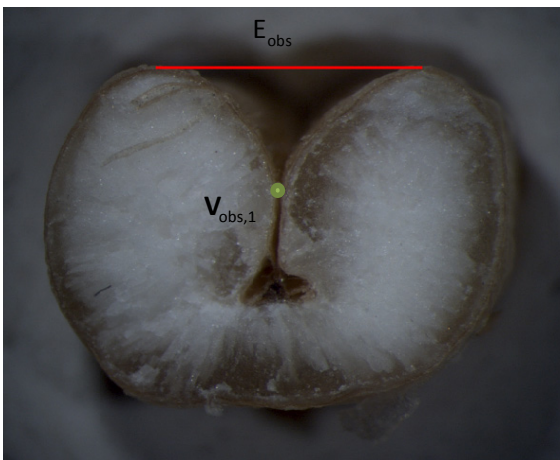
Figure 3.17: Identification of the characteristic "bow" vertex $\mathbf{V}_{obs,1}$ and orientating "bow" edge E_{obs}
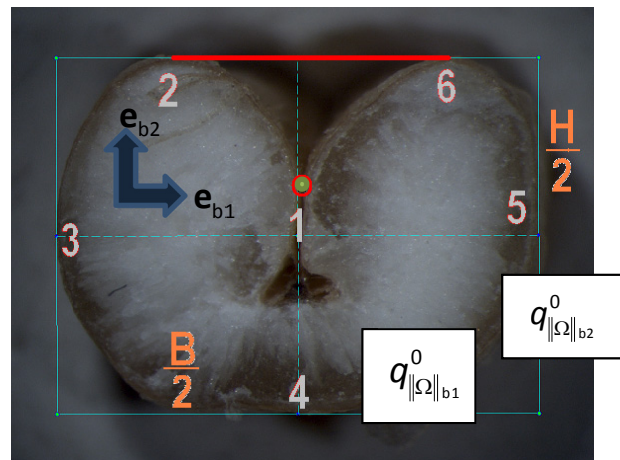
Figure 3.18: Six Landmark vertices and the bounding frame $\{\mathbf{e}_{b1}, \mathbf{e}_{b2}, \mathbf{e}_{b3}\}$

As a result of the landmark identification, the characteristic "bow" vertex $\mathbf{V}_{obs,1}$ and the orientating "bow" edge E_{obs} are uniquely identified for each object as illustrated in Figure 3.17. The "bow" vertex is defined as the first observation vertex $\mathbf{V}_{obs,1}$, see Figure 3.18.

3.1.5.4   Vectors and Scalars

For each cross-section, the bounding window (represented by a bounding rectangle in Figure 3.18) is defined by a number of bounding vertices labeled from "1" up to "6". Vertices "2" to "6" are the intersections between the polygon and the bounding window. The anti podal pairs constellations with two touching bounding vertices (see Figure 3.14 *top right*) are not observed for any object in the sample. The illustrated vertex "4" was the single vertex at the lowest bounds in the entire sample.

First, the two vertices labeled "2" and "6," from the a set of polygonal vertices $\mathbf{V}_{obs}$, were used to orient the first bounding base vector $\mathbf{e}_{b1}$. Then, the characteristic "bow" vertex, labeled "1", is used to define the second bounding base vector $\mathbf{e}_{b2}$. It is then defined as the vector, oriented from "1", which is orthogonal to the edge, spanned by "2" and "6". Finally, the third bounding base vector is found using the cross product $\mathbf{e}_{b3} = \mathbf{e}_{b1} \times \mathbf{e}_{b2}$. Then, the nominal breadth B was identified as the distance between the two vertices, labeled "3" and "6", which are furthest away from the line through "1", which is oriented by $\mathbf{e}_{b2}$. The nominal height H was identified as the distance between the vertex, labeled "4" and the edge, spanned by "2" and "6". By these operations, the unique bounding rectangle illustrated in Figure 3.18 is fully defined.

3.1.6   The Master Mesh

The master mesh is then formed by introducing six segments. It includes six tortuosity poles and six directed segment chords. The positive chord directions follow the standard counter-clockwise rule.

Segmentation
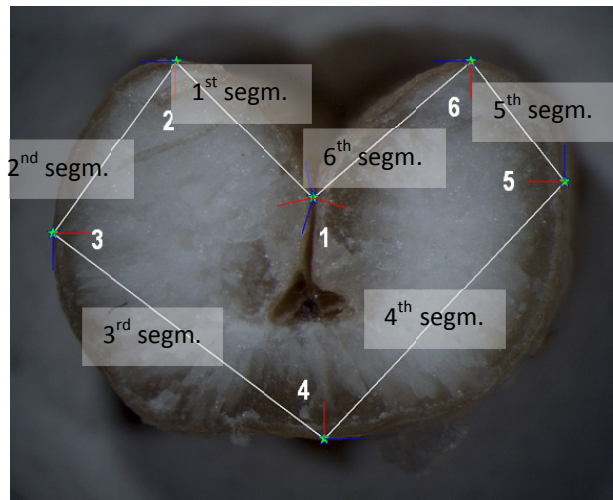
Figure 3.19: Master mesh with six tortuosity poles and six segments. (Pole 1 has valence two)

The bounding semi-range

For each sample element the bounding frame is extracted. From these values, and in accordance with paragraph 2.2.10.2.2, an upper bounding semi-range is defined. This is done by assuming that the probability to find bigger bounding ranges for new observation images above $1000 \left[pixels \right]$ is close to zero.

Figure 3.20: Curvatures are estimated from neighborhood vertices

Only two independent orientation DOF's for the "bow" vertex are required since the tangents for the other landmarks follow the bounding edges. These two "bow" orientation DOF's are derived from the observed tangents as the average orientation and its central deviation (see 3.1.3.5). The curvatures are estimated in accordance with ANNEX 6.3.

3.1.7   Decoupling of Size and Shape

For the parameterization, it is further assumed that size and shape for the observation set investigated is decoupled. Details for the decoupling of size and shape are given in ANNEX 22-25.This enables cross-sections to be size normalized, but also require an inspection of correlation coefficients to ensure that the parameters used in the further segmentation are uncorrelated.

3.1.8   Independent parameters

In ANNEX 25, the full correlation matrix for the eighteen master parameters is reproduced. In general, low correlation coefficients are found. The biggest Pearson product-moment correlation coefficient (ρ = 0.66) appears for the pair of parameters represented by vertex (No 4) and the bow-line tangent (No 11), see Figure 3.20. This indicates a weak correlation. Therefore, it is assumed that all parameters in the constellation used in the following section can be modeled as independent random variables and used as master parameters for the master mesh.

3.1.9   Master Parameters

The parameterization of the observation mesh into a set of master parameters q^0 is performed in the preceeding paragraphs. This means that a subset of size parameters $q^0_{\|\Omega\|}$, and another subset of landmark parameters q^0_P, are extracted to form the master parameters, i.e. $q^0 \supseteq \left\{ q^0_{\|\Omega\|}, q^0_P \right\}$. The total number of degrees of freedom in the master constellation is eighteen, i.e. $n^0_{DOF} = 18$.

3.1.9.1   Size Parameters

In accordance with paragraph 2.2.10.2.1, each polygon is normalized and its values are stored in an n_{obs} -tuple

of size parameters $q^0_{\|\Omega\|_A} \supseteq \left\{ q^0_{\|\Omega\|_1}, ..., q^0_{\|\Omega\|_i}, ..., q^0_{\|\Omega\|_{n_{obs}}} \right\}$ as $q_{\|\Omega\|_{A,i}} = \dfrac{x_i}{A_i^{1/2}}$, $\forall i \in [1; n_{obs}]$. Afterwards, these parameters

are stored in a bank of natural parameters. These size parameters are not influential in this case study, where size and shape are assumed to be decoupled. However, the two quantities representing the bounding dimensions $(B1, B2)$ in Figure 3.22 are parameterized into $\left\{ q^0_{\|\Omega\|_{B1}}, q^0_{\|\Omega\|_{B2}} \right\}$.

3.1.9.2   Parameter Listing

To obtain a simpler listing in subsequent statistical analysis, a forth running parameter, index p, is applied. This means that the two bounding dimensions are the first two parameters in this list of all eighteen DOF-parameters:

$$q^0_{\|\Omega\|_b} = \{ q_1, q_2 \} \ , \ p \in \{1, 2\}$$

To maintain the discretization hierarchy, the seven curvature parameters are listed as the last DOF-parameters and are therefore given the numbers from twelve to eighteen.

$$q^0_{\|\Omega\|_{L-1}} = \{ q_{12}, ..., q_{18} \} \ , \ q^0_P = q^0_{\|\Omega\|_A} \kappa \ , \ \forall \kappa \ , \ p \in \{12, ..., 18\}$$

The entire set of size parameters for each observation mesh and its number of DOF (see Figure 3.22) is

$$q^0_{\|\Omega\|} = \{ q_1, q_{2,} q_{12}, q_{13}, q_{14}, q_{15}, q_{16}, q_{17}, q_{18} \} \rightarrow n_{dof(\|\Omega\|)} = 9 \ .$$

Landmark parameters q_P^0 are represented by two subsets: location parameters q_x^0, and orientation parameters q_θ^0.

Six landmark vertices are extracted as $\{\mathbf{V}_1,...,\mathbf{V}_6\}$ (see Figure 3.22). From equation (2.28), their corresponding landmark location parameters q_x^0 are found. Note that vertex one has two degrees of freedom for $p\in\{3,4\}$.

$$q_x^0 \supseteq \{q_3,q_4,q_5,q_6,q_7,q_8,q_9\} \ , \ q_p = \frac{x}{r_{b_p}^0} \ , \ p\in\{3,...,9\} \ , \ q_P^0 \supseteq q_x^0$$

This means that a total of seven degrees of freedom is linked to this constellation of landmark vertices.
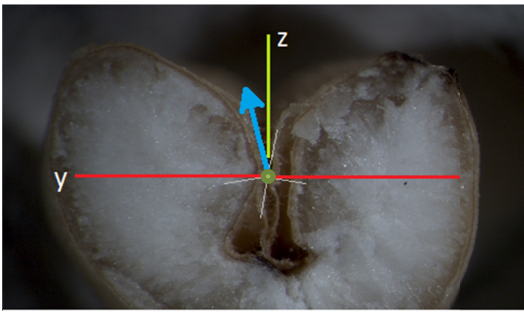
For each of the six landmark vertices their tangents are given from the observation mesh.

Only the "bow" vertex is considered a variable with two degrees of freedom for the tangents (and two degrees of freedom for the curvatures, see 3.1.9.1).

At the "bow" vertex, the two DOF tangents were parameterized as orientation parameters q_θ:

$$q_\theta^0 \supseteq \{q_{10},q_{11}\} \ , \ q_p = \frac{\theta}{r_{b_p}} \ , \ p\in\{10,11\} \ , \ q_P^0 \supseteq q_\theta^0$$

The entire set of landmark parameters is formed as:

Figure 3.21: Parameterization of a "bow" tangent in spherical coordinates

$$q_P^0 \supseteq \{q_x,q_\theta\} = \{q_3,q_4,q_5,q_6,q_7,q_8,q_9,q_{10},q_{11}\} \rightarrow n_{\text{dof}(P)} = 9$$

3.1.9.4   Tortuosity Poles

The information gathered at each landmark is now stored in six tortuosity poles $P_{\tau,i}$, $i\in\{1,...,6\}$. Note that tortuosity pole $P_{\tau,1}$ has the valence two, i.e. $n_{\{F\},1}=2$, whereas the other tortuosity poles have valence one, i.e. $n_{\{F\},i}=1$, $i\in\{2,...,6\}$.

Symbolically, the tortuosity pole $P_{\tau,1}$ with valence two is defined on non-parametric and parametric form as

$$P_{\tau,1} = \begin{bmatrix} \mathbf{V}_1^T & \mathbf{V}_1^T \\ \mathbf{T}_{11}^T & \mathbf{T}_{62}^T \\ \mathbf{N}_{11}^T & \mathbf{N}_{62}^T \\ \mathbf{B}_{11}^T & \mathbf{B}_{62}^T \\ \mathbf{X}_{11}^T & \mathbf{X}_{62}^T \end{bmatrix} \rightarrow q_{\Omega,P_{\tau,1}} = \begin{Bmatrix} q_3, q_4 \\ q_{10}, q_{11} \\ q_{10}, q_{11} \\ q_{10}, q_{11} \\ q_{12}, q_{18} \end{Bmatrix}, \quad n_{DOF(P_{\tau,1})} = 6;$$

The remaining five tortuosity poles are defined similarly, although simpler.

3.1.9.5   Segmentation

The segmentation indicated by the chord lines in Figure 3.19, is controlled by connectivities that define six individual bi-mesh master meshes. The corresponding connectivity array is defined as:

$$\begin{bmatrix} M_{\tau,bi,j}^0 \supseteq & \{P_{\tau,A} & P_{\tau,B}\} \\ j=1 & 1 & 2 \\ j=2 & 2 & 3 \\ j=3 & 3 & 4 \\ j=4 & 4 & 5 \\ j=5 & 5 & 6 \\ j=6 & 6 & 1 \end{bmatrix}$$

At the first level of refinement $k_\tau = 1$, the local first axis coordinate (ξ_1) is bound to the positive orientation of the segments from $P_{\tau,A}$ towards $P_{\tau,B}$.

3.1.9.6   Master Parameters – Overview

Finally, the eighteen master parameters extracted for each observation mesh are stored in a bank of natural parameters.

$$\hat{Q} \leftarrow q^0 \supseteq \left\{ q_{\|\Omega\|}^0, q_P^0 \right\}$$
$$= \left\{ q_1, q_2, q_{12}, q_{13}, q_{14}, q_{15}, q_{16}, q_{17}, q_{18} \quad, q_3, q_4, q_5, q_6, q_7, q_8, q_9, q_{10}, q_{11} \right\}$$
$$\rightarrow n_{DOF}^0 = n_{DOF(\|\Omega\|)} + n_{DOF(P)} = 9 + 9 = 18$$

Statistics

The statistics for the eighteen master parameters for the set of the one hundred grains is reproduced in Table 3.2.
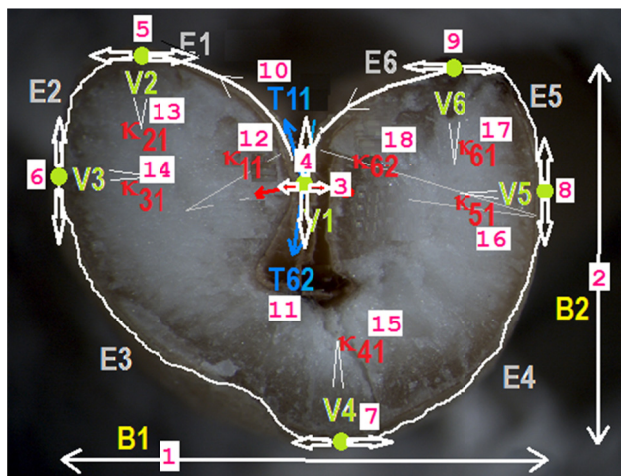
Figure 3.22: The eighteen master parameters

NOTATION   The master parameters are auto scaled (mean centered and standard deviation normalized) prior to the data treatment[34]. The following notations are used for chemometrics to emphasize the parameters relation to the frame indices of the tortuosity poles and segments.

Local directions:
(1) = First dir. (Local X).
(2) = Second dir. (Local Y)

B = Boundings (0, DIR).

V = Vertices are identified by (IDX, DIR). IDX = vertex No.

T = Tangentsare identified by (IDX, DIR). IDX = segment No.

K = Curvatures are identified by (IDX, DIR). IDX = segment No.

NOTATION EXAMPLE - The end tangent of edge "E6" is denoted "T62" since "EndEnd" of segments are indexed by the cipher "2".

The corresponding master parameter subsets are:

- 01-02 – Bounding parameters: .... {(B01),(B02)}
- 03-09 – Vertex parameters: ...... {(V11),(V12),(V21),(V32),(V41),(V52),(V61)}
- 10-11 – Tangent parameters: ..... {(T11),(T62)}
- 12-18 – Curvature parameters: ... {(K11),(K21),(K31),(K41),(K51),(K61),(K62)}

Table 3.2: Master Parameters - Statistics

No	1	2	3	4	5	6	7	8	9	10	11	12	13	14	15	16	17	18
Tag	B01	B02	V11	V12	V21	V32	V41	V52	V61	T11	T62	K11	K21	K31	K41	K51	K61	K62
Mean	0.71	0.55	-0.008	0.32	-0.56	0.22	0.085	0.18	0.55	0.13	0.14	0.08	0.15	0.081	0.087	0.088	0.17	0.080
Std	0.050	0.041	0.035	0.15	0.087	0.16	0.24	0.19	0.095	0.097	0.082	0.037	0.067	0.028	0.028	0.046	0.093	0.046

---

[34] The data treatment is performed by use of MATLAB Statistics Toolbox® and the LATENTIX® software

3.1.10 Frenet Subdivision

To replicate the outline polygon of each observation mesh, Frenet subdivision is applied for each of the six segments (see 3.1.9.5).

Level of refinement

For the cross-section polygons studied, the highest number of observation vertices used around the circumference was one-hundred twenty eight. The maximum level of refinements chosen was five so that subdivision would result inthirty two edges for each of the six segments. This means that a total of one hundred and ninety two edges around the circumference are generated for each phantom.

$$n_\tau = 5 \rightarrow n_E = 2^5 \times 6 = 32 \times 6 = 192 > n_{E_{obs,max}} = 137 , \quad \forall M_{obs}$$

During the Frenet subdivision

$$k_\tau = 1,...,n_\tau = 1,...,5 , \quad \forall M_{obs}$$

a set of iterated parameters is extracted from a multiresolution setup, which is defined by a replication problem that will be further described.

157

3.1.11 Iterated Parameters

The reduced set of iterated parameters
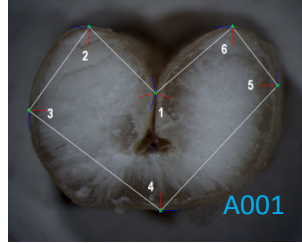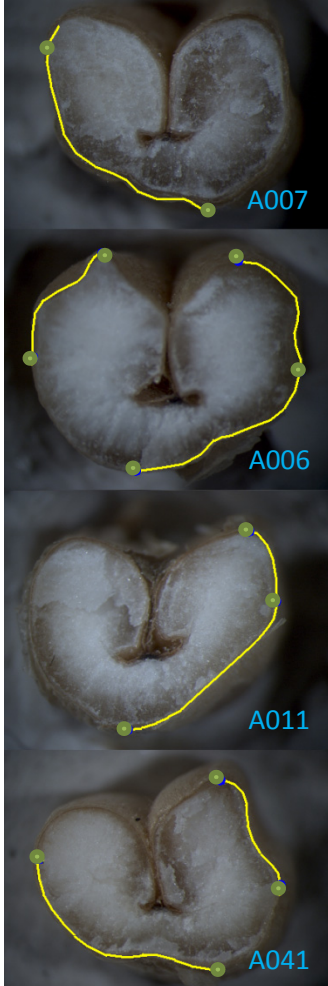
As it appears from the tortuous yellow curves in Figure 3.23, the six curve segments must be modelled with some degrees of freedom to obtain a fair replication of the various cross-section outlines. In this problema, where only two local coordinate axes are apparent, the relevant parameter candidates are:

$$q_{\xi_1}, q_{\xi_2}, q_{\mathbf{T}}, q_{\mathbf{N}}.$$

In this case study the parameterization only includes one location parameter q_{ξ_1} (the longitudinal pole translation parameter) and two orientation parameters $q_{\mathbf{T}}, q_{\mathbf{N}}$ (the parameter for T-impact and the parameter for N-impact).

The mixed three-tuple of location and orientation parameters was represented by the array

$$\mathbf{q}^{k_\tau} = \left[q_{\xi_1}, q_{\mathbf{T}}, q_{\mathbf{N}} \right]^{k_\tau}$$

For further details on the applied parameters, see Table 3.3.

To reduce the number of DOFs (see 2.2.12.3) even further, the orientation parameters are unified so the same single parameter is used for both ends of each of the six bi-meshes.

Figure 3.23: Tortuous curve segments modeled with three degrees of freedom only

Multi-resolution modeling

The multiresolution modeling is applied by letting the location parameter be active at the first level of refinement, i.e. at $k_\tau = 1$ and the orientation parameters being active at any level $k_\tau = 1, 2, ... n_\tau$. However, with only three degrees of freedom, and this simplified multiresolution setup, the efficiency of replication of highly irregular segments (as illustrated in Figure 3.13) is expected to be poor. This also keeps the CPU expenses down.

Conclusively, the reduced set of iterated parameters and the number of DOFs for each of the six bi-meshes $j=1,...,6$ are defined as

$$\mathbf{q}_j^{k_\tau} = \left[q_{\xi_{1,j}}^{k_\tau=1}, q_{\mathbf{T}_j}^{k_\tau}, q_{\mathbf{N}_j}^{k_\tau} \right] \rightarrow n_{\text{DOF},j}^{k_\tau} = 3 \; , \;\; \forall j=1,...,6$$

This subdivision parameterization is homogenously applied on all cross-section segments.

Table 3.3: Reduced set of iterated parameters for the planar cross-section outline*

Parameter Classification		Parameter identification		Parameter Description
Name	**Symbol**	**Name**	**Symbol**	(ξ_1, ξ_2, ξ_3) **represents local coordinates**
Location parameters	$q_\xi^{k_\tau}$	First location parameter	q_{ξ_1}	Controls the perturbation of an iterated pole in the first local axis direction
Orientation parameters	$q_f^{k_\tau}$	First orientation parameter	$q_\mathbf{T}$	Controls the influence from the segment curvature from each pole respectively
		Second orientation parameter	$q_\mathbf{N}$	Controls the influence from the conventional curvature at a bimesh end.

*Compare with Table 2.4.

Since six bi-meshes are included, the entire set includes eighteen iterated parameters.

At the first level of refinement all these parameters are active, i.e.:

$$q_j^{k_\tau=1} = \begin{bmatrix} q_{\xi_{1,1}} & \cdot & q_{\xi_{1,j}} & \cdot & \cdot & q_{\xi 6} \\ \cdot & \cdot & \cdot & \cdot & \cdot & \cdot \\ q_{\mathbf{T}_1} & \cdot & q_{\mathbf{T}_j} & \cdot & \cdot & q_{\mathbf{T}_6} \\ q_{\mathbf{N}_1} & \cdot & q_{\mathbf{N}_j} & \cdot & \cdot & q_{\mathbf{N}_6} \end{bmatrix}^\mathrm{T} , \; \forall j=1,...,6 \;\; \rightarrow n_{\text{DOF}}^{k_\tau} = 3 \times 6 = 18$$

Note that the matrix is typed in open format to emphasize that it can easily be extended to include more parameters in future runs. Also note that iterated location parameters listed in the first row are active only at the first level of refinement $k_\tau = 1$.

3.1.11.1   The Replication Problem

In order to extract the eighteen iterated parameters from each of the one hundred observation meshes a replication problem (see 2.2.1) is defined. The upper bound $\varepsilon_{\tau,\text{upp}}$ for the fault of replication is fixed at

$$\varepsilon_{\tau,\text{upp}} = 15\%$$

The set of indicator metrics $\{m_\mho\}$, which define the replication problem for each of the six tortuous segments, are derived from the discrete Soerjadi moments of area (Soerjadi, 1968) defined in ANNEX 3. Differentiated weighting was not included (see ANNEX 2).

The actual set of imitation parameters is selected as a subset of the set of standard imitation metrics defined in ANNEX 3.4. The selected set of standard imitation metrics used was:

$$\{m_{\mho,\text{std}}\} = \{m_{\mho,2,\text{std}}, m_{\mho,3,\text{std}}, m_{\mho,6,\text{std}}, m_{\mho,7,\text{std}}\},$$

where the individual imitation metrics are: $m_{\mho,2}$ centroid first axis coordinate, $m_{\mho,3}$ centroid second axis coordinate, $m_{\mho,6}$ moment of inertia around first principal axis, and $m_{\mho,7}$ moment of inertia around second principal axis. Furthermore, this standard set is supplemented with the *perimeter*. However, many complications are envisaged in the effort to obtain a high efficiency of replication.

3.1.11.2 Goodness of Replication

Complications in the multivariate optimization of replication extremals

Curves with bad efficiency of replication

High efficiency of replication - but CPU costly.
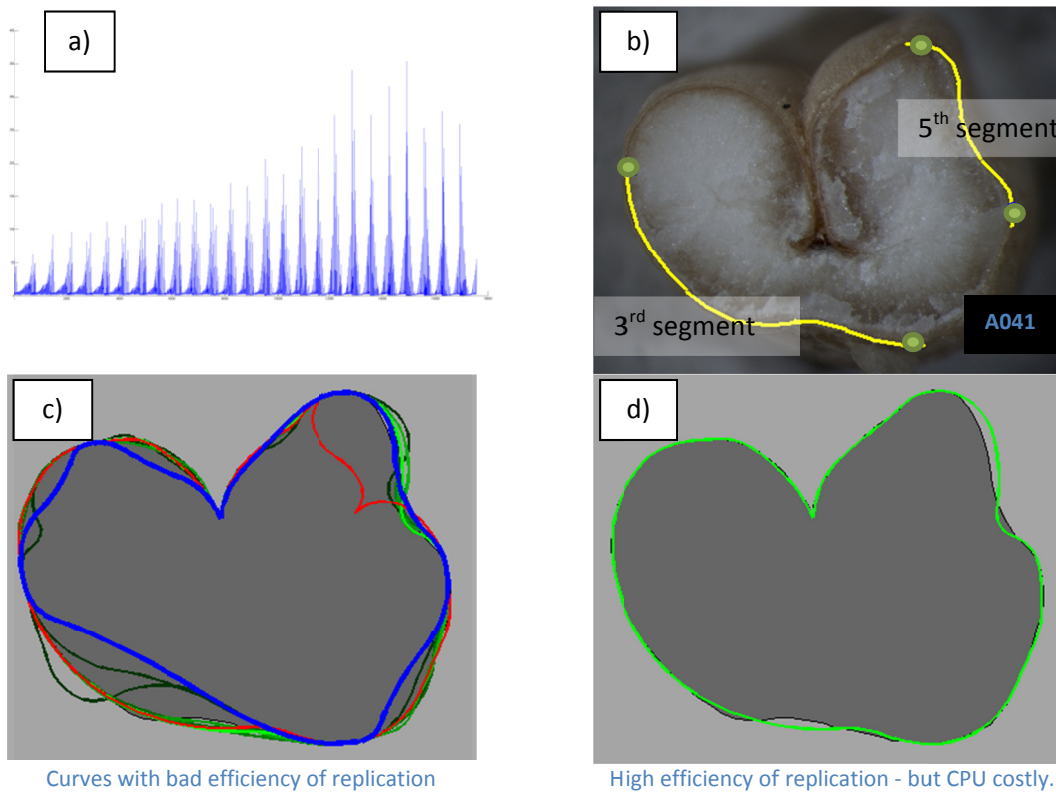
Figure 3.24: The non-linearities complicate fast convergence with high efficiency of replication

The development of a robust efficient optimization algorithm, which is able to solve the replication problem for curve segments of natural boundaries, is still in its infancy. This numerical problem and other algorithmic problems are key barriers in natural parameterization development. A few complications envisaged are illustrated above and are now commented for the replication of the boundary outline for sample object A041.

COMMENTS   The blue graph a) displays the fault of replication for a set of systematically generated feasible curves of the fifth segmentfor cross-section A041, see b). They are generated from the combination of evenly spaced values of the three iterated parameters, i.e. the graph display an example-run with grid-spacing defined in a three dimensional parametric space as one twenty fifth part of one giving $(25+1)^3 = 17{,}576$ curves. A high number of local minima are one of the sources that slow down the search process for a distinct global minimum. Furthermore, as illustrated by a few colored curves in c), the non-linear generation of the curve segments is also problematic. Curves in dark illustrate replication extremals from a small number of generated curves included in the optimization process. Curves colored from dark green to light green illustrate extremals found with an increasing number of iterations. As expected, the curve (in lightest green) with the highest number of iterations also reflects the highest efficiency of replication. The red curve possesses even higher efficiency of replication; however, it does not fulfill its end constraint with respect to regular G^1 continuity. Evidently, it is in fact a false replication (see red curve 5th segment). The blue curve on the other hand has small tortuosity (especially at the 3rd segment) but it is not feasible since its fault of replication is too high. Finally, in d), a replication extremal colored in light green is found. It has a fair efficiency of replication its; tortuosity is minimized; but the CPU expenses supplied are big.

Number of runs

The numerical approach used to extract the iterated parameters in accordance with the concept of goodness of replication (see 2.2.2) is performed by multivariate optimization based on Monte Carlo simulations.

The realization range used for all iterated parameters is:

$$q^{k_r} \in [0;1] \ , \ \ \forall q^{k_r}$$

The number of Monte Carlo simulations for the replication of each of the six segments, for each of the one hundred observation meshes, is limited to twenty five thousand:

$$n_{run} = 25{,}000 \times 6, \ \forall M_{obs} \qquad \text{(Per wheat grain)}$$

This means that fifteen million replication checkings were performed in this study to obtain values for three iterated parameters per section.

With regards to the applied upper bound for the fault of replication (see 3.1.11.1), each observation mesh was checked so at least one feasible solution exists for each of its six segments.

3.1.11.3   Iterated Parameters – Overview

The following reduced set of iterated parameters is used for the six segments:

$$\mathbf{q}^{k_\tau} = \left[q_{\xi_1}, q_{\mathbf{T}}, q_{\mathbf{N}} \right]^{k_\tau}$$

The following mean values and standard deviations were found from the one hundred replications:

Table 3.4: Iterated Parameters - Statistics

Segm.	1			2			3			4			5			6		
ID	q_{ξ_1}	$q_{\mathbf{T}}$	$q_{\mathbf{N}}$	q_{ξ_1}	$q_{\mathbf{T}}$	$q_{\mathbf{N}}$	q_{ξ_1}	$q_{\mathbf{T}}$	$q_{\mathbf{N}}$	q_{ξ_1}	$q_{\mathbf{T}}$	$q_{\mathbf{N}}$	q_{ξ_1}	$q_{\mathbf{T}}$	$q_{\mathbf{N}}$	q_{ξ_1}	$q_{\mathbf{T}}$	$q_{\mathbf{N}}$
Mean	-0.02	0.56	0.49	0.03	0.46	0.53	0.12	0.62	0.57	-0.01	0.54	0.59	-0.06	0.48	0.54	0.03	0.56	0.50
Std	0.30	0.16	0.30	0.27	0.19	0.31	0.28	0.20	0.32	0.28	0.23	0.30	0.24	0.24	0.30	0.31	0.20	0.29

3.1.12   SUMMARY - Parameter Extraction - RESULTS

a

b

Replication A053
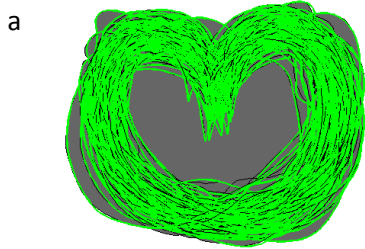
For each object in the sample, a total of eighteen master parameters, ($n_q^0 = 18$) and eighteen iterated parameters (three iterated parameters for each of the six segments, i.e. $n_q^{k_\tau} = 3 \times 6 = 18$) are stored. This means that a total of thirty six natural parameters are stored for each object:

$$n_q = n_q^0 + n_q^{k_\tau} = 18 + 18 = 36$$

Therefore, since the entire observation set containing one hundred meshes, a total of thirty six hundred data points are collected, i.e.:

$$n_q = 100 \times 36 = 3600$$

The entire data set is stored in a bank of natural parameters.

The maximum relative error for the replication of the cross-section areas was found to 0.59% for replication A053. See Figure 3.25 (b).

Figure 3.25: (a) The one hundred replications plotted on top of each other. (b) Replication with max error of repl.

In Figure 3.25 (a), the replicated cross-section outlines, based on these three parameters per segment, are plotted on top of each other to give an impression of the variations in the one hundred results.

3.2 CHEMOMETRICS

In this section, the stochastic preprocessing, including quality checking of the collected data, is performed. In this study only Frenet subdivision for tortuous curves is in use. Therefore, alpha-beta decomposition is not relevant (see 2.3.2.2). However, a key requirement is that master parameters must be verified to be uncorrelated (see 3.2.1.1 and ANNEX 25). Furthermore, as described in 3.2.1.2, there is a need for second order Frenet subdivision with explicit curvatures for the modeling of the wheat grain cross-sections.

3.2.1   Stochastic Preprocessing

3.2.1.1   Checking Master Parameters

To ensure that the eighteen master parameters (see 3.1.9.6) are uncorrelated a full correlation matrix is defined (see ANNEX 25). The full correlation matrix indicates that there is a weak correlation between the "bow" landmarks location in the second direction q_4 and the two curvatures: q_{12} (sample correlation coefficient $r_{4,12} = 0.66$), and q_{18} ($r_{4,18} = 0.60$) respectively. Even weaker correlations are found between the lower bounding q_7 and the two bounding landmarks q_6 ($r_{7,6} = 0.55$) and q_8 ($r_{7,8} = -0.55$). Finally, small correlations are observed between breadth q_1, and height q_2 ($r_{1,2} = 0.50$). The correlations between other pairs of parameters are even less. In conclusion, the correlations found are all considered to be small. Therefore, it cannot be rejected that the set of iterated parameters are uncorrelated. The data set is therefore accepted for further treatment.

3.2.1.2   Degrees of freedom minimization
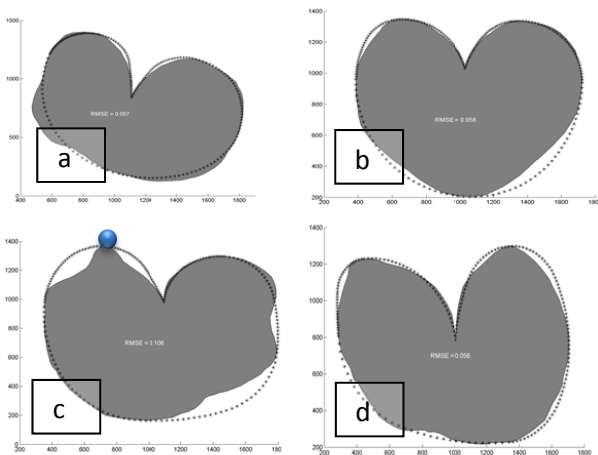
In this study, the three iterated parameters defined in 3.1.11.3 were selected as a compromize between the ability to obtain a fair efficiency of replication and the cost related to the number of degrees of freedom[35]. However, an alternative non-parametric setup was also investigated with Frenet subdivision in its simplest form. In general, this zero degrees of freedom alternative replicated most of the phantoms with a fair accuracy, see Figure 3.26 (a), (b) and (d). However, a few grain cross-sections that had large curvatures were badly replicated, see Figure 3.26 (c).

Figure 3.26: Fitting performed with zero degrees of freedom, i.e. with Frenet subdivision in its simplest form

---

[35] In general, the optimization of the parametric setup is extremely CPU demanding. It is in the pipeline for future studies.

The replication in (c) shows a RMS-fault[36] of 10.6 % for the entire cross section. Clearly the big curvature observed at the top pole, indicated in blue, is the cause of this. Therefore, if extreme curvature values are found in the sample under investigation, second order fittings are needed. This finding was, in fact, the background for the development of Frenet subdivision as a mesh generator explicitly based on curvatures. Consequently, in the sample of wheat grain cross-sections, a detection of inconsistent data was performed in order to verify the existence of significant curvatures.

"Curvature outliers"

To investigate the data set for "curvature outliers," i.e. as inconsistent data, the data set was examined by multivariate analysis (see ANNEX 22-24). The PCA showed that for replication by Frenet subdivision in its simplest form, two grain cross-sections were considered as outliers due to significantly big curvatures. In all, three objects with significant curvatures were identified from influence plots.
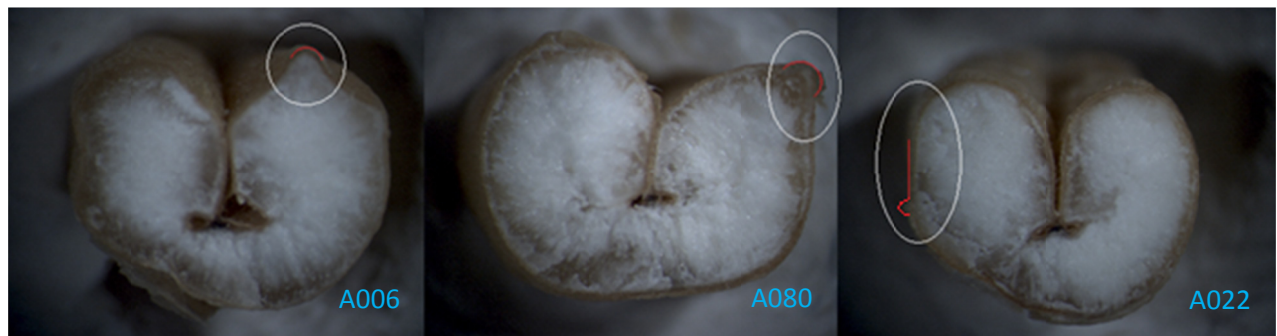
Figure 3.27: Significant curvatures are found for "A006", "A080" and "A022"

The following data were found to possess significant curvatures: A006, A080 and A022, see Figure 3.27.

Figure 3.28: The significant curvatures for"A006", "A080" and "A022" are standard inputs for Frenet subdivision

The replication based on second order Frenet subdivision gives high efficiency of replication see Figure 3.28 since curvatures are explicitly included.

NOTE   It is likely that many natural objects posses large curvatures. Therefore, second order fitting methods such as Frenet based subdivision might be required in future modeling of natural geometries.

---

[36] The RMS-fault is based on the five indicator metrics defined in 3.1.11.1.

3.3 REPARAMETERIZATION

In this section, a set of feasible stochastic phantoms are generated[37] and tested in accordance with the concept of goodness of imitation (see 2.4.3). First, the mean value phantom for wheat grain cross-sections is presented in 3.3.1. Then, some general comments are given on feasible stochastic simulations (see 3.3.2) as well as the Kolmogorov-Smirnov test (see 3.3.3). Finally, a series of stochastic phantoms are presented and tested. The results from the KS-tests are provided in 3.3.5.

3.3.1 The Mean Value Phantom
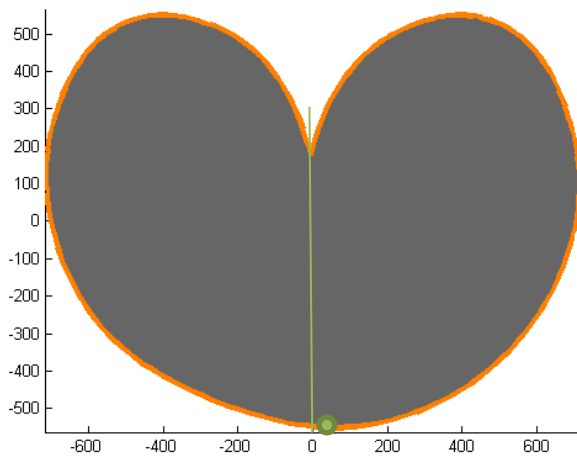
Figure 3.29: The mean value phantom of wheat grain cross-sections

$$\hat{\mu}_{A_{phan}} \equiv \hat{\mu}_{A_{obs}} = 1.23\text{e}{+}006 \text{ [pixel}^2]$$

The shape of the mean value phantom is defined as the phantom generated from the mean values of the natural parameters and adjusted so its size matches the mean size of the observation meshes. The mean values of the master parameters are given in Table 3.2. The mean values of the iterated parameters are given in Table 3.4.

As expected, the mean value phantom has a low tortuousity and is G^2 continous, except for the "bow-line" discontinuity.

Note that the mean value phantom is displayed in pixel coordinates with the first bounding axis parallel to the first axis of the display.

It was found that the mean of the hundred wheat grains have a minor offset of the lower landmark, which appears as a small asymmetry (see Figure 3.29).

In future research this mean value phantom for wheat grain cross-sections and similar mean value phantoms for other natural objects might be used as a nominal reference.

---

[37] In this case study the Monte Carlo simulations of the entire set of natural parameters were based on the normal (or Gaussian) distribution. However, in future studies advanced distribution fitting with finite distributions which meet the ranges of the natural parameters must be performed.

3.3.2 Feasible Phantom Simulations

Natural parameters are defined in a finite interval (see 2.2.10.2). Therefore, stochastic phantom simulation from infinite distributions such as the normal (or Gaussian) distribution must be post-processed to meet the requirement for a finite realization space.
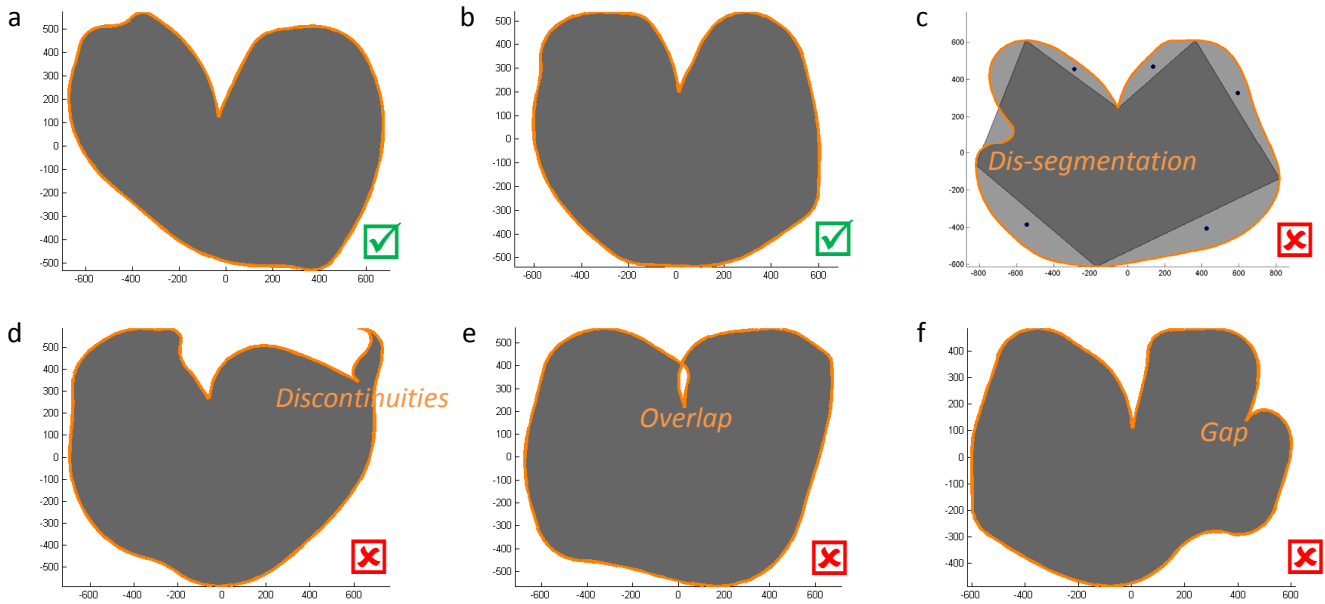
Figure 3.30: Feasible phantoms, (a), (b). Non-feasible phantoms, (c-f)

Furthermore, since the natural parameters are simulated independently, geometric faults such as *dis-segmentation, discontinuity*, *overlap,* or *gap* are likely to occur (see Figure 3.29, c-f). This means that the reparameterization process must be designed so that the "new" phantoms meet the physical constraints of the "real" object. However, the built-in non-linearity of natural parameterization complicates the mathematical formulation of such constraints. In this case study, the phantoms were Monte Carlo simulated by the continuous normal (or Gaussian) distribution. The process was controlled by a combination of simple range constraints and segmentation checking. Finally, simulated phantoms with discontinuity, overlap, or gap were identified by manual inspection and rejected. Such non-feasible phantoms, as illustrated in Figure 3.29 (c-f), were excluded in the final set which was called the *set of feasible imitations*. This final set includes phantoms that are all unique and comply with the physical constraints of the "real" wheat grain cross-sections. In Figure 3.29 (a-b), two such unique phantoms are illustrated. The two feasible imitations illustrated were randomly drawn amongst the set of feasible imitations. This set of feasible imitations wasconsiderably larger than the observation set. , Theoretically, the number of element in the imitation set should go towards infinity. However, in this case study, where the observation set includes one hundred "real" objects, a total of only three hundred "new" phantoms were generated. Out of these three hundred "new" phantoms, one hundred and eighty five were found to be feasible.

3.3.3   Kolmogorov-Smirnov Test

In accordance with the concept of goodness of imitation, the Boolean test factor h_{imi} , in (2.89), was designed for a two-sample test. In this case study, the non-parametric Kolmogorov-Smirnov (KS) test (Massey, 1951) was used for the imitation problems. The inputs for KD-tests are two data vectors, represented by observation-data-vectors and imitation-data-vectors. The images of the generated phantoms were numbered from "P001" to "P300". The distributions for values of area for the one hundred and eighty five feasible imitations were tested against the one hundred values from the observation set. First, the cross-section areas were tested. It was found that their distributions did not differ significantly at 5% significance level. Secondly, the six segment areas were tested in six separate tests. Again, it was found that their distributions did not differ significantly at 5% significance level. These tests indicate that the master mesh, and its set of thirty six natural parameters, imitate the cross-section outline of the one hundred wheat grain cross sections with a high efficiency of imitation. The detailed results of these The Kolmogorov-Smirnov[38] tests are summarized in 3.3.5.

3.3.4   Stochastic Phantoms

For illustration purposes, a minor subset of one hundred stochastic phantoms were drawn from the set feasible phantoms. Three of these stochastic phantoms (P114, P121 and P123) are presented in Figure 3.31. One phantom (P001) is presented in 3.3.5, and the remaining ninety six stochastic phantoms are presented in Table 3.5.
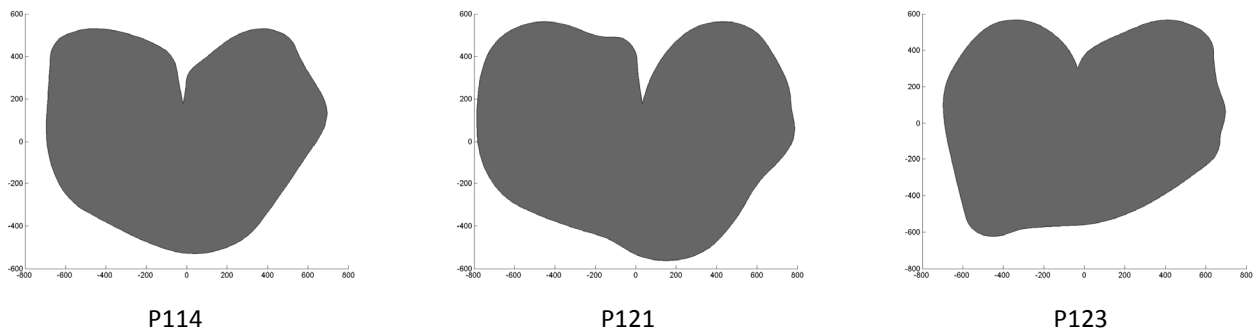
P114   P121   P123

Figure 3.31: Three stochastic phantoms from a set of feasible imitations

Figure 3.31 illustrates three stochastic phantoms (P114, P121 and P123) selected from the set of one hundred and eighty five feasible imitations.

---

[38] The Kolmogrov-Smirnov test is a built-in function named kstest2 in MATLAB® Statistics Toolbox. This built-in function is used directly with two data vectors as input and the Boolean test result $h=h_{imi}$ as output. The default setting 'unequal' for two-sided tests are kept unchanged.

P001
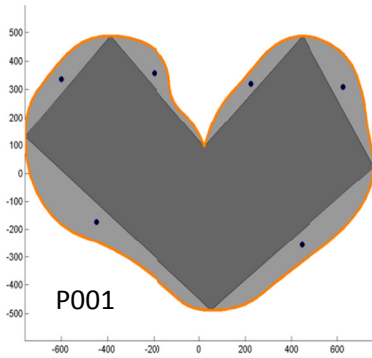
From a sample of one hundred wheat grain cross-sections it was posible to reparametrize a master mesh with thirty six natural parameters into one hundred stochastic phantoms. The imitation process was governed by the concept of imitation. It was found that the area distributions for a set of feasibel Gauss distributed imitations did not differ significantly from the area distributions of the observed wheat grain cross-sections. The KS-test result for distribution of cross-section areas, as well as the KS-test results for distributions of segment areas, concludes this case study.

Distributions of Cross-section Areas
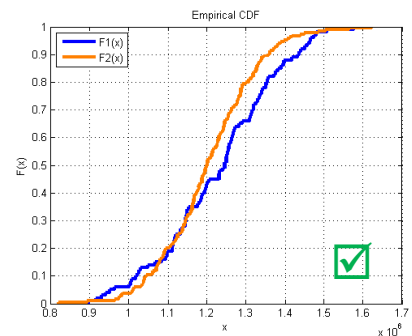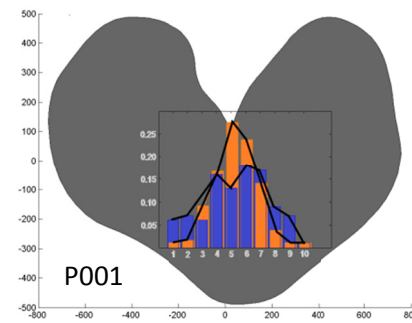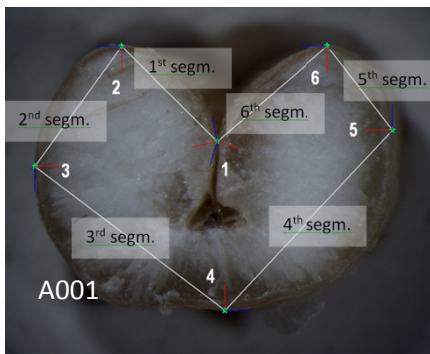
A KS-test showed that the cross-sction areas did not differ at 5% significance level.

Distributions of Segment Areas

Replications   Observations   Imitations

Segment 1	Segment 2	Segment 3	Segment 4	Segment 5	Segment 6
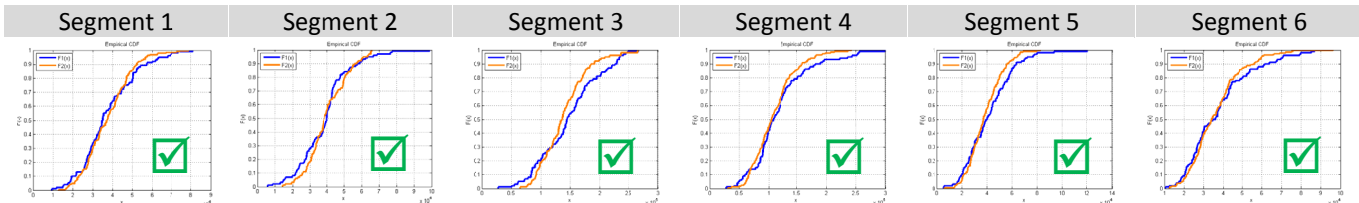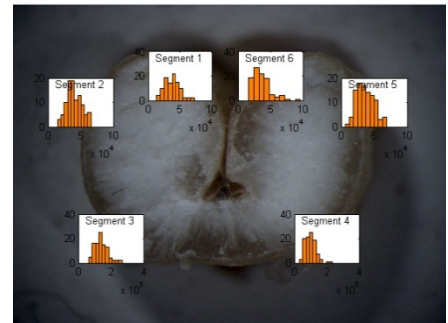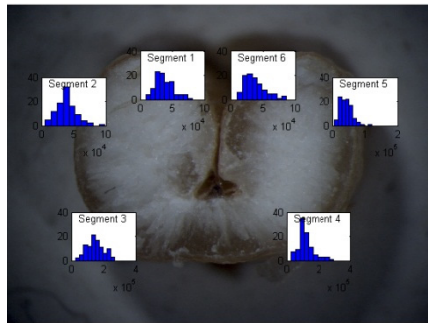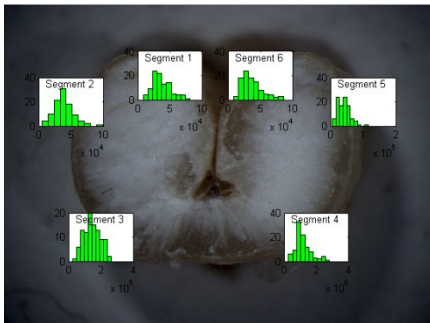
Six KS-tests showed individually that the values for the segment areas did not differ at 5% significance level.

Table 3.5: Ninety six stochastic pantoms from a reparameterized set of feasible imitations[39]

---
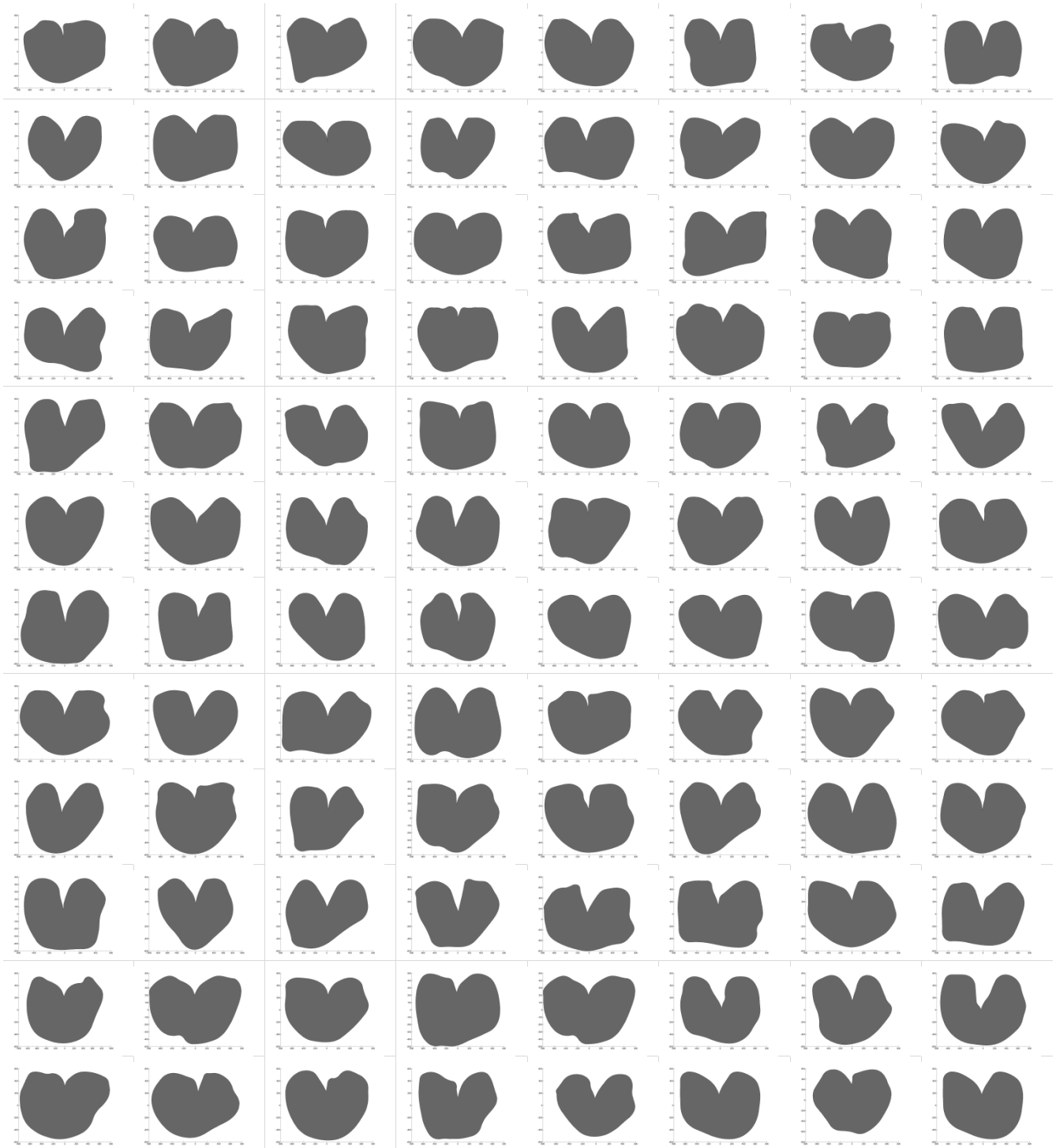
[39] The ninety-six stochastic phantoms are drawn from a set of one hundred and eighty five feasible imitations. In ANNEX 17 a list of stereo-microscopic images for the sample of one hundred "real" wheat grain cross-sections is found.

4 DISCUSSION & OUTLOOK

This chapter includes a discussion of the study methods as well as key findings from the case study on wheat grains and the finding are discussed and put into broader perspectives. Emergent questions are listed in section (4.1), followed by perspectives in section (4.2).

4.1 UN-ANSWERED QUESTIONS

Landmarks

Is it possible to identify natural shape characteristics for natural objects other than Triticum aestivum with its characteristic "bow-line" landmark? There is a long tradition for landmark identification using human beings (see 1.3.2.3). Therefore, it is likely that landmarks can be defined for other natural objects as well. However, the quality of these landmarks for use as controls in a master mesh needs further consideration.

Distinctiveness

Wheat farmers state that the "bow-line" of a wheat grain has an inevitable shape characteristic. It can be stated that the "bow-line" has a high classification quality since it enables characterization of a subjective shape *pattern* or *traits*. Furthermore, if these characteristics appear distinctively for every biomass object in a representative sample, they are classified as good *landmarks*. For the cross-section of wheat, the "bow-line" will appear as a *landmark vertex* whereas it will appear as a *landmark edge* for the surface of a grain. Biometric distinctiveness is characterized by significant variation, or difference, relative to some reference metrics for the object. The "bow-line" characteristics possess a high degree of distinctiveness since the distance from its landmark vertex to the outline convex hull is bigger than all other distances from vertices around the outline. Farmers state that the "bow-line" is not only a distinct pattern for wheat, but also for barley, oats, and other grains. Therefore, the "bow-line" could presumably be a general *convex hull classifier* for various grain species. Furthermore, the "bow line" biometrics can be used as a reference for other landmarks that are not classified by distinctiveness, but by their *dimension* relative to their bounding box, or, to the bounding rectangle for grain cross-sections. However, further investigation into whether or not the distinctiveness of landmarks from new natural objects is strong enough to define algorithms that have the potential to enable their automated identification and further parameterization?

Measurability

In the study of grains of wheat, some geometrical characteristics can be classified from their *dimension*. These characteristics are also called landmarks. However, these landmarks do not possess a high degree of distinctiveness. Instead, they are characterized from their position on the edge of the bounding box of the

object. Today, landmarks for grains, which are based on bounding, are based on conventionally maximum and minimum Feret diameters. These metrics are defined from their axial dimensions such as length, width, and height (or thickness). In that resepect they represent *bounding classifiers*. The *measurability* of such bounding classifiers is important since it enables comparison with existing measurements. For seeds, bounding measurements are anchored in a long professional tradition. Standardized measurement techniques and measurement plans are developed over decades. Therefore, the *landmarks* based on bounding boxes in numerical approaches should be easily measureable from relevant sensors to ensure validation. Modern sensing methods and principles include, among others, *calipers*, *dielectric shift sensors*, *image recognition*, acoustic transmission loss spectrum (TL), and X- ray computer tomography scanning (X-ray CT). Recent studies (Fératlégil-Durmus et al., 2010) based on image recognition of various seeds show that axial bounding can be used to model the shape by ellipsoids. These ellipsoid models estimate thousand seeds weight (TSW) with good precision when compared to conventional mass measurements. In the case study on wheat grains, the imitation meshes, as well as the materialized phantoms, carry this measurability automatically. This is due to the bounding box parameterization, which is built into the master mesh. However, new case studies must investigate which relevant metrics can be built into a new master mesh in order to enable such measurability relative to the objects traditional metrics.

Robustness

One key assumption behind natural parameterization is that carefully selected classifiers carry an adequate amount of information to model geometrical objects with detail, accuracy, and *robustness*. The robustness is regarded high for biometrics that are not subject to significant changes over time. Therefore, "bow-line" biometrics are assumed to possess high robustness since bio-chemical or bio-mechanical changes, such as aging, diseases, or environmental exposure, are not supposed to change its distinctiveness during the period where measurements are taking place.

Since "bow-line" biometrics are assumed to possess high robustness, the extracted master mesh is also assumed to pertain high robustness. In general, this might also lead to robust imitations for metrics such as axial dimensions, surface area, and volume. Dimension landmarks in 2D can be defined from two dimension metrics, i.e. width and height. For 3D models, at least three dimension metrics are required.

Mathematically, dimension landmarks are parameterized by dimension parameters relative to the location, or relative to the orientationof the bounding frame. If these orientation and location parameters are extracted with small standard deviations, it indicates that the bounding box is also a robust approach for natural parameterization using dimension parameters. Therefore, in relation to robustness of the extracted landmarks, it must also be investigated whether or not a bounding box approach is applicable?

Number of degrees of freedom

When the modeler requires a small degree of customization and perturbation modeling, it might be rational to keep the number of landmarks down to a minimum so the number of "tuning factors" is small. Alternatively, when high degree of freedom is required the master mesh might include a high number of landmarks in its

parameterization. In general, the choice of an appropriate set of parameters must rely on a sensitivity study and finding a balance between modeling accuracy and economy. At this stage, neither estimates for computational costs, nor any sensitivity analysis have been performed. Does the fineness of the master mesh, measured in terms of the number of degrees of freedom, influence the final result significantly? This is hard to anticipate since in multiresolution modeling, the final result may be influenced more by the iterated parameter setup than the number of freedom associated to the master parameters.

Extraction of iterated parameters

Algorithmically, the extraction of iterated parameters represents a highly non-linear multivariate optimization problem. Let it be assumed that this optimization includes a finite set of iterated meshes. Unfortunately, a high number of runs (which is costly) might minimize the maximum error of replication. It is not simple to anticipate the optimal number of iterated parameters. Furthermore, how sensitive is the maximum fault of replication relative to the replication extremal?

However, the actual replication extremal found is not only dependent on the number of iterated meshes available, but also on the choice of the optimization method applied. It seems that purely gradient based methods should be avoided. In fact, a thorough sensitivity analysis of the choice of optimization algorithm for natural problems with many distinct minima and non-distinct global minima is needed to ensure that the extraction of iterated natural parameters becomes reliable.

Sensitivity analysis

Sensitivity analysis might also be relevant in attempting to answer the following questions: which parameter among the different types of parameters can be identified as the most influential during parameter extraction? and, which parameter drives the most variation in the reparameterization process? Such questions, which may be answered by sensitivity analysis, are important issues for future study. In general, many different sensibility indexes are in use and several sensitivity methods are available. For a thorough discussion on the of choice of such sensitivity index and methods see (Saltelli, 2009). A starting point for a reparameterization analysis might be to use a sensitivity index s_{idx} for each parameter q_i by measuring the effect on a re-parameterized domain Ω_τ of perturbing the realization q_i of Q_i by a fixed fraction of the mean values μ_{Q_i} which forms the phantom.

$$s_{idx} = \frac{\partial q}{\partial q_i} \frac{\mu_{Q_i}}{\mu_Q}$$

However, only a thorough sensitivity study could reveal if this is a proper starting point.

Texture modeling alternatives

As an alternative to roughness modeling by pure Frenet subdivision, various IFS approaches seem easy to integrate. An illustration of the impressive texture capabilities of one such approach is previously defined in Figure 0.4 (right). Here, a set of control points are used to define the desired roughness pattern of the surface (Gouaty, 2009). Such IFS approaches can easily be integrated in Frenet subdivision either at the limit level, or at preceding levels of quad and tri-meshes. However, currently unidentified meshing approaches might also be relevant.

Subdivision alternatives

Other similar algorithms based on *formulas from analytic geometry* can be developed for standard geometries such as: elliptic cylinder, elliptic cone, hyperboloid of one sheet, hyperboloid of two sheets, elliptic paraboloid, and hyperbolic paraboloid. Also, irregular curves can be formed by *direct integration,* as illustrated in ANNEX 7, by post manipulation of NURBS or by implicit functions (also known as implicit surfaces) (Bloomenthal, 1998), (Osher & Fedkiw, 2003), (Sclaroff & Pentland, 1991). However, it is not likely that complex natural objects can be modeled from analytic expressions, even as mean value approaches.

Goodnes of imitation alternatives

How can natural and abnormal natural variations be generated so that they reflect observed variations? Is the proposed concept of *goodness of imitation* applicable for a wide range of objects? Is it possible to set up standardized decision rules for validation of generated phantom variations? How can a generated variation spectra be accepted/rejected statistically in a compliance test with the observed variation spectra for a given biomass object? Can standard performance metrics such as false accept rate (FAR), false match rate (FMR), or equal error rate (EER) be applied on imitation modeling too? These questions are all considered important areas for future research.

Random number generation

In natural parameterization, imitations are created from random number generation. However, in the alpha-bet decomposition, a thorough study on the convolution of PDFs required is still missing. A number of further research issues have arisen in that respect. Stating these as questions: Is the efficiency of imitation weakly or strongly dependent on the used PDFs? Is it possible to optimize the alpha-beta decomposition by standard random number generators, or must new randomization algorithms be developed? How does the aspect of a finite realization space influence the abnormality modeling? Can the bounds for realizations be loosened without loosing control of the generated phantoms?

The many open scientific research questions listed above clearly indicate that natural parameterization is a piloting study. Further research and case studies must be conducted to further advance the field of natural parameterization.

4.2 PERSPECTIVES

The novel Baek-Lee method and the natural parameterization approach might be the starting point for future experimentation on pseudo-natural objects. It is expected that todays empirically based research on natural objects will be replaced with experimentation on phantoms. In the distant future it is possible that experiments on real human beings, animals, biomasses, vegetation, soil, fracture, flows, or other objects and phenomena with an underlying stochastic behavior, will be conducted using advanced multi-physics software and geometrically modeled stochastic phantoms. Such experimentation on stochastic phantoms will provide new opportunities in experimentally based sciences and perhaps assist in the explanation of a number of todays unsolved problems. In this study, a very simple planar 2D case study was performed. However, case studies on rough surfaces and the volumetric distribution of matter in solids might revise the proposed formulations of "goodness of replication" and "goodness of imitation". In particular, the inclusion of indicator parameters other than moment of area and perimeter (as used in the present case study), is an obvious area to be studied in the near future. Multi-subdomain and multi-object studies are also relevant. However, they are much more complicated than the one-domain cross-section problem investigated here. After such multi- studies, future research will also need to include cluster and subcluster geometries.

Cluster and subcluster modeling

Movement of a subcluster in an air stream

Domain modeling including clusters and subclusters is in the pipeline for further study. However, in studies including flow of objects, the dynamic contact problems are expected to be a huge challenge. Modeling of the tortuous geometries is further complicated because the mutual connectivities must be updated incrementally over time.

In Biosystems engineering, flow modeling through non-solid domains is relevant for drying of grain clusters, for water and air flow trough soil, and for acoustic transmission through grain and soil clusters.
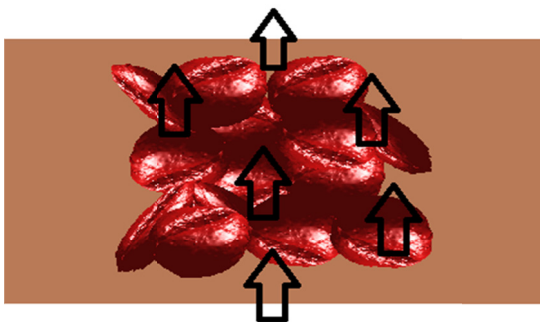
Flow through a stationary cluster constellation

Even the geometric modeling of such stationary cluster constellations might require some new strategies in order to form the connectivity arrays. When the cluster constellations themselves are assumed to be stochastic by nature, it is likely to complicate the tortuous geometry modeling even further.

Furthermore, some of today's animations and animated movies, which include models of natural objects and phenomena, might benefit from some of the geometrical features included in natural parameterization.

5 CONCLUSION

In this thesis, a novel generic approach for imitation of geometrical objects with random variation has been presented. The approach is called "natural parameterization" and its objective is to imitate the geometry of "real" objects that are characteristically unique and possess an underlying stochastic behavior. The stochastic behavior was modeled by a set of independent random variables called the natural parameters. In popular language, the constellation of these parameters is called the "geometric DNA" of that object. Two key steps are comprised in the novel approach. During the first step, called parameter extraction, the natural parameters of an object are identified from scanned data. In the second step, called reparameterization, these extracted parameters are reused to simulate "new" phantoms that imitatate the "real" object. To bridge the two key steps, chemometrics was applied and a new stochastic decomposition technique was introduced. Not only does this technique compensate for the numerical difficulty induced by the numerical iterations, it also allows for modeling of extreme geometries such as natural abnormalities. Technically, the natural parameterization approach was used as a theoretical framework for the development of dedicated algorithms for a case study. In the following section, conclusive remarks are given on the two key steps of natural parameterization, as well as on some algorithmic details and complications and their application as a tool to study the rough outline of wheat grain cross-sections.

The input for natural parameterization was found to be a mix of scanned data and expert knowledge

Since the geometries used must be tetrahedral volume meshes, triangulated surface meshes, or simple polygonal curves, the "real" objects were preprocessed prior to the initiation of the parameter extraction. However, in this work, case studies from volumetric data or surface data from rough geometries are not included. Only planar polygonal curves are included in the case study on wheat grain cross-sections. This case study is based on a sample of one hundred cross-sections of *Triticum aestivum*. The individual cross-sections are captured by a stereo microscope. One of the first observations was that the captured cross-section outlines were rough, tortuous, and included a characteristic discontinuity. Amongst farmers and other experts, this discontinuity is known as the "bow-line." Experts state that this "bow-line" is a unique characteristic of wheat grains.

Based on this expert knowledge, a new algorithm was developed which was able to identify the "bow-line" automatically. However, one severe complication was that the pixel outlines appeared very diffuse in the images. Therefore, investigations on background settings, post-coloring of test specimens, and natural self-distortion were performed. In an attempt to enhance the outline contrast, a flatbed scanner was also used to capture supplementary images. Due to the high degree of self-distortion, it was concluded that automatic outline detection by standard software was not reliable. It was found that the extracted outlines did not match the outlines recognized by the human eye. Therefore, it was decided to extract the one hundred cross-sections by manual detection. This detection produced one hundred polygonal point sets that could be used directly as input for a dedicated identification algorithm.

The parameter extraction from rough geometries was designed to ensure maximum "goodness of replication"

This dedicated identification algorithm was able to identify the "bow-line" from simple distance calculations between the polygonal points and a convex hull. After this, an anti podal pairs constellation was used to specify the orientation of the polygonal bounding rectangle. From this orientation specification, it was possible to form a unique frame of reference for each single grain. Using the "touching points" between the bounding rectangle and the input polygon, five additional points were then automatically identified. Hereby, the set of landmarks was extended to a set comprising six parameters. These six landmarks were subsequently used to establish six so-called "tortuosity poles" representing a geometric constellation like a coarse FE mesh. In contrast to the nodal points used in FE formulations, these new tortuosity poles also include geometric information on orientation quantities. In 3D, these orientation quantities cover tangents, normals, binormals, curvatures, and torsions. However, for the planar wheat grain, cross-sections torsion was not used.

By introducing such tortuosity poles, it was found that the extra information on geometric orientation could be captured and used to define explicit geometric G^1 and G^2 continuity. This explicit information on continuity was later found to be an important starting point for non-linear extrapolations. From the landmark parameters and the various orientation parameters, a complete set of so-called master parameters was then formed. These master parameters represent a coarse mesh in parameter space similar to the master elements used in FE. For the wheat grain cross-sections, the master mesh was further subdivided into six segments. By this segmentation, each wheat polygon was split into six rough curve segments. An important finding was that when the modeling was based on tortuosity poles, the mathematical representation of these six curves was exactly the same for the bow-line pole with the discontinuity as it was for the other five poles with G^2 continuity.

Technically, this means that in natural parameterization, rough and smooth geometries are modeled in the same way. This geometrical invariance is due to the use of orientation invariant bi-meshes bounded by frames of poles. For the six rough grain segments, a novel iteration approach called "Frenet subdivision" was applied as a generator to obtain rough curves. It was found that this generator was able to generate rough curves that were able to fulfill the geometrical end conditions at the bi-mesh poles. For the wheat grain curves, three so-called iterated parameters were introduced in the parameterization of the roughness. In this way, the degrees of freedom were dramatically extended. Six segments with three parameters added an extra eighteen parameters for each of the one hundred cross-sections.

To determine these parameters, which control the shape and the roughness for the curves, a novel iterative optimization process was formulated as a variational problem. This problem is called a replication problem and it is numerically formulated as a multivariate non-linear optimization problem. In the formulation, two complementary measures, called the efficiency of replication and the fault of replication, are introduced. The purpose of this formulation strategy is to assure that the result from the optimization process is a single extremal. This is achieved by claiming that the extremal is a particular rough curve that possesses the minimum tortuosity amongst the set of feasible rough curves with the highest efficiency of replication. For the case study, the maximum relative error for replication of the cross-section area was less than one percent. The fitting was in fact indirect, since the goodness of replication was based on a minimization of the differences of five cross-section properties for the six segments. These properties included four moments of area metrics and the perimeter.

In conclusion, it was found that the developed identification algorithm was able to extract eighteen master parameters and another eighteen iterated parameters in total. This means that an automatic parameter extraction of thirty-six natural parameters for each cross-section of the one hundred wheat grains was established. Therefore, the total number of extracted data points reached thirty six hundred. Finally, these data points were stored in a bank of parameters for treatment by chemometrics and for further stochastic decomposition.

A novel stochastic decomposition compensates for numerical errors induced during roughness modeling

Unfortunately, the iterative algorithms used for the generation of rough surfaces and solids by nature induce some numerical errors. Specifically, this numerical complication arises when two or more rough curves are required to pass through a common point as required by subdivision. In terms of small pole translations, this error is compensated for via an adjustment of the rough curves. Modeling wise, these adjusted translations were perceived as small fluctuations around the mean value for a random roughness variable. Using a minor modification of the well-known Reynolds decomposition, it was found that these numerical fluctuations could be compensated for in a rational way. More specifically, a random roughness variable was first decomposed, before being used for simulation in two individual parts. In the first part, a small fluctuation was simulated by a random number generator. It used the overall mean value and the small part of the standard deviation as input parameters. In the second part, the dominant fluctuations of the rough geometry were simulated by a major contribution of the variation. This variant of Reynolds decomposition is called alpha-beta decomposition. Here, the alpha part represents the dominant fluctuations, whereas the beta part represents the non-dominant fluctuations. However, before the parameters from the bank of parameters were used for stochastic simulation, it was verified that they were weakly correlated. The maximum correlation coefficient between pairs of the eighteen master parameters was found to be 66%. As a whole, the parameters were considered a set of independent random variables.

The novel approach was able to simulate "look-alike" phantoms from the bank of natural parameters

The mean values and the standard deviations were drawn from the parametric bank. The natural parameter made up of thirty-six parameters was all modeled by the standardized uniform distribution during all Monte Carlo simulations. First, a mean value phantom of the cross-section was generated. It represented a pseudo-stochastic representation of the one hundred wheat grains. Then, one hundred "new" wheat grains were simulated in accordance with the new concept of goodness of imitation. It was found that the distribution of the variations in the geometry of the "new" grains did not differ significantly from the distribution of the variations in the "real" grains. The tests were based on area variations of the six segments and of the area variations of the entire cross-section. The two-sample Kolmogorov-Smirnov test at a significance level of 5% was used. The test showed that for the six segments, as well as for the entire cross-section, the null-hypotheses ("the two area distributions were equal") was not rejected for the corresponding data vectors of area variations. From these results, it was concluded that the reparameterization process was able to simulate "new" wheat grain cross-sections with high efficiency of imitation based on a sample of one hundred "real" wheat grains.

Closing the research gap between today's smooth semi-deterministic geometry modeling and tomorrow's rough stochastic simulations

As a whole, it has been shown that a conglomerate of dedicated algorithms was able to perform an extraction of natural parameters, and reparameterization into stochastic phantoms, from wheat grain cross-sections. Technically, this algorithm was developed using observation meshes and expert knowledge as INPUT and new stochastic phantoms as OUTPUT. It was further found that the developed software was able to perform these tasks automatically.

With regards to the case study on wheat grains, a few general aspects are notable:

From an INPUT set of one hundred stereo microscopic image-files of wheat grain cross-sections, and expert knowledge on the landmark called the "bow-line," it was possible to extract the same set of natural parameters for each of the one hundred image files. Based on the parameter extraction process, an important finding is that "at least one unique parametric constellation exists" for all objects in the sample investigated.

From the bank of parameters, Monte Carlo simulation was later applied to simulate the OUTPUT, consisting of a set of "new" wheat grain cross-sections. It was found that these "new" wheat grain cross-sections fulfilled the requirement on uniqueness. In conclusion, the "new" stochastic phantoms were able to imitate the "real" wheat grain cross-sections in such a way that they all differed from each other, and from the "real" objects.

Ultimately, the piloting INPUT/OUTPUT algorithm[40] was developed to model the rough geometries. It unifies the set of identification algorithms from the parameter extraction process with the set of simulation algorithms from the reparameterization into one stochastic approach.

The number of unanswered questions that emerged during this study is larger than the number of answers found by the research. Therefore, it must be concluded that the field of natural parameterization is still in its youth.

---

[40] Algorithms have been developed within the MATLAB® environment. The graphics presented has been handled by MATLAB® `line` and `patch` objects. Graphics settings for FE post-processing are stored in the MATLAB Handle Graphics® format.

6   ANNEX

ANNEX 1   DISCRETIZATION OF NATURAL GEOMETRIES

This annex provides a few details on some of the main concepts for discretization of natural geometries in order to supplement the brief description given in the Methods chapter.

ANNEX 1.1.1   Configurations and Constellations

The term *natural configuration* is used to designate the *material* or *substance* distribution within clusters, subclusters, object/species or subdomains thereof. The term *natural constellation*, on the other hand, is used to designate the *geometrical distribution* in *time* of the space, which contains the material or substance.

ANNEX 1.1.2   Geometric Continuity

Here, geometry models in three spaces are said to possess geometric continuity G^n of order n. Higher order geometric continuity $n \geq 3$ is not considered here. In the discrete formulation used here, continuity is restricted to the close neighborhood of tortuosity poles. The geometric continuity of an embedded curve is defined in the following table.

Table A. 1: Geometric continuity in the close neighborhood of tortuosity poles

Order	Symbol	Term	Description
$n=0$	G^0	*Vertex continuity*	*Zero order geometric continuity* G^0 exists for an embedded curve C_τ passing through a vertex of a tortuosity pole P_τ if, it is bound by one or two of the pole tangents. This is also called *zero-order G-continuity of C_τ at* P_τ or simply *vertex continuity*.
$n=1$	G^1	*Tangent continuity*	*First order geometric continuity* G^1 exists for an embedded curve C_τ with G^0 continuity at a tortuosity pole P_τ if, it is bound by one pole tangent or by two aligning pole tangents. This is also called *first-order G-continuity of C_τ at* P_τ or simply *tangent continuity*.
$n=2$	G^2	*Curvature continuity*	*Second order geometric continuity* G^2 exists for an embedded curve C_τ with G^1 continuity at a tortuosity pole P_τ if, it is bound by one Frenet triple with non-zero curvature or by two Frenet triples sharing the same center of curvature. This is also called *second-order G-continuity of C_τ at* P_τ or simply *curvature continuity*.

NOTE   Geometric continuity is invariant to the underlying parameterization of the geometry.

ANNEX 1.2   DOMAIN DEFINITIONS

The discretization of natural geometries includes both *domain* and *boundary* objects. The discretization is hierarchical in nature and affects the resolution level by adding more and more detail into the final model. As mentioned in the introduction, the hierarchical discretization model for 3D volume as it appears in the software package [COMSOL® Multiphysics](#) is adopted. This discretization model includes one type of *domain objects* called *subdomains* and three types of *boundary elements* namely: *faces*, *edges* and *vertices*.

To facilitate the modeling of natural objects, it is rational to extend the above model with new elements.

Three domain elements called *cluster*, *subcluster* and *species* are added. The nomenclature used for these extra elements is intended to be in line with the well-known multi-physics notation for objects in $\Re^3$. Some boundary elements are also added. These elements include: *Frenet quantities,* and two hybrid primitives called *tortuosity poles* and *tortuosity elements*. They are introduced as the general basis for multiresolution parametric subdivision. For the irregular shape, modeling *tortuosity* metrics are also included.

The extended geometric discretization setup is designed to fit conventional multi-physics modeling. As it appears, the core of the notation is adopted directly from [COMSOL® Multiphysics](#).

ANNEX 1.2.1   Regular and irregular meshes

A *mesh* M is a numerical representation of a *discretized constellation*. In classical FEA, such meshes are usually defined by: *coordinate arrays* **X** of *location vectors,* and *connectivity arrays* **C** connecting the *nodal points*. For tortuous meshes M_τ, this classical mesh concept is extended to represent a general *information set* comprising not only location vertices **V**, but also *orientation vectors* such as frames **TNB**, *curvatures* **χ**, and other parameters which are useful for the modeling of *tortuous* geometries with *smooth* or *rough* characteristics.

ANNEX 1.2.2   Cluster

A **cluster** Σ_ψ is a constellation of species that are connected at contact zones only through friction, cohesion or adhesion.

The species of a cluster does not necessarily belong to the same genus. In general, clusters of natural objects contain impurities i.e. proportions of species which do not belong to the same genus as the majority of species. Therefore, a cluster is considered non-homogenous in general. Generically, a cluster represents the highest level in the discretization hierarchy.

ANNEX 1.2.3   Subcluster

A **subcluster** Ω_ψ is a constellation of a homogenous subset of species sampled from the same cluster, i.e. a sample without impurities which means that it models individual species that belong to the same genus only.

ANNEX 1.2.4   Object/Species

An *object/species* Ψ_Ω is a geometric model of a single natural object. Generically, species Ψ_Ω are children of subclusters. Statistically, a species can often be seen as an element randomly taken from a subcluster. In Biosystems engineering, a species usually represents the geometric model of a biomass such as a grain of wheat, rice, maize, or other seeds. However, it might just as well represent a grain from a soil sample or other natural objects.

ANNEX 1.2.5   Subdomain

A *subdomain* Ω represents a characteristic part of a species. Generically, subdomains Ω are children of species Ψ_Ω. Therefore, species are said to be discretized into subdomains. A subdomain is not a member of any special element group. At least one single subdomain must be specified in a natural parameterization model. Therefore, subdomains represent the *master elements* of any 3D parameterization; while clusters, subclusters and species are all super elements formed as geometric super sets of subdomains.

In a multi-physics context the modeler assigns *characteristic physical properties* of the natural object for each of these subdomains.

ANNEX 1.3   BOUNDARY DEFINITIONS

Boundary primitives $\delta^p\Omega$, $p \in \{1,2,\ldots,5\}$ define the geometrical bounds of tortuous domain objects Ω_τ. The various boundary primitives are sometimes referred to as *geometric primitives*.

Groups of boundary primitives

The boundary primitives are grouped as:

- **Derived primitives** (syn. *topological primitives*): *Faces* and *edges*
- **Core primitives**: *Vector primitives* (*location* and *orientation* vectors) and *scalar primitives* (*generalized curvatures* and *tortuosity metrics*)
- **Hybrid primitives**: *Tortuosity poles* and *tortuosity elements*

ANNEX 1.3.1   Faces

Natural surfaces can be discretized into *face elements* $\delta^1\Omega$ (see ANNEX 16.2), which are simply polygons. Faces are *first generation elements of subdomains,* which they bound geometrically. Generically, face elements are children of subdomains. Sometimes, it is rational to define triangular and quadrilateral face elements by two natural coordinates or by two barycentric coordinates.

ANNEX 1.3.2   Edges

Curves C_τ are discretized into constellations of *edge elements* $\delta^2\Omega$. Edges are second generation elements of a subdomain and bound the face elements of the subdomain. Generically, edge elements are children of faces. Sometimes, it is rational to define edges by a single natural coordinate or a single barycentric coordinate. In natural parameterization it must be emphasized that curves of natural geometries are assumed to be non-smooth.

ANNEX 1.3.3   Vectors

Vector primitives $\delta^3\Omega$ are third generation elements of subdomains. They bound the *location* and *orientation* of edges, which will be defined hereafter.

Location vectors

Location vectors are *position vectors* and are symbolized here by $\mathbf{r}_V$. The initial point, i.e. the tail of such a location vector, is assumed to be located at the origin of a Cartesian coordinate system. The terminal point, i.e. the tip, is assumed to locate an indexed point termed a *vertex* and is symbolized by $\mathbf{V}$.

The notation *master vertex* $\mathbf{V}^0$, is used to designate a vertex in a master mesh M^0.

NOTE   In FEA and subdivision, various synonyms for vertices such as *nodal points, nodes, master nodes, control points* or *control vertices* are in use.

Orientation vectors

A *chord* in a mesh is an oriented line segment defined from a location vector by a normalized direction vector $\mathbf{e}_{AB}$ oriented from vertex $\mathbf{V}_A$ towards a neighboring vertex $\mathbf{V}_B$. This unit vector $\mathbf{e}_{AB} = -\mathbf{e}_{BA}$ is said to radiate positively from $\mathbf{V}_A$ towards $\mathbf{V}_B$, and negatively from $\mathbf{V}_B$ towards $\mathbf{V}_A$.

A *face normal* $\mathbf{N}_F$ is a surface normal evaluated at the corner vertex of an approximating rectifying plane spanned by two edges.

An *edge normal* $\mathbf{N}_E$ is a surface normal evaluated at the edge end of an approximating rectifying plane restricted to the neighborhood of that edge end. An edge normal fulfills the orthogonality and perpendicularity conditions.

The *central vertex normal* or simply the *vertex normal* $\mathbf{N}_V$ is a normalized surface normal evaluated at the vertex of the approximating rectifying plane in the close neighborhood of that vertex. By default, the vertex normal is used to represent the *outward central normal* of smooth analytic surfaces.

The *generalized curvatures* $\delta^4\Omega$ represent the fourth generation scalar property of a subdomain. Generalized curvatures seem to be of utmost importance for natural parameterization. Therefore, the concepts of Frenet orthogonalities, Frenet order transformation, and the Camille Jordan generalization (previously defined) are essential in natural parameterization.

Frenet based core primitives

Let the core primitives be a group of objects used to define the end of an edge spanned by two vertices of a discretized geometry so an end tangent **T** , and an end normal **N** , represent estimates of the corresponding Frenet normals. The corresponding end vertex is termed a *Frenet vertex.* The triple of orthogonal right handed orientation vectors **TNB** are termed a *Frenet frame*.

A summary of such Frenet based core primitives for natural geometries are listed here for convenience:

- **V** - Vertices. (Locate edge ends).
- **T** - Frenet tangents. (Orientate normal planes).
- **N** - Frenet normals. (Orientate rectifying planes).
- **B** - Frenet binormals. (Orientate osculating planes).
- $\{F\}$ - Frenet frames. (Orientate edge ends).
- κ - Conventional curvature (Measure the variation in the tangential direction **T'** after **N**)
- τ - Tortuosity (Measure the variation in the binormal direction **B'** after **N**)

Note that two other types of normal vectors are also in use, namely: vertex normals $\mathbf{N}_V$, and face normals $\mathbf{N}_F$ (see ANNEX 1.3.3).

Remarks on points and vertices

In the modeling of natural geometries, a point is defined as a location in space that is NOT connectively constrained by other objects. However, when constraints are applied its status changes and it becomes a location vertex, which is explicitly included in a connectivity array. In FEM, such location vertices are usually referred to as *nodal points*. When biomasses are observed, landmarks are identified as points or vectors and are used in the discretization process. In mathematics, such landmark vertices are usually termed *invariant points* or *fixed points*.

ANNEX 1.4   OVERVIEW - Domain and Boundary Elements

The generic hierachy amongst geometric objects is summarized below.

The domain hierachy

- **Clusters** Σ_Ψ are parents of subclusters.
- **Subclusters** Ω_Ψ are children of clusters and parents of species.
- **Species** Ψ are children of subclusters and parents of subdomains.
- **Subdomains** Ω are children of species and parents of faces.

The boundary hierachy

- **Faces** are children of subdomains and parents of edges. A non-subdivided face is symbolized by F^0 and termed the *master face*.
- **Edges** are children of faces and parents of core primitives. A non-subdivided edge is symbolized by E^0 and termed the *master edge*.
- **Core primitives** are children of edges. Core primitives have no children themselves. Core primitives include vertices, and Frenet frames (which include Frenet vectors i.e. Frenet tangents, Frenet normals and Frenet binormals). Furthermore, Frenet chord vectors, vertex normals, and face normals are considered core primitives. In section 2.6 it is demonstrated how core primitives can be parameterized and thereby form the basis for parametric mesh generation.

ANNEX 1.5   Other Special Notations

- A **boundary segment** ℧ represents a sub-region. It can be a line segment, a surface segment, or a volume segment.
- **Cells** represent a special group of boundary objects that contain faces, edges and vertices only.
- A **triangular face** includes three edges and three vertices.
- A **quadrilateral face** includes four non-intersecting edges and four vertices.

As an alternative to a tagged data structure, standard FEM matrices can be used to describe the fundamental data flow. These more conventional matrix descriptions are used in this presentation since they usually ease the reading.
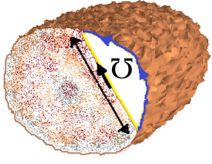
In this annex, details for determination of the total fault of replication are provided under the assumption that planar cross-section segments are used as control geometries. The total fault of replication ε_τ, in (2.2), for any segments is defined as the average of a number of replication faults taken at relevant levels of refinement for that segment, i.e.

$$\varepsilon_t = \frac{1}{n_{\text{relevant}}} \sum_{j=1}^{n_{\text{relevant}}} \varepsilon_{\mho,j}^{k_\tau}, \quad \forall k_\tau \in \left\{ k_{\tau_{\text{relevant}}} \right\}, \tag{A.1}$$

where the relevant levels of refinement are

$$\left\{ k_{\tau_{\text{relevant}}} \right\} = \left\{ k_{1_{\text{relevant}}}, ..., k_{n_{\text{relevant}}} \right\}, \quad n_{\tau_{\text{relevant}}} \in \left\{ 1, ..., n_\tau \right\} \tag{A.2}$$

In general each segment fault $\varepsilon_{\mho,j}^{k_\tau}$, $j = 1, ..., n_{\text{relevant}}$ is supposed to go towards zero

$$0 \leftarrow \varepsilon_{\mho,j}^{k_\tau} = \mathbf{w}^{k_\tau} \bullet \boldsymbol{\varepsilon}^{k_\tau} \leq \varepsilon_{\tau,\text{upp}}^{k_\tau}, \quad \forall k_\tau \in \left\{ k_{\tau_{\text{relevant}}} \right\}, \tag{A.3}$$

where

$$\mathbf{w}^{k_\tau} = \left[w_1^{k_\tau}, w_2^{k_\tau}, ..., w_i^{k_\tau}, ..., w_{n_\mho}^{k_\tau} \right], \quad \sum_{i=1}^{n_\mho} w_i \equiv 1 \tag{A.4}$$

is a row vector of weights and

$$\boldsymbol{\varepsilon}^{k_\tau} = \left[\varepsilon_1^{k_\tau}, \varepsilon_2^{k_\tau}, ..., \varepsilon_i^{k_\tau}, ..., \varepsilon_{n_\mho}^{k_\tau} \right]^{\mathrm{T}} \tag{A.5}$$

is a column vector containing the $n_\mho$ individual faults.

Each individual fault is defined as

$$\varepsilon_i^{k_\tau} = \left| q_{\mho,i}^{k_\tau} \right|, \quad i = 1, ..., n_\mho, \tag{A.6}$$

where $q_{\mho,i}^{k_\tau}$ represents a segment indicator reflecting the discrepancy between a generated indicator metrics $m_{\mho_{\text{phan}}}$ and an observed indicator metrics $m_{\mho_{\text{obs}}}$ as

$$q_{\mho,i}^{k_\tau} = \frac{m_{\mho_{\text{phan},i}}^{k_\tau}}{m_{\mho_{\text{obs},i}}^{k_\tau}} - 1, \quad i = 1, ..., n_\mho \tag{A.7}$$

NOTE   In contrast to the conventional relative error, the segment indicator metric $q_{\mho,i}$ can take negative values. From a parameterization point of view such indicator metrics are parameters. However, indicator metrics are not considered to belong to the set of natural parameters.

ANNEX 3   *NATURAL INDICATOR METRICS*

ANNEX 3.1   MOMENTS OF AREA

As indicator metrics for cross-section areas, the various moments of area for a closed polygon defined by $\mathbf{V}_i$, $i \in \{1,\dots,n_{\mathbf{V}}\}, \mathbf{V}_1 = \mathbf{V}_{n_{\mathbf{V}}}$ are used. In general, (Soerjadi 1968), any such moment of area identified by an index couple (p,q) is determined by numerical recurrence relations which estimate the analytical formula

$$m_{\eth_{p,q}} = \iint_A x^p y^q dxdy \tag{A.8}$$

The six moments conventionally used in science and technology are given by the following index-couples:

$$(p,q) \in \{(0,0),(0,1),(1,0),(0,2),(2,0),(1,1)\} \tag{A.9}$$

ANNEX 3.2   SOERJADI RECURRENCE RELATIONS

Details for the technical computing including tags and the Soerjadi recurrence relations are defined here for convenience. The Soerjadi formulas are defined for a closed non-intersecting polygon.

$$x_1 = \mathbf{V}_{i,1} \ x_2 = \mathbf{V}_{i+1,1} \ y_1 = \mathbf{V}_{i,2} \ y_2 = \mathbf{V}_{i+1,2} \tag{A.10}$$

$$d = x_1 y_2 - x_2 y_1 \tag{A.11}$$

Table A. 2: The first six Soerjadi recurrence relations

p,q	Tag	Recurrence Relation
0,0	Area	$m_{\eth_{0,0}} = m_{\eth_{0,0}} + d/2$
0,1	FirstMomentX	$m_{\eth_{0,1}} = m_{\eth_{0,1}} + \dfrac{d}{6}(y_1 + y_2)$
1,0	FirstMomentY	$m_{\eth_{1,0}} = m_{\eth_{1,0}} + \dfrac{d}{6}(x_1 + x_2)$
0,2	SecondMomentX	$m_{\eth_{0,2}} = m_{\eth_{0,2}} + \dfrac{d}{12}(y_1 y_1 + y_1 y_2 + y_2 y_2)$
2,0	SecondMomentY	$m_{\eth_{2,0}} = m_{\eth_{2,0}} + \dfrac{d}{12}(x_1 x_1 + x_1 x_2 + x_2 x_2)$
1,1	ProductMomentXY	$m_{\eth_{1,1}} = m_{\eth_{1,1}} + \dfrac{d}{24}(x_1(2y_1 + y_2) + x_2(y_1 + 2y_2))$

ANNEX 3.3   REFLECTION INVARIANCE

The polygon must be non-self-intersecting and closed. In principle, the Soerjadi moments of polygons are signed moments of area. This means that the sign changes, if the polygon vertices are numbered in opposite order. However, *reflection invariance* (Pavsic, 1974) is ensured in the natural parameterization algorithm by reversing signs of all moments if the area is found to be negative.

ANNEX 3.4   STANDARD INDICATOR METRICS

Table A. 3: Standard indicator metrics

Symbol	Tag, Tech symbol	Formulas
$m_{\mho,1,std}$	Area, A	$m_{\mho,1} = m_{\mho_{0,0}}$ *
$m_{\mho,2,std}$	CentroidX, C_x	$m_{\mho,2} = m_{\mho_{0,1}} m_{\mho_{0,0}}^{-1}$
$m_{\mho,3,std}$	CentroidY, C_y	$m_{\mho,3} = m_{\mho_{1,0}} m_{\mho_{0,0}}^{-1}$
$m_{\mho,4,std}$	CentroidSecondMomentX, I_{C_x}	$m_{\mho,4} = m_{\mho_{0,2}} - m_{\mho_3}^2 m_{\mho_{0,0}}^{-1}$ *
$m_{\mho,5,std}$	CentroidSecondMomentY, I_{C_y}	$m_{\mho,5} = m_{\mho_{2,0}} - m_{\mho_2}^2 m_{\mho_{0,0}}^{-1}$ *
$m_{\mho,6,std}$	PrincipalSecondMomentX, I_{xx}	$m_{\mho,6} = \dfrac{1}{2}\left(m_{\mho_4} + m_{\mho_5} + \sqrt{\left(m_{\mho_4} - m_{\mho_5}\right)^2 + \left(K_{\mho}\right)^2} \right)$
$m_{\mho,7,std}$	PrincipalSecondMomentY, I_{yy}	$m_{\mho,7} = \dfrac{1}{2}\left(m_{\mho_4} + m_{\mho_5} + \sqrt{\left(m_{\mho_5} - m_{\mho_4}\right)^2 + \left(K_{\mho}\right)^2} \right)$

The factor $K_{\mho}$ used in the formulas for the principal second moments is defined as

$$K_{\mho} = 2\left(m_{\mho_{1,1}} - m_{\mho_{0,0}} m_{\mho_2} m_{\mho_3} \right)$$

NOTE   The algorithms developed during this study include the above four metrics. Above these four moments of area metrics the perimeter is also included. In future developments some of the metrics defined in 1.3.3 are likely to be included too.

*The area and two centroid second moments (displayed in grey) are included for reasons of completeness only.

ANNEX 4   *ANALYTICAL SOLUTION OF THE REVERSED DIDO'S PROBLEM*
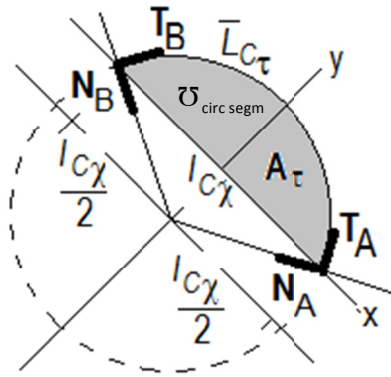
Figure A. 1: The analytical solution to the "reversed" Dido's Problem is a circular segment

Let Dido's problem see (2.2.4) be "reversed" in the sense that the "reversed" task is to find a particular curve $\overline{C}_\tau$ amongst a set of feasible curves C_τ which minimizes the arc-chord tortuosity given by $\tau = \dfrac{L_{C_\tau}}{l_{C_\chi}}$ when the area A_τ is kept fixed at an observed value A_{obs} between the curve with length L_{C_τ} and the chord C_χ with a given length l_{C_χ}. Furthermore, let the chord ends be bound at the same distance $0.5 l_{C_\chi}$ to its middle point. The problem is described in rectangular coordinates $x = x(t), y = y(t)$, where t is a parameter. The vector $\mathbf{r} = \mathbf{r}(t) = (x(t), y(t))$ is a position vector representing the points on any feasible curve C_τ.

This isoareametric problem is now defined as to minimize a tortuosity functional when the area under the curve is fixed.

Since only one constraint $n_\lambda = 1$ exist (1.12) can be presented in its simplest form:

$$L = L_\tau - \sum_{i=1}^{n_\lambda=1} \lambda_{\mho,i} L_{\mho,i} = L_\tau - \lambda_{\mho,1} L_{\mho,1} \tag{A.13}$$

In this first application of the concept of goodness of replication the tortuosity functional J_τ is chosen as the simple arc-chord tortuosity.

$$J_\tau : \; J_\tau = \frac{L_{C_\tau}}{l_{C_\chi}} = \int_{t_A}^{t_B} \frac{1}{l_{C_\chi}} \sqrt{x'^2 + y'^2}\, dt \;\rightarrow\; L_\tau = \frac{1}{l_{C_\chi}} \sqrt{x'^2 + y'^2} \tag{A.14}$$

However, other tortuosity metrics exist, see 1.3.3.7.

188

The fixed area constraint is given by

$$A_\tau = \int_{c_\tau} \frac{1}{2}\|\mathbf{r} \times d\mathbf{r}\| = \int_{t_A}^{t_B} \frac{1}{2}(xy' + yx')dt = I_{\eth,1} = A_{\text{obs}} \rightarrow L_{\eth,1} = \lambda\frac{1}{2}(xy' - yx') \ , \quad \lambda = \lambda_{\eth,1} \tag{A.15}$$

The function L for the Euler-Lagrange equation then becomes

$$L = \frac{1}{l_{c_\chi}}\sqrt{x'^2 + y'^2} - \lambda\frac{1}{2}(xy' - yx') \tag{A.16}$$

Setting $t = \xi$ the Euler-Lagrange equations gives the following two simultaneous second order differential equations:

$$L'_x - \frac{d}{dt}L'_{x'} = -\lambda\frac{1}{2}y' - \frac{d}{dt}\left[\frac{1}{l_{c_\chi}}\frac{x'}{\sqrt{x'^2 + y'^2}} + \lambda\frac{1}{2}y\right] = 0 \tag{A.17}$$

$$L'_y - \frac{d}{dt}L'_{y'} = \lambda\frac{1}{2}x' - \frac{d}{dt}\left[\frac{1}{l_{c_\chi}}\frac{y'}{\sqrt{x'^2 + y'^2}} - \lambda\frac{1}{2}x\right] = 0 \tag{A.18}$$

In this special situation, the analytic solution can be found by direct integration, i.e.

$$-\lambda\frac{1}{2}y - \frac{1}{l_{c_\chi}}\frac{x'}{\sqrt{x'^2 + y'^2}} - \lambda\frac{1}{2}y = c_1 \tag{A.19}$$

$$\lambda\frac{1}{2}x - \frac{1}{l_{c_\chi}}\frac{y'}{\sqrt{x'^2 + y'^2}} + \lambda\frac{1}{2}x = c_2 \tag{A.20}$$

After reorganization the following two expressions appear

$$-\frac{1}{l_{c_\chi}}\frac{x'}{\sqrt{x'^2 + y'^2}} = c_1 + \lambda y \quad and \quad -\frac{1}{l_{c_\chi}}\frac{y'}{\sqrt{x'^2 + y'^2}} = c_2 - \lambda x \tag{A.21}$$

Dividing by λ and squaring gives

$$\left(\frac{1}{\lambda l_{c_\chi}}\right)^2 \frac{x'^2}{x'^2 + y'^2} = \left(\frac{c_1}{\lambda} + y\right)^2 \quad and \quad \left(\frac{1}{\lambda l_{c_\chi}}\right)^2 \frac{y'^2}{x'^2 + y'^2} = \left(-\frac{c_2}{\lambda} + x\right)^2 \tag{A.22}$$

Finally, adding these two equations gives the solution

$$\left(x - \frac{c_2}{\lambda}\right)^2 + \left(y + \left(\frac{c_1}{\lambda}\right)\right)^2 = \frac{1}{\lambda^2 l_{c_\chi}^2}, \quad l_{c_\chi} > 0, \quad \lambda \neq 0 \tag{A.23}$$

Graphically, this solution represents a circular segment with radius of curvature defined as $\rho_\tau = \frac{1}{\lambda l_{c_\chi}}$.

However, these extremals must comply with the side conditions for the local x-y coordinate system, i.e.

$$x = -\frac{1}{2}l_{c_\chi} \rightarrow y = 0 \quad and \quad x = +\frac{1}{2}l_{c_\chi} \rightarrow y = 0 \tag{A.24}$$

Inserting these two side conditions and subtracting gives $c_2 = 0$. This means, that the x-coordinate of the centroid is zero, as expected. Then, by inserting the two side conditions and $c_2 = 0$ to the equation (A.23) it becomes

$$\left(\frac{1}{2}l_{c_\chi}\right)^2 + \left(\frac{c_1}{\lambda}\right)^2 = \frac{1}{\lambda^2 l_{c_\chi}^2} \tag{A.25}$$

Then, reorganizing gives

$$\frac{c_1}{\lambda} = \sqrt{\frac{1}{\lambda^2 l_{c_\chi}^2} - \frac{1}{4}l_{c_\chi}^2} \tag{A.26}$$

Graphically, this *constrained solution* represents a circular segment $\mho_{circ\ segm}$ with centroid located at:

$$(x,y) = (0, -\sqrt{\frac{1}{\lambda^2 l_{c_\chi}^2} - \frac{1}{4}l_{c_\chi}^2}) \tag{A.27}$$

The unique relation between observed area and chord length can be found from circular segments formulas.

NOTE   A circular segment is here defined as a segment where the central angle is less than or equal to π.

Operationally, a very simple Monte Carlo simulation can be applied to generate feasible polyline meshes in a situation where the analytic solution is defined by half circles. To illustrate the concept of goodness of replication in a simple way, the random mesh generator, called a "tortuous half-circle generator," is defined on the unit circle in polar coordinates with the single radial perturbation parameter $\hat{q}_{\xi_1}$. It is applied as follows:

$$\hat{\rho}_{\tau_n} = \hat{q}_{\xi_1} + \rho_{\tau_0} = \text{rand}_z p_\alpha + \rho_{\tau_0} \,, \tag{A.28}$$

where ρ_{τ_0} is the unit radius of curvature and rand_z is the standardized uniform random number generator with zero mean and a standard deviation of one. The four illustrations in Figure 2.7, of a half circle with random perturbations, are all feasible polyline meshes of the reversed Dido's problem since there area is identical to the observed. Figure 2.7 *s*hows four realizations with different perturbation levels:

$$\left(p_\alpha = 0.00, \quad p_\alpha = 0.02, \quad p_\alpha = 0.10, \quad p_\alpha = 0.20 \right).$$

Each realization is adjusted so that its area equals the area of the perfect half-circle $A_{\tau_0} = \dfrac{\pi}{2} \rho_{\tau_0}^2$ of the non-pertubative realization for $p_\alpha = 0.00$. The half circle generator also adjusts its symmetrical end tangents $(\mathbf{T}_A, \mathbf{T}_B)$ to be identical with the end tangents of the circular segment $(\mathbf{T}_{circle,A}, \mathbf{T}_{circle,B})$ in the limit, i.e. the following ordinary replication problem appears:

$$\min J_\tau : \quad A_\tau = A_{\text{obs}} \quad \lim_{p_\alpha \to 0}(\overline{\mathbf{T}}_A, \overline{\mathbf{T}}_B) = (\mathbf{T}_{circle,A}, \mathbf{T}_{circle,B}) \tag{A.29}$$

For the non-pertubative situation $p_\alpha = 0.00 \to \hat{q}_{\xi_1} = 0$ the polyline is realized from vertices $\mathbf{V}_n$, $n = 1, ..., n_\mathbf{V}$ located exactly on the unit circular segment with radius of curvature $\rho_{\tau_0} = 1.00$. For pertubative realizations in the range $p_\alpha < \,]0; 0.20]$, it generates realizations around the non-pertubative radius of curvature ρ_{τ_0} so the generated radius has a range $q_{\xi_1} \in \left[-0.2\sqrt{3}; 0.20\sqrt{3} \right] = \left[-0.346; 0.346 \right]$ symmetrically around the unit radius.

Therefore, all four realizations are feasible and their efficiency of replication is identically one. However, the polyline mesh generated with $p_\alpha = 0$ has the smallest tortuosity and due to the concept of goodness of replication it becomes the solution.

In conclusion, when the concept of goodness of replication is applied on the reversed Dido's problem, the numerical solution found by simple Monte Carlo simulation is the same as the analytical solution determined by calculus of variations.

ANNEX 6.1   CENTRAL VERTEX AND CURVATURE ESTIMATES

Let an observed polyline $p_{\tau_{obs}}$ be defined by a set of vertices

$$\left\{ \mathbf{V}_{obs_1}, \mathbf{V}_{obs_2}, ..., \mathbf{V}_{obs_i}, ..., \mathbf{V}_{obs_{C-1}}, \mathbf{V}_{obs_C}, \mathbf{V}_{obs_{C+1}}, ..., \mathbf{V}_{obs_{n_i}} \right\}, \quad n_i \in N_+$$

of which one central vertex $\mathbf{V}_{obs_C}$ is identified as the only vertex which belongs to a Gauss map with Gauss normal $\mathbf{n}_G$. This vertex $\mathbf{V}_{obs_C}$ is assumed to be the initial estimate of a master vertex. However, another vertex $\mathbf{V}_{est_C}$, which has a bigger distance to the Gauss map, might exist in the close neighborhood of its nearest neighbors $\left(\mathbf{V}_{obs_{C-1}}, \mathbf{V}_{obs_{C+1}} \right)$.
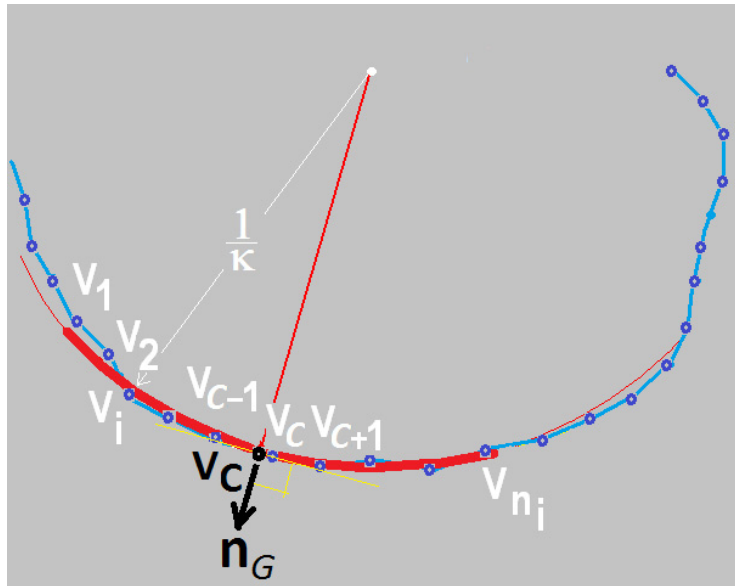
Figure A. 2: Central Vertex and Curvature Estimates from Observation Vertices

The problem of finding a new central vertex $\mathbf{V}_{est_C}$, which is assumed to be a better approximation than the observed vertex $\mathbf{V}_{obs_C}$, can be formulated as a replication problem.

$$\min J_\tau : \varepsilon_\tau (M_{phan}, M_{obs}) \leq \varepsilon_{\tau, upp} \rightarrow 0 \ , \ \left\{ q^0_{M_{phan}} \right\} = \left\{ q^0_{M_{obs}} \right\} \tag{A.30}$$

where the phantom mesh M_{phan} is a bi-mesh generated by Frenet subdivision. If the segment area is used as segment indicator metrics, then the problem represents a reversed Dido's problem. Beyond finding a central vertex estimate $\mathbf{V}_{est_C}$, the central curvature estimate κ_{est_C} is an automatic spin-off from this solution.

The following bounds are used in the natural parameterization algorithm

$$\left(\mathbf{V}_{est_C} - \mathbf{V}_{obs_C}\right) \bullet \mathbf{n}_G \geq 0 \wedge \left\| \mathbf{V}_{est_C} - \frac{\mathbf{V}_{obs_{C+1}} + \mathbf{V}_{obs_{C+1}}}{2} \right\|^2 < \frac{\left\| \mathbf{V}_{obs_{C+1}} + \mathbf{V}_{obs_{C+1}} \right\|^2}{2} \tag{A.31}$$

$$\frac{\left(\mathbf{V}_{est_C} - \mathbf{V}_{obs_C}\right) \bullet \left(\mathbf{V}_{est_C} - \mathbf{V}_{obs_{C-1}}\right)}{\left\| \left(\mathbf{V}_{est_C} - \mathbf{V}_{C_{obs}}\right) \bullet \left(\mathbf{V}_{est_C} - \mathbf{V}_{obs_{C-1}}\right) \right\|} < 1 \wedge \frac{\left(\mathbf{V}_{est_C} - \mathbf{V}_{obs_C}\right) \bullet \left(\mathbf{V}_{est_C} - \mathbf{V}_{obs_{C+1}}\right)}{\left\| \left(\mathbf{V}_{est_C} - \mathbf{V}_{obs_C}\right) \bullet \left(\mathbf{V}_{est_C} - \mathbf{V}_{obs_{C+1}}\right) \right\|} < 1 \tag{A.32}$$

ANNEX 6.2   SEGMENT CURVATURE ESTIMATES

Let a segment curvature be bound to a tortuosity pole $P^0_{\tau,A2}$, of a bi-pole $\left\{P^0_{\tau,A2}, P^0_{\tau,B2}\right\}$, with chord direction vector $\mathbf{e}_{\chi_2}$, and chord length l_{χ_2}. Then, an estimate of this segment curvature $\tilde{\kappa}_{\chi_{A2}}$ is defined from an osculating circle, which passes through $\left(\mathbf{V}_{A2}, \mathbf{V}_{B2}\right)$, and follows the pole tangent $\mathbf{T}_{A_2}$ as:

$$\tilde{\kappa}_{\chi_{A2}} = \frac{2\sqrt{1 - c^2_{\theta_{A2}}}}{l_{\chi_2}} , \tag{A.33}$$

where the direction cosine $c_{\theta_{A2}}$ is determined as $c_{\theta_{A2}} = \mathbf{T}_{A_2} \bullet \mathbf{e}_{\chi_2}$.

ANNEX 6.3   CENTRAL CURVATURE ESTIMATE
The central curvature for a bi-mesh is defined as the average of the estimated segment curvatures:

$$\tilde{\kappa}_{\tau_c} = \frac{\tilde{\kappa}_{\chi_{A2}} + \tilde{\kappa}_{\chi_{B2}}}{2} \tag{A.34}$$

ANNEX 7.1   GENERAL FRENET EXTRAPOLATION
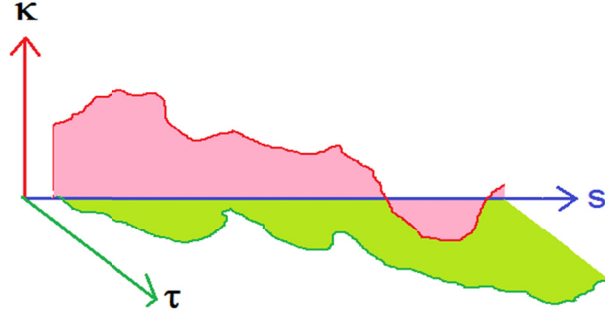
Figure A. 3: Arbitrary natural equations

From the *mean value theorem,* an extrapolation based on the Frenet formulas (1.4) can be defined as:

$$\{F(s_0 + \Delta s)\} = \begin{bmatrix} \mathbf{T}(s_0 + \Delta s) \\ \mathbf{N}(s_0 + \Delta s) \\ \mathbf{B}(s_0 + \Delta s) \end{bmatrix} \approx \{F(s_0)\} + \Delta\{F\}, \tag{A.35}$$

where the evaluation of derivatives is taken place at a suitable location $s = s_s$ between s_0 and $s_0 + \Delta s$.

Assuming the natural equations $\kappa(s)$, $\tau(s)$ and chord length increments Δs to be given, then an incremental relation for each step in a sequence of $n_{\Delta s}$ steps is given by

$$\{F\}_i = \{F\}_{i-1} + \Delta\{F\}_{i-1}, i = 1, ..., n_{\Delta s} \tag{A.36}$$

where the increment $\Delta\{F\} = \Delta s\{F'(s_s)\}$, $\Delta s \to 0$ in full writing is defined as

$$\Delta\{F(s_s)\} = \begin{bmatrix} \Delta\mathbf{T} \\ \Delta\mathbf{N} \\ \Delta\mathbf{B} \end{bmatrix} = \Delta s\{F'(s_s)\} = \Delta s \begin{bmatrix} 0 & \kappa(s_s) & 0 \\ -\kappa(s_s) & 0 & \tau(s_s) \\ 0 & -\tau(s_s) & 0 \end{bmatrix} \{F(s_s)\}. \tag{A.37}$$

Since the location increment is defined as

$$\Delta\mathbf{V} = \Delta s \left(\mathbf{T} + \Delta\mathbf{T} \right) \qquad \text{(A.38)}$$

the new location and orientations are

$$\mathbf{V}_i \approx \mathbf{V}_{i-1} + \Delta\mathbf{V}_{i-1} \ , \quad \Delta\mathbf{V}_0 = 0 \qquad \text{(A.39)}$$

$$\mathbf{T}_i \approx \{F\}_i^{\mathbf{T}} , \mathbf{B}_i \approx \{F\}_i^{\mathbf{B}} , \mathbf{N}_i \approx \{F\}_i^{\mathbf{N}} \qquad \text{(A.40)}$$

Finally, at a goal point A_1 for $s = s_{A_1} = \sum\limits_{i=1}^{n_{\Delta s}} \Delta s_i$, the location and orientation vectors are

$$\mathbf{V}_{A_1} \approx \mathbf{V}_A + \sum_{i=1}^{n_{\Delta s}} \Delta\mathbf{V}_i \qquad \text{(A.41)}$$

$$\{F\}_{A_1} = \begin{bmatrix} \mathbf{T}_{A_1} \\ \mathbf{N}_{A_1} \\ \mathbf{B}_{A_1} \end{bmatrix} \approx \begin{bmatrix} \mathbf{T}_{n_{\Delta s}} \\ \mathbf{N}_{n_{\Delta s}} \\ \mathbf{B}_{n_{\Delta s}} \end{bmatrix} \qquad \text{(A.42)}$$

$$\partial^3\Omega = \left[\mathbf{V}_{A1}, \mathbf{T}_{A1}, \mathbf{N}_{A1}, \mathbf{B}_{A1} \right]^T \qquad \text{(A.43)}$$

Conclusively, the location and orientation vectors for an extrapolated tortuosity pole are defined by

$$\mathrm{P}_{\tau,A1} \ni \left\{ \partial^3\Omega \right\} \qquad \text{(A.44)}$$

The formulas (A.35) - (A.42), represent a general incremental formulation for a sequence of valence one tortuosity poles, extrapolated from a master pole, at an initial location A, i.e. it is a general purpose approximation for incremental generation of space curves from their natural equations.

In the following annex, a general constant average form of this extrapolation approach is presented.
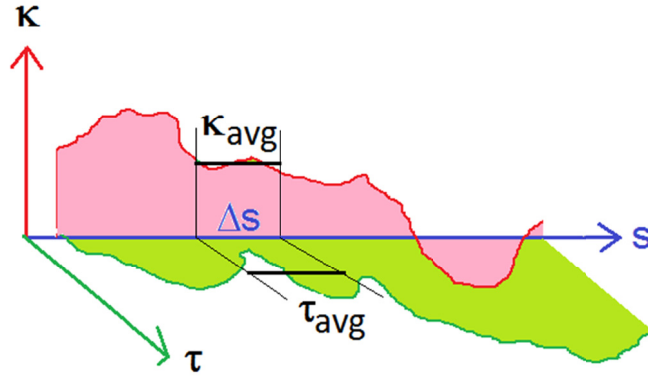
Figure A. 4: Constant averaging of natural equations

If the natural equations are assumed to be averaged, piecewise, constant functions; then the formulas (A.35)-(A.44) can be expressed in a constant average form as follows.

Let it be assumed that the natural equations are approximated as piecewise constant functions.

$$\chi_1\left(s_s\right)=\kappa\left(s_s\right)\approx\kappa_{avg}=Const \tag{A.45}$$

$$\chi_2\left(s_s\right)=\tau\left(s_s\right)\approx\tau_{avg}=Const \tag{A.46}$$

Then, the formulas (A.35) to (A.44) still hold in the mean if the constant values for the partitioned natural equations fulfill the following averaging conditions:

$$\kappa_{avg,i}=\frac{1}{\Delta s_i}\int_{s_i}^{s_i+\Delta s_i}\kappa(s)\,ds,\quad\forall i \tag{A.47}$$

$$\tau_{avg,i}=\frac{1}{\Delta s_i}\int_{s_i}^{s_i+\Delta s_i}\tau(s)\,ds,\quad\forall i \tag{A.48}$$

However, to obtain a limited number of degrees of freedom, this constant average form can be parameterized as demonstrated in the following annexes. The term incremental Frenet extrapolation, or simply Frenet extrapolation, will be used frequently as synonyms for constant average form of general Frenet extrapolation.
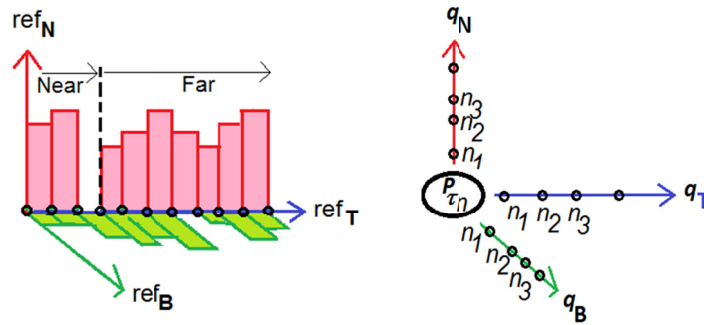
Figure A. 5: Parametric Frenet extrapolation by reference

Definitions: The constant average form of general Frenet extrapolation (A.45)-(A.48) can be parameterized with a three-DOF parameter set $q = \left\{ q_{\mathbf{T}_{i,j}}, q_{\mathbf{N}_{i,j}}, q_{\mathbf{B}_{i,j}} \right\}, \forall i, \ j = 1, \ldots n_{\{F\},i}$ which relates by reference (see Figure A5), or directly (see Figure A6), to the jth Frenet frame of the ith tortuosity pole. In general, each parameter $q_{i,j}$ represents one degree of freedom and belongs to an ordered DOF-set, i.e. $q_n = \left\{ q_{n,1}, q_{n,2}, q_{n,3}, \ldots \right\}, n = 0, 1, \ldots$

Each of these can be further defined for specific levels of refinement $k_\tau \in [1, \ldots, n_\tau]$. In situations where the extrapolation limit is a parametric tortuosity pole itself, its parameterization is called a goal set. In general, Frenet parameterization forms a set of non-linear equations and is based on triple-DOF parameter sets (TDOF). However, reduced parameter setups, such as double-DOF sets (DDOF) or single-DOF sets (SDOF), are also used. Frenet extrapolation is called "far-field" if more than three increments are in use, and "near-field" if no more than three increments are in use.

In the following discussion, the essence of the above definitions is referred to as parametric Frenet extrapolation.

NOTE   For an introduction to the algorithmic implementation of Frenet curves, investigate the files for an alternative SDOF Frenet approximation under *Curvature-Torsion Defined Curve* by Panarese, P. provided at MATLAB Central® at www.mathworks.com.

Direct parameterization vs. parameterization by reference

The simplest Frenet parameterization is to let the parameters be expressed directly as the values for the natural equations themselves. An example of a direct parameterization for far-field extrapolation is first presented in ANNEX 9.1.1. Extrapolations based on parameterization by reference are presented in ANNEX 9.4. Later, parameterization relative to a geometric length quantity is described. Here, the parameterization is controlled by some upper bounds, which are defined by the modeler or by restrictions related to the parameterization itself.

ANNEX 8   DIRECT PARAMETRIZATION of FRENET EXTRAPOLATION

ANNEX 8.1   DIRECT FRENET PARAMETERIZATION by EXAMPLE

Direct parameterization of Frenet Extrapolation is introduced here using a simple example.

EXAMPLE   Direct Frenet parameterization
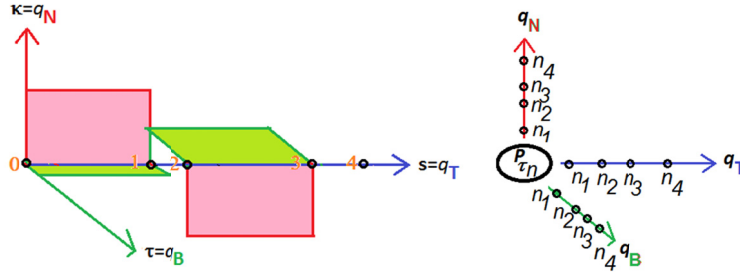
Figure A. 6: Constant averaged natural equations defined over four increments with direct parameterization

Figure A. 6 illustrates direct parameterization of a Frenet far-field extrapolation. It is based on four increments with given natural equations in the neighborhood of a given master pole. In the first increment $n=1$ and the third increment $n=3$, the natural equations are non-zero-valued. For the second $n=2$ and the fourth $n=4$, they are zero-valued. See Table A. 4 for further details. The extrapolated tortuosity poles $n=1,...4$ are found from (A.41) and (A.42). A plot of the TNB field is illustrated in Figure A. 7.

The direct parameterization approach is defined as

$$q = \left\{ q_{\mathbf{T},n}, q_{\mathbf{N},n}, q_{\mathbf{B},n} \right\}, \quad n=1,...4$$

(A.49)

where

$$q_{\mathbf{T},n} = \Delta s_n = s_n - s_{n-1}$$

(A.50)

$$q_{\mathbf{N},n} = \kappa_{\tau,n}$$

(A.51)

$$q_{\mathbf{B},n} = \tau_{\tau,n}$$

(A.52)

Data: The master tortuosity pole is located at a master vertex $\mathbf{V}^{\mathrm{T}} = \begin{bmatrix} V_{x_0} & V_{y_0} & V_{z_0} \end{bmatrix} = \begin{bmatrix} 3.846 & 0.000 & 0.000 \end{bmatrix}$ in a rectangular coordinate system. Its master tangent is $\mathbf{T}^{\mathrm{T}} = \begin{bmatrix} T_{x_0}, T_{y_0}, T_{z_0} \end{bmatrix} = \begin{bmatrix} 0 & 0.9806 & 0.1961 \end{bmatrix}$, and its master normal is $\mathbf{N}^{\mathrm{T}} = \begin{bmatrix} N_{x_0} & N_{y_0} & N_{z_0} \end{bmatrix} = \begin{bmatrix} -1.000 & 0.000 & 0.000 \end{bmatrix}$. The master binormal is found from the cross product between the master tangent and the master normal.

Table A. 4: Natural equations partitioned into four increments (far-field)

Controls / n	Master = 0	1	2	3	Goal = 4
s	0.00	5.07	6.28	11.36	12.81
κ	0.25	0.25	0.00	−0.25	0.00
τ	0.05	0.05	0.00	−0.20	0.00
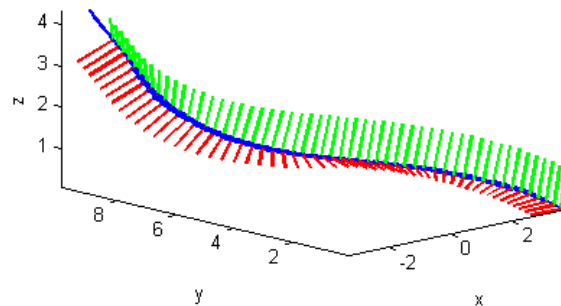
Figure A. 7: TNB field of a tortuous curve from direct parameterization (T=blue, N=red, B=green)

Note that negative curvatures are applied in the third step. This means that in this step, the corresponding trihedra are not exact Frenet frames. However, they are exact up to sign. Furthermore, note that in step two and step four, curvatures are zeroed. This means that the Frenet formulas make no sense here, and that the **TNB** trihedrons are simply translated incrementally. Consequently, the incremental formulations defined in ANNEX 7.1 allow the **TNB** trihedra to be controlled with a high degree of customization, and to form arbitrary tortuous curves by allowing positive and negative curvatures and torsions. However, the drawback is that the signs of the Frenet frames generated are not in control. Therefore, signs must be managed by an aposteori correction routine or by subdividing the path into subparts, which are all convexive.

In the following annex, the alternative to direct parameterization, namely parameterization by reference, is demonstrated by three consequtive SDOF pole extrapolations.

ANNEX 9   *PARAMETRIC EXTRAPOLATION by REFERENCE*

In this annex, Frenet parameterization by reference is introduced. Solely length references are in focus.

ANNEX 9.1 F_B EXTRAPOLATION
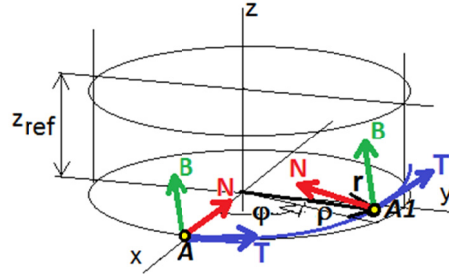
Figure A. 8: Constant curvature and constant torsion defines a helix

In the following section, a SDOF Frenet parameterization by reference, which models a tortuous curve with *constant torsion and constant curvature* from a length reference, is defined.

A curve that possesses constant curvature and torsion is known as a helix. In Cartesian coordinates, the position vector $\mathbf{r}$, its first derivative $\mathbf{r}'$, and its second derivative $\mathbf{r}''$, can be expressed in terms of right handed cylindrical coordinates $(\rho, \varphi, z) = (\rho, \varphi, b\varphi)$ as

$$\mathbf{r}(\varphi) = \left(\rho \cos(\varphi), \rho \sin(\varphi), b\varphi \right) \tag{A.53}$$

$$\mathbf{r}'(\varphi) = \left(-\rho \sin(\varphi), \rho \cos(\varphi), b \right) \tag{A.54}$$

$$\mathbf{r}''(\varphi) = \left(-\rho \cos(\varphi), -\rho \sin(\varphi), 0 \right) \tag{A.55}$$

$$\rightarrow \quad \mathbf{T}(\varphi) = \frac{\mathbf{r}'(\varphi)}{\left\| \mathbf{r}'(\varphi) \right\|} \tag{A.56}$$

$$\rightarrow \quad \mathbf{N}(\varphi) = \frac{\mathbf{r}''(\varphi) - \left(\mathbf{r}''(\varphi) \cdot \mathbf{T}(\varphi) \right) \mathbf{T}(\varphi)}{\left\| \mathbf{r}''(\varphi) - \left(\mathbf{r}''(\varphi) \cdot \mathbf{T}(\varphi) \right) \mathbf{T}(\varphi) \right\|} \tag{A.57}$$

$$\rightarrow \quad \mathbf{B}(\varphi) = \mathbf{T}(\varphi) \times \mathbf{N}(\varphi) \quad , \tag{A.58}$$

where $\varphi = \varphi(t)$ is a rotational angle function defined from a parameter t, ρ is the radius of the circumscribed cylinder, and b is a pitch factor defined from the reference pitch z_{ref} for one turn as

$$z_{\text{ref}} = 2\pi b \ . \tag{A.59}$$

In the special situation where there is no pitch i.e. $z_{ref} = 0$ the torsion is also zero.

The triple **TNB** expresses Frenet vectors. Furthermore, the arc length function, the constant curvature κ, and the constant torsion τ are given by:

$$l_\tau(\varphi) = \varphi\sqrt{\rho^2 + b^2} \ , \quad \kappa = \frac{\rho}{\rho^2 + b^2} \ , \quad \tau = \frac{b}{\rho^2 + b^2} \tag{A.60}$$

From (A.60), the two helix constants b, ρ of the circumscribed cylinder can be expressed as

$$b = \frac{\tau}{\left(\kappa^2 + \tau^2\right)}, \quad \rho = \frac{\kappa}{\tau} b \ , \quad \tau \neq 0 \tag{A.61}$$

In the situation where the torsion is zero, the radius is defined by the curvature.

$$\tau = 0 \ \rightarrow \ \rho = \frac{1}{\kappa} \ , \quad \kappa > 0 \tag{A.62}$$

However, when the curvature is zero, and the torsion is not zero, then the helix constant is still definable as

$$\kappa = 0 \ \rightarrow \ b = \frac{1}{\tau} \ , \quad \tau \neq 0 \tag{A.63}$$

In the situation where curvature and torsion are not zero, the frame coordinates for a tortuosity pole is given as

$$\mathbf{V}_A = \mathbf{r}(\varphi = 0) = [\rho, 0, 0]^{\mathrm{T}} \tag{A.64}$$

$$\mathbf{T}_A = \mathbf{T}(\varphi = 0) = \frac{1}{\sqrt{\rho^2 + b^2}}[0, \rho, b]^{\mathrm{T}} \tag{A.65}$$

$$\mathbf{N}_A = \mathbf{N}(\varphi = 0) = \frac{1}{\sqrt{\rho^2}}[-\rho, 0, 0]^{\mathrm{T}} = [-1, 0, 0]^{\mathrm{T}} \tag{A.66}$$

$$\mathbf{B}_A = \mathbf{T}_A \times \mathbf{N}_A \tag{A.67}$$

$$\mathbf{X}_A = \begin{bmatrix} \kappa_\chi & \kappa_\tau = const & \tau_\tau = const \end{bmatrix}^{\mathrm{T}} \tag{A.68}$$

NOTE   The segment curvature κ_χ, in (A.68), is kept for later use. The conventional curvature and torsion are indexed with tau to avoid confusion with the segment curvature, indexed with chi.

Reversely, the basis vectors of the local Cartesian coordinates can be expressed as

$$\mathbf{e}_x = -\mathbf{N}_A \tag{A.69}$$

$$\mathbf{e}_y = \frac{\mathbf{T}_A - \dfrac{b}{\rho}\mathbf{B}_A}{\left\| \mathbf{T}_A - \dfrac{b}{\rho}\mathbf{B}_A \right\|} \ , \tag{A.70}$$

$$\mathbf{e}_z = \mathbf{e}_x \times \mathbf{e}_y \tag{A.71}$$

In the special situation where the torsion is zero or the curvature is zero, the second base vector is simply identical with the tangent.

Parameterization
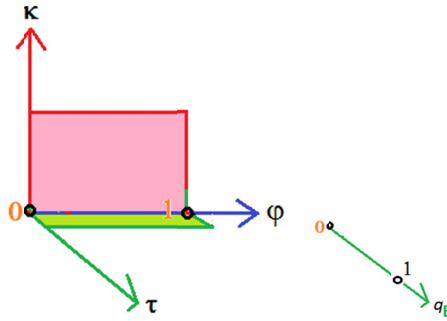
Figure A. 9: Parameterization by length reference $q_{\mathbf{B}} = \dfrac{l_{q_{\mathbf{B}}}}{l_{\mathbf{B},\text{ref}}}$

A parameterization of a Frenet near-field extrapolation is now defined as:

$$q = \{q_{\mathbf{B},n}\}, \quad n = 1 \tag{A.72}$$

where

$$q_{\mathbf{B}} = \frac{l_{q_{\mathbf{B}}}}{l_{\mathbf{B},\text{ref}}} = \frac{l_y}{l_{\mathbf{B},\text{ref}}\,\mathbf{T}_A \bullet \mathbf{e}_y} \ \rightarrow \ l_y = q_{\mathbf{B}} l_{\mathbf{B},\text{ref}}\,\frac{\rho}{\sqrt{\rho^2 + b^2}} \tag{A.73}$$

A regular extrapolation does not exceed a quarter of the circle:

$$q_{\mathbf{B}_{\text{upper}}} \equiv 1: \ l_y \le \rho \ \rightarrow \ l_{\mathbf{B},\text{ref}} \le \sqrt{\rho^2 + b^2}\ , \tag{A.74}$$
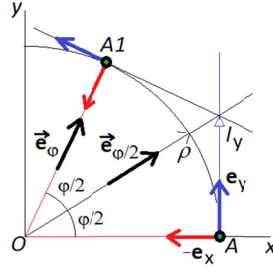
Figure A. 10: Helix (x, y)-plane

Figure A. 10 shows the helix (x, y)-plane through the tortuosity pole $P_{\tau,A}$. The distance l_y is used to define the parameterization by the length reference $l_{B,ref}$.

Note that ρ is the radius of the circle and NOT the radius of curvature ρ_τ related to the helix curvature κ_τ.

The half angle from origin to the intersection point, at a distance l_y from A, is defined from $\mathbf{e}_{\varphi/2}$ as

$$\tan(\varphi/2) = \frac{l_y}{\rho} = \frac{q_B l_{B,ref}}{\sqrt{\rho^2+b^2}} = \frac{l_{q_B}}{\sqrt{\rho^2+b^2}} \rightarrow \varphi = 2\ \text{atan}\left(\frac{l_{q_B}}{\sqrt{\rho^2+b^2}}\right) \tag{A.75}$$

It is clearly seen that the angle is defined uniquely from the length parameter l_{q_B}.

Hereafter, the direction cosine and the direction sine for unit vector $\mathbf{e}_\varphi$ in the (x, y)-plane are defined as

$$\mathbf{e}_\varphi = \begin{bmatrix} c_\varphi \\ s_\varphi \\ 0 \end{bmatrix} = \begin{bmatrix} \cos(\varphi) \\ \sqrt{1-c_\varphi^2} \\ 0 \end{bmatrix} \tag{A.76}$$

Finally, the vectors of the extrapolated tortuosity pole at $A1$ are determined as

$$\mathbf{V}_{A1} = \mathbf{V}_A - \rho(1-c_\varphi)\mathbf{e}_x + \rho s_\varphi \mathbf{e}_y + b\varphi \mathbf{e}_z \tag{A.77}$$

$$\mathbf{T}_{A1} = \frac{\rho\left(-s_\varphi \mathbf{e}_x + c_\varphi \mathbf{e}_y\right) + b\mathbf{e}_z}{\left\|\rho\left(-s_\varphi \mathbf{e}_x + c_\varphi \mathbf{e}_y\right) + b\mathbf{e}_z\right\|} \tag{A.78}$$

$$\mathbf{N}_{A1} = -c_\varphi \mathbf{e}_x - s_\varphi \mathbf{e}_y + 0\mathbf{e}_z \tag{A.79}$$

$$\mathbf{B}_{A1} = \mathbf{T}_{A1} \times \mathbf{N}_{A1} \tag{A.80}$$

$$\boldsymbol{\chi}_{A1} = \begin{bmatrix} \kappa_\chi & \kappa_\tau & 0 \end{bmatrix}^\mathsf{T} \tag{A.81}$$

$$P_{\tau_{A1}} = \begin{bmatrix} \mathbf{V}_{A1}, \mathbf{T}_{A1}, \mathbf{N}_{A1}, \mathbf{B}_{A1}, \boldsymbol{\chi}_{A1} \end{bmatrix}^\mathsf{T} \tag{A.82}$$

Since the mapping $\hat{f}_{F_B} : P_{\tau_A} \to P_{\tau_{A1}}$ represents an approximation, it is symbolized as a prediction function $\hat{f}_{F_B}$ in I_{q_B} called F_B extrapolation.

$$P_{\tau_{A1}} = \hat{f}_{F_B}\left(P_{\tau_A}, I_{q_B}\right) \tag{A.83}$$

When torsion is zero or curvature is zero, then the new pole $P_{\tau_{A1}}$ is defined in accordance with the general formulas (A.35) - (A.42) with an increment of I_{q_B}.

Let a tangent length reference $l_{B,ref}$ with respect to **B**, be defined by the upper bound restriction (A.74). Let the SDOF parameterization be defined by the values given in the following table.

Table A. 5: F_B extrapolation

Tortuosity Pole	$q_B = 0.000$ $P_{\tau_A} = \hat{f}_{F_B}\left(P_{\tau_A}, q_B\right)$	$q_B = 1.000$ $P_{\tau_{A1}} = \hat{f}_{F_B}\left(P_{\tau_A}, q_B\right)$
$\mathbf{V}^T$	$\begin{bmatrix} 3.846 & 0.000 & 0.000 \end{bmatrix}$	$\begin{bmatrix} 0.000 & 3.846 & 1.208 \end{bmatrix}$
$\mathbf{T}^T$	$\begin{bmatrix} 0 & 0.9806 & 0.1961 \end{bmatrix}$	$\begin{bmatrix} 0.9806 & 0.000 & 0.1961 \end{bmatrix}$
$\mathbf{N}^T$	$\begin{bmatrix} -1.000 & 0.000 & 0.000 \end{bmatrix}$	$\begin{bmatrix} 0.000 & -1.000 & 0.000 \end{bmatrix}$
$\mathbf{B}^T$	$\begin{bmatrix} 0.0000 & -0.1961 & 0.9806 \end{bmatrix}$	$\begin{bmatrix} 0.1961 & 0.0000 & 0.9806 \end{bmatrix}$
$\mathbf{X}^T$	$\begin{bmatrix} \kappa_\chi & 0.2500 & 0.0500 \end{bmatrix}$	$\begin{bmatrix} \kappa_\chi & 0.2500 & 0.0000 \end{bmatrix}$

Figure A. 11: F_B extrapolation

A run for $q_B \in [0.000:0.0100:1.000]$ is illustrated in the Figure above. A single data set for the extrapolated tortuosity pole at A_1 for $q_B = 1.000$ is also provided in the last column of the table.

In this annex, a simpler SDOF parameterization by length reference, which models a tortuous curve with *constant curvature and no torsion,* is in focus. Therefore, this parameterization, called F_N parameterization, is just a simplification of F_B extrapolation.

Since there is no torsion, the tortuous curve now forms a circular segment.
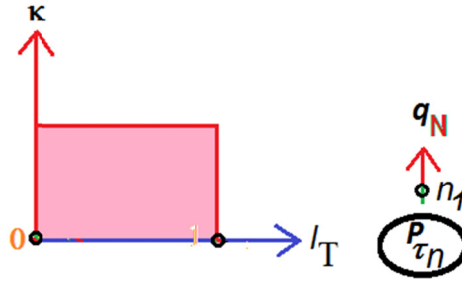
Figure A. 12: Frenet Parameterization $q_N = \dfrac{l_{q_N}}{l_{N_{ref}}}$

A parameterization of such an extrapolation by a length reference $l_{N_{ref}}$ can be defined as:

$$q = \{q_{N,n}\} \ , \quad n = 1 \tag{A.84}$$

where

$$q_N = \frac{l_{q_N}}{l_{N_{ref}}} = \frac{l_y}{l_{N_{ref}}} \to l_{q_N} = l_{N_{ref}} q_N \tag{A.85}$$

A regular extrapolation should not exceed a quarter of the circle:

$$l_{T_1} \le \rho_1 \ \to \ l_{N,ref} \le \rho_1 \tag{A.86}$$

Since $\tau = 0$, the formluas are simplified into:

$$\mathbf{e}_x = -\mathbf{N}_A \tag{A.87}$$

$$\mathbf{e}_y = \mathbf{T}_A \tag{A.88}$$

$$\mathbf{e}_z = \mathbf{e}_x \times \mathbf{e}_y \tag{A.89}$$

$$\tan(\varphi/2) = \frac{l_y}{\rho} = \frac{q_N l_{N,ref}}{\rho} = \kappa_\tau l_{q_N} \to \varphi = 2 \operatorname{atan}\left(\kappa_\tau l_{q_N}\right) \tag{A.90}$$

Hereafter, the direction cosine and the direction sine for the unit vector $\mathbf{e}_\varphi$ in the xy-plane are defined as

$$\mathbf{e}_\varphi = \begin{bmatrix} c_\varphi \\ s_\varphi \\ 0 \end{bmatrix} = \begin{bmatrix} \cos(\varphi) \\ \sqrt{1-c_\varphi^2} \\ 0 \end{bmatrix} \tag{A.91}$$

Finally, the vectors of the extrapolated tortuosity pole at $A2$ are determined as

$$\mathbf{V}_{A2} = \mathbf{V}_{A1} - \rho(1-c_\varphi)\mathbf{e}_x + \rho s_\varphi \mathbf{e}_y + 0\mathbf{e}_z \tag{A.92}$$

$$\mathbf{T}_{A2} = -s_\varphi \mathbf{e}_x + c_\varphi \mathbf{e}_y + 0\mathbf{e}_z \tag{A.93}$$

$$\mathbf{N}_{A2} = -c_\varphi \mathbf{e}_x - s_\varphi \mathbf{e}_y + 0\mathbf{e}_z \tag{A.94}$$

$$\mathbf{B}_{A2} = \mathbf{T}_{A2} \times \mathbf{N}_{A2} \tag{A.95}$$

$$\boldsymbol{\chi}_{A2} = \begin{bmatrix} \kappa_\chi & 0 & 0 \end{bmatrix}^\mathsf{T} \tag{A.96}$$

$$P_{\tau_{A2}} = \begin{bmatrix} \mathbf{V}_{A2}, \mathbf{T}_{A2}, \mathbf{N}_{A2}, \mathbf{B}_{A2}, \boldsymbol{\chi}_{A2} \end{bmatrix}^\mathsf{T} \tag{A.97}$$

The mapping $\hat{f}_{F_N} : P_{\tau_{A1}} \to P_{\tau_{A2}}$ is symbolized by an SDOF prediction function $\hat{f}_{F_N}$ in l_{q_N}, called F_N extrapolation.

$$P_{\tau_{A2}} = \hat{f}_{F_N}\left(P_{\tau_{A1}}, l_{q_N}\right) \tag{A.98}$$

In the special situation where the curvature is zero, the pole $P_{\tau_{A2}}$ is simple formed as a translation of $P_{\tau_{A1}}$ over a distance l_{q_N} along the tangent.

ANNEX 9.2.1 *EXAMPLE – F_N* **Extrapolation**

Let a tangent length reference $l_{N,ref}$ with respect to **N** be defined by ANNEX 9.2, and let the one set parameterization be defined by the values given in the following table.

Table A. 6: F_N extrapolation

Tortuosity Pole	$q_N = 0.000$ $P_{\tau_{A2}} = \hat{f}_{F_N}\left(P_{\tau_{A1}}, l_{q_N}\right)$	$q_N = 1.000$ $P_{\tau_{A2}} = \hat{f}_{F_N}\left(P_{\tau_{A1}}, l_{q_N}\right)$
$\mathbf{V}^T$	$\begin{bmatrix} 4.000 & 0.000 & 0.000 \end{bmatrix}$	$\begin{bmatrix} 0.000 & 4.000 & 0.000 \end{bmatrix}$
$\mathbf{T}^T$	$\begin{bmatrix} 0 & 1.000 & 0.000 \end{bmatrix}$	$\begin{bmatrix} 1.000 & 0.000 & 0.000 \end{bmatrix}$
$\mathbf{N}^T$	$\begin{bmatrix} -1.000 & 0.000 & 0.000 \end{bmatrix}$	$\begin{bmatrix} 0.000 & -1.000 & 0.000 \end{bmatrix}$
$\mathbf{B}^T$	$\begin{bmatrix} 0.000 & 0.000 & 1.000 \end{bmatrix}$	$\begin{bmatrix} 0.000 & 0.000 & 1.000 \end{bmatrix}$
$\mathbf{X}^T$	$\begin{bmatrix} \kappa_\chi & 0.2500 & 0.0000 \end{bmatrix}$	$\begin{bmatrix} \kappa_\chi & 0.0000 & 0.0000 \end{bmatrix}$

Figure A. 13: F_N extrapolation

Figure A1.13 illustrates a run for $q_N \in [0.000:0.0100:1.000]$ from the data given in the table.
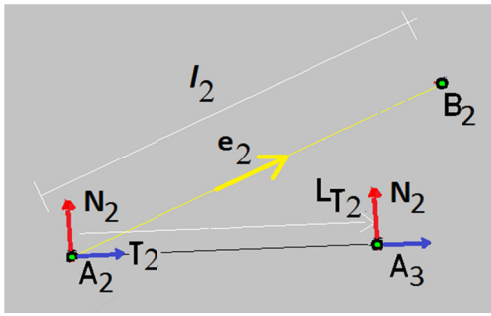
Finally, a third SDOF Frenet parameterization by reference is in focus. It models a tortuous curve with no curvature and no torsion.

Geometrically, it defines a *pure translation*.

Figure A. 14: Translation of a tortuosity pole along a tangent line of a section

The chord vector is defined as

$$\mathbf{e}_{\chi_2} = \frac{\left(\mathbf{V}_{B2} - \mathbf{V}_{A2}\right)}{\left\|\left(\mathbf{V}_{B2} - \mathbf{V2}\right)\right\|}$$

(A.99)
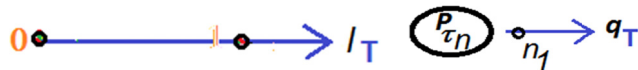
Figure A. 15: Frenet Parameterization by tangent length proportion $q_T = \dfrac{l_{q_T}}{l_{T_{ref}}}$

A simple parameterization of a Frenet translation by reference tangent length $l_{T_{ref}}$, can be defined as:

$$q = \left\{q_{T,n}\right\}, \quad n=1$$

(A.100)

where

$$q_T = \frac{l_{q_T}}{l_{T_{ref}}} \rightarrow l_{q_T} = l_{T_{ref}} q_T$$

(A.101)

From simple geometric considerations, see

Figure A. 14, the refernce length $l_{T_{ref}}$ is defined from the segment curvature $\kappa_{\chi_{A2}}$ as

$$l_{T_{ref}} = \frac{1}{\kappa_{\chi_{A2}}} \left(\frac{1 - c_{\theta_{A2}}}{\sqrt{1 - c_{\theta_{A2}}^2}} \right) l \chi_2 \quad , \quad \kappa_{\chi_{A2}} \neq 0, \ c_{\theta_{A2}}^2 < 1$$

(A.102)

From simple geometric considerations (see Figure A.14), the estimated curvature and the ratio between the reference tangent length and the chord length, can be defined as

$$\tilde{\kappa}_{\chi_{A2}} = \frac{2\sqrt{1-c_{\theta_{A2}}^2}}{l\chi_2} \quad\rightarrow\quad \frac{l_{T_{ref}}}{l\chi_2} = \frac{1}{2}\left(\frac{1-c_{\theta_{A2}}}{1-c_{\theta_{A2}}^2}\right) , \quad l\chi_2 \neq 0, \ c_{\theta_{A2}}^2 < 1.$$
(A.103)

If $c_{\theta_{A2}}^2 = 1$ the tangent reference length is set to $l_{T_{ref}} = \frac{1}{4}l_{\chi_2}$.

$$l_{T_{rel}}/l_{\chi_{A2}} = (1-c_{\theta_{A2}})/(2(1-c_{\theta_{A2}}^2)) \text{ versus } \theta_{A2}$$
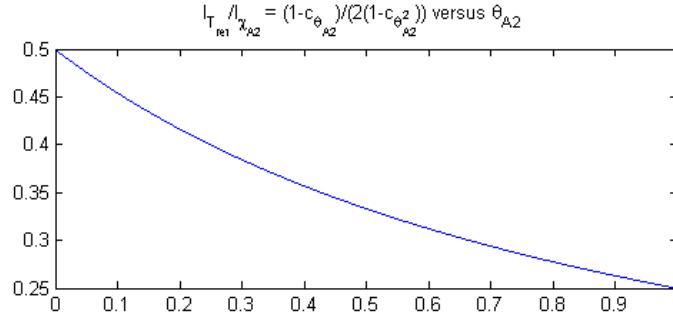
Figure A. 16: Tangent reference length vs. direction cosine

If the segment curvature is not given, it is estimated (see (A.103)) from an osculating circle with its tangent following the current pole and passing through both pole vertices. Note that the ratio between the reference length and the chord length goes towards one quart when the direction cosine goes towards one. Therefore, a regular extrapolation is governed by the simple bounds:

$$\frac{1}{4}l_{\chi_2} \leq l_{T_{ref}} \leq \frac{1}{2}l_{\chi_2} .$$
(A.104)

It follows from

Figure A. 14, that the vertex of the extrapolated tortuosity pole at $A3$ can be found from a simple tangential translation with reference at $A2$.

$$\mathbf{V}_{A3} = \mathbf{V}_{A2} + l_{q_T}\mathbf{T}_{A2}$$
(A.105)

$$\mathbf{T}_{A3} = \mathbf{T}_{A2}$$
(A.106)

$$\mathbf{N}_{A3} = \mathbf{N}_{A2}$$
(A.107)

$$\mathbf{B}_{A3} = \mathbf{B}_{A2}$$
(A.108)

$$\mathbf{\chi}_{A3} = \begin{bmatrix} 0 & 0 & 0 \end{bmatrix}^T$$
(A.109)

$$\mathbf{P}_{\tau_{A3}} = \begin{bmatrix} \mathbf{V}_{A3}, \mathbf{T}_{A3}, \mathbf{N}_{A3}, \mathbf{B}_{A3}, \mathbf{\chi}_{A3} \end{bmatrix}^T$$
(A.110)

Since the mapping $\hat{f}_{q_T} : P_{\tau_{A2}} \rightarrow P_{\tau_{A3}}$ represents a numerical extrapolation, it is symbolized as a one-set prediction function $\hat{f}_{q_T}$ in l_{q_T} , called F_T extrapolation.

$$P_{\tau_{A3}} = \hat{f}_{F_T}\left(P_{\tau_{A2}}, l_{q_T}\right)$$
(A.111)

Let a tangent length reference $l_{T,ref}$ with respect to **T** , be defined by (A.103) .   Let the one set parameterization be defined by the values given in the table below. In this example the chord has length $l_{\chi_2} = 8.000$. Its direction vector is given by $\mathbf{e}_{\chi_2} = \begin{bmatrix} -1.000 & 0.000 & 0.000 \end{bmatrix}$.

Table A. 7: F_T extrapolation

Tortuosity Pole	$q_T = 0.000$ $\hat{P}_{\tau_{A3}} = \hat{f}_{F_T}\left(P_{\tau_{A2}}, l_{q_T}\right)$	$q_T = 1.000$ $\hat{P}_{\tau_{A3}} = \hat{f}_{F_T}\left(P_{\tau_{A2}}, l_{q_T}\right)$
V^T	$\begin{bmatrix} 4.000 & 0.000 & 0.000 \end{bmatrix}$	$\begin{bmatrix} 0.000 & 4.000 & 0.000 \end{bmatrix}$
T^T	$\begin{bmatrix} 0 & 1.000 & 0.000 \end{bmatrix}$	$\begin{bmatrix} 1.000 & 0.000 & 0.000 \end{bmatrix}$
N^T	$\begin{bmatrix} -1.000 & 0.000 & 0.000 \end{bmatrix}$	$\begin{bmatrix} 0.000 & -1.000 & 0.000 \end{bmatrix}$
B^T	$\begin{bmatrix} 0.000 & 0.000 & 1.000 \end{bmatrix}$	$\begin{bmatrix} 0.000 & 0.000 & 1.000 \end{bmatrix}$
χ^T	$\begin{bmatrix} 0.2500 & 0.0000 & 0.0000 \end{bmatrix}$	$\begin{bmatrix} 0.0000 & 0.0000 & 0.0000 \end{bmatrix}$

Figure A. 17: F_T extrapolation

NOTE   The plot above illustrates a run for $q_T \in \begin{bmatrix} 0.000 : 0.0100 : 1.000 \end{bmatrix}$.
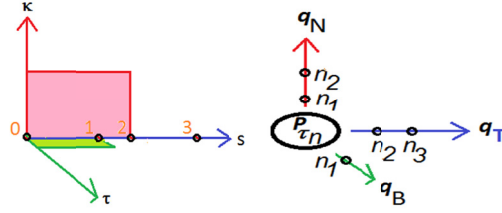
Figure A. 18: Three-set successive Frenet parameterizations: $q_B = \dfrac{l_{q_B}}{l_{B_{ref}}} \rightarrow q_N = \dfrac{l_{q_N}}{l_{N_{ref}}} \rightarrow q_T = \dfrac{l_{q_T}}{l_{T_{ref}}}$

In the following a TDOF extrapolation, q_B, q_N, q_T is performed as a successive mapping.

$$\hat{f}_{F_{TNB}} : P_{\tau_A} \rightarrow P_{\tau_{A1}} \rightarrow P_{\tau_{A2}} \rightarrow P_{\tau_{A3}} \tag{A.112}$$

This mapping leads to a TDOF prediction function in the parameters (q_T, q_N, q_B) for a near-field extrapolation of a tortuosity pole, i.e.:

$$P_{\tau_{A3}} = \hat{f}_{F_{TNB}} \left(P_{\tau_A}, l_{q_T}, l_{q_N}, l_{q_B} \right) \tag{A.113}$$

Algorithmically, this parametric near-field extrapolation can be deployed as nested prediction functions and thereby used for any TDOF, DDOF or SDOF parameterization.

TDOF: $\quad P_{\tau_{A3}} = \hat{f}_{F_{TNB}} \left(P_{\tau_A}, l_{q_T}, l_{q_N}, l_{q_B} \right) = \hat{f}_{F_T} \left(\hat{f}_{F_N} \left(\hat{f}_{F_B} \left(P_{\tau_A}, l_{q_B} \right), l_{q_N} \right), l_{q_T} \right)$ $\qquad$ (A.114)

DDOF: $\quad P_{\tau_{A3}} = \hat{f}_{F_{TNB}} \left(P_{\tau_A}, l_{q_T}, l_{q_N} \right) = \hat{f}_{F_T} \left(\hat{f}_{F_N} \left(P_{\tau_A}, l_{q_N} \right), l_{q_T} \right)$ $\qquad$ (A.115)

SDOF: $\quad P_{\tau_{A3}} = \hat{f}_{F_{TNB}} \left(P_{\tau_A}, l_{q_T} \right) = \hat{f}_{F_T} \left(P_{\tau_A}, l_{q_T} \right)$ $\qquad$ (A.116)

ANNEX 9.4.1   *EXAMPLE – F*_{TNB} *Extrapolation*

In this example, a successive three set extrapolation in accordance with (A.114) is presented. The three length references $l_{B,ref}$, $l_{N,ref}$, $l_{T,ref}$, are defined in accordance with (A.74) and (A.104) respectively. The chord length is $l_{\chi_2} = 8.000$ and the chord direction vector is given by $\mathbf{e}_{\chi_2} = \begin{bmatrix} -1.000 & 0.000 & 0.000 \end{bmatrix}$.
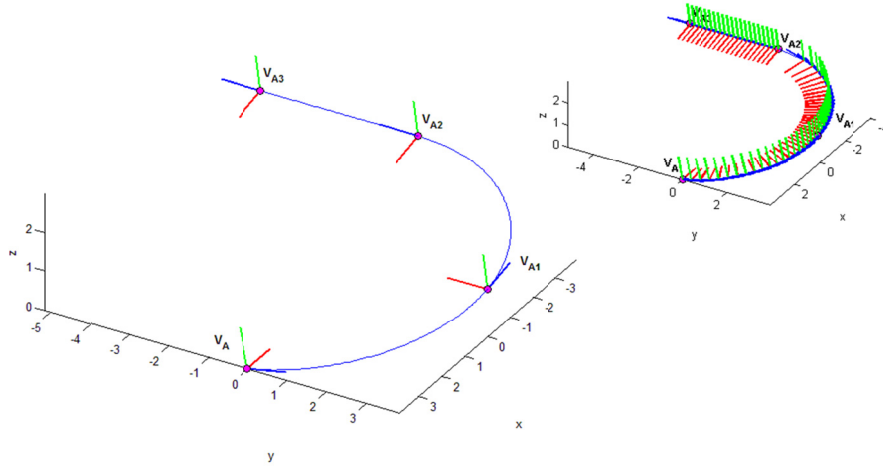
Figure A. 19: *F*_{TNB} extrapolation: Control Poles (left), plot for various parameter values (right)

Frenet extrapolation is illustrated in the Figure above here using two plots. Left: A standard pole plot with the poles marked at the control points. Right: a parametric plot defined by $(q_B, q_N, q_T) \in [0.000 : 0.0500 : 1.000]$ which illustrates the poles from various parameter values. The following table summarizes the example results.

Table A. 8: *F*_{TNB} extrapolation

Pole	$q_B = 0.000$ $P_{\tau_A} = \hat{f}_{F_B}\left(P_{\tau_A}, l_{q_T}\right)$	$q_N = 0.000$ $P_{\tau_{A1}} = \hat{f}_{F_N}\left(P_{\tau_{A1}}, l_{q_N}\right)$	$q_T = 0.000$ $P_{\tau_{A2}} = \hat{f}_{F_T}\left(P_{\tau_{A1}}, l_{q_T}\right)$	$q_T = 1.000$ $P_{\tau_{A3}} = \hat{f}_{F_T}\left(P_{\tau_{A2}}, l_{q_T}\right)$
$\mathbf{V}^T$	$\begin{bmatrix} 3.846 & 0.000 & 0.000 \end{bmatrix}$	$\begin{bmatrix} 0.000 & 3.846 & 1.208 \end{bmatrix}$	$\begin{bmatrix} -3.922 & -0.154 & 1.993 \end{bmatrix}$	$\begin{bmatrix} -3.922 & -4.154 & 1.993 \end{bmatrix}$
$\mathbf{T}^T$	$\begin{bmatrix} 0 & 0.9806 & 0.1961 \end{bmatrix}$	$\begin{bmatrix} 0.9806 & 0.000 & 0.1961 \end{bmatrix}$	$\begin{bmatrix} 0.000 & -1.000 & 0.000 \end{bmatrix}$	$\begin{bmatrix} 0.000 & -1.000 & 0.000 \end{bmatrix}$
N^T	$\begin{bmatrix} -1.000 & 0.000 & 0.000 \end{bmatrix}$	$\begin{bmatrix} 0.000 & -1.000 & 0.000 \end{bmatrix}$	$\begin{bmatrix} 0.986 & 0.000 & -0.196 \end{bmatrix}$	$\begin{bmatrix} 0.986 & 0.000 & -0.196 \end{bmatrix}$
$\mathbf{B}^T$	$\begin{bmatrix} 0.000 & -0.196 & 0.981 \end{bmatrix}$	$\begin{bmatrix} 0.196 & 0.000 & 0.981 \end{bmatrix}$	$\begin{bmatrix} 0.196 & 0.000 & 0.981 \end{bmatrix}$	$\begin{bmatrix} 0.196 & 0.000 & 0.981 \end{bmatrix}$
χ^T	$\begin{bmatrix} \kappa_\chi & 0.2500 & 0.0500 \end{bmatrix}$	$\begin{bmatrix} \kappa_\chi & 0.250 & 0.000 \end{bmatrix}$	$\begin{bmatrix} 0.250 & 0.000 & 0.000 \end{bmatrix}$	$\begin{bmatrix} 0.000 & 0.000 & 0.000 \end{bmatrix}$

G^2, G^1 and G^0 continuity

In this annex, a set of non-parametric central segment predictions for a control vertex, orientation vectors, and a central location vertex, are defined from simple interpolations. First, the normal and the binormal vectors relating to G^2 continuity are defined. Thereafter, the tangent vector relating to G^1 continuity is defined. Finally, the location vertex relating to G^0 continuity is interpolated between the chord planes.

ANNEX 10.1   *G^2* INTERPOLATION
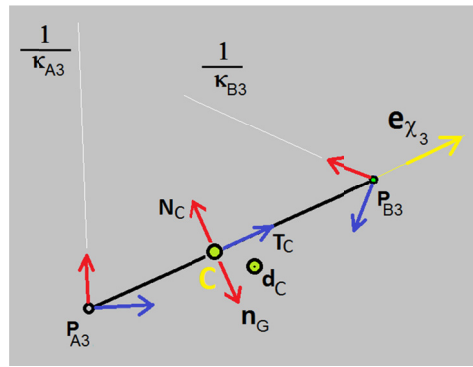
Figure A. 20: Interpolated normal, binormal and curvature for a central tortuosity pole P$_c$

Let two tortuosity poles P_{A3}, P_{B3} form a geometric constellation with a chord vector $\mathbf{e}_{\chi_3}$ as illustrated above

$$\mathbf{e}_{\chi_3} = \frac{(\mathbf{V}_{B3} - \mathbf{V}_{A3})}{\left\| (\mathbf{V}_{B3} - \mathbf{V}_{A3}) \right\|}, \quad (\mathbf{V}_{B3} - \mathbf{V}_{A3}) \neq \mathbf{0} \tag{A.117}$$

When a rectifying vector $\mathbf{d}_c$ is specified, then a central Gauss normal between the BegEnd A and the EndEnd B is estimated as $\mathbf{n}_G = (\mathbf{e}_{\chi_3} \times \mathbf{d}_c)$. This means that a central Frenet normal estimate is

$$\mathbf{N}_C = -(\mathbf{e}_{\chi_3} \times \mathbf{d}_c) = \mathbf{d}_c \times \mathbf{e}_{\chi_3} . \tag{A.118}$$

Finally, the binormal is estimated as

$$\mathbf{B}_C = (\mathbf{e}_{\chi_3} \times \mathbf{N}_C) \tag{A.119}$$

NOTE   When the rectifying vector is a zero vector, the normal and binormal also becomes zero vectors.

In general, the segment curvature κ_χ is set to zero.

$$\boldsymbol{\chi}_C = \begin{bmatrix} 0 & 0 & 0 \end{bmatrix}^{\mathrm{T}} \tag{A.120}$$

However, when the orientation vectors of the tangents and the normals are almost mirrored vector pairs in the chord plane, then the central segment curvature can be predicted. This prediction can be expressed as the average of the two segment end curvatures.

$$\boldsymbol{\chi}_C = \begin{bmatrix} \dfrac{\kappa_{\chi_{A3}} + \kappa_{\chi_{B3}}}{2} & 0 & 0 \end{bmatrix}^{\mathrm{T}} \tag{A.121}$$

Herby, the G^2 part of a central tortuosity pole is formed as

$$P_{\tau_C} \ni \begin{bmatrix} \mathbf{N}_C, \mathbf{B}_C, \boldsymbol{\chi}_C \end{bmatrix}^{\mathrm{T}} \tag{A.122}$$

Since the mapping $f_{G^2} : P_{A_3}, P_{B_3} \rightarrow P_{\tau_C} \ni \begin{bmatrix} \mathbf{N}_C, \mathbf{B}_C, \boldsymbol{\chi}_C \end{bmatrix}^{\mathrm{T}}$ represents a numerical interpolation, which estimates G^2 continuity, it is symbolized as a non-parametric prediction function $\hat{f}_{G^2}$ called G^2 interpolation.

$$P_{\tau_C} = \hat{f}_{G^2} \left(P_{A3}, P_{B3}, \mathbf{d}_C \right) \tag{A.123}$$

ANNEX 10.2 G^1 INTERPOLATION

Let it be assumed that at least the normal, binormal, and curvature vectors contribute to a tortuosity pole $P_{\tau_C} \ni \begin{bmatrix} \mathbf{N}_C, \mathbf{B}_C, \boldsymbol{\chi}_C \end{bmatrix}^{\mathrm{T}}$ in accordance with (A.122). Further, let it be assumed that a chord vector $\mathbf{e}_{\chi_3}$ is defined from (A.117) . Then, a central tangent is determined as

$$\mathbf{T}_C = \mathbf{N}_C \times \mathbf{B}_C = \mathbf{e}_{\chi_3} \tag{A.124}$$

Herby, the G^1 part of a central tortuosity pole is formed.

$$P_{\tau_C} \ni \begin{bmatrix} \mathbf{T}_C \end{bmatrix}^{\mathrm{T}} \tag{A.125}$$

Since the mapping $\hat{f}_{G^1} : P_{A3}, P_{B3} \rightarrow P_{\tau_C} \ni \begin{bmatrix} \mathbf{T}_C \end{bmatrix}^{\mathrm{T}}$ represents a numerical interpolation, which estimates G^1 continuity, it is symbolized as a non-parametric prediction function $\hat{f}_{G^1}$ called G^1 interpolation.

$$P_{\tau_C} = \hat{f}_{G^1} \left(P_{A3}, P_{B3}, \mathbf{d}_C \right) \tag{A.126}$$
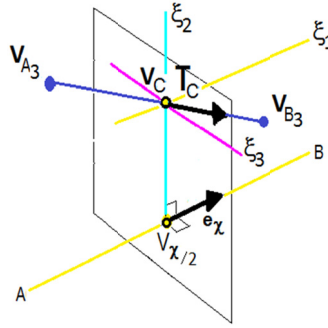
Figure A. 21: Interpolation of the vertex of a central tortuosity pole

Let it be assumed that three vertices $\mathbf{V}_{\chi/2}, \mathbf{V}_{A3}, \mathbf{V}_{B3}$, a chord vector $\mathbf{e}_\chi$, and a tangent $\mathbf{T}_C$ are extracted from four tortuosity poles P_A, P_{A3}, P_B, P_{B3} and a central pole P_C, as defined by (A.125). The vector $\mathbf{e}_\chi$ directs the chord as illustrated in Figure A. 21. Then, a central vertex $\mathbf{V}_C$ is defined as the intersection between the plane through the central chord vertex $\mathbf{V}_{\chi/2}$ with unit normal $\mathbf{e}_\chi$, and the line passing through $\mathbf{V}_{A3}$ directed by $\mathbf{T}_C$. I.e a new central vertex $\mathbf{V}_C$ is defined as a direction vector from $\mathbf{V}_{A3}$ to $\mathbf{V}_C$, and composed as the sum of the vector from $\mathbf{V}_{\chi/2}$ to $\mathbf{V}_{A3}$ and the vector from $\mathbf{V}_{A3}$ to $\mathbf{V}_C$ respectively. This means that the central vertex $\mathbf{V}_C$ lies on the normal plane, if the vector $\mathbf{V}_C - \mathbf{V}_{\chi/2}$ is perpendicular to $\mathbf{e}_\chi$:

$$\mathbf{V}_C = \mathbf{V}_{A3} + \frac{\left(\mathbf{e}_\chi \bullet \left(\mathbf{V}_{\chi/2} - \mathbf{V}_{A3}\right)\right)}{\mathbf{e}_\chi \bullet \mathbf{T}_C} \mathbf{T}_C \ , \quad \mathbf{e}_\chi \bullet \mathbf{T}_C \neq 0 \tag{A.127}$$

If $\mathbf{e}_\chi \bullet \mathbf{T}_C = 0$, then the central vertex is set equal to the central chord vertex.

Herby, the G^0 part of a central tortuosity pole is defined:

$$P_{\tau_C} \ni \left[\mathbf{V}_C\right]^T \tag{A.128}$$

Since the mapping $\hat{f}_{G^1} : P_A, P_{A3}, P_B, P_{B3} \rightarrow P_{\tau_C} \ni \left[\mathbf{V}_C\right]^T$ represents a numerical interpolation which estimates G^0 continuity, it is symbolized as a non-parametric prediction function $\hat{f}_{G0}$ called G^0 interpolation:

$$P_{\tau_C} = \hat{f}_{G^0}\left(P_A, P_{A3}, P_B, P_{B3}, \mathbf{d}_C\right) \rightarrow P_{\tau_C} \ni \left[\mathbf{V}_C\right]^T \tag{A.129}$$

The three interpolations (G^2, G^1 and G^0) in the preceding annexes are assumed to represent a successive mapping, which can be expressed as an overall interpolation function deployed by nested interpolations.

$$P_{\tau_C} = \hat{f}_{G^0}\left(\hat{f}_{G^1}\left(\hat{f}_{G^2}\left(P_A, P_{A3}, P_B, P_{B3}, \mathbf{d}_C\right)\right)\right) \tag{A.130}$$

Algorithmically, the interpolation of a full tortuosity pole is then defined as

$$P_{\tau_C} \ni \left[\mathbf{V}_C, \mathbf{T}_C, \mathbf{N}_C, \mathbf{B}_C, \mathbf{\chi}_C\right]^{\top} = \hat{f}_{G^{012}}\left(P_A, P_{A3}, P_B, P_{B3}, \mathbf{d}_C\right) \tag{A.131}$$

Inspired by (Tobler et al., 2002), location modifications for a central tortuosity pole of a segment can be performed as vertex increments in orthogonal directions. In the following section, a sequence of three such orthogonal vertex modifications are defined in a local coordinate system.

Let a segment chord be defined by its chord direction vector $\mathbf{e}_{\chi_2}$, its length l_{χ_2}, and its middle vertex $\mathbf{V}_{\chi_{1/2}}$. Further, let a vertex $\mathbf{V}_C$ be defined in the central part between the end chord planes and not on the chord line itself. Then, a simple parametric location specification scheme is given in the following table. In general, normals and binormals are not definable after location specifications are applied. Therefore, Frenet normals and binormals are first defined after the limit level of refinement is iterated. However, Frenet tangents are assumed to be kept intact at all levels of refinement.

As it appears from the figures in ANNEX 12.3, location specifications are defined as height levels relative to some reference planes, i.e. the location specification $\Delta\mathbf{V}_{\xi_1} = l_{q_{\xi_1}}\mathbf{e}_{\xi_1}$, directed by ξ_1, is equivalent to the height level H_1 in ξ_1 relative to the central chord plane. The location specification $\Delta\mathbf{V}_{\xi_2} = l_{q_{\xi_2}}\mathbf{e}_{\xi_2}$ is equivalent to the height level H_2 in ξ_2 relative to the radial plane. Finally, the pole translation $\Delta\mathbf{V}_{\xi_3} = l_{q_{\xi_3}}\mathbf{e}_{\xi_3}$ is equivalent to the height level H_3 in ξ_3 relative to the angular plane.

Table A. 9: Pole translations for a central pole vertex

Direction	Coordinate	Parameter	Basis vector	Vertex Translation	New Vertex
Longitudinal	ξ_1	q_{ξ_1}	$\mathbf{e}_{\xi_1} = \mathbf{e}_{\chi_2}$	$\Delta\mathbf{V}_{\xi_1} = l_{q_{\xi_1}}\mathbf{e}_{\xi_1}$	$\mathbf{V}_{C_1} = \mathbf{V}_C + \Delta\mathbf{V}_{\xi_1}$
Radial	ξ_2	q_{ξ_2}	$\mathbf{e}_{\xi_2} = \dfrac{\mathbf{V}_C - \mathbf{V}_{\chi_{1/2}}}{\left\| \mathbf{V}_C - \mathbf{V}_{\chi_{1/2}} \right\|}$	$\Delta\mathbf{V}_{\xi_2} = l_{q_{\xi_2}}\mathbf{e}_{\xi_2}$	$\mathbf{V}_{C_2} = \mathbf{V}_{C_1} + \Delta\mathbf{V}_{\xi_2}$
Angular	ξ_3	q_{ξ_3}	$\mathbf{e}_{\xi_3} = \mathbf{e}_{\xi_1} \times \mathbf{e}_{\xi_2}$	$\Delta\mathbf{V}_{\xi_3} = l_{q_{\xi_3}}\mathbf{e}_{\xi_3}$	$\mathbf{V}_{C_3} = \mathbf{V}_{C_2} + \Delta\mathbf{V}_{\xi_3}$

In the special situation where the central vertex and the middle vertex coincide on the chord, the radial basis vector must be estimated from vectors of the tortuosity poles at the chord ends or as a random unit vector perpendicular to the chord direction vector. The corresponding prediction functions are named the H_1-, H_2- and H_3-Frenet pole translation functions, respectively. This is in accordance with the height analogy.

ANNEX 11.1 H_1 POLE TRANSLATION

The mapping $\hat{f}_{H_1} : \left[\mathbf{e}_{\chi_2}, \mathbf{V}_{\chi/2}, \mathbf{V}_C, \mathbf{T}_C, \mathbf{N}_C, \mathbf{B}_C \right]^{\mathsf{T}} \rightarrow P_{\tau_{C'}}$ represents a one-dimensional translation and is symbolized as a prediction function $\hat{f}_{H_1}$, called H_1 pole translation.

$$ P_{\tau_{C'}} = \hat{f}_{H_1}\left(\left[\mathbf{e}_{\chi_2}, \mathbf{V}_{\chi/2}, \mathbf{V}_C, \mathbf{T}_C, \mathbf{N}_C, \mathbf{B}_C \right]^{\mathsf{T}} \right) \tag{A.132} $$

ANNEX 11.2 H_2 POLE TRANSLATION

The mapping $\hat{f}_{H_2} : \left[\mathbf{e}_{\chi_2}, \mathbf{V}_{\chi/2}, \mathbf{V}_C, \mathbf{T}_C, \mathbf{N}_C, \mathbf{B}_C \right]^{\mathsf{T}} \rightarrow P_{\tau_{C'}}$ represents a one-dimensional translation and is symbolized as a prediction function $\hat{f}_{H_2}$, called H_2 pole translation.

$$ P_{\tau_{C'}} = \hat{f}_{H_2}\left(\left[\mathbf{e}_{\chi_2}, \mathbf{V}_{\chi/2}, \mathbf{V}_C, \mathbf{T}_C, \mathbf{N}_C, \mathbf{B}_C \right]^{\mathsf{T}} \right) \tag{A.133} $$

ANNEX 11.3 H_3 POLE TRANSLATION

The mapping $\hat{f}_{H_3} : \left[\mathbf{e}_{\chi_2}, \mathbf{V}_{\chi/2}, \mathbf{V}_C, \mathbf{T}_C, \mathbf{N}_C, \mathbf{B}_C \right]^{\mathsf{T}} \rightarrow P_{\tau_{C'}}$ represents a one-dimensional translation and is symbolized as a prediction function $\hat{f}_{H_3}$, called H_3 pole translation.

$$ P_{\tau_{C'}} = \hat{f}_{H_3}\left(\left[\mathbf{e}_{\chi_2}, \mathbf{V}_{\chi/2}, \mathbf{V}_C, \mathbf{T}_C, \mathbf{N}_C, \mathbf{B}_C \right]^{\mathsf{T}} \right) \tag{A.134} $$

ANNEX 11.4 H_{321} POLE TRANSLATION

The three interpolations in the preceding annexes are now assumed to represent a successive mapping, which can be unified into a single parametric interpolation function $\tilde{f}_H$ in $\left(P_{\tau_C} \right)$ called H-pole translation:

$$ P_{\tau_{C'}} = \hat{f}_{H_{321}}\left(P_{\tau_C}, \mathbf{q}_{\xi} \right) \tag{A.135} $$

Algorithmically, these parametric pole translations are deployed as nested interpolations.

$$ P_{\tau_{C'}} = \hat{f}_{H_{321}}\left(P_{\tau_C}, I_{q_{\xi 2}}, I_{q_{\xi 3}}, I_{q_{\xi 3}} \right) = \hat{f}_{H_3}\left(\hat{f}_{H_2}\left(\hat{f}_{H_1}\left(P_{\tau_C}, I_{q_{\xi 1}} \right), I_{q_{\xi 2}} \right), I_{q_{\xi 3}} \right) \tag{A.136} $$

ANNEX 12.1   THE DATA FLOW FOR BI-MESH SUBDIVISION

In this sub-annex, the entire data flow for bi-mesh Frenet subdivision is summarized in the following table.

Table 6.1: Determination of a new subdivision pole V_{C_3} by nested prediction functions

Classification	Identification	IO-Description					
Type	Pred. Fcn.	Curvature	Nat. Para.	Main Controls		Ref.	Output
Extrapolation*	$\hat{f}_{F_B}$	τ_τ	q_{B_A}	B_A	N_A	V_A	$V_{A_1}\ T_{A_1}\ N_{A_1}\ B_{A_1}\ \tau_\tau = 0$
	$\hat{f}_{F_N}$	κ_τ	q_{N_A}	N_{A_1}	T_{A_1}	V_{A_1}	$V_{A_2}\ T_{A_2}\ N_{A_2}\ B_{A_2}\ \kappa_\tau = 0$
	$\hat{f}_{F_T}$	κ_χ	q_{T_A}	T_{A_2}	V_{A_2}		$V_{A_3}\ T_{A_3}\ N_{A_3}\ B_{A_3}\ (\kappa_\chi)$
Interpolation	$\hat{f}_{G^2}$			V_{A_2}	V_{B_2}		$e_{\chi_2}\ \kappa_{\chi_C}^{n_\tau},(k_\tau = n_\tau)$
	$\hat{f}_{G^1}$			V_{A_3}	V_{B_3}	d_C	$T_C\ N_C\ B_C$
	$\hat{f}_{G^0}$			V_{A_3}	T_C	e_{ξ_1}	$V_C\ e_{\xi_2}\ e_{\xi_3}$
Perturbation	$\hat{f}_{H_1}$		q_{ξ_1}	e_{ξ_1}	V_C		$V_{C_1}\ T_C$
	$\hat{f}_{H_2}$		q_{ξ_2}	e_{ξ_2}	V_{C_1}		$V_{C_2}\ T_C$
	$\hat{f}_{H_3}$		q_{ξ_3}	e_{ξ_3}	V_{C_2}		$V_{C_3}\ T_C$

The parametric Frenet subdivision input-output flow is summarized in Table 6.1. The extrapolations are defined from the BegEnd (A) only. However, extrapolations from the EndEnd (B) are performed as from the BegEnd (A) reversing the chord direction vector. Furthermore, at each extrapolation step, pole vectors are sign adjusted. This is in accordance with the bi-pole convexivity requirements.

NOTE   The hierarchical naming of extrapolation functions follows the reverse ordering of Frenet frames i.e. $\mathbf{B} \rightarrow \mathbf{N} \rightarrow \mathbf{T}$. The naming of interpolation functions follows reversely the first three geometric continuity orders i.e. $G^2 \rightarrow G^1 \rightarrow G^0$. Finally, the naming of the perturbation functions follows the conventional ordering of Cartesian coordinate's i.e. $\xi_1 \rightarrow \xi_2 \rightarrow \xi_3$.

The parameters of Frenet subdivision are related to the length references. Upper bound values,[41] often used in this presentation, are provided in the following table.

Table A. 10: Length reference bounds for bi-mesh Frenet subdivision

Classification	Identification	Upper bound	Current Bound
Extrapolation	$\hat{f}_{F_B}$	$l_{\mathbf{B},ref,upp} = \min\left(k_\mathbf{B} l_\chi,\ \tan(k_\mathbf{B}\pi)\sqrt{\rho^2+b^2}\right)$	$l_{q_\mathbf{B}} = q_\mathbf{B} l_{\mathbf{B},ref}$
	$\hat{f}_{F_N}$	$l_{\mathbf{N},ref,upp} = \min\left(k_\mathbf{N} l_{\chi_1},\ \dfrac{\tan(k_\mathbf{N}\pi)}{\kappa_\tau}\ (\kappa_\tau>0)\right)$	$l_{q_\mathbf{N}} = q_\mathbf{N} l_{\mathbf{N},ref}$
	$\hat{f}_{F_T}$	$l_{\mathbf{T},ref,upp} = \min\left(k_\mathbf{T} l_{\chi_2},\ \dfrac{1-c_{\theta_{A2}}}{\kappa_{\chi_{A2}}\sqrt{1-c^2_{\theta_{A2}}}} l_{\chi_2}, \kappa_{\chi_{A2}}\neq 0, c^2_{\theta_{A2}}<1\right)$	$l_{q_\mathbf{T}} = q_\mathbf{T} l_{\mathbf{T},ref}$
Perturbation	$\hat{f}_{H_1}$	$l_{\xi_1,ref,upp} = k_{\xi_1} l_\chi$	$l_{q_{\xi_1}} = q_{\xi_1} l_{\xi_1,ref}$
	$\hat{f}_{H_2}$	$l_{\xi_2,ref,upp} = k_{\xi_2} l_\chi$	$l_{q_{\xi_2}} = q_{\xi_2} l_{\xi_2,ref}$
	$\hat{f}_{H_3}$	$l_{\xi_3,ref} = k_{\xi_2} l_\chi$	$l_{q_{\xi_3}} = q_{\xi_3} l_{\xi_3,ref}$
tdof	$\tilde{f}_{F_T}\left(\tilde{f}_{F_N}\left(\tilde{f}_{F_B}(.)\right)\right)$	$\tau_\tau>0, \kappa_\tau>0:\ k_\mathbf{B}=1/8,\ k_\mathbf{N}=1/4,\ k_\mathbf{T}=1/4,\ k_{\xi_1}=1/4,\ k_{\xi_2}=1/4,\ k_{\xi_3}=1/$	
ddof	$\tilde{f}_{F_T}\left(\tilde{f}_{F_N}(.)\right)$	$\kappa_\tau>0:\ k_\mathbf{N}=1/4,\ k_\mathbf{T}=1/4,\ k_{\xi_1}=1/4,\ k_{\xi_2}=1/4,\ k_{\xi_3}=1/4$	
sdof	$\tilde{f}_{F_T}(.)$	$\mathbf{V}_{A2}\neq\mathbf{V}_{B2}, \kappa_\chi>0:\ k_\mathbf{T}=1/4,\ k_{\xi_1}=1/4,\ k_{\xi_2}=1/4,\ k_{\xi_3}=1/4$	

---

[41] A thorough upper bound study is not included in this work. The selected upper bounds are chosen under the following conditions: Extrapolation factors $k_\mathbf{B}, k_\mathbf{N}, k_\mathbf{T}$ are designed to create geometries so that $q_\mathbf{B}=q_\mathbf{N}=q_\mathbf{T}=1$ produce an asymptotic circular shape at the ends of bi-meshes. The pole translation factor k_{ξ_1} is selected so the perturbed pole lies in planes which intersect the central region of the master chord. The two pole translation factors k_{ξ_2}, k_{ξ_3} are set so the tortuosity pole is translated by distances of the same size as the master chord length itself. Dispite these relatively narrow bounds fractal-like geometries can occur. For perturbation modeling the above pole translation factors are not in use since perturbation modeling is a tool for the modeler to perform deterministic or pseudo-stochastic simulations, i.e. the bounds for perturbation modeling are left open to be defined by the modeler.

Table A. 11: DOF-combinations for parametric bi-mesh subdivision

Class	Name	nDOF$_{BegEnd}$	nDOF$_{EndEnd}$	Description
Symmetric	SSDOF	1	1	SingleSingle
	DDDOF	2	2	DoubleDouble
	TTDOF	3	3	TripleTriple
Non-symmetric	SDDOF	1	2	SingleDouble
	STDOF	1	3	SingleTriple
	DSDOF	2	1	DoubleSingle
	DTDOF	2	3	DoubleTriple
	TSDOF	3	1	TripleSingle
	TDDOF	3	2	TripleDouble

Table A. 12: Illustrated Selections of DOF-combinations

Class	Name	Description
Symmetric	SSDOF	ANNEX 12.3.1
	DDDOF	ANNEX 12.3.2
	TTDOF	ANNEX 12.3.1
Non-symmetric	DSDOF	ANNEX 12.3.4
	TSDOF	ANNEX 12.3.5
	TDDOF	ANNEX 12.3.4

In the following sub-annexes the full data flow are given for six selected combinations defined in the table above. The tortuosity poles $\left(P_{\tau_A}, P_{\tau_B} \right)$ and the parameterization values are the same for all selections. However, the constant Frenet vectors **TNB** and the rectifying vector $\mathbf{d}_C$ are simulated by a random number generator.

ANNEX 12.3.1   SSDOF –Symmetric Subdivision

Parametric Bi-Mesh Subdivision
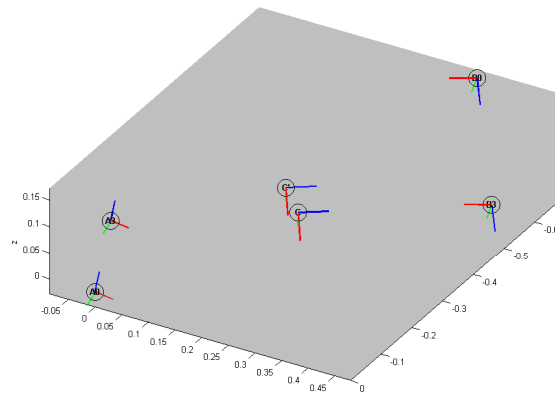
Rectifying vector:

dC = [-0.40825   -0.40825   -0.8165]

dof (location): 3

dof (orientation [A B]): [1 1]

dof (total): 5

A

Tortuosity Poles and Parameterization Values

	x	y	z
V	0	0	0
T	-0.9129	-0.3651	0.1826
N	-0.2582	0.5164	-0.2582
B	0	-0.2828	-0.5657
X	0	2.5000	-0.0500

	[-]
dof	1

A0

	x	y	z
V	0	0	0
T	-0.9129	-0.3651	0.1826
N	-0.2582	0.5164	-0.2582
B	0	-0.2828	-0.5657
X	0	2.5000	-0.0500

	[-]
q	0.9000
kq	0
IX_ref	0.7638
Iq_ref	0
Iq	0

A1

	x	y	z
V	0	0	0
T	-0.9129	-0.3651	0.1826
N	-0.2582	0.5164	-0.2582
B	0	-0.2828	-0.5657
X	0	2.5000	-0.0500

	[-]
q	0.8500
kq	0
IX_ref	0.7638
Iq_ref	0
Iq	0

A2

	x	y	z
V	-0.1663	-0.0665	0.0333
T	-0.9129	-0.3651	0.1826
N	-0.2582	0.5164	-0.2582
B	0	-0.2828	-0.5657
X	0	2.5000	-0.0500

	[-]
q	0.8000
kq	0.2500
IX_ref	0.7638
Iq_ref	0.2277
Iq	0.1821

A3

C = Non-Translated

	x	y	z
V	-0.3327	0.1901	0.0391
T	-0.5441	0.8388	0.0190
N	0.6771	0.4520	-0.5646
B	-0.4821	-0.2943	-0.8139
X	0	0	0

C' = Pole Translated

	x	y	z
q	-0.0100	-0.0300	0
kq	0.2500	2	1
IX_ref	0.7638	0.7638	0.7638
Iq_ref	0.1909	1.5275	0.7638
Iq	-0.0019	-0.0458	0

	x	y	z
V	-0.3322	0.1670	0.0795
T	-0.5441	0.8388	0.0190
N	0.6771	0.4520	-0.5646
B	-0.4821	-0.2943	-0.8139
X	0	0	0

B

Tortuosity Poles and Parameterization Values

	[-]
dof	1

B0

	x	y	z
V	-0.6667	0.3333	0.1667
T	0.6960	0.5145	-0.5145
N	0.5941	-0.6931	0.0990
B	-0.3057	-0.3736	-0.7811
X	0	3.5000	-0.4000

	[-]
q	0.9800
kq	0
IX_ref	0.7638
Iq_ref	0
Iq	0

B1

	x	y	z
V	-0.6667	0.3333	0.1667
T	0.6960	0.5145	-0.5145
N	0.5941	-0.6931	0.0990
B	-0.3057	-0.3736	-0.7811
X	0	3.5000	-0.4000

	[-]
q	0.9600
kq	0
IX_ref	0.7638
Iq_ref	0
Iq	0

B2

	x	y	z
V	-0.6667	0.3333	0.1667
T	0.6960	0.5145	-0.5145
N	0.5941	-0.6931	0.0990
B	-0.3057	-0.3736	-0.7811
X	0	3.5000	-0.4000

	[-]
q	0.9200
kq	0.2500
IX_ref	0.7638
Iq_ref	0.2569
Iq	0.2363

B3

	x	y	z
V	-0.5045	0.4549	0.0451
T	0.6960	0.5145	-0.5145
N	0.5941	-0.6931	0.0990
B	-0.3057	-0.3736	-0.7811
X	0	3.5000	-0.4000

ANNEX 12.3.2   DDDOF –Symmetric Subdivision

Parametric Bi-Mesh Subdivision
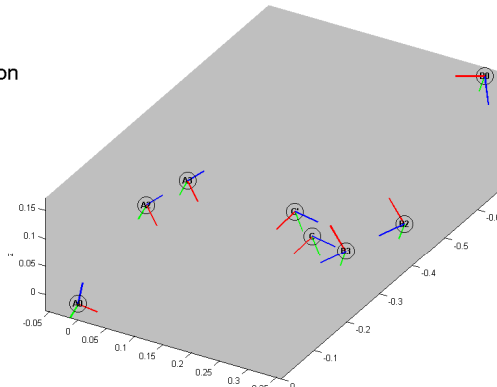
Rectifying vector:

dC = [-0.40825   -0.40825   -0.8165]

dof (location): 3

dof (orientation [A B]): [2 2]

dof (total): 7

A

Tortuosity Poles and Parameterization Values

	x	y	z
V	-0.9129	-0.3651	0.1826
T	-0.2582	0.5164	-0.2582
N	0	-0.2828	-0.5657
B	0	2.5000	-0.0500
X			

	[-]
dof	2

A0

	x	y	z
V	0	0	0
T	-0.9129	-0.3651	0.1826
N	-0.2582	0.5164	-0.2582
B	0	-0.2828	-0.5657
X	0	2.5000	-0.0500

	[-]
q	0.9000
kq	0
IX_ref	0.7638
Iq_ref	0
Iq	0

A1

	x	y	z
V	-0.2836	-0.0434	0.0217
T	-0.8347	0.0979	-0.0490
N	0.4509	0.6248	-0.3124
B	0	-0.2828	-0.5657
X	0	0	-0.0500

	[-]
q	0.8500
kq	0.2500
IX_ref	0.7638
Iq_ref	0.1909
Iq	0.1623

A2

	x	y	z
V	-0.3883	-0.0311	0.0155
T	-0.8347	0.0979	-0.0490
N	0.4509	0.6248	-0.3124
B	0	-0.2828	-0.5657
X	0	0	-0.0500

	[-]
q	0.8000
kq	0.2500
IX_ref	0.4097
Iq_ref	0.1568
Iq	0.1254

A3

C = Non-Translated

	x	y	z
V	-0.3137	0.2321	0.0309
T	0.2723	0.9606	0.0561
N	0.7614	-0.1994	-0.2810
B	-0.2587	0.1193	-0.7857
X	0	0	0

C' = Pole Translated

	x	y	z
q	-0.0100	-0.0300	0
kq	0.2500	2	1
IX_ref	0.7638	0.7638	0.7638
Iq_ref	0.1909	1.5275	0.7638
Iq	-0.0019	-0.0458	0

	x	y	z
V	-0.3247	0.1954	0.0587
T	0.2723	0.9606	0.0561
N	0.7614	-0.1994	-0.2810
B	-0.2587	0.1193	-0.7857
X	0	0	0

B

Tortuosity Poles and Parameterization Values

	[-]
dof	2

B0

	x	y	z
V	-0.6667	0.3333	0.1667
T	0.6960	0.5145	-0.5145
N	0.5941	-0.6931	0.0990
B	-0.3057	-0.3736	-0.7811
X	0	3.5000	-0.4000

B1

	[-]
q	0.9800
kq	0
IX_ref	0.7638
Iq_ref	0
Iq	0

	x	y	z
V	-0.6667	0.3333	0.1667
T	0.6960	0.5145	-0.5145
N	0.5941	-0.6931	0.0990
B	-0.3057	-0.3736	-0.7811
X	0	3.5000	-0.4000

B2

	[-]
q	0.9600
kq	0.2500
IX_ref	0.7638
Iq_ref	0.1909
Iq	0.1833

	x	y	z
V	-0.3895	0.3515	0.0495
T	0.8260	-0.4156	-0.1245
N	-0.3759	-0.7566	0.5089
B	-0.3057	-0.3736	-0.7811
X	0	0	-0.4000

B3

	[-]
q	0.9200
kq	0.2500
IX_ref	0.4097
Iq_ref	0.1263
Iq	0.1162

	x	y	z
V	-0.2936	0.3032	0.0351
T	0.8260	-0.4156	-0.1245
N	-0.3759	-0.7566	0.5089
B	-0.3057	-0.3736	-0.7811
X	0	0	-0.4000

ANNEX 12.3.3   TTDOF – Symmetric Subdivision

Parametric Bi-Mesh Subdivision
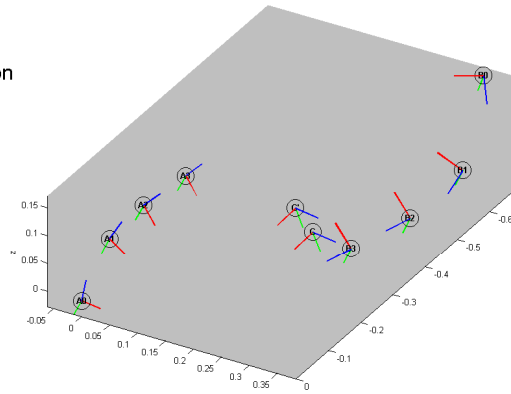
Rectifying vector:

dC = [-0.40825   -0.40825   -0.8165]

dof (location): 3

dof (orientation [A B]): [3 3]

dof (total): 9

C = Non-Translated   C' = Pole Translated

ANNEX 12.3.4   DSDOF – Non-Symmetric subdivision

Parametric Bi-Mesh Subdivision
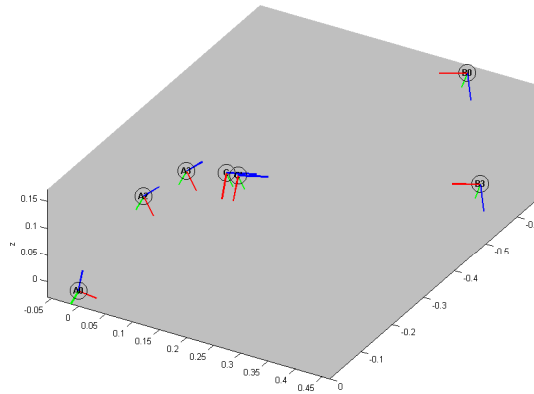
Rectifying vector:

dC = [-0.40825   -0.40825   -0.8165]

dof (location): 3

dof (orientation [A B]): [2 1]

dof (total): 6

C = Non-Translated   C' = Pole Translated

ANNEX 12.3.5   TSDOF – Non-Symmetric subdivision

Parametric Bi-Mesh Subdivision
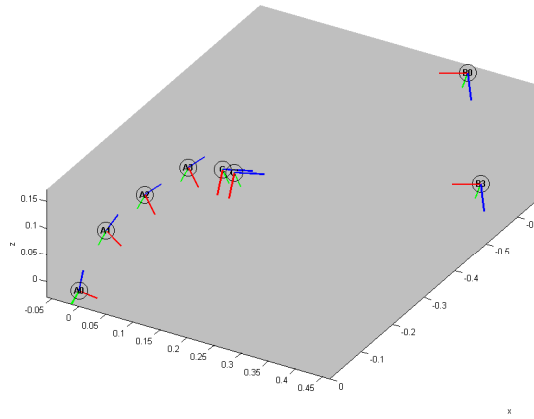
Rectifying vector:

dC = [-0.40825   -0.40825   -0.8165]

dof (location): 3

dof (orientation [A B]): [3 1]

dof (total): 7

A — Tortuosity Poles and Parameterization Values

A0

	x	y	z		[-]
V	0	0	0	dof	3
T	-0.9129	-0.3651	0.1826		
N	-0.2582	0.5164	-0.2582		
B	0	-0.2828	-0.5657		
X	0	2.5000	-0.0500		

A1

	x	y	z		[-]
V	-0.1590	-0.0417	0.0209	q	0.9000
T	-0.0606	-0.1260	0.0646	kq	0.1250
N	0.1395	0.6231	-0.3058	lX_ref	0.7638
B	-0.0016	-0.2936	-0.5991	lq_ref	0.0955
X	0	2.5000	0	lq	0.0859

A2

	x	y	z		[-]
V	-0.2882	-0.0444	0.0226	q	0.8500
T	-0.8962	0.0886	-0.0411	kq	0.1250
N	0.4623	0.6297	-0.3098	lX_ref	0.6478
B	-0.0016	-0.2936	-0.5991	lq_ref	0.0810
X	0	0	0	lq	0.0688

A3

	x	y	z		[-]
V	-0.4067	-0.0325	0.0171	q	0.8000
T	-0.8962	0.0886	-0.0411	kq	0.2500
N	0.4623	0.6297	-0.3098	lX_ref	0.5538
B	-0.0016	-0.2936	-0.5991	lq_ref	0.1673
X	0	0	0	lq	0.1338

B — Tortuosity Poles and Parameterization Values

B0

	[-]			x	y	z
dof	1		V	-0.6667	0.3333	0.1667
			T	0.6960	0.5145	-0.5145
			N	0.5941	-0.6931	0.0990
			B	-0.3057	-0.3736	-0.7811
			X	0	3.5000	-0.4000

B1

	[-]			x	y	z
q	0.9800		V	-0.6667	0.3333	0.1667
kq	0		T	0.6960	0.5145	-0.5145
lX_ref	0.7638		N	0.5941	-0.6931	0.0990
lq_ref	0		B	-0.3057	-0.3736	-0.7811
lq	0		X	0	3.5000	-0.4000

B2

	[-]			x	y	z
q	0.9600		V	-0.6667	0.3333	0.1667
kq	0		T	0.6960	0.5145	-0.5145
lX_ref	0.6478		N	0.5941	-0.6931	0.0990
lq_ref	0		B	-0.3057	-0.3736	-0.7811
lq	0		X	0	3.5000	-0.4000

B3

	[-]			x	y	z
q	0.9200		V	-0.5271	0.4380	0.0620
kq	0.2500		T	0.6960	0.5145	-0.5145
lX_ref	0.5538		N	0.5941	-0.6931	0.0990
lq_ref	0.2212		B	-0.3057	-0.3736	-0.7811
lq	0.2035		X	0	3.5000	-0.4000

C = Non-Translated   **C' = Pole Translated**

	x	y	z		[-]			x	y	z
V	-0.4208	0.0223	0.0223	q	-0.0100	-0.0300	0	V	-0.3980	0.0573	0.0377
T	-0.2467	0.9647	0.0921	kq	0.2500	2	1	T	-0.2467	0.9647	0.0921
N	0.7501	0.2390	-0.4946	lX_ref	0.7638	0.7638	0.7638	N	0.7501	0.2390	-0.4946
B	-0.4991	-0.0529	-0.7826	lq_ref	0.1909	1.5275	0.7638	B	-0.4991	-0.0529	-0.7826
X	0	0	0	lq	-0.0019	-0.0458	0	X	0	0	0

ANNEX 12.3.6   TDDOF – Non-Symmetric Subdivision

Parametric Bi-Mesh Subdivision
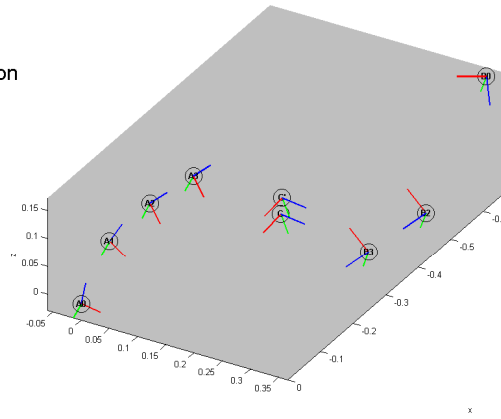
Rectifying vector:

dC = [-0.40825   -0.40825   -0.8165]

dof (location): 3

dof (orientation [A B]): [3 2]

dof (total): 8

A — Tortuosity Poles and Parameterization Values

A0

	x	y	z		[-]
V	0	0	0	dof	3
T	-0.9129	-0.3651	0.1826		
N	-0.2582	0.5164	-0.2582		
B	0	-0.2828	-0.5657		
X	0	2.5000	-0.0500		

A1

	x	y	z		[-]
V	-0.1590	-0.0417	0.0209	q	0.9000
T	-0.0606	-0.1260	0.0646	kq	0.1250
N	0.1395	0.6231	-0.3058	lX_ref	0.7638
B	-0.0016	-0.2936	-0.5991	lq_ref	0.0955
X	0	2.5000	0	lq	0.0859

A2

	x	y	z		[-]
V	-0.2882	-0.0444	0.0226	q	0.8500
T	-0.8962	0.0886	-0.0411	kq	0.1250
N	0.4623	0.6297	-0.3098	lX_ref	0.6478
B	-0.0016	-0.2936	-0.5991	lq_ref	0.0810
X	0	0	0	lq	0.0688

A3

	x	y	z		[-]
V	-0.4014	-0.0330	0.0173	q	0.8000
T	-0.8962	0.0886	-0.0411	kq	0.2500
N	0.4623	0.6297	-0.3098	lX_ref	0.4340
B	-0.0016	-0.2936	-0.5991	lq_ref	0.1597
X	0	0	0	lq	0.1277

B — Tortuosity Poles and Parameterization Values

B0

	[-]			x	y	z
dof	2		V	-0.6667	0.3333	0.1667
			T	0.6960	0.5145	-0.5145
			N	0.5941	-0.6931	0.0990
			B	-0.3057	-0.3736	-0.7811
			X	0	3.5000	-0.4000

B1

	[-]			x	y	z
q	0.9800		V	-0.6667	0.3333	0.1667
kq	0		T	0.6960	0.5145	-0.5145
lX_ref	0.7638		N	0.5941	-0.6931	0.0990
lq_ref	0		B	-0.3057	-0.3736	-0.7811
lq	0		X	0	3.5000	-0.4000

B2

	[-]			x	y	z
q	0.9600		V	-0.4246	0.3663	0.0562
kq	0.2500		T	0.2348	0.9713	0.0376
lX_ref	0.6478		N	-0.2533	-0.8084	0.4858
lq_ref	0.1619		B	-0.3057	-0.3736	-0.7811
lq	0.1555		X	0	0	-0.4000

B3

	[-]			x	y	z
q	0.9200		V	-0.3141	0.3279	0.0313
kq	0.2500		T	0.8714	-0.3025	-0.1963
lX_ref	0.4340		N	-0.2533	-0.8084	0.4858
lq_ref	0.1378		B	-0.3057	-0.3736	-0.7811
lq	0.1267		X	0	0	-0.4000

C = Non-Translated   **C' = Pole Translated**

	x	y	z		[-]			x	y	z
V	-0.3578	0.1473	0.0243	q	-0.0100	-0.0300	0	V	-0.3414	0.1587	0.0647
T	0.2348	0.9713	0.0376	kq	0.2500	2	1	T	0.2348	0.9713	0.0376
N	0.7777	-0.1763	-0.3007	lX_ref	0.7638	0.7638	0.7638	N	0.7777	-0.1763	-0.3007
B	-0.2854	0.0998	-0.7968	lq_ref	0.1909	1.5275	0.7638	B	-0.2854	0.0998	-0.7968
X	0	0	0	lq	-0.0019	-0.0458	0	X	0	0	0

ANNEX 12.4   REDUCED DEGREES OF FREEDOM

In this annex, a few examples on various parameter-constellations, which represent reduced number of degrees of freedom, are given.

EXAMPLE   When prior knowledge does not exist on the balance between the orientation influences at the two tortuosity poles of a bi-mesh, the same influence parameters can be used for both poles. This reduces the number of degrees of freedom to six. (A.137)

$$
\left(q_{T_A} = q_{T_B} \equiv q_T \right), \left(q_{N_A} = q_{N_B} \equiv q_N \right), \left(q_{B_A} = q_{B_B} \equiv q_B \right) \rightarrow
$$
$$
q^k = \left(q_{\xi_1}, q_{\xi_2}, q_{\xi_3}, q_T, q_N, q_B \right) \rightarrow n_{DOF} = 6 \tag{A.137}
$$

EXAMPLE   When prior knowledge does not exist on torsion, the parameter q_B can be ignored. This reduces the number of degrees of freedom to five.

$$
q^{k_\tau} = \left(q_{\xi_1}, q_{\xi_2}, q_{\xi_3}, q_T, q_N \right) \rightarrow n_{DOF} = 5 \tag{A.138}
$$

EXAMPLE   When prior knowledge does not exist on embedded curvatures, the parameter q_N can be ignored. This reduces the number of degrees of freedom to four.

$$
q^{k_\tau} = \left(q_{\xi_1}, q_{\xi_2}, q_{\xi_3}, q_T \right) \rightarrow n_{DOF} = 4 \tag{A.139}
$$

EXAMPLE   Finally, when the simulation is assumed not to include vertex pole translations, the degrees of freedom can be reduced to one and the subdivision representation then appears as a smooth curve in general.

$$
q^{k_\tau} = \left(q_T \right) \rightarrow n_{DOF} = 1 \tag{A.140}
$$

NOTE   When prior knowledge does not exist on the segment curvatures, they are to be estimated (see ANNEX 6.2).

ANNEX 13   COORDINATE TRANSFORMATIONS

In general, any vertex $\mathbf{V}$ of a limit mesh $\mathrm{M}_\tau^{n_\tau}$ is represented in local Cartesian coordinates as

$$\left[V\right]_{\text{local}} = \begin{bmatrix} V_{\tau,x}^{n_\tau} \\ V_{\tau,y}^{n_\tau} \\ V_{\tau,z}^{n_\tau} \end{bmatrix}_{\text{local}} \tag{A.137}$$

During reparameterization, such limit meshes need to be retransformed into a phantom M_{phan} in global coordinates. This retransformation from limit mesh to phantom mesh is defined by an affine coordinate transformation in homogeneous coordinates. The 3D affine transformation is represented by a multiple of three 4x4 matrices each defined in global coordinates as

$$\begin{bmatrix} V_x \\ V_y \\ V_z \\ 1 \end{bmatrix}_{\text{global}} = \begin{bmatrix} q_{\|\Omega\|} & 0 & 0 & 0 \\ 0 & q_{\|\Omega\|} & 0 & 0 \\ 0 & 0 & q_{\|\Omega\|} & 0 \\ 0 & 0 & 0 & 1 \end{bmatrix} \begin{bmatrix} 1 & 0 & 0 & t_x \\ 0 & 1 & 0 & t_y \\ 0 & 0 & 1 & t_z \\ 0 & 0 & 0 & 1 \end{bmatrix} \begin{bmatrix} e_{1x} & e_{2x} & e_{3x} & 0 \\ e_{1y} & e_{2y} & e_{3y} & 0 \\ e_{1z} & e_{2z} & e_{3z} & 0 \\ 0 & 0 & 0 & 1 \end{bmatrix} \begin{bmatrix} V_{\tau,x}^{n_\tau} \\ V_{\tau,y}^{n_\tau} \\ V_{\tau,z}^{n_\tau} \\ 1 \end{bmatrix}_{\text{local}}, \tag{A.138}$$

where $\left[q_{\|\Omega\|} \right]$ is a size scaling matrix, $\left[t\right]$ a translation matrix, and $\left[e\right]$ a rotation matrix.

On compact form, and still in homogeneous coordinates, this can be expressed as

$$\left[V\right]_{\text{global}} = \left[q_{\|\Omega\|} \right] \left[t\right] \left[e\right] \left[V_\tau^{n_\tau} \right]_{\text{local}}. \tag{A.139}$$

Table 6.2: Natural Parameters

Parameter Classification		Parameter identification		Parameter Description
Name	Symbol	Name	Symbol	Control
Master parameters	q^0	length normalization parameter	$q^0_{\|\Omega\|_L}$ $q^0_{\|\Omega\|_{L^{-1}}}$	Controls the size normalization of geometries in $\mathbb{R}^1$ by a length reference
		area normalization parameter	$q^0_{\|\Omega\|_A}$	Controls the size normalization of geometries in $\mathbb{R}^2$ by an area reference
		volume normalization parameter	$q^0_{\|\Omega\|_V}$	Controls the size normalization of geometries in $\mathbb{R}^3$ by a volume reference
		First dimension parameter	$q^0_{\|\Omega\|_{b1}}$	Controls the extent of an object in the first dimension axis direction
		Second dimension parameter	$q^0_{\|\Omega\|_{b2}}$	Controls the extent of an object in the second bounding axis direction
		Third dimension parameter	$q^0_{\|\Omega\|_{b3}}$	Controls the extent of an object in the third bounding axis direction
		first master location parameter	$q^0_{\xi_1}$	Controls the location of pole vertices in the first axis direction
		second master location parameter	$q^0_{\xi_2}$	Controls the location of pole vertices in the second axis direction
		third master orientation parameter	$q^0_{\xi_3}$	Controls the location of pole vertices in the third axis direction
		first master orientation parameter	$q^0_{\theta_1}$	Controls the orientation of free frame tangents, normals and binormals in the first angle direction
		second master orientation parameter	$q^0_{\theta_2}$	Controls the orientation of free frame tangents, normals and binormals in the second angle direction
Iterated parameters	q^{k_τ}	First iterated location parameter	$q^{k_\tau}_{\xi_1}$	Controls the translation of an iterated pole in the first local axis direction
		Second iterated location parameter	$q^{k_\tau}_{\xi_2}$	Controls the translation of an iterated pole in the second local axis direction
		Third iterated location parameters	$q^{k_\tau}_{\xi_3}$	Controls the translation of an iterated pole in the third local axis direction
		First iterated orientation parameter	$q^{k_\tau}_{\mathbf{T}_A}, q^{k_\tau}_{\mathbf{T}_B}$	Controls the influence from the segment curvature from the ends of a bi-mesh chord
		Second iterated orientation parameter	$q^{k_\tau}_{\mathbf{N}_A}, q^{k_\tau}_{\mathbf{N}_B}$	Controls the influence from the conventional curvature from the ends of a bi-mesh chord
		Third iterated orientation parameter	$q^{k_\tau}_{\mathbf{B}_A}, q^{k_\tau}_{\mathbf{B}_B}$	Controls the influence from the conventional torsion from the ends of a bi-mesh chord

Formally, the conditions in (2.89) can be specified as follows:

During iterations of a new subdivision tortuosity pole from a set of beta-simulated curves, the beta-perturbations necessary for these curves to intersect in a central vertex must be minimized.

In the subsequent alpha-beta simulation, the assumed continous distributions of the individual boundary indicators must not differ significantly from the distributions of the observed indicator metrics. Similarily, the distributions for the first integrals must not differ significantly.

Imitation modeling as a variational problem

Mathematically, these criterions can be expressed as a variational problem: find a particular stochastic simulation approach defined on a set of feasible subdivision operators $\left\{S_\tau^{k_\tau}\right\}$ and a set of feasible master meshes $\left\{M_\tau^0\right\}$ so that a particular set of imitations $\left\{\overline{M}_{\tau,\alpha\beta}\right\}$ amongst a set of feasible imitations $\left\{M_{\tau,\alpha\beta}\right\}$ reflects the underlying stochastic behavior of the natural object with a high degree of efficiency.

Alpha-beta simulation

More specifically, when the mutual distance metric, see (2.69), between a set of beta-simulated Frenet subdivision curves $\left(C_{\tau,1},...,C_{\tau,i},...,C_{\tau,n_{\{F\}}}\right)$ and a vertex $\mathbf{V}_C$ is at its minimum, then this vertex is said to represent a central beta estimate for the semi-stationary location of the new iterated tortuosity pole.

From this beta-estimated location, a subsequent pole translation, performed as an alpha simulation, is said to reflect the dominant dispersion.

Shape imitation

If the distribution of selected imitation metrics (which reflects the segment shape), from the generated meshes and from the observed meshes, do not differ significantly in a two-sample test, then the segment imitations are said to reflect the underlying stochastic behavior of the segent shape with high efficiency of imitation. Statistically, a test factor rejects the null hypothesis of the following non-parametric two-sample hypotheses test:

H$_0$: (Null hypothesis): paired data sets of imitation metrics $\left(m_{\mho,\text{obs},i}, \hat{m}_{\mho_{\alpha\beta,i}}\right), \forall i$, are from the same continuous distribution.

H$_1$: (Alternative hypothesis): The paired data sets are from different distributions.

Size imitation

If the distribution of first integrals, which reflect the overall size of the object, do not differ significantly from the size distribution of the observation meshes in a two-sample test, then the imitation of size is said to reflect the underlying stochastic behavior of size with high efficiency of imitation. Specifically, a test factor rejects the null hypothesis of the following non-parametric two-sample hypotheses test:

H_0: (Null hypothesis): paired data sets of first integrals $(\int d\Omega_{obs,i}, \int d\hat{\Omega}_{phan,i})$, $\forall i$, are from the same continuous distribution.

H_1: (Alternative hypothesis): The paired data sets are from different distributions.

The imitation problem

Combining size and shape imitation leads to the following imitation problem

$$\min J_{|\beta|}: \quad \frac{\alpha_{two}}{1-h_{imi}} \leq \alpha_{two_{upp}} \quad , \quad \forall i \in 1,...,n_{\alpha\beta}, \quad h_{imi} \neq 1. \tag{A.144}$$

Where $J_{|\beta|}$ is the beta functional to be minimized, $\alpha_{two_{upp}}$ is an upper limit for the significance level, and h_{imi} is a test parameter defined as

$$h_{imi} = \sum h_{\mho}(m_{\mho,obs,i}, \hat{m}_{\mho,phan,i}) + \sum h_{\int d\Omega}(\int d\Omega_{obs,i}, \int d\hat{\Omega}_{phan,i}) \quad , \quad \forall i, \tag{A.145}$$

where $h_{\mho}$ is a two-sample test statistic* for segments, and $h_{\int d\Omega}$ is a two-sample test statistic[42] for first integrals. In this first study,[43] the overall imitation test parameter h_{imi}, is assumed to be modeled as a Boolean variable. Consequently, if just a single pair fails, the entire sample of phantoms is rejected.

In general, the alpha-beta simulated indicator metrics $\hat{m}_{\mho_{\alpha\beta,i}}$ are found from realizations at relevant levels of refinement.

$$\hat{m}_{\mho,\alpha\beta}^{k_\tau} = \hat{m}_{\mho,\alpha\beta}^{k_\tau}\left(M_\tau^{k_\tau} \leftarrow S_{\tau,\alpha\beta}^{k_\tau} M_\tau^0\right). \tag{A.146}$$

NOTE   For the case study (see chapter 3), only one relevant level of refinement is selected; namely the limit level of refinement. For the case study, the segment area is used as a single indicator metric for the imitation problem; whereas for the replication problem, the two centroids, the two principal second moments, and the perimeter are used.

---

[42] In the case study, see chapter 3, the two test statistics are defined as for the two-sample Kolmogorov-Smirnov test included in the function `kstest2` from the MATLAB® Statistics Toolbox.

[43] However, in a future definition of the imitation parameter it might be rational to consider it as a real number between zero and one.

In this annex details on the interpretation of domain and boundary discretization for wheat grains are given.

ANNEX 16.1   DOMAINS FOR WHEAT GRAINS

To illustrate the proposed discretization notation (see 2.1.4), four domain types: cluster, subcluster, species and subdomain, are specified for wheat grains and commented on from a Biosystems engineering perspective.

ANNEX 16.1.1   Cluster

Figure A. 22: Cluster with impurities

For wheat grains, a cluster is a constellation of species that are connected at contact zones only through friction, cohesion, or adhesion. The species of a cluster does not necessarily belong to the same genus. In general, such clusters contain impurities, i.e. proportions of species which do not belong to the same genus as the majority of species. Therefore, they are considered non-homogenous in general. Generically, a cluster represents the highest level in the discretization hierarchy.

In Biosystems engineering, the investigation of natural objects forming a cluster includes gravitational packing effects as well as the way in which biomasses are spread into the storage room. Mathematically, the configurations are considered stochastic of nature. Physically, the resulting packing matrix induces internal air channels. Therefore, the cluster can sometimes be considered as a *porous medium* and be treated like an entity. One important geometric porosity characteristic of such air channels is the tortuosity. The inclusion of tortuosity in the study of porous media was originally introduced by [M.A. Biot 1956]. Such tortuosity effects are clearly geometric in nature. Therefore, some of the geometric approaches presented here are relevant for a general study on tortuosity metrics. A more detailed study of tortuosity metrics is planned to be included in the research on acoustic based non-invasive measurement systems, which is currently under development by [O. Green 2010]. A recent non-invasive experiment [V. G. Totajada et al 2010] on soil properties also shows that acoustic measurement can be an inexpensive tool in soil-characterization.

Figure A. 23: A Subcluster without impurities

A *subcluster* Ω_Ψ is a constellation of a homogenous subset of species sampled from the same cluster, i.e. a subcluster is a sample without impurities which means that it models individual species that belong to the same genus only.

ANNEX 16.1.3   Species

Figure A. 24: Two wheat grain species

A *species* Ψ_Ω is a geometric model of a single natural object. Generically, species are children of sub clusters. Statistically, a species can often be seen as an element randomly taken from a subcluster. In Biosystems engineering, a species usually represents the geometric model of a biomass such as a grain of wheat, rice, maize or other seeds. However, it might just as well represent a grain from a soil sample or other natural objects.

ANNEX 16.1.4   Subdomains
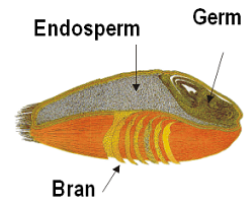
Figure A. 25: Three subdomain candidates of wheat grains

A *subdomain* Ω represents a characteristic part of a species. Generically, subdomains are *children* of species. Therefore, species are said to be discretized into subdomains. A subdomain is not a member of any special element group. At least one single subdomain must be specified in a natural parameterization model, i.e. subdomains represent the **master elements** of any 3D parameterization. Clusters, subclusters, and species are all super elements and formed as geometric super sets manifested as subdomains constellations.

In a multi-physics context, beyond the geometry modeling, the modeler must also assign *characteristic physical properties* for each of these subdomains. In Figure A.25 it is illustrated that for grains of wheat a coarse 3D discretization might include three subdomains namely: endosperm, germ, and bran.

Boundary primitives $\partial^p\Omega$, $p \in \{1,2,...,5\}$ set up the geometrical bounds for subdomains. The various boundary primitives are often called *geometric primitives*.

The boundary primitives are grouped as

- **derived primitives** *faces* and *edges*, see Figure A.26
- **core primitives**: *vector primitives*, see Figure A.27 and finally
- **hybrid primitives**: *Tortuosity poles* **VTNB** , see Figure A.27
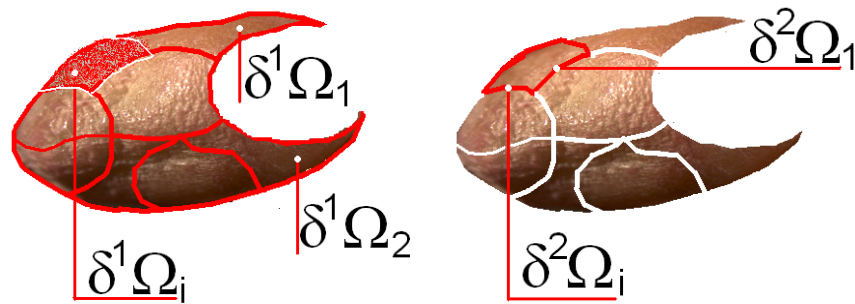
Figure A. 26: Faces and edges (Derived primitives)

ANNEX 16.2.1   Vector primitives
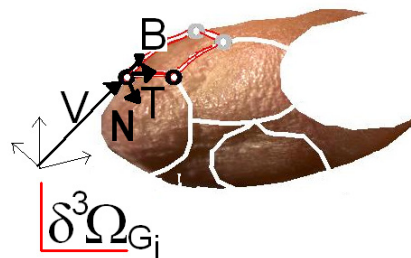
Figure A. 27: Vector primitives (left), Frenet frames (middle) & Master segment chords (right)

Vector primitives $\partial^3\Omega$ are third generation elements of subdomains. They are used to bind the *location* and *orientation* of edges.

Location vectors

Location vectors are *position vectors* and are symbolized by $\mathbf{r}_v$ and they designate vertices **V** , see Figure A.27.

Landmark vertices are characteristic vertices of natural objects, whereas bounding vertices are vertices defined on the edge of the bounding box for the object. Such vertices are always included in master meshes.

Orientation vectors

Orientation vectors are unit direction vectors. In natural parameterization, an orientation vector is always supposed to be one of the vectors from a Frenet triple **TNB**, see Figure A.27.

ANNEX 16.2.2   Scalar Primitives

The *generalized curvatures* $\partial^4\Omega$ represent the fourth generation scalar property of a subdomain. Generalized curvatures are of utmost importance for second order natural parameterization. Therefore, the concepts of Frenet orthogonalities, Frenet order transformation, and the Camille Jordan generalization (as already defined in the introduction) are essential for natural parameterization. Curvatures can also be estimated (see ANNEX 6.1 & ANNEX 6.2).

ANNEX 16.3   SEGMENTATION

Supplementary segmentation illustrations for wheat grain surfaces are given below.
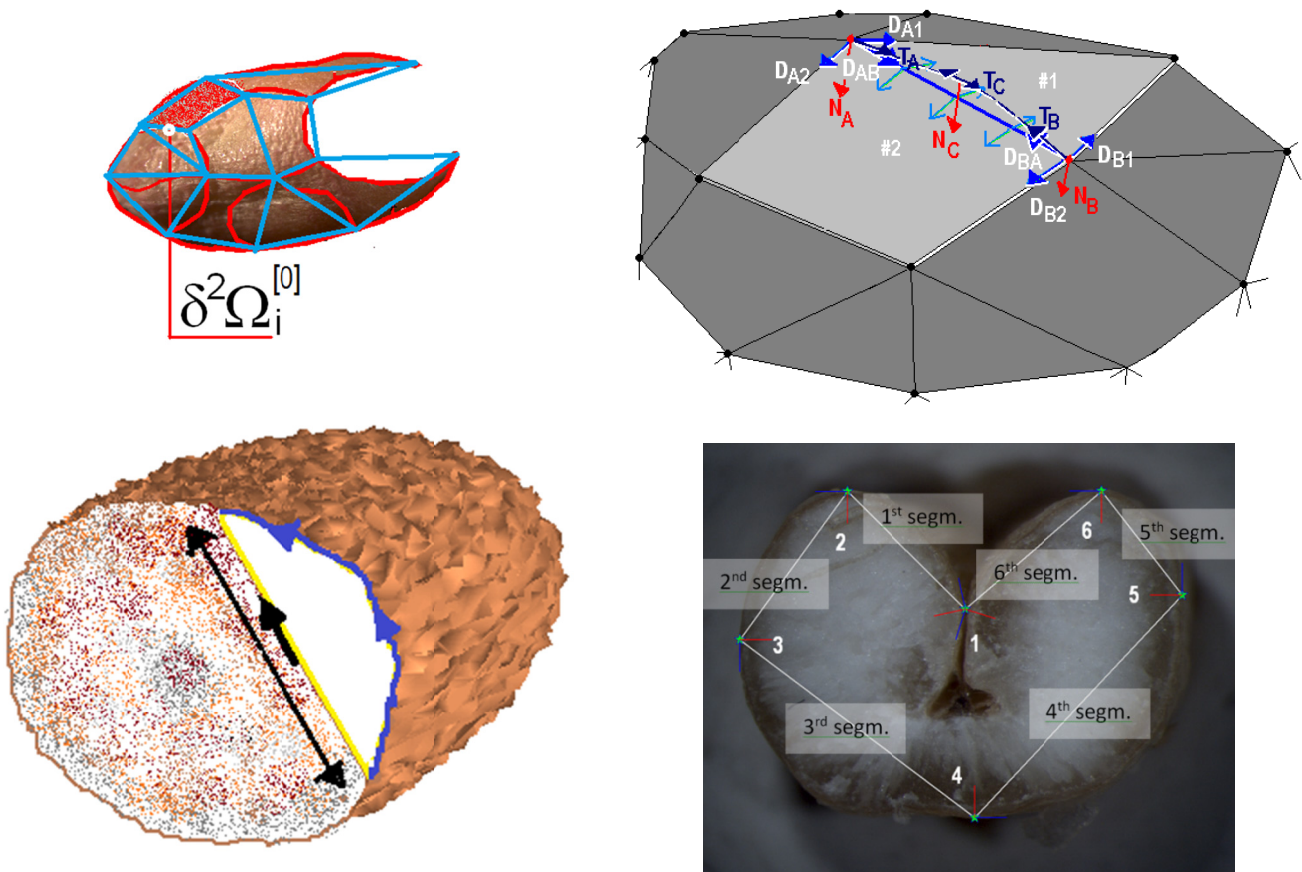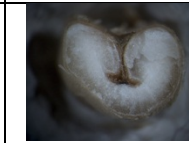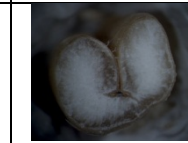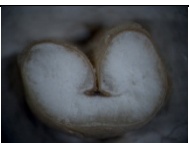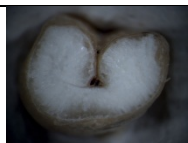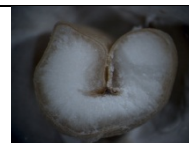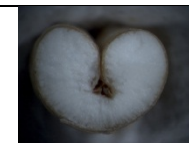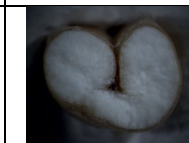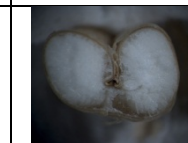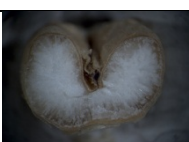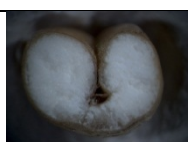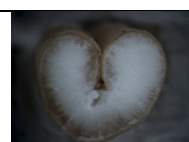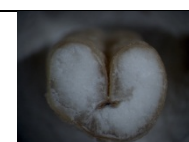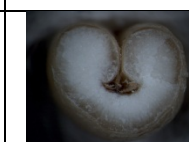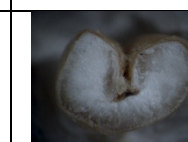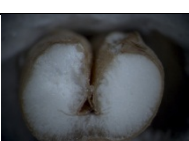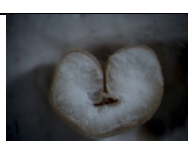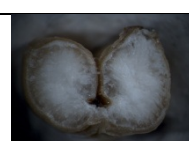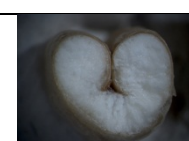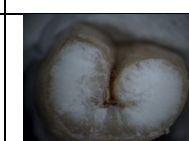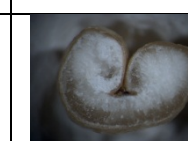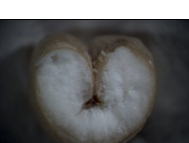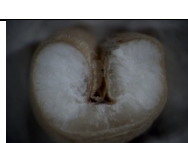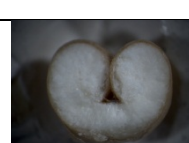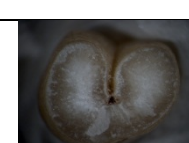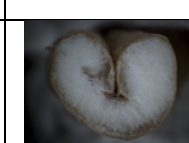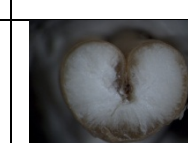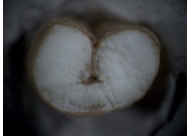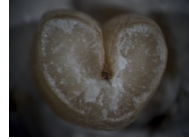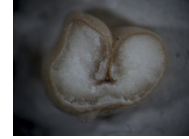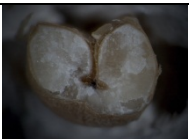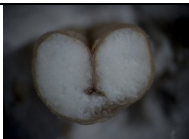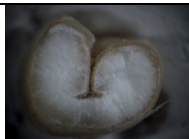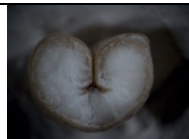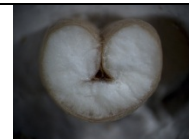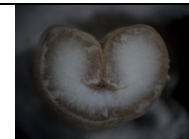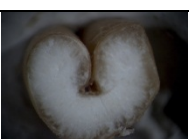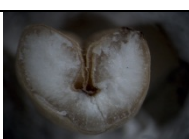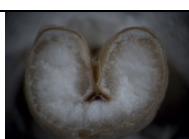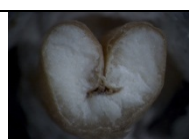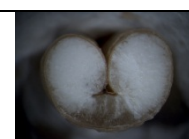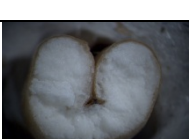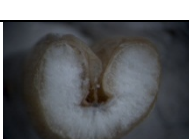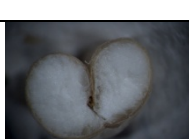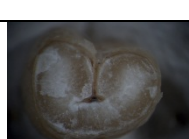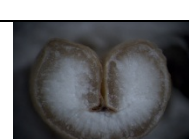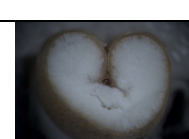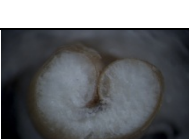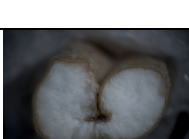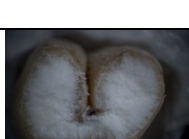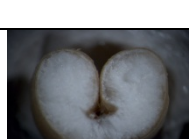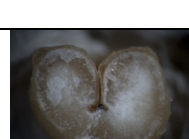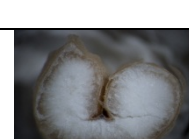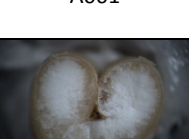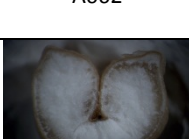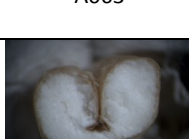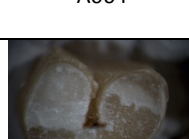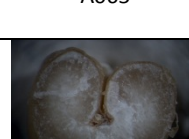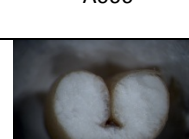
Figure A. 28: Segmentations of surfaces and cross-sections

234

Table 6.3: Stereo-microscopic images A001-A036

A001	A002	A003	A004	A005	A006
A007	A008	A009	A010	A011	A012
A013	A014	A015	A016	A017	A018
A019	A020	A021	A022	A023	A024
A025	A026	A027	A028	A029	A030
A031	A032	A033	A034	A035	A036
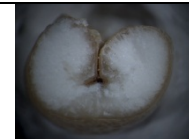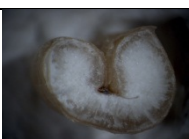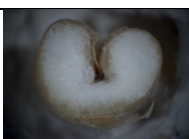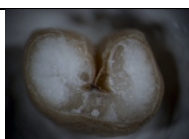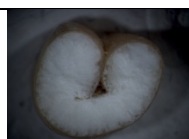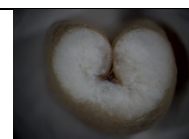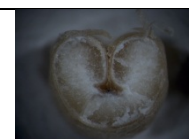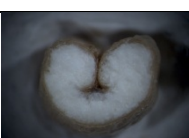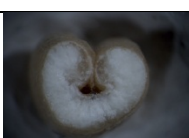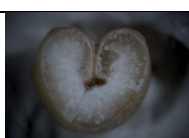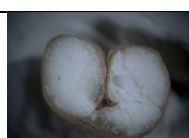
Table 6.4: Stereo-microscopic images A037-A072

A037	A038	A039	A040	A041	A042
A043	A044	A045	A046	A047	A048
A049	A050	A051	A052	A053	A054
A055	A056	A057	A058	A059	A060
A061	A062	A063	A064	A065	A066
A067	A068	A069	A070	A071	A072

Table 6.5: Stereo-microscopic images A073-A100

A073	A074	A075	A076	A077	A078
A079	A080	A081	A082	A083	A084
A085	A086	A087	A088	A089	A090
A091	A092	A093	A094	A095	A096
A097	A098	A099	A100		

A random collection of cross-sections captured with light and dark background is reproduced below.

Table 6.6: The Influence of the threshold level on the BW-separation
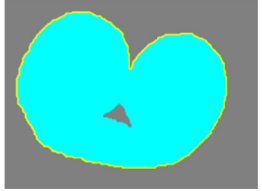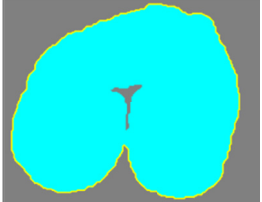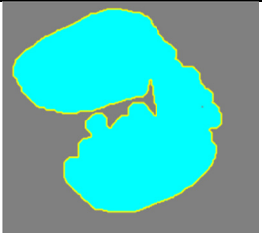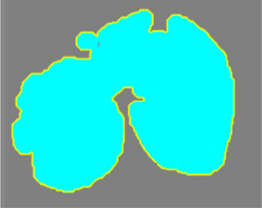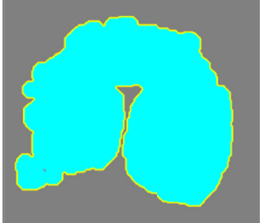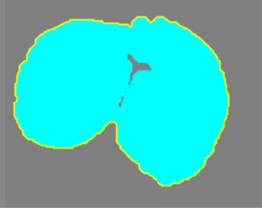
B072	B072_80	B072_100	B072_120	B072_140	B072_160
B055	B055_80	B055_100	B055_120	B055_140	B055_160
B012	B012_80	B012_100	B012_120	B012_140	B012_160
B075	B075_80	B075_100	B075_120	B075_140	B075_160
B068	B068_80	B068_100	B068_120	B068_140	B068_160
B044	B044_80	B044_100	B044_120	B044_140	B044_160

Table 6.7: Automatic Boundary Recognition. Threshold level: 100

B072	B072_100	
B055	B055_100	
B012	B012_100	
B075	B075_100	
B068	B068_100	
B044	B044_100	

Sample size: n_{obs} = 100
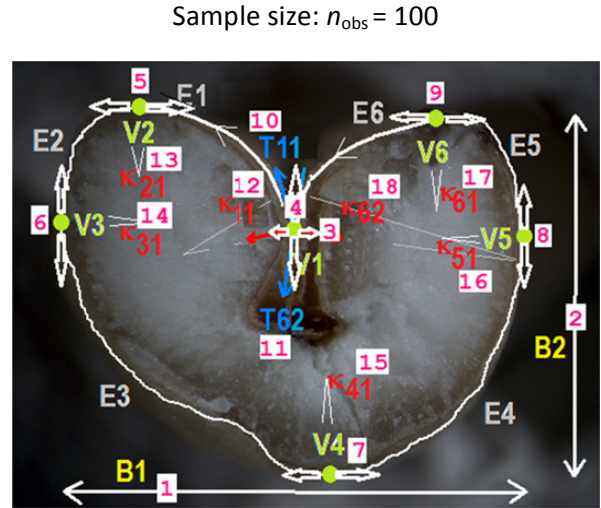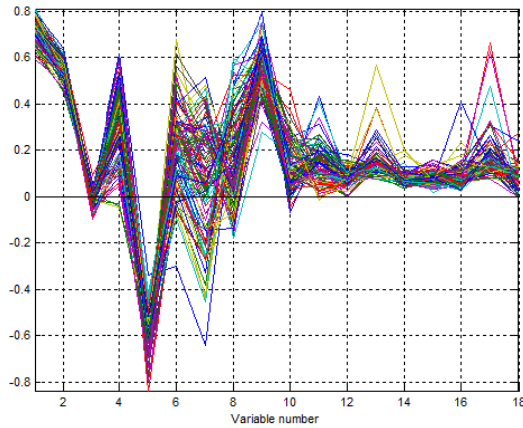
The raw data plot indicates that the biggest variations are found amongst the curvature factors K11...K62 (Variable numbers: 12-18). Also the "center bottom vertex", (Variable number 7) exhibit large variations.

Notations:

- 1 = First dir. (Local X).
- 2 = Second dir. (Local Y)
- B = Boundings (1, DIR).
- V = Vertices are identified by (IDX, DIR). IDX = vertex No.
- T = Tangents are identified by (IDX, DIR). IDX = segment No.
- K = Curvatures are identified by (IDX, DIR). IDX = segment No.
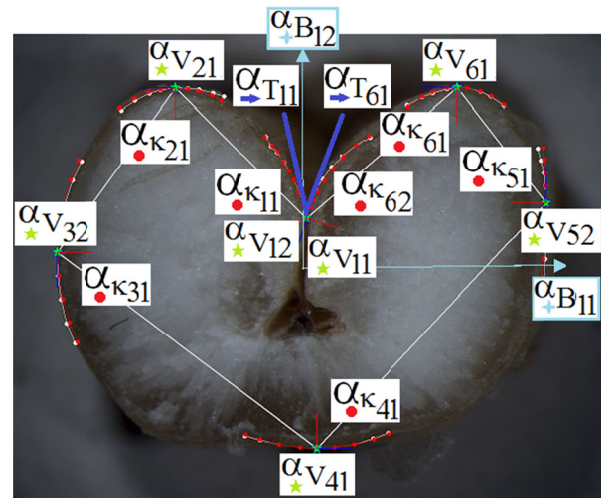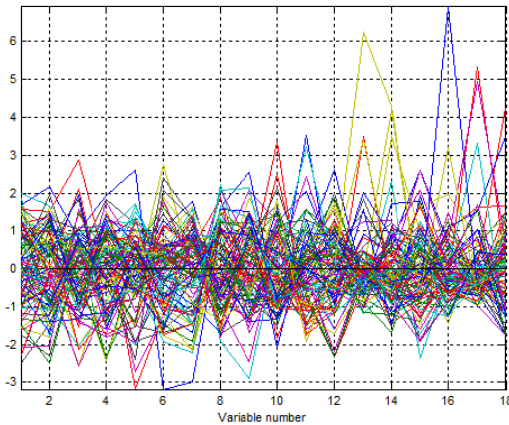
After autoscaling the curvatures (Variable number 12-18) still show the largest variations.

Notations

- α = auto scaled factor
- Local directions:
- (1) = First dir. (Local X)
- (2) = Second dir. (Local Y)
- B = Bounding dimension factors are normalized (1, DIR).
- V = Vertices are identified by (IDX, DIR). IDX = vertex No.
- T = Tangents are identified by (IDX, DIR). IDX = segm. No.
- K = Curvatures are identified by (IDX, DIR). IDX = segm. No.

ANNEX 22   DETECTION OF INCONSISTENT MASTER DATA FOR COMPARISON OF FIRST INTEGRALS

ANNEX 22.1   INCONSISTENT DATA

The location of deviating objects will mainly be based on the inspection of the multivariate *influence plot,* which combines the *residual of variance plot* and the *Hotellings T^2 plot* within the PCA.

ANNEX 22.1.1   *Detection of Outliers from PCA*

The first PCA model was developed from the raw data and all variables which where organized as a 100-by-18 data matrix. Outliers were detected from a successive ranking of inconsistent data. A total of three outliers were detected during the following three-step elimination process.

Sample size: n_{obs}=100

PCA plots
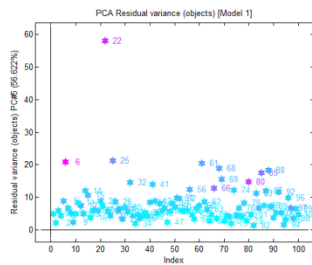
 Residual Varaiance Plot	• PC#1: **006** **022** **080** (066) (085) • PC#2: **006** **022** **080** (066) (085) (025) (097) • PC#3: **022** **006** **085** (097) (066) • PC#4: **022** **006** **085** (061) (025) • PC#5: **022** **006** 025 (061) (068) • PC#6: **022** 025 061 **(088) (085)** Inconsistent data ranking: • **022** **006** (085) (080)
 Hotellings T^2 Plot	• PC#1: 042 018 043 (050) (040) • PC#2: **006** **080** 013 (042) (040) (043) • PC#3: **080** **006** 066 (027) (029) • PC#4: **080** **006** 066 (027) (097) • PC#5: **006** **080** 066 (085) (097) • PC#6: **006** 080 022 (066) (085) Inconsistent data ranking: • **006** **080** (066) (085) (022)
 Influence Plot	• PC#1: **006** **080** 085 (066) (022) • PC#2: **006** **080** 085 (022) (066) (025) • PC#3: **006** **080** 022 (066) (085) • PC#4: **006** **080** 022 (066) (085) • PC#5: **006** **022** 080 (085) (066) • PC#6: **006** 022 080 (085) (025) Inconsistent data ranking: • **006 080 (022) (085) (080)**
	Conclusion: Data point A006 is found inconsistent.
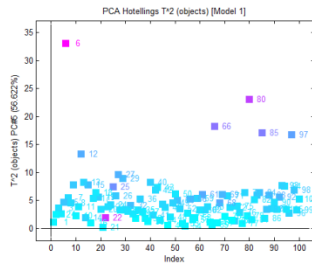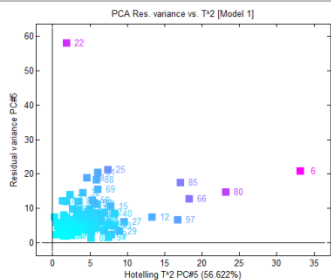
	Step 2	Step 3:
Step 2 and step 3 reported to the right are performed in the same way as step 1 above.	**Model 2** was created by recalculating model 1 without: A006. Its influence plot indicated the following inconsistent data.	**Model 3** was created by recalculating model 1 without: A006 and A080. Its influence plot indicated the following inconsistent data:
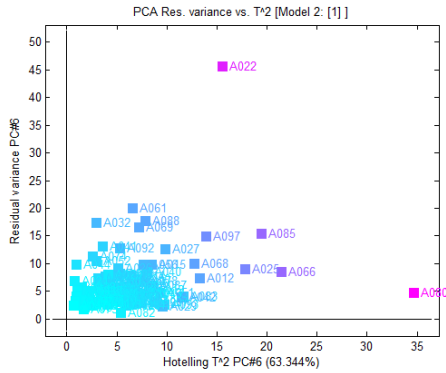
PCA Res. variance vs. T^2 [Model 2: [1]]

• PC#1: (.) • PC#2: **080** • PC#3: **080** 022 • PC#4: **080** 022 • PC#5: **080** 022 • PC#6: **080** 022 Inconsistent data point: • **080**	• PC#1: **022** (27) • PC#2: **022** (085) (066) • PC#3: **022** 066 (085) • PC#4: **022** (066) (085) • PC#5: **022** (085) (066) • PC#6: **022** (085) (066) Inconsistent data point: • **022**

Conclusive remarks

Model 4 was created by recalculating model 1 without: A006, A080 and A022. No more inconsistent data points were found.

Since a minimum of three cross-sections in the sample possess significant curvatures, second order Frenet subdivision with at least F_N extrapolation is required in the case study.

The full correlation matrix for the eighteen master parameters is reproduced below. In general, it is seen that the master parameters are very weakly correlated indeed. This gives reason to believe that the selected set of master parameters can be perceived as generalized coordinates, which may be non-linear dependent but un-correlated.

Table 6.8: Correlation Matrix for the Master Parameters

	1	2	3	4	5	6	7	8	9	10	11	12	13	14	15	16	17	18
1	1.0000	0.5018	-0.0293	-0.2600	-0.1142	-0.1891	0.0224	-0.2160	0.1259	0.0025	-0.0193	-0.1261	0.2066	0.1144	-0.0035	0.0555	0.1918	0.0031
2	0.5018	1.0000	-0.0904	0.0617	-0.1035	-0.1440	0.0633	-0.0196	-0.0783	0.0076	-0.0004	0.0112	0.2982	-0.1935	0.0369	0.0355	0.1733	-0.0252
3	-0.0293	-0.0904	1.0000	0.0789	0.2189	0.1467	0.3230	-0.1702	0.1372	0.0317	0.1685	0.0971	-0.1345	0.2011	-0.0019	-0.1029	0.3111	-0.1704
4	-0.2600	0.0617	0.0789	1.0000	0.1776	0.0775	0.0568	0.0389	-0.2885	0.2379	0.2338	0.6576	-0.0950	-0.0381	-0.1287	-0.0047	-0.0977	0.6039
5	-0.1142	-0.1035	0.2189	0.1776	1.0000	-0.0885	-0.3316	0.0589	-0.1265	-0.1053	0.1290	0.0368	-0.2970	0.0102	-0.0042	-0.0164	-0.1003	-0.0415
6	-0.1891	-0.1440	0.1467	0.0775	-0.0885	1.0000	0.5454	-0.3405	0.2036	0.1682	-0.1592	0.0492	-0.1790	0.1954	-0.0781	0.0028	0.0398	0.0505
7	0.0224	0.0633	0.3230	0.0568	-0.3316	0.5454	1.0000	-0.5501	-0.1223	0.1377	0.0089	0.0617	-0.1312	0.0880	-0.1579	-0.1114	0.2476	0.0205
8	-0.2160	-0.0196	-0.1702	0.0389	0.0589	-0.3405	-0.5501	1.0000	0.1989	-0.1062	0.0806	0.0022	0.0079	-0.2179	0.1437	-0.2260	-0.3144	-0.0528
9	0.1259	-0.0783	0.1372	-0.2885	-0.1265	0.2036	-0.1223	0.1989	1.0000	-0.1271	0.0988	-0.1424	0.0123	0.0849	0.1148	-0.0281	0.1576	-0.0570
10	0.0025	0.0076	0.0317	0.2379	-0.1053	0.1682	0.1377	-0.1062	-0.1271	1.0000	-0.2324	-0.4314	0.2115	0.1418	-0.1275	-0.0229	-0.0132	0.4237
11	-0.0193	-0.0004	0.1685	0.2338	0.1290	-0.1592	0.0089	0.0806	0.0988	-0.2324	1.0000	0.3518	-0.2928	-0.1980	0.1050	-0.0809	0.1155	-0.2596
12	-0.1261	0.0112	0.0971	0.6576	0.0368	0.0492	0.0617	0.0022	-0.1424	-0.4314	0.3518	1.0000	-0.1156	-0.0703	-0.1199	-0.0193	-0.0300	0.2591
13	0.2066	0.2982	-0.1345	-0.0950	-0.2970	-0.1790	-0.1312	0.0079	0.0123	0.2115	-0.2928	-0.1156	1.0000	0.2194	-0.0328	0.2441	0.0484	0.1344
14	0.1144	-0.1935	0.2011	-0.0381	0.0102	0.1954	0.0880	-0.2179	0.0849	0.1418	-0.1980	-0.0703	0.2194	1.0000	0.0058	0.1527	0.0084	0.0495
15	-0.0035	0.0369	-0.0019	-0.1287	-0.0042	-0.0781	-0.1579	0.1437	0.1148	-0.1275	0.1050	-0.1199	-0.0328	0.0058	1.0000	-0.0073	0.0576	-0.1742
16	0.0555	0.0355	-0.1029	-0.0047	-0.0164	0.0028	-0.1114	-0.2260	-0.0281	-0.0229	-0.0809	-0.0193	0.2441	0.1527	-0.0073	1.0000	0.0533	0.0187
17	0.1918	0.1733	0.3111	-0.0977	-0.1003	0.0398	0.2476	-0.3144	0.1576	-0.0132	0.1155	-0.0300	0.0484	0.0084	0.0576	0.0533	1.0000	-0.0154
18	0.0031	-0.0252	-0.1704	0.6039	-0.0415	0.0505	0.0205	-0.0528	-0.0570	0.4237	-0.2596	0.2591	0.1344	0.0495	-0.1742	0.0187	-0.0154	1.0000
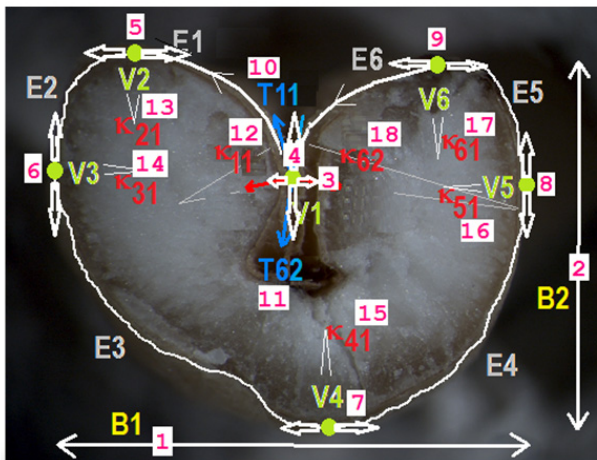
Figure A. 29: Master parameters.

(Repeated here for convenience)

It appears from the correlation matrix that the biggest Pearson product-moment correlation coefficient ($\rho=0.66$) (marked by the red boxes) appears for the pair of parameters represented by the location vertex (No 4) and the bow-line tangent (No 11). However, this value only indicates a relatively weak correlation. At the same time the mutual correlation ($\rho< 0.25$) (marked by the blue boxes) between the tangents (No 10 and No 18) is very weak indeed. This indicates that the "bow-line" does not reflect tangential symmetry.

7 REFERENCES

7.1 LITTERATURE

Ahmadi, H., Mollazade, K., Khorshidi, J., Mohtasebi, S. S., & Rajabipour, A. (2009). Some physical and mechanical properties of fennel seed (*Foeniculum vulgare*). *Journal of Agricultural Science, 1,* 66-75.

Akhavan, A., Shafaatian, S., & Rajabipour, F. (2012). Quantifying the effects of crack width, tortuosity, and roughness on water permeability of cracked mortars. *Cement and Concrete Research, 42,* 313-320.

Allen, B., Curless, B., & Popovic, Z. (2003). The space of human body shapes: reconstruction and parameterization from range scans. In (pp. 587-594). ACM New York, NY, USA.

Amaral, A. L., Rocha, O., Goncalves, C., Ferreira, A. A., & Ferreira, E. C. (2009). Application of image analysis to the prediction of EBC barley kernel weight distribution. *Industrial Crops and Products, 30,* 366-371.

ANSI/ASAE S319.3 (1997). *Method of determining and expressing fineness of feed materials by sieving, ANSI/ASAE S319.3 JUL97*.

Anza, J. J. & Esteves, M. A. (2011). Fluid Structure Interaction Applied to Upper Aorta Blood Flow. In Excerpt from the Proceedings of the 2011 COMSOL Conference in Stuttgart.

Armesto-Gonzales, J., Riveiro-Rodríguez, B., & Riva-Brea, M. T. (2010). Terrestrial laser scanning intensity data applied to damage detection for historical buildings. *Journal of Archaeological Science, 37,* 3037-3047.

Ashbaugh, M. & Benguria, R. (2010). The problem of Queen Dido, an overview of the subject of isoperimetry. In *International Conference on the Isoperimetric Problem of Queen Dido and its Mathematical Ramifications* Carthage, Tunisia.

Baddeley, A. (2010). Analysing spatial point patterns in R - Workshop notes. In CSIRO.

Baek, SY. & Lee, K. (2012). Parametric human body shape modeling framework for human-centered product design. *Computer-Aided Design, 44,* 56-67.

Barnhill, R. E. (1974). Smooth interpolation over triangles. *Computer Aided Geometric Design,* 45-70.

Barnsley, M. F. (1988). *Fractals Everywhere*. Academic Press.

Barnsley, M. F., Devaney, R. L., Mandelbrot, B. B., Peitgen, H. O., Saupe, D., & Voss, R. F. (1988). *The Science of Fractal Images*. New York Berlin Heidelberg London Paris Tokyo: Springer-Verlag.

Baroncini, M. (2012). MRI atlas of the human hypothalamus. *NeuroImage, 59,* 168-180.

Barone, S., Paoli, A., & Razionale, A. V. (2012). Shape measurement by a multi-view methodology based on the remote tracking of a 3D optical scanner . *Optics and Lasers in Engineering, 50,* 380-390.

Bathe, K. J. (1982). *Finite element procedures in engineering analysis*. Englewoods Cliffs, NJ: Prentice Hall.

Benamar, A., Ahfir, N.-D., Wang, H., & Alem, A. (2007). Particle transport in a saturated porous medium. *Comptes Rendus Geoscience, 39,* 674-681.

Biot, M. A. (1956a). Theory of Propagation of Elastic Waves in A Fluid-Saturated Porous Solid .1. Low-Frequency Range. *Journal of the Acoustical Society of America, 28,* 168-178.

Biot, M. A. (1956b). Theory of Propagation of Elastic Waves in A Fluid-Saturated Porous Solid .2. Higher Frequency Range. *Journal of the Acoustical Society of America, 28,* 179-191.

Blanz, V. & Vetter, T. (1999). A Morphable Model For The Synthesis Of 3D Faces. In (pp. 187-194).

Bloomenthal, J. (1998). Polygonization of implicit surfaces. *Computer Aided Geometric Design, 5,* 341-355.

Brown, R. A. & Lewis, J. M. (2005). PATH TO NEXRAD: Doppler Radar Development at the National Severe Storms Laboratory. *Bulletin of the American Meteorological Society, 86,* 1459-1470.

Bullitt, E., Gerig, G., Pizer, S. M., Lin, W. L., & Aylward, S. R. (2003). Measuring tortuosity of the intracerebral vasculature from MRA images. *Ieee Transactions on Medical Imaging, 22,* 1163-1171.

CAESER. (22-4-2012). Civilian American and European Surface Anthropometry Resource (CAESAR) web site. URL: http://www.hec.afrl.af.mil/cardlab/CAESAR/index.html - located 22-04-2012.

Caslon Analytics - biometrics. (2012). Landmarks.

Catmull, E. & Clark, J. (1978). Recursively Generated B-Spline Surfaces on Arbitrary Topological Meshes. *Computer-Aided Design, 10,* 350-355.

Cham, J. CW., Beckers, P., Spanhove, T., & Borre, J. V. (2012). An evaluation of ensemble classifiers for mapping Natura 2000 heathland in Belgium using spaceborne angular hyperspectral (CHRIS/Proba) imagery . *International Journal of Applied Earth Observation and Geoinformation, 18,* 13-22.

Coskun, M. B., Yalcin, I., & Ozarslan, C. (2006). Physical properties of sweet corn seed (Zea mays saccharata Sturt.). *Journal of Food Engineering, 74,* 523-528.

Courant, R. L. (2007, April 1). The finite-element method, Part I. *Antennas and Propagation Magazine, IEEE, Historical Corner, 49,* 180-182.

CRD-C 104-80. (1-3-1980). Method of Calculation of The Fineness Modulus of Aggregate, CRD-C 104-80.
Dacorogna, B. (2004). *Introduction to the calculus of variations*. Imperial College Press.

Deng, C. & Ma, W. (2012). Weighted progressive interpolation of Loop subdivision surfaces. *Computer-Aided Design, 44,* 424-431.

Dixon, A. R., Kirby, G. H., & Wills, D. P. M. (1994). A Data Structure for Artificial Terrain Generation. *Computer Graphics Forum, 13,* 37-47.

Dodson, M. M. & Kristensen, S. (2004). Hausdorff dimension and Diophantine approximation. *Proceedings of Symposia in Pure Mathematics, 71.*

Doo, D. & Sabin, M. (1978). Behavior of Recursive Division Surfaces Near Extraordinary Points. *Computer-Aided Design, 10,* 356-360.

Dyn, N., Levin, D., & Micchelli, C. A. (1990). Using parameters to increase smoothness of curves and surfaces generated by subdivision. *Computer-Aided Design, 7,* 129-140.

Edwards, G. & Brøchner, T. (2011). A method for smoothed headland paths generation for agricultural vehicles. In *CIGR/NJF seminar 441 – Automation and system technology in plant production*.

Entis, J. J., Barrett, L. F., & Dickerson, B. C. (2012). A reliable protocol for the manual segmentation of the human amygdala and its subregions using ultra-high resolution MRI. *NeuroImage, 60,* 1226-1235.

FAOSTAT. (2010). URL: www.faostat.fao.org.   Food and Agriculture Organization of the United Nations (FAO).
Fathi, H. & Brilakis, I. (2011). Automated sparse 3D point cloud generation of infrastructure using its distinctive visual features. *Advanced Engineering Informatics, 25,* 760-770.

Feragen, A., Hauberg, S., Nielsen, M., & Lauze, F. B. (2011). Means in spaces of tree-like shapes. In *International Conference of Computer Vision* (pp. 736-746).

Féralégil-Durmus, E., Sýkorová, A., Šárka, E., Bubník, Z., Schejbal, M., & Príhoda, J. (2010). Geometric parameters of wheat grain determined by image analysis and FEM approach. *Cereal Research Communications, 38,* 122-133.

Fourie, Z., Damstra, J., Schepers, R. H., Gerrits, P. O., & en, Y. (2012). Segmentation process significantly influences the accuracy of 3D surface models derived from cone beam computed tomography. *European Journal of Radiology, 81,* e524-e530.

François, C. J., Srinivasan, S., Schiebler, M. L., Reeder, S. B., Niespodzany, E., Landgraf, B. R. et al. (2012). 4D cardiovascular magnetic resonance velocity mapping of alterations of right heart flow patterns and main pulmonary artery hemodynamics in tetralogy of Fallot. *Journal of Cardiovascular Magnetic Resonance, [PubMed - in process]*.

Gálvez, A., Iglesias, A., & Puig-Pey, J. (2012). Iterative two-step genetic-algorithm-based method for efficient polynomial B-spline surface reconstruction. *Information Sciences, 182,* 56-76.

Gasso-Tortaja, V., Ward, A. J., Mansur, H., Brøchner, T., Sørensen, C. G., & Green, O. (2010). A novel acoustic sensor approach to classify seeds based on sound absorption spectra. *Sensors, 10,* 10027-10039.

Gasso-Tortajada, V., Dubasaru, V., Rojas, C., Brøchner, T., & Green, O. (2010). The potentials of a novel acoustic sensor approach for determining soil texture and structure. In NJF seminar 438: Sensors for soil and plant mapping and terrain analysis. Vol. 6 NJF, 2010. (pp. 53-55).

Gheno, R., Nectoux, E., & Herbaux, B. (2012). Three-dimensional measurement of the lower extremity in children and adolescents using a low-dose biplanar X-ray device. *EUROPEAN RADIOLOGY, 22,* 765-771.

Ghommam, J., Mnif, F., Benali, A., & Derbel, N. (2009). Nonsingular Serret-Frenet Based Path Following Control for an Underactuated Surface Vessel. *Journal of Dynamic Systems Measurement and Control-Transactions of the Asme, 131*.

Goldman, R. (2004). The Fractal Nature of Bezier Curves. In (pp. 3-11). GMP.

Gommes, C. J., Bons, A.-J., Blacher, S., Dunsmuir, J. H., & Tsou, A. T. (2009). Practical Methods for Measuring the Tortuosity of Porous Materials from Binary or Gray Tone Tomographic Reconstructions. *AIChE Journal, 55,* 2000-2012.

Gonzales, R. C., Woods, R. E., & Eddins, S. L. (2009). *Digital Image Processing Using MATLAB*. (vols. Second Ed.) McGraww-Hill Publishing Company.

Gonzáles-Jorge, H., Gonzales-Aquilera, P., Rodriguez-Gonzalvez, P., & Arias, P. (2012). Monitoring biological crusts in civil engineering structures using intensity data from terrestrial laser scanners. *Construction and Building Materials, 31,* 119-128.

Gouaty, G. (2009). *Modélisation géométrique itérative sous contraintes.* PhD Thesis EPFL, Lausanne, Switzerland.

Goyal, M. M. S., Piya, C., Benjamin, W., Liu, M., & Ramani, K. (2012). Towards locally and globally shape-aware reverse 3D modeling. *Computer-Aided Design, 44,* 537-553.

Grisan, E., Foracchia, M., & Ruggeri, A. (2003). A novel method for the automatic evaluation of retinal vessel tortuosity. In (pp. 866-869). Engineering in Medicine and Biology Society, 2003. Proceedings of the 25th Annual International Conference of the IEEE.

Grisan, E., Foracchia, M., & Ruggeri, A. (2008). A novel method for the automatic grading of retinal vessel tortuosity. *Ieee Transactions on Medical Imaging, 27,* 310-319.

Guérin, E., Tosan, E., & Baskurt, A. (2001). Fractal Approximation of surfaces based on projected IFS attractors. In *EUROGRAPHICS 2001*.

Hameiri E, S. I. (2003). Estimating the principal curvatures and the Darboux frame from real 3-D range data. *IEEE Transactions on Systems, Man, and Cybernetics, Part B: Cybernetics*.

Hart, J. V., Goldbaum, M., Cote, B., Kube, P., & Nelson, M. (1997). Automated measurement of retinal vascular tortuosity. *Journal of American Medical Informatics Association, Supplement: S,* 459-463.

Healtheephan, A. S. (2010). Study on Structural Behaviour of Human Vertebral Column Using Staad.Pro. *INTERNATIONAL JOURNAL OF CIVIL AND STRUCTURAL ENGINEERING, 1,* 1-12.

Heneghan, C., Flynn, J., O'Keefe, M., & Cahill, M. (2002). Characterization of changes in blood vessel width and tortuosity in retinopathy of prematurity using image analysis. *Medical Image Analysis, 6,* 407-429.

Heumann, H. & Wittum, G. (2009). The Tree-Edit-Distance, a Measure for Quantifying Neuronal Morphology. *Neuroinformatics, 7,* 179-190.

Holland, J. H. (1992). *Adaptation in Natural and Artificial Systems: An Introductory Analysis with Applications to Biology, Control, and Artificial Intelligence*. MIT Press Cammbridge, MA, USA.

Hwang, T. G., Dog, D. H., & Okamoto, K. (2005). 4D-PTV Measurement of an Impinged Jet with a Dynamic 3D-PTV. *Journal of Visualization, 8,* 245-252.

ISO 8000-2 (2009). *Mathematical signs and symbols to be used in the natural sciences and technology* ISO, IEC.

Jaboyedoff, M., pikofer, T., Abellán, A., Derron, M.-H., Loye, A., Metzger, R. et al. (2012). Use of LIDAR in landslide investigations: a review. *Natural hazards, 61,* 5-28.

Kirkpatrick, L. A. & Weishampel, J. F. (2005). Quantifying spatial structure of volumetric neutral models. *Ecological Modelling, 186,* 312-325.

Klett, R. & Zunic, J. (2012). ADR shape descriptor - Distance between shape centroids versus shape diameter. *Computer Vision and Image Understanding, 116,* 690-697.

Koch, B. (2010). Status and future of laser scanning, synthetic aperture radar and hyperspectral remote sensing data for forest biomass assessment. *ISPRS Journal of Photogrammetry and Remote Sensing, 65,* 581-590.

Koenderink, J. J. & J van Doom, A. (2003). Surface shape and curvature scales. *Image and Vision Computing, 10,* 557-564.

Kotoyori, Y., Yokoo, N., Ito, K., Murase, H., Sato, F., & Nambo, Y. (2012). Three-dimensional ultrasound imaging of the equine fetus. *Theriogenology, 77,* 1480-1486.

Kou, JL., Tang, XM., Zhang, HY., Lu, HJ., Wu, FM., Xu, YS. et al. (2012). Tortuosity for streamlines in porous media. *CHINESE PHYSICS B, 21*.

Kroese Dirk, P. (2011). *Handbook of Monte Carlo Methods*. John Wiley & Sons.

Kwon, Y. W. & Bang, H. (2000). *The finite element method using MATLAB*. (2nd ed.) Washington D.C.: CRC Press.

Lamon, J. (2009). Stochastic approach to multiple cracking in composite systems based on the extreme-values theory. *Composites Science and Technology, 69,* 1607-1614.

Lane, J. M. & Riesenfeld, R. F. (1977). *The application of total positivity to computer aided curve and surface design* Salt Lake City, Utah: Technical Report, Dept. of Computer Science, University of Utah.

Langner, J. (18-4-2006). Leaves Recognition v1.0. Neural Network based recognition system of leaf images.   LightSpeed Communications Gbr, Dresden, Germany.

Lazutkin, D., Harkara, A., & Husar, P. (2010). Magnetic Stimulation of the Human Brain with Low-Intensity Field. In Excerpt from the Proceedings of the COMSOL Conference 2010 Paris.

Lee, C., Lodwicj, D., Hurtado, J., Pafundi, D., Williams, J. L., & Bolch, W. E. (2010). The UF Family of Reference Hybrid Phantoms for Computational Radiation Dosimetry. *Physicis in Medicine and Biology, 55,* 339-363.

Lee, WJ., Wilkinson, C. M., & Hwang, HS. (2012). An Accuracy Assessment of Forensic Computerized Facial Reconstruction Employing Cone-Beam Computed Tomography from Live Subjects. *Journal of Forensic Sciences, 57,* 318-327.

Li, Y. & Zhong, Y. (2012). Automatic detecting anthropometric landmarks based on spin image. *Textile Research Journal, 82(6),* 622-632.

Lin, KY., Huang, CY., Lai, JY., Tsai, YC., & Ueng, WD. (2012). Automatic reconstruction of B-spline surfaces with constrained boundaries. *Computers & Industrial Engineering, 62,* 226-244.

Lund, K. O. (2009). A Moisture Transfer Model for Drying of Grain. In Excerpt from the Proceedings of the COMSOL Conference 2009 Boston.

Mandelbrot, B. B. (1983). *The Fractal Geometry of Nature*. (3rd ed.) Freeman.

Massey, F. J. (1951). The Kolmogorov-Smirnov Test for Goodness of Fit. *Journal of the American Statistical Association, 46,* 68-78.

Mohsenin, N. N. (1970). *Physical properties of plant and animal materials*. New York: Gordon and Breach Science Publishers.

Moldrup, P., Olesen, T., Komatsu, T., Schjønning, P., & Rolston, D. E. (2001). Tortuosity, Diffusivity, and Permeability in the Soil Liquid and Gaseous Phases. *Soil Science Society of America Journal, 65,* 613-623.

Monga, O., bousso, M., Garnier, P., & Pot, V. (2009). Using pore space 3D geometrical modelling to simulate biological activity: Impact of soil structure . *Computers & Geosciences, 35,* 1789-1801.

Moran, K., Pezoa, S., Fairall, C., Williams, C., Ayers, T. E., Brewer, A. et al. (2012). A Motion-Stabilized W-Band Radar for Shipboard Observations of Marine Boundary Layer Clouds. *Boundary-Layer Meteorology, 143,* 3-24.

Morsdorf, F., Mårell, A., Koetz, B., Cassagne, N., Pimont, F., Rigolot, E. et al. (2010). Discrimination of vegetation strata in a multi-layered Mediterranean forest ecosystem using height and intensity information derived from airborne laser scanning. *Sensors, 114,* 1403-1415.

Morse, D. R., Lawton, J. H., Dodson, M. M., & Williamson, M. H. (1985). Fractal Dimension of Vegetation and the Distribution of Arthropod Body Lengths. *Nature, 314,* 731-733.

Newmark, N. M. (1959). A method of computation for structural dynamics. *Engineering Mechanics Division, 85,* 67-94.

Ngom, N. F., Monga, O., Mohammed, M. M. O., & Garnier, P. (2011). 3D shape extraction segmentation and representation of soil microstructures. *Computers & Geosciences, 39,* 50-63.

Novelline, R. A. & Squire, L. F. (2004). *Squire's fundamentals of radiology*. Cambridge, Mass. : Harvard University Press.

O'Neil, B. (1997). *Elementary differential geometry*. Academic Press.

Osher, S. & Fedkiw, R. P. (2003). Level set methods and dynamic implicit surfaces. *Applied Mathematical Sciences, 153*.

Ottosen, N. S. & Petersson, H. (1992). *Introduction to the finite element method*. Prentice Hall.

Overveld, C. W. A. M. v. (1990). Family of recursively defined curves, related to the cubic Bézier curve. *Computer-Aided Design, 22,* 591-597.

Pan, R. & Skala, V. (2012). Surface reconstruction with higher-order smoothness. *The Visual Computer, 28,* 155-162.

Pavsic, M. (1974). External Inversion, Internal Inversion and Reflection Invariance. *Int.Journal Theoretical Physics, 9,* 229-224.

Peitgen, H. O. & Richter, P. (1986). *The Beauty of Fractals*. New York Berlin Heidelberg London Paris Tokyo: Springer-Verlag.

Peters, J. & Reif, U. (2008). *Subdivision Surfaces*. Berlin Heidelberg: Springer-Verlag.

Peters, J. & Reif, U. (1997). The simplest subdivision schema for smoothing polyedra. *Transactions on Graphics, 16,* 420-431.

Petrie, G. & Toth, CK. (2008). Chapter 3. Terrestrial Laser Scanners, Topographic Laser Ranging and Scanning. In (CRC Press.

Poli, D. & Toutin, T. (2012). Review of developments in geometric modelling for high resolution sattelite pushbroom sensors. *The Photogrammetric Record, 27(137),* 58-73.

Polo, J. R. R., Sanz, R., & Llorens, J. U. (2009). A tractor-mounted scanning LIDAR for the non-destructive measurement of vegetative volume and surface area of tree-row plantations: A comparison with conventional destructive measurements. *Biosystems Engineering,* 128-134.

Ponomareva, A. A. & Polygalova, O. O. (2012). Changes in Mitochondrial Shape in Wheat Root Cells Exposed to Mitochondrial Poisons. *Russian Journal of Plant Physiology, 59,* 466-471.

Pryor, R. W. (2011). *Multiphysics Modeling using COMSOL*. Jones and Bartlett Publishers, LLC.

Ratha, N. K. & Govindaraju, V. (2008). *Advances in biometrics: sensors, algorithms and systems*. London: Springer.

Rojas, A. (1996). Neural Networks. Chapter 7: The Backpropagation Algorithm. In (Springer-Verlag, Berlin, 1996.

Rosell, J. R., llorens, J. U., Sanz, R., Arnó, J., Ribes-Dasi, M., Masip, J. et al. (2009). Obtaining the three-dimensional structure of tree orchards from remote 2D terrestrial LIDAR scanning. *Agricultural and Forest Meteorology*.

Salandin, A. (2004). *Contribución al diseño de elementos absorbentes para el control del tiempo de reverberación.* PhD Thesis Editorial de la Universidad Politècnica de València, Valencia Spain**.**

Saltelli, A. (2009). *Sensitivity Analysis*. John Wiley & Sons.

Schaefer, S., Levin, D., & Goldman, R. (2005). Subdivision Schemes and Attractors. In *Eurographics Symposium on Geometry Processing (2005)*.

Sclaroff, S. & Pentland, A. (1991). Generalized implicit functions for computer graphics. *Computer Graphics, 25*.

Shan, J. & Toth, CK. (2008). *Topographic Laser Ranging and Scanning: Principles and Processing*. CRC.

Shivaswamy, S. (2010). *Finite element analysis and programming: an introduction*. Oxford: Alpha Science International.

Soerjadi, R. (1-1-1968). On the Computation of the Moments of a Polygon, with some Applications.   Delft University of Technology.
Stam, J. & Loop, C. (2003). Quad/triangle subdivision. *Computer Graphics Forum, 22,* 79-85.

Stein, E. (2009). Olgierd C. Zienkiewicz, a pioneer in the development of the finite element method in engineering science. *Steel Construction, 2,* 264-272.

Stone, M. & Goldbart, P. (2002). Calculus of variations. In *Mathematics for Physics. A guided tour for graduate students* (pp. 1-42). Pimander-Casaubon.

Stotz, I., Gouaty, G., & Weinand, Y. (2009). Iterative Geometric Design for Architecture. *Journal of the International Association for Shell and Spatial Structures, 50,* 11-20.

Sun, N. & Weng, F. (2011). Retrieval of Cloud Ice Water Path from Special Sensor Microwave Imager/Sounder (SSMIS). *Journal of Applied Meteorology and Climatolog, 51,* 366-379.

Sykorova, A., Sarka, E., Bubnik, Z., Schejbal, M., & Dostalek, P. (2009). Size Distribution of Barley Kernels. *Czech Journal of Food Sciences, 27,* 249-258.

Tian, X., Su, Z., Chen, E., Li, Z., van der Tol, C., Guo, J. et al. (2012). Estimation of forest above-ground biomass using multi-parameter remote sensing data over a cold and arid area. *International Journal of Applied Earth Observation and Geoinformation, 14,* 160-168.

Tobler, R. F., Maierhofer, S., & Wilkie, A. (2002). A multiresolution mesh generation approach for procedural definition of complex geometry. *Shape Modeling International,* 35-43.

van Overveld, C. W. A. M. (1990). Family of recursively defined curves, related to the cubic Bézier curve. *Computer-Aided Design, 22,* 591-597.

van Sint Jan (2007). *Color atlas of skeletal landmark definitions; guidelines for reproducible manual and virtual palpations.* Churchill Livingstone.

Versteeg H.K. & Malalasekera W. (2007). *An introduction to computational fluid dynamics - the finite volume method*. Pearson Eucation Limited.

Viola, R., Zama, F., Tuller, M., & Mesini, E. (2009). Simulation of Incompressible Flow through Rhombohedric Pores. In Excerpt from the Proceedings of the COMSOL Conference 2009 Milan.

Vladimir V.Savchenko, A. A. P. O. G. O. a. T. L. K. (1995). Function representation of solids reconstructed from scattered surface points and contours. *Computer Graphics Forum,* 181-188.

Wadell, H. (1935). Volume, shape, and roundness of quartz particles. *Journal of Geology, 43,* 250-280.

Walton, W. H. (1948). Feret's Statistical Diameter as a Measure of Particle Size. *Nature, 162,* 329-330.

Warren, J. & Schaefer, S. (2004). A factored approach to subdivision surfaces. *Ieee Computer Graphics and Applications, 24,* 74-81.

Warren, J. & Weimer, H. (2001). *Subdivision Methods for Geometric Design: A Constructive Approach*. Morgan Kaufmann.

Wayson, M., Lee, C., Sgouros, g., Treves, S. T., Frey, E., & Bolch, W. E. (2012). Internal photon and electron dosimetry of the newborn patient-a hybrid computational phantom study. *Physicis in Medicine and Biology, 57,* 1433-1457.

Wehr, A. & Lohr, U. (1999). Airborne laser scanning-an introduction and overview. *ISPRS Journal of Photogrammetry & Remote Sensing, 54,* 68-82.

Weinmann, M., Weinmann, M., Hinz, S., & Jutzi, B. (2011). Fast and automatic image-based registration of TLS data. *ISPRS Journal of Photogrammetry and Remote Sensing, 66,* S62-S70.

Woodard, D. L. & Flynn, P. J. (2005). Finger surface as a biometric identifier. *Computer Vision and Image Understanding, 100,* 357-384.

Wu, X. B. & Peters, J. (2004). Interference detection for subdivision surfaces. *Computer Graphics Forum, 23,* 577-584.

Xu, X. G. & Eckerman, K. F. (2010). *Handbook of anatomical models for radiation dosimetry*. New York: Taylor & Francis.

Zienkiewicz, O. C., Taylor, R. L., & Zhu, J. Z. (2005). *The finite element method: its basis and fundamentals*. Elsevier Buttorworth-Heinemaa.

Zorin, D. (2006). Modeling with multiresolution subdivision surfaces. In *International Conference on Computer Graphics and Interactive Techniques* New York University.

Zorin, D., Schröder, P., & Sweldens, W. (2006). Interpolating subdivision for meshes with arbitrary topology. *SIGGRAPH '96: Proceedings of the 23rd annual conference on Computer graphics and interactive techniques,* 189-192.

7.2 SOFTWARE

ANSYS®	A registered trademark of ANSYS, Canonsburg, Pennsylvania, U.S.A.	www.ansys.com
COMSOL Multiphysics®	A registered trademark of COMSOL, Stockholm, SWEDEN.	www.comsol.com
GSI STUDIO®	A registered trademark of Geometry Systems Inc., San Francisco, USA	www.geometrysystems.net
LATENTIX™	A registered trademark of Latent5 Aps, Copenhagen, DENMARK	www.latentix.com
Mathcad®	A registered trademark of PTC Corporate Headquarters, Needham, MA, USA.	www.ptc.com
MATLAB®	A registered trademark of The MathWorks, Natick, MA, USA.	mathworks.com
R	A free software environment for statistical computing and graphics.	www.r-project.org
Rhinoceros®	A registered trademark of Robert McNeel & Associates, Seattle, USA	www.rhino3d.com www.en.na.mcneel.com
STAAD PRO®	A registered trademark of Bentley EMEA Bentley Systems International Ltd., Dublin, Ireland.	www.bentley.com
VeriFinger®	A registered trademark of Neurotechnology, Vilnius, LT-06118, Lithuania	www.neurotechnology.com
3ds Max Design®	A registered trademark of Autodesk Inc., Worldwide Headquarters, San Rafael, CA, USA	usa.autodesk.com

Brøchner, T.: Natural Parameterization, 2013

Department of Engineering   Tel.: +45 4189 3000
Aarhus University
Edison, Finlandsgade 22
8200 Aarhus N
Denmark